The structure and formation of the Tyrrhenian basin in the Western Mediterranean back-arc setting

Formación y estructura de la cuenca del Tirreno en el contexto de retrarco del Mediterráneo Occidental

Manuel Prada Dacasa

Aquesta tesi doctoral està subjecta a la llicència ***Reconeixement- NoComercial 3.0. Espanya de Creative Commons***.

Esta tesis doctoral está sujeta a la licencia ***Reconocimiento - NoComercial 3.0. España de Creative*** **Commons.**

This doctoral thesis is licensed under the ***Creative Commons Attribution-NonCommercial 3.0. Spain License.***

Instituto de Ciencias del Mar

Departament de Geodinàmica i Geofísica

Unidad deTecnología Marina

Barcelona Center for Subsurface Imaging

Consejo Superior de Investigaciones Científicas

The structure and formation of the Tyrrhenian basin in the Western Mediterranean back-arc setting

---

Formación y estructura de la cuenca del Tirreno en el contexto de retrarco del Mediterraneo Occidental

---

Memoria de Tesis Doctoral presentada por

Manuel Prada Dacasa

para optar al grado de Doctor en Geología por la Universidad de Barcelona

Esta memoria se ha realizado dentro del programa de Doctorado de Ciencias de la Tierra de la Universidad de Barcelona bajo la dirección del Dr. Valentí Sallarès Casas y Dr. César Rodríguez Ranero, y bajo la tutela de Pilar Queralt Capdevila

Barcelona, Enero de 2014

Para todo aquel que desee descubrir…

Agradecimientos

Para empezar, quiero agradecer a mis dos directores de Tesis, Valentí y César, el esfuerzo dedicado en mí durante estos cuatro años y medio de Doctorado. A Valentí, por su disposición a ayudar y la confianza depositada en mí, pero sobre todo por ser un buen consejero y maestro, gracias. A César, por enseñarme a ser un poco más exigente conmigo mismo, y por sus lecciones geológicas, su amplia visión me ha permitido "empezar" a comprender algunos de los procesos de formación de cuencas extensivas. Gracias a los dos por haber hecho que el camino sea un poco más llano.

Quiero agradecer también a Nevio por haberme acogido en Bolonia y haber hecho que mi estancia allí sea provechosa. Sus conocimientos de la cuenca Tirrena son realmente extensos y han sido muy útiles para poder finalizar esta tesis. A Bill, por acogerme en Granada, ciudad de la perdición, y compartir conmigo sus conocimientos sobre geología estructural, pero sobre todo por recordarme que la vida no es solo trabajo.

A los Lombardi, por acogerme en su piso de Bolonia. Grazie per tutto, è stato un piacere imparare italianio con voi. A la gente de Granada, Edu, Antonio, Julia, Yasmina, Idaira, Edu, Enric, Moha, Juan Antonio, Flavio,....gracias por haber estado y estar como amig@s.

A Alci, por echarme más que un cable con la sísmica de reflexión y el apasionante mundo del procesado. Por supuesto, gracias a Rafa, por estar siempre dispuesto a ayudar a buscar una solución racional a los problemas. A Hector, por su buen humor y ánimos en estos últimos meses.

A la gent de MT, Maik, Savitri, Estelle, Xavi gràcies per compartir bones experiències durant les campanyes a Olot. A mi galleguiña favorita, Alejandra, por hacer que los desayunos sean más divertidos y estar siempre dispuesta a sentarse a mi lado y ayudarme con todo. A l'Adrià, company de trinxera, gracies per ser un bon amic, i a la Montse, per fer més agradables les guàrdies durant la campanya MEDOC i ajudar-me amb el processat de sísmica de reflexió.

A la gent del despatx, especialment, a la Sara per estar, riure, aconsellar….en fi per estar sempre pessigant-me l'orella. A Jhon por su incombustible y contagiosa energía positiva, y a Guille por sus buen rollo. De verdad gracias.

També agrair al Dani, Sergi, Estela, Jaume, Laura, Clauia, Marina, Naiara, Ximena, Agnese....en fi en general a la gent del CMIMA que han estat allà pel que fos.

A la gent de la Faculat, Aritz, Alba, Meli, Roger, Olga, Oriol, Raul….per compartir birres encara que no continuem el mateix camí.

A los *castañas*, porque a pesar de estar desperdigados por estos mundos seguimos compartiendo buenas experiencias.

Al Marc per ser com un germà i aguantar-me durant més de dos anys de convivència. A la Noe per tallar-me el cabell i ser bona amiga. Al Marco i la Gemma per compartir divertides sessions de Catan. Però sobretot a la Bea, companya de fatiga, qui m'ha aguantat estoicament més que ningú durant l'elaboració d'aquesta tesis, gracies per agafar-me la mà i acompanyar-me en els moments més difícils.

Finalmente, un especial agradecimiento a la familia por comprender que esto de la ciencia absorbe…..Sobretodo, a mi madre, por ser madre y consejera de la vida. A mi padre por los momentos de cine, y a mi hermana por su sonrisa y positividad, gracias. Y a mi abuelo por su interés en lo que hago y por enseñarme con su experiencia a ser un corredor de fondo.

Funding

The author of this thesis benefits from a four-year Jae Pre-Doc fellowship from CSIC between 2009 and 2013. The author was also granted within the framework of the Jae Pre-Doc with the following stays: 2 months at the Istituto di Scienze Marine (IMSAR) of the Consiglio Nazionale delle Ricerche (CNR) in Bologna (Italy), and 3 months at the Department of Geodynamics of the University of Granada (Spain). The Jae Pre-Doc was supported by the MEDOC project and the Complementary Action OSMART, which were funded by the Spanish Ministry of Science and Education, with reference CTM2007-66179-C02-01/MAR and CTM2007-66179-C02-02/MAR, and CTM2009-07772-E/MAR, respectively. The data used in this work was acquired within the MEDOC project onboard of the R/V Sarmiento de Gamboa and R/V Urania. This work was also supported by project CO-DOS funded by Repsol, the Grup de Recerca de la Generalitat de Catalunya (2009SGR146), and by the International Correlation Programme (IGCP) Project 559.

CONTENTS

SUMMARY i

Part I: Introduction 1

Chapter 1: General Introduction 3

1.1 Background and motivations 3

1.2 Objectives 7

1.3 Basic concepts 9

1.3.1 Plate tectonics 9

1.3.1.1 Extension and continental rifting at divergent boundaries 11

1.3.1.2 Subduction at convergent boundaries 14

1.3.1.2.1 Slab rollback 16

1.3.1.2.2 Back-arc basins 17

1.3.2 Nature of the basement 21

1.3.2.1 Continental crust 22

1.3.2.2 Oceanic crust 27

1.3.2.3 Exhumed mantle 30

Chapter 2: Geological & Geodynamics setting 35

2.1 The Western Mediterranean back-arc basins 35

2.2 The Tyrrhenian back-arc basin 38

2.2.1 Geodynamic evolution of the Tyrrhenian basin region 39

2.2.2 Tectonic setting of the Tyrrhenian basin 40

2.2.3 Previous work on the rock-type distribution of the Tyrrhenian basin 46

2.2.4 Neogene-Quaternaty Volcanism 54

Part II: Methodology 59

Chapter 3: Acquisition & Modeling of Wide-Angle Seismics 61

3.1 Introduction 61

3.2 Acquisition system 61

3.3 Wide-Angle seismic data processing and seismic phase identification 65

3.4 Wide-Angle seismic modeling 67

    3.4.1 Layer-stripping strategy 72

    3.4.2 Uncertainty analysis 73

Chapter 4: Gravity 77

4.1 Introduction 77

4.2 Data acquisition and corrections 77

4.3 Empirical relationships between compressional-wave velocity (Vp) and density (ρ) 79

4.4 Gravity modeling 82

Chapter 5: Acquisition, Analysis & Processing of Multichannel Seismics 85

5.1 Introduction 85

5.2 Acquisition system and geometry of the experiment 85

5.3 Data processing 89

Part III: Results & Discussion 105

Chapter 6: Line GH/MEDOC-6 107

6.1 Data analysis 107

    6.1.1 Wide-Angle Seismic Data 108

6.2 Results 109

    6.2.1 Velocity structure 109

        6.2.1.1 Uncertainty analysis 112

    6.2.2 Tectonic structure 113

    6.2.3 Automatized interpretation of basement affinity based on P-wave depth-velocity profiles 123

    6.2.4 Density structure 126

6.3 Characterization of geological domains along Line GH/MEDOC-6 128

6.3.1 The continental margins of Sardinia (Domain 1) and Campania (Domain 5) 128

6.3.2 Magmatic crust in the Cornaglia Terrace (Domain 2) and the Campania Terrace (Domain 4) 129

6.3.3 Exhumed mantle-rock basement at the Magnaghi and Vavilov basins (Domain 3) 130

6.3.4 Volcanic intrusions in mantle-rock basement 132

Chapter 7: Line EF/MEDOC-4 135

7.1 Data analysis 135

7.1.1 Wide-Angle Seismic Data 135

7.2 Results 138

7.2.1 Velocity structure 138

7.2.1.1 Uncertainty analysis 141

7.2.2 Tectonic structure 142

7.2.3 Automatized interpretation of the basement affinity based on P-wave depth-velocity profiles 151

7.2.4 Density structure 154

7.3 Characterization of geological domains along Line EF/MEDOC 4 156

7.3.1 Contiental crust in the Sardinia and Campania margins, and the Sechi segment (Domains 1a, 1b, and 5) 156

7.3.2 Magmatic back-arc crust in the Cornaglia and Campania Terraces (Domains 2a and 4), and in the Farfalla segment (Domain 2b) 157

7.3.3 Possible presence of exhumed mantle rocks at the northernmost Vavilov basin (Domain 3) 158

Chapter 8: Geological domains of the Central Tyrrhenian: Geodynamic implications 159

8.1 Distribution of the geological domains in the Central Tyrrhenian basin 159

8.1.1 Continental crust 160

8.1.2 Magmatic back-arc crust 164

8.1.3 Exhumed mantle 166

8.2 Implications of the new geological domains defined in the Central Tyrrhenian basin 167

8.3 Conceptual model of the basement formation in the Central Tyrrhenian basin 169

Part IV: Conclusions 175

Chapter 9: Conclusions 177

9.1 Geophysical cross-sections 177

9.2 Basement formation model 180

Chapter 10: Outlook 183

10.1 Geophysical transects 183

10.2 Drilling and dredging 185

10.3 Numerical Modeling 186

Part V: References 189

ANNEX 207

A.1 Wide-Angle Seismic record sections 209

A.1.1. Line GH 209

A.1.2 Line EF 240

A.2 Multichannel Seismic profiles 273

A.2.1 MEDOC 6 273

A.2.2 MEDOC 4 275

A.2.2.1 MEDOC 4 Processing evolution 277

Summary

In this thesis I present a geophysical study that aims to define the structure and petrological nature of the main geological domains in the Central Tyrrhenian basin, and to investigate the mechanisms involved in their formation.

The geophysical data used in this thesis was acquired during the MEDOC (2010) survey within the framework of the MEDOC project, which was designed to improve our understanding of the origin and evolution of rifted margins. The MEDOC survey was focused on the Tyrrhenian back-arc basin, an extraordinary natural laboratory to investigate the structure and evolution of back-arc basins, and hence rifted margins, since 1) extension evolves from north to south [Kastens and Mascle, 1990], 2) the original structure is preserved, and 3) it is small enough to be investigated with a single marine survey.

The present work is based on the analysis, processing, modeling, and interpretation of coincident Wide-Angle Seismic (WAS), Multichannel Seismic (MCS), and gravity data corresponding to the two longest transects acquired during the MEDOC survey in the Central Tyrrhenian basin, the southern Line GH/MEDOC-6 (~450 km) and the northern Line EF/MEDOC-4 (~400 km). Both lines run across the Central Tyrrhenian basin from Sardinia to the Campania margin.

The processing of MCS data provides the tectonic structure and geometry of the sedimentary basins, whereas the modeling of WAS data from travel-time tomography provides 2D seismic velocity models from which the velocity distribution of the crust and uppermost mantle, and the geometry of the crust-mantle boundary are inferred. The WAS models are then converted to density models using existing empirical relationships for different lithologies in order to test which of the different hypothesis concerning the petrological nature of the basement (e.g. continental/oceanic crust or exhumed mantle) explain better the observed gravity data. The results obtained from the MCS, WAS and gravity data of each line, have been complemented with a thorough analysis of the velocities of the WAS-derived models, which consisted of comparing the depth-velocity structure of the models with existing 1D velocity-depth references of continental and oceanic crust, and exhumed mantle [White et al., 1992; Christensen and Mooney, 1995; Dean et al., 2001; Sallarès et al., 2013a]. All these results, together with the integration of geological data from rock sampling of the seabed [Colantoni et al.,

1981; Kastens and Mascle, 1990] reveals the existence of three geological domains in the Central Tyrrhenian, that is: continental crust, magmatic crust, and exhumed mantle.

Along both lines, **continental crust** is observed beneath the island of Sardinia, and beneath the Sardinia and Campania margins. In Sardinia the crust is ~25 km thick, whereas in the margins the crust thins toward the center of the basin from 25-22 km to 10-13 km thick, implying a stretching factor $\beta > 2$. Only in the northern Line EF/MEDOC-4, continental crust is observed in between both continental margins, in the so-called Sechi segment, being ~8 km thick ($\beta > 3$).

The **magmatic crust** is observed beneath the Cornaglia Terrace and the new-defined Campania Terrace in both lines. This type of crust is characterize by a seismic velocity structure that closely resembles to an oceanic crust (e.g. Atlantic oceanic crust) [White et al., 1990], but with lower velocity gradient in the L3 region. Based on observations made in other back-arc basins of the world, such as in the western Pacific [e.g. Martinez et al., 2007], it is suggested in this thesis that this type of crust could be formed by back-arc rifting and/or back-arc spreading processes near the volcanic arc, so that its formation would be influenced by two types of magmas: 1) those produced by pressure-release melting or related with the passive decompression of the underlying mantle, and 2) those produced by hydrous flux melting or derived from the subducted slab.

The **exhumed mantle** domain is observed beneath the V-shaped Magnaghi and Vavilov basins. The basement beneath these basins is characterized by the lack of Moho reflections in both WAS and MCS data and by a vertical velocity structure similar to other regions where basement is made of serpentinized mantle [Dean et al., 200; Sallarès et al., 2013a]. Additionally, this domain hosts large basaltic structures (i.e. Magnaghi and Vavilov seamounts, and D'Ancona and Gortani Ridges) that are intersected by Line GH/MEDOC-6, and hence imaged in depth by the velocity model.

The comparison between the results of Line EF/MEDOC-4 (northern line) with those of the Line GH/MEDOC-6 (southern line) reveals that the velocity and tectonic structure of the three geological domains differ in some regions from north to south. These differences are most likely attributed to the southward increase of extension that characterizes the Tyrrhenian basin [e.g. Faccena et al., 2001; Sartori et al., 2004].

Finally, to explain the mechanism involved in the formation of these domains, I examine the modes of back-arc basin formation proposed to explain the formation of the western Pacific basins [Martinez et al., 2007; Dunn and Martinez, 2011], as well as the causes that may have led to mantle exhumation [Pérez-Gussinyé, et al., 2006]. In summary, the proposed conceptual model is based on a slab rollback and depleted mantle setting, in which production of extension-related melting is limited, thus, crustal accretion is attributed to hydrous flux melting. The model presents 5 stages of opening that includes: **(I)** a normal subduction scenario followed by **(II)** development of back-arc rift, **(III)** initiation of back-arc spreading, **(IV)** mantle exhumation, and finally **(V)** emplacement of large volcanic edifices in the central parts of the basin.

In summary, the basement configuration presented in this thesis led to a completely new definition of geological domains in the Central Tyrrhenian. According to the presented distribution of the basement, rifting in the Central Tyrrhenian basin would have started with continental crust extension, continued with back-arc spreading leading to generation of magmatic back-arc crust, and followed by mantle exhumation intruded by later magmatic episodes. The interpretation of these results differ from current conceptual models of the formation of rifting systems involving mantle exhumation and indicate that the response of the continental lithosphere to extension processes may be more complex than previously assumed.

Part I:

Introduction

Chapter 1: General Introduction

1.1 Background and motivations

Rifted continental margins are one of the most distinctive morphological features of the world's oceans, being the location of the transition between continental and oceanic crust. They are also globally the location of the largest accumulations of sediments and hence represent one of the remaining frontiers to find substantial geological resources, especially hydrocarbons. Additionally, as they undergo slope instability processes , rifted continental margins also represent a source of natural hazards, particularly to coastal communities. Because of their overall significance in many aspects of high scientific and societal relevance, a large number of recent international programs such as the GeoPRISMS (US), IODP (*Integrated Ocean Drilling Program and the new Integrated Ocean Discovery Program*), or Euromargins (Europe) have focused on the understanding of processes governing their evolution. Traditionaly, a limited number of continental rifted margins (e.g. west Iberia, Newfoundland, Western Mediterranean) have been the goal of interdisciplinary geophysical studies during the past few decades, to investigate their structure and internal architecture, their nature [e.g. Boillot et al., 1987b; Reston et al., 1996, Chian et al., 1999; Dean et al., 2000; Pérez-Gusinyé et al., 2003; Van Avendonk et al., 2006; White et al., 2008; Gailler et al., 2009; Sallarès et al., 2011], and their mechanisms of formation [e.g. McKenzie, 1978; Pichon and Sibuet, 1981; Mutter et al., 1988; White and McKenzie, 1989; Pérez-Gusinyé and Reston, 2001; Lavier and Manatschal, 2006; White et al., 2008; Reston, 2007; Ranero and Pérez-Gusinyé, 2010]. In the overall context of formation of rifted margins, back-arc basins represent a particular case of extensional basins that form above subduction zones by rifting and accretion of new volcanic seafloor [e.g. Karig, 1970; Martinez et al., 2007; Dunn and Martinez, 2011].

Despite the large amount of work, there is still significant lack of knowledge on key questions concerning the structure, formation processes and evolution of rifted margins, and particularly of back-arc basins. Some of the most relevant open questions are related with the timing and kinematics of the extension, and with the petrological nature and processes involved in the formation of the continent-ocean transition zone [e.g. Taylor et al., 1995; Benes et al., 1997; Dean et al., 2000; Pérez-Gusinyé and Reston, 2001; Ranero and Pérez-Gusinyé, 2010]. The main motivation of this work is thus to contribute to answer part of these open questions.

In order to contribute to this quest for knowledge, the MEDOC project (Estudio geofísico de las cuencas del **MED**iterráneo **OC**cidental, funded by the National Programme of the former Spanish MICINN under grant number CTM2007-66179-C02) was designed to carry out a geological and geophysical comparative study of the Western Mediterranean back-arc basins to improve our understanding of the origin and evolution of rifted continental margins, in general, and back-arc basins, in particular. The Tyrrhenian basin was selected as a case study area to develop this project because it meets some conditions that make it a natural *laboratory* to investigate the structure and evolution of back-arc basins. The main characteristics that make the Tyrrhenian basin an excellent case study are:

- The basin was formed within the last ~10 million years [e.g. Kastens and Mascle, 1990] and most of the original structure that formed during its evolution is not overprinted by subsequent deformation.

- It has been proposed that the basin structure evolved from north to south from little extended continental crust in the north to full continental break-up and formation of oceanic basins [Kastens and Mascle, 1990], so that it is possible to trade space by time in order to study the temporal evolution of rifting.

- The evolution of the Tyrrhenian basin occurs within a region small enough to be studied within a single marine survey.

Thus, in 2010 an amphibious geophysical survey was carried out in the Tyrrhenian basin within the framework of the MEDOC project (i.e. MEDOC survey) (Figure 1.1). During this survey a total of 17 Multichannel Seismic (MCS) lines with a total length of 2,808 km, and 5 long Wide-Angle Seismic (WAS) profiles crossing the basin from side to side, were acquired with the Spanish R/V Sarmiento de Gamboa, with the support of the Italian R/V Urania. The WAS data were also recorded by several land-stations installed in Corsica and Sardinia. The seismic data were combined with coincident multibeam, sediment profiler and gravity data. The geophysical data were complemented by oceanographic measurements of water properties that were acquired by deploying Conductivity-Depth-Temperature (CTD) profilers and a large number of

Expandable Bathythermographic (XBT). The goal of this experiment was to obtain information on the thermohaline fine-structure of the water layer using recently developed seismic oceanography techniques to better understand the hydrographic system of the Tyrrhenian basin.

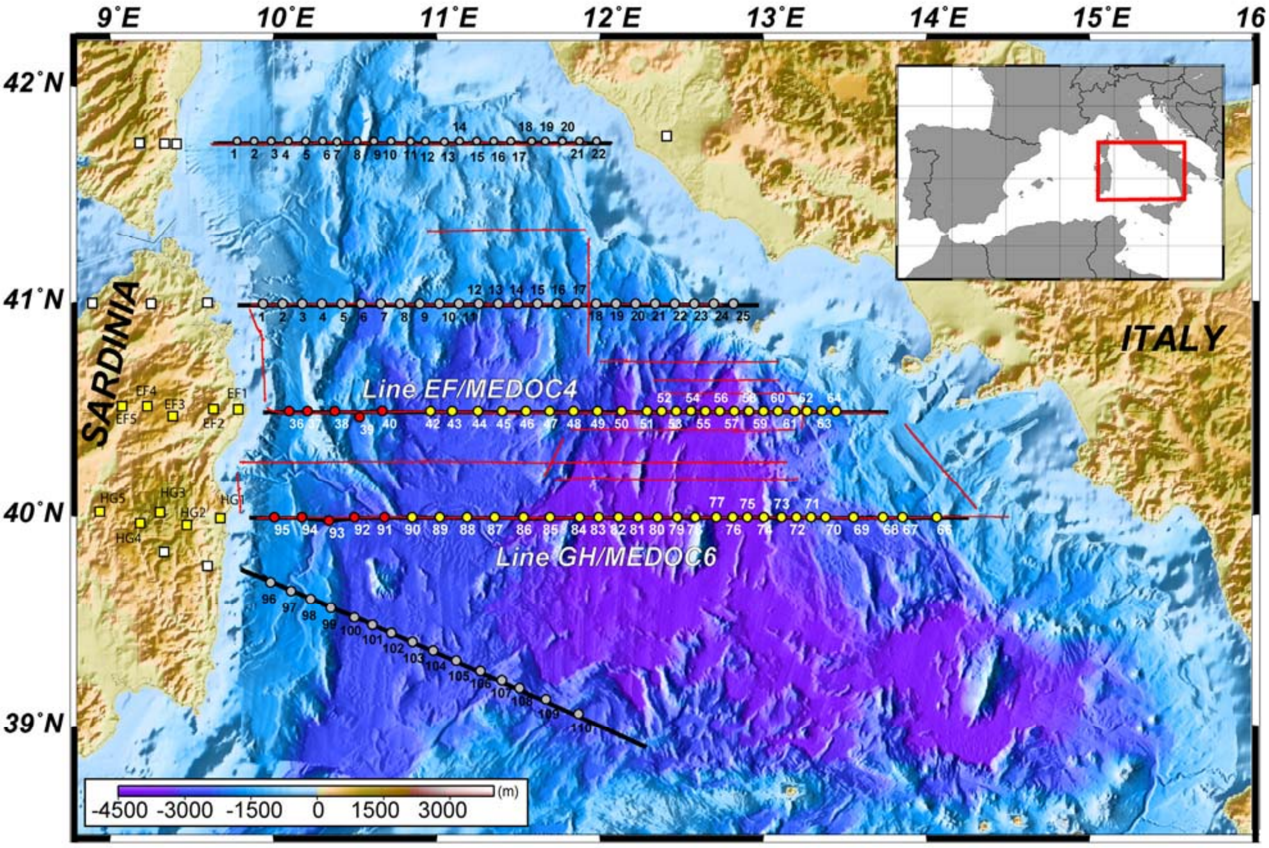

Figure 1.1 .- *Bathymetric and topographic map of the Tyrrhenian Sea located at the eastern region of the Western Mediterranean Sea (see inset). Wide-angle seismic (black thick lines) and multichannel seismic (red lines) profiles acquired during the MEDOC survey are depicted in the image. Lines EF/MEDOC-4 and LineGH/MEDOC-6 are those included in this thesis. Red and yellow circles represent the Ocean Bottom Seismometers (OBS) and Ocean Bottom Hydrophones (OBH), respectively, used to acquire Line EF and GH. Yellow squares define the location of land stations used to complement Line EF and GH on land. Multichannel seismic profiles MEDOC 4 and 6 are coincident with Lines EF and GH, respectively. Grey circles and white squares show the location of the rest of OBS/H and land stations used during the MEDOC survey to accomplish the rest of wide-angle seismic lines.*

The work presented in this thesis consisted on the analysis, processing, modeling, and interpretation of the coincident WAS, MCS and gravity data corresponding to the two longest transects acquired during the MEDOC survey in the Central Tyrrhenian basin, Line GH/MEDOC-6 (~450 km) and Line EF/MEDOC-4

(~400 km) (Figure 1.1). MCS data processing provides the tectonic structure and geometry of the sedimentary basins, whereas the modeling of WAS data provides 2D seismic velocity models from which the velocity distribution of the crust and uppermost mantle, and the geometry of the crust-mantle boundary can be inferred. The WAS velocity models are then converted to density models using existing empirical relationships for different lithologies in order to test which of the different hypotheses concerning the petrological nature of the basement (e.g. continental/oceanic crust or exhumed mantle) explain better the gravity data. Hence, the overall **goals** of the work are:

I. To define the crustal structure of the rifted continental margin

II. To constrain the petrological nature of the main geological domains across the basin

III. To investigate of the processes involved during the back-arc extension in the Central Tyrrhenian basin

In summary, this study will help to further understand fundamental questions on the mechanisms of rifted margins formation, and particularly those formed in a back-arc setting.

1.2 Objectives

In order to achieve the overall goals defined in the previous section, I have defined the following ***objectives*** with their specific activities and tasks:

I To obtain the seismic velocity distribution of the crust and uppermost mantle across the Central Tyrrhenian basin:

i. Processing, interpretation and modeling of the WAS data corresponding to Line GH and EF to obtain the corresponding 2D seismic velocity models of the crust and uppermost mantle, and the geometry of the crust-mantle boundary.

ii. Quantifying the uncertainty of the velocity model parameters; that is, seismic velocity, and geometry/depth of the crust-mantle boundary.

II To characterize the tectonic structure across the Central Tyrrhenian basin:

iii. Analyzing and processing the MCS data to provide a final time-migrated seismic section.

iv. Combine the information provided by the seismic velocity models (i) with that provided by the MCS time-migrated sections (iii).

III To classify the petrological nature of the main geological domains across the Central Tyrrhenian basin:

v. Defining the most likely lithological affinities of both 2D seismic velocity models by comparing their 1D velocity-depth structure with existing 1D velocity-depth reference profiles for continental crust, oceanic crust, and exhumed mantle regions.

vi. Calculating the density model of the crust and uppermost mantle from both 2D velocity models using empirical seismic velocity-density relationships for the different rock types corresponding to the different crustal affinities defined in (v).

vii. Performing the gravity modeling of the obtained density models (v) to check the consistency with the results obtained in the velocity analysis (iv).

IV To define the spatial distribution of the main geological domains in the Central Tyrrhenian basin and propose the processes that may have lead to their formation:

viii. Integrating all the results obtained from the analysis, processing and modeling of WAS, MCS and gravity data for the different lines to define the distribution of the main geological domains.

ix. Comparing the interpretation of both profiles to determine the variations and limits between the geological domains defined north and south of the Central Tyrrhenian basin. This task will be complemented by integration of rock sampling information and geomorphological observations based on bathymetry to present a plan view distribution of the main geological domains in the region.

x. Investigating the mechanisms involved in the formation of the main geological domains in the Central Tyrrhenian basin and presenting a conceptual model to explain their formation during the opening of the basin as well as their present layout.

1.3 Basic concepts

In this section I introduce some basic concepts that are necessary to understand the geological context of this work. First, I present the fundamentals of rifting at divergent margins, subduction processes, slab rollback, and formation of back-arc basins, which jointly conform the geodynamic setting of the Tyrrhenian basin. Then, I describe the different types of basement affinities that can be found in passive rifted margins to better understand the rationale of the petrological classification.

1.3.1 Plate tectonics

The theory of *plate tectonics* was proposed in the 60's to explain seafloor spreading, a process that explains continental drift, which had been originally proposed in 1915 by Alfred Wagner based on the movement of the Earth's continents relative to each other over geological time [Fowler, 2005]. The theory of plate tectonics states that the Earth's outermost rigid layer, the *lithosphere*, is fragmented into a small number of nearly rigid *plates* that are moving relative to one another as they ride on top of hotter, more viscous material, the *asthenosphere*. This theory describes the large-scale motion of these plates, stating that most of the deformation that results from their motion is accommodated along the edge, or boundary of the plates. Observing the seismicity Earth's map (earthquake activity) (Figure 1.2) one can then define these boundaries, since most of earthquakes and volcanism of the Earth occur along plate boundaries [Fowler, 2005].

There are three types of plate boundaries (Figure 1.3):

1. **Divergent**, where plates move away from each other. At such boundaries new plate material is added to the lithosphere. They are normally represented by *mid-ocean-ridges systems.*
2. **Convergent**, where plates approach each other. Most such boundaries are represented by island-arc systems of *subduction zones*, although some convergent boundaries also occur on land, where are represented by large mountain ranges like the Himalayas.

3. **Conservative**, where lithospheric plates are neither created nor destroyed. In this case plates move laterally relative to each other creating *transform faults.* A well-known example is the San Andreas fault in California, USA.

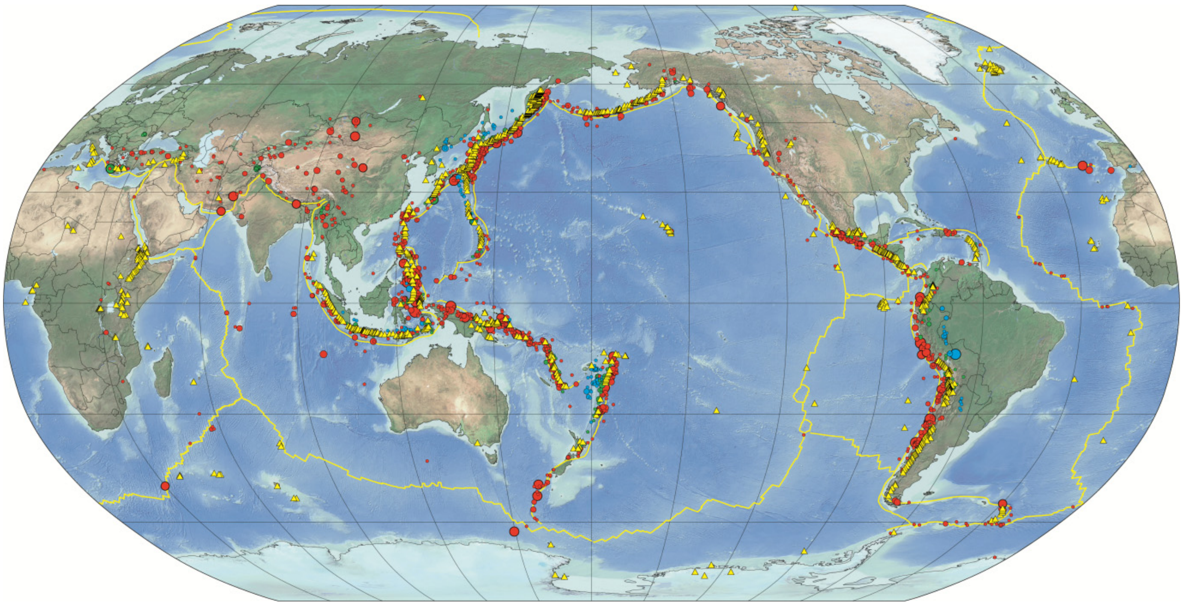

Figure 1.2 .- *Worldwide seismicity map (1900-2012) showing earthquake's epicenters (circles) and volcanism (yellow triangles). Yellow lines define plate boundaries. Extracted from http://earthquake.usgs.gov/earthquakes/world/seismicity_maps/index.php*

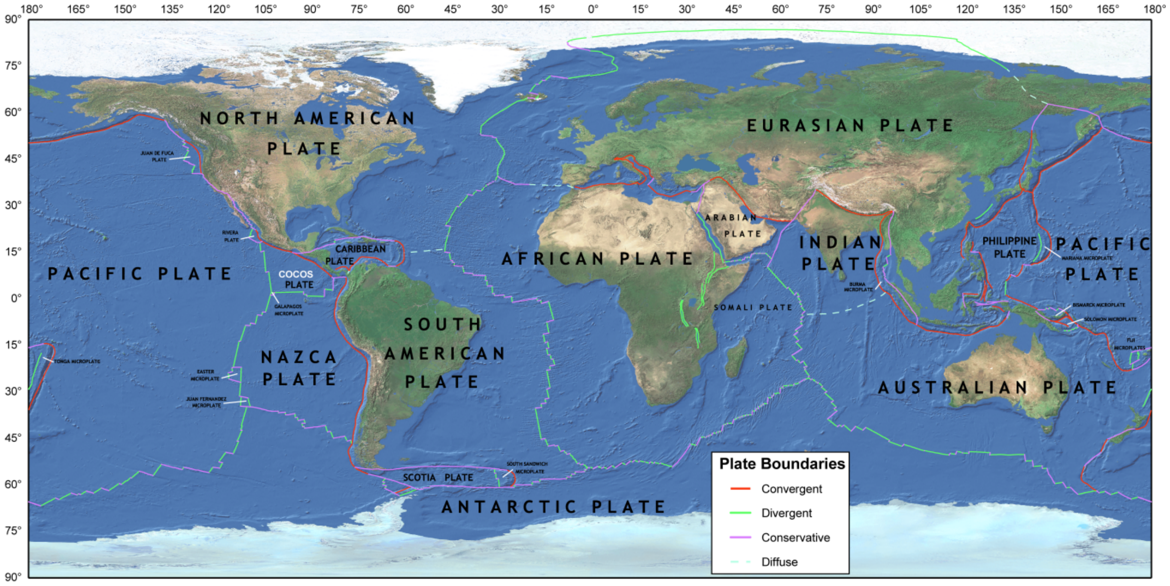
180° 165° 150° 135° 120° 105° 90° 75° 60° 45° 30° 15° 0° 15° 30° 45° 60° 75° 90° 105° 120° 135° 150° 165° 180°
90° 75° 60° 45° 30° 15° 0° 15° 30° 45° 60° 75° 90°
NORTH AMERICAN PLATE
JUAN DE FUCA PLATE
RIVERA PLATE
CARIBBEAN PLATE
COCOS PLATE
GALAPAGOS MICROPLATE
PACIFIC PLATE
TONGA MICROPLATE
EASTER MICROPLATE
JUAN FERNANDEZ MICROPLATE
NAZCA PLATE
SOUTH AMERICAN PLATE
SCOTIA PLATE
SOUTH SANDWICH MICROPLATE
ANTARCTIC PLATE
EURASIAN PLATE
ARABIAN PLATE
AFRICAN PLATE
SOMALI PLATE
INDIAN PLATE
BURMA MICROPLATE
PHILIPPINE PLATE
MARIANA MICROPLATE
PACIFIC PLATE
BISMARCK MICROPLATE
SOLOMON MICROPLATE
FIJI MICROPLATES
AUSTRALIAN PLATE
Plate Boundaries
Convergent
Divergent
Conservative
Diffuse

Figure 1.3.- *Topographic and bathymetric map of the Earth showing the different types of plate boundaries, and the name of each tectonic plate. Modified from http://earthquake.usgs.gov/learn/topics/plate_tectonics/plates.php*

The formation and evolution of all these boundaries are tightly inter-related. This is especially evident in the case of small basins as the Mediterranean ones, where continental extension (i.e. rifting) is triggered by the retreat of subduction fronts. In the next sections I revise the fundamentals of these two processes.

1.3.1.1 Extension and continental rifting at divergent boundaries

Continental rifting, or simply rifting, is the process that occurs when the continental lithosphere is pulled apart by divergent tectonic forces (Figure 1.4). During rifting, the lithosphere stretches with a component roughly perpendicular to the trend of the rift (Figure 1.4). The formation and evolution of rifts depends on many factors including the thermal structure of the mantle, and the mechanical structure of the lithosphere [e.g. McKenzie, 1978; Pluijm and Marshak, 2004].

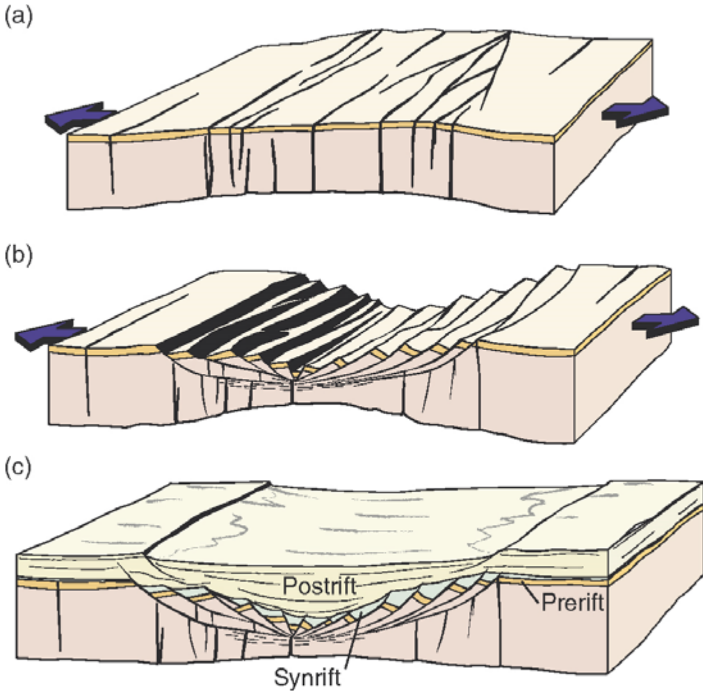

Figure 1.4.- *Conceptual illustration of three stages of rifting. (a) In the early stage, rifting creates or reactivates old fractures. (b) Then, stretching evolves forming major faults. The sediments deposited during this stage are those of the synrift sequence. (c) Finally with the end of rifting, postrift thermal subsidence and sedimentation takes place. Blue lines display the main direction of the divergent tectonic forces responsible of rifting. From Fossen [2010].*

Based on the timing of extension, rifts can be classified as **active** and **inactive rifts**. Active rifts refer to those places where extension currently takes place, like in the East African Rift [Ebinger, 1989]. These rifts are characterized by a notorious seismic activity and by occasional volcanic eruptions. In contrast, inactive rifts are those places where extensional deformation ceased some time ago. This last type includes in turn two subgroups of rifts; those that have stopped before continental break-up, known as **unsuccessful** or **failed rifts**, and those in which extensional deformation completely splits a continent into two pieces, known as **successful rifts**. In this last type, mid-ocean ridges form between two continental margins, and seafloor spreading produces new oceanic lithosphere (see sections 1.3.2.2). Hence, the geometry of successful rifts is characterized by a relict rift that underlies a continental margin on either side of a new oceanic basin (Figure 1.15). These regions are also known as **rifted margins** and are better explained in section 1.3.2.1. Successful rifts are found in the North Atlantic margins [e.g. Louden and Chian, 1999] and in some of the Western Mediterranean basins [e.g. Rollet et al., 2002].

The amount of lithospheric stretching that takes place prior to the full continental break-up is variable. This value is usually measured with the **stretching factor**, β:

$$\beta = l_0/l_1 ,$$

where, l_0 is the undeformed crustal thickness and l_1 the stretched crustal thickness after rifting. Typically, the continental lithosphere stretches by a β factor >3 before full continental break-up and separation [e.g. Pérez-Gussinyé et al., 2003; Pluijm and Marshak, 2004].

Concerning the geometry of rifts, in the pre-70's rift models assumed a **symmetric** system of extensional or normal faults (Figure 1.5). In this model, pairs of normal faults that dip toward each other outline grabens, while pairs of faults that dip away from each other form horst structures (Figure 1.5) [Pluijm and Marshak, 2004; Fossen, 2010]. However, symmetric rifts are rare, modern seismic reflection surveys show that most rifts are typically **asymmetric** [e.g. Ranero and Pérez-Gussinyé, 2010].

The stretching and thinning of the lithosphere results on the formation of elongated troughs, which are filled with large amounts of sediments as they form (Figure 1.4). Hence, the extensional evolution of a rift is reflected in the sedimentary record (Figure 1.4). Based on the timing of deposition three sedimentary sequences can be then differentiated in a rift system: **prerift, synrift**, and **postrift**. The prerift sediments are those deposited prior to extension, while the synrift sequence is constituted by those sediments deposited contemporaneously to extension. These deposits display thickness variations across the growth of faults. Finally, the postrift sequence is deposited after rifting, and is controlled by the geometry of the fault blocks and the thermal subsidence.

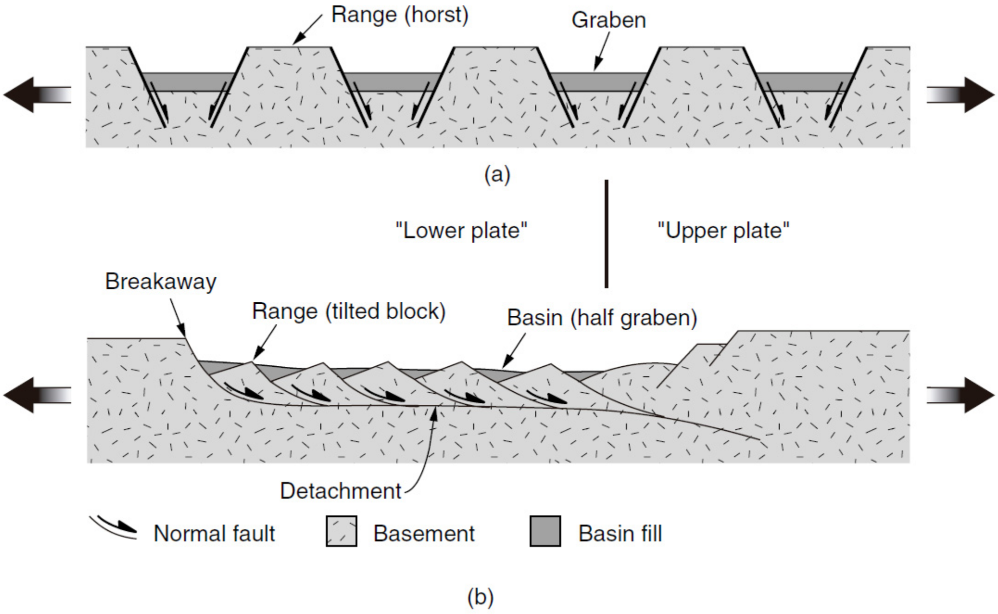

Figure 1.5.- *Cross section illustrating (a) symmetric horst and grabens and (b) the asymmetric model of tilted fault blocks and half grabens, over a detachment fault. Form Pluijm and Marshak [2004].*

Once rifting is over and hence stretching ceases, the thinned lithosphere gradually subsides. This process happens because the lithosphere, which has been heated during extension, cools. With cooling, the lithosphere thickens and thus sinks to maintain isostatic compensation. This process of cooling, thickening, and sinking of the lithosphere is called **thermal subsidence**, and as stated above is one of the parameters that control the postrift sedimentation [McKenzie, 1978].

Another relevant feature of continental rifts is that rifting is often accompanied by variable amounts of melting and igneous activity. This **magmatic activity** is triggered by the decrease of confining pressure in the asthenosphere as a result of progressive thinning of the lithosphere, a process known as **decompression melting**. When decompression occurs, partial melting takes place [e.g. White and McKenzie, 1989]. The magmas produced by this process are less dense than the overlying lithosphere, and thus they rise across it. Part of these magmas get trapped and solidified at the base of the crust, a process called **magmatic underplating**. Decompression melting is also the main process involved in the assemblage and formation of new oceanic lithosphere at mid-ocean ridges (see section 1.3.2.2).

1.3.1.2 Subduction at convergent boundaries

The process of subduction in a convergent boundary occurs when one of the colliding plates moves under another plate and sinks into the mantle (Figure 1.6). Usually the downgoing lithosphere (i.e. slab) is that generated at mid-ocean-ridges (i.e. oceanic lithosphere) that as it moves away from the ocean ridge, cools, thickens, and becomes denser because of the thermal contraction (Figure 1.6) [Turcotte and Schubert, 2002]. The density increase makes the lithosphere gravitationally unstable with respect the hot mantle rocks immediately underlying the lithosphere. Thus, when both plates collide this dense lithosphere begins to bend downward, defining the location of the oceanic trench, and sinks into the mantle; whereas the other plate, which is less dense, remains in the surface overriding the subducting lithosphere (Figure 1.6).

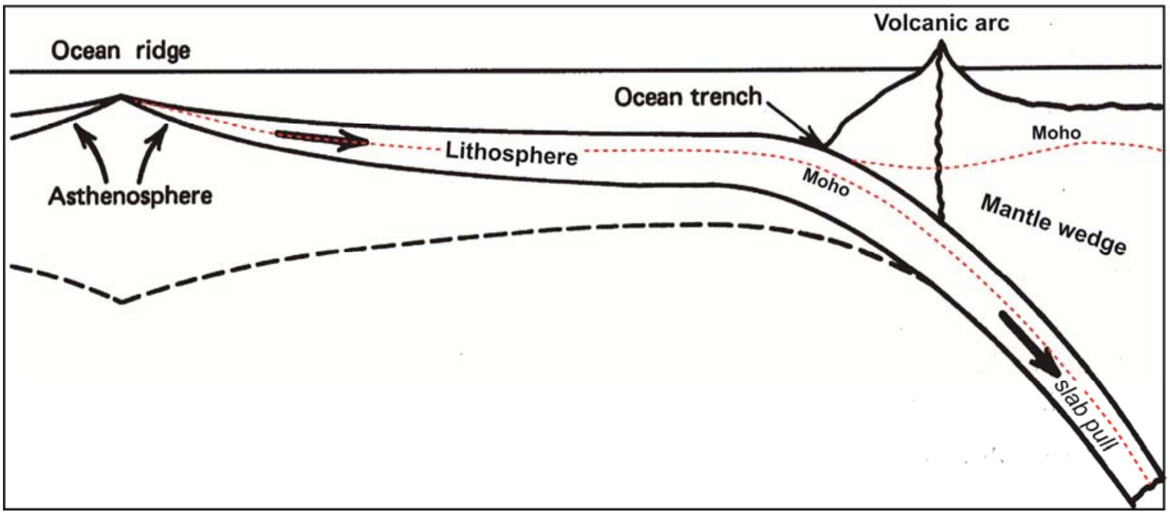

Figure 1.6.- *Cross-section of a conceptual model of creation of lithosphere at mid-ocean ridges, and destruction of it at subduction zones. The sketch shows the location of the oceanic ridge, the oceanic trench, the volcanic arc, the mantle wedge, and the Moho or crust-mantle boundary in red (see section 1.3.2). Modified from Turcotte and Schubert [2002].*

The negative buoyancy of the dense rocks of the descending lithosphere results in a downward body force. Since the lithosphere deforms elastically it may transmit this body force to the surface section of the lithosphere, which is pulled toward the oceanic trench (Figure 1.6). This driving force is also known as **slab pull**, and it is considered to be the main mechanism causing plate tectonics and continental drift (Figure 1.6) [Turcotte and Schubert, 2002].

Subduction velocity may vary from mm yr^{-1} to cm yr^{-1}. The fastest subduction zones are found around the Pacific Ocean, where plates subducts at rates of ~9 cm yr^{-1} [Molnar and Atwater, 1978]. The interaction between the downgoing lithosphere and the surrounding mantle at depths < ~70 km is mostly accommodated by great **subduction earthquakes**, such as the 1960 Chilean earthquake (Mw~9.5) or the more recent 2004 Andaman (Mw~9.1) and 2011 Tohoku (Mw ~9) ones (Magnitudes from the United States Geological Survey "USGS"). Earthquakes within a cold subducted lithosphere are caused by a wealth of mechanisms and extend to depths of ~660 km, defining the so-called **Wadati-Benioff zone** that in turn allows the definition of the location and geometry of the descending slab [e.g. Turcotte and Schubert, 2002].

Another peculiarity of subduction zones is the existence of a line of approximately regularly spaced volcanoes nearly parallel to the oceanic trench. This structure is known as the **volcanic arc** (Figure 1.6). Its distance to the oceanic trench is controlled by the dip angle of the subducting slab (Figure 1.6). Volcanic arcs that are close to the trench are usually related to steep subduction angles, while those located far from the trench indicate flatter subduction angles. The average dip angle for subduction zone is near 45º, which results in a trench-volcanic arc distance of ~175 km [Isack and Barazangi, 1977]. The volcanic arc is built on top of the overriding plate and composed of **slab-derived magmas**. This type of magmas are generated by water released from heating of hydrated minerals of the subducted lithosphere that can contribute to melting by depressing the solidus of adjacent mantle wedge rocks (Figure 1.6) [Turcotte and Schubert, 2002]. The mantle wedge of the overriding plate partially melts and the products rise then buoyantly through the mantle. A fraction of these melts is underplated at the base of the overriding plate crust, another fraction intrudes the overriding plate's crust, and finally the lighter fraction of the melt erupts and forms the volcanic arc.

Subduction zones over the Earth are mainly found around the Pacific Ocean defining a region of nearly continuous series of oceanic trenches and volcanic belts known as the **Ring of Fire** (Figure 1.7). Other regions of the planet governed by this type of plate tectonics are found in the Mediterranean Sea (see Figure 2.1 in chapter 2). In this region, though, subduction is driven by a process known as **slab rollback**, which is also linked to continental rifting and **back-arc basins** formation. The concepts of **slab rollback** and **back-arc basins** are explained in the next sections.

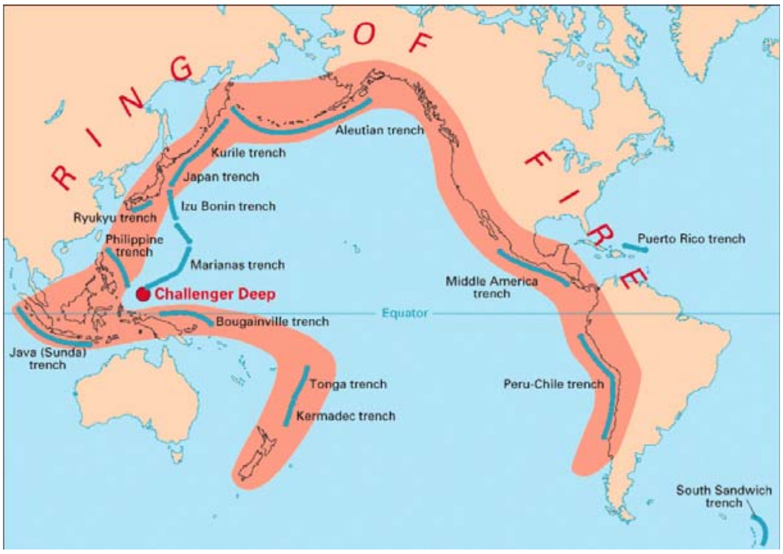
RING OF FIRE
Aleutian trench
Kurile trench
Japan trench
Izu Bonin trench
Ryukyu trench
Philippine trench
Marianas trench
Challenger Deep
Bougainville trench
Equator
Java (Sunda) trench
Tonga trench
Kermadec trench
Middle America trench
Puerto Rico trench
Peru-Chile trench
South Sandwich trench

Figure 1.7.- *Subduction zones(blue lines) around the Pacific ocean forming the so-called Ring of Fire. Extracted from http://pubs.usgs.gov/publications/text/fire.html*

1.3.1.2.1 Slab rollback

As explained in the previous section, the negative buoyancy of the subducted oceanic lithosphere with respect to the surrounding mantle generates the slab pull force (Figure 1.8). The negative buoyancy, and hence the intensity of the slab pull force depend on the density of the lithosphere that in turn increases with the age of the slab [Turcotte and Schubert, 2002; Heuret and Lallemand, 2005].

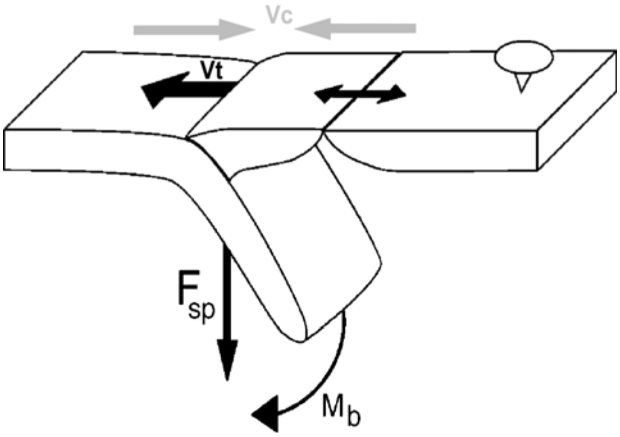

Figure 1.8.- *Slab rollback model. Where,* F_{sp} *represents the slab pull force and* M_b *the bending moment.* ***Vc*** *represents the rate of convergence between plates, and* ***Vt*** *the rate of trench retreat, which is dependent on the age of the slab (i.e. density). When* ***Vc << Vt*** *extension in the overriding region occurs as shown by the sketch, causing back-arc extension. Modified from Heuret and Lallemand [2005]*

Therefore, old oceanic lithospheres are denser than young ones. The negative buoyancy of a given old, dense, and cold oceanic lithosphere results in steep angles of subduction. The steepening of the subduction angle may make that the slab pull force focuses on the vicinity of the bending point, or hinge of the slab, causing a spontaneous retreat of the oceanic trench in surface, which results in **slab rollback** in depth (Figure 1.8) [Mollnar and Atwater, 1978; Royden, 1993].

Slab rollback, then, is controlled by the age of the slab, the older and colder a slab is, the harder it should pull down on the hinge and the faster it should rollback [Heuret and Lallemand, 2005]. Thus, when the rate of slab rollback exceeds plate convergence rate –i.e. the overriding plate is considered to be fixed (Figure 1.8)- subduction fronts (i.e. frontal part of the overriding plate) migrate with the hinge of the slab causing tensional stresses in the overriding plate (Figure 1.8). This occurrence causes extension of the overriding plate and formation of the so-called **back-arc or marginal basins** [Nur et al., 1993; Royden, 1993]. **The Tyrrhenian basin** is an example of basin formed under these circumstances (see chapter 2).

1.3.1.2.2 Back-arc basins

Formation and evolution of back-arc basins has been a matter of discussion in plate tectonics since the 70's. Figure 1.9 illustrates two general concepts or models of back-arc basin formation based on geophysical and geological observations of several well-known examples in the Western Pacific (Figure 1.10).

A first model assumes that they develop in a slab rollback setting (Figure 1.9 left-hand panels), whereas a second model proposes that is the overriding plate the one that moves away from the trench. In this new scenario the slab acts as a sea anchor in the mantle resisting the migration of the oceanic trench [Martinez et al., 2007]. Both models, however, coincide in the fact that extension initiates near the volcanic arc. This is based on the fact that heating of the lithosphere due to intrusions of arc-related magmas weakens the overriding lithosphere sufficiently so that it fails under tensional stresses (Figure 1.9) [Mollnar and Atwater, 1978; Taylor, 1995; Turcotte and Schubert, 2002; Martinez et al., 2007].

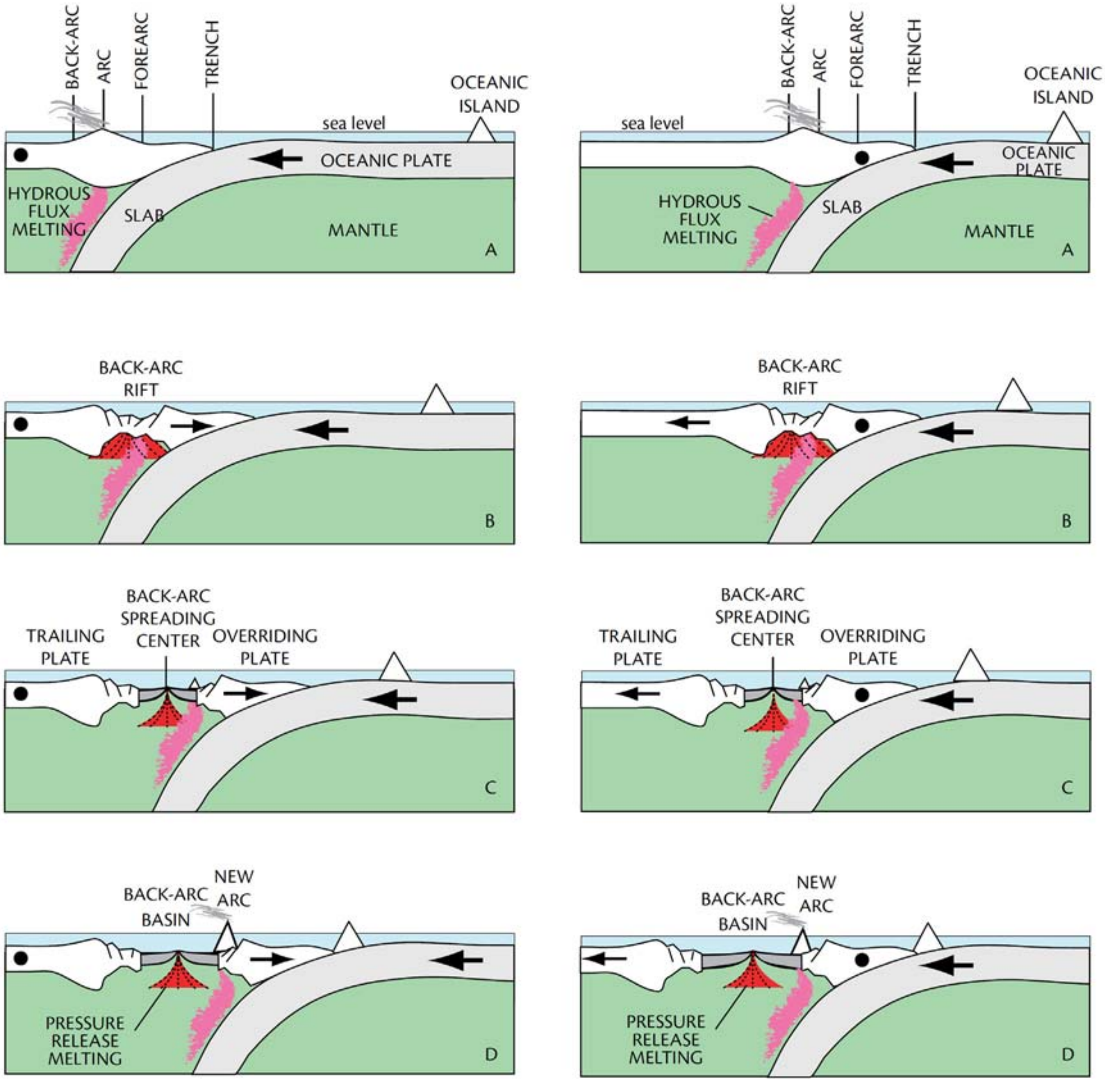
BACK-ARC
ARC
FOREARC
TRENCH
OCEANIC ISLAND
sea level
OCEANIC PLATE
HYDROUS FLUX MELTING
SLAB
MANTLE
A
BACK-ARC
ARC
FOREARC
TRENCH
OCEANIC ISLAND
sea level
OCEANIC PLATE
HYDROUS FLUX MELTING
SLAB
MANTLE
A
BACK-ARC RIFT
B
BACK-ARC RIFT
B
TRAILING PLATE
BACK-ARC SPREADING CENTER
OVERRIDING PLATE
C
TRAILING PLATE
BACK-ARC SPREADING CENTER
OVERRIDING PLATE
C
BACK-ARC BASIN
NEW ARC
PRESSURE RELEASE MELTING
D
BACK-ARC BASIN
NEW ARC
PRESSURE RELEASE MELTING
D

Figure 1.9 .- *Back-arc basin formation models shown in Martinez et al. [2007]. Left-hand panels show the back-arc opening under slab rollback conditions (i.e. proximal stresses). Note that the trailing plate is considered to be fixed (mark with black dot) while the oceanic trench moves away from it. In contrast, right-hand panels show the opening of back-arc basins assuming a slab "sea anchor" model. Here the frontal section of the overriding plate is considered to resist migration due to the slab "sea anchor" force, and hence is represented as the fixed point in the model (black dot). Conversely, the trailing part of the overriding plate migrates to the left causing the onset of back-arc extension (i.e. far-filed stresses). Red and pink areas define the seafloor spreading-like and slab-derived magmas, respectively.*

Regardless of the model that governs the opening of the basin, it has been well-documented in the Western Pacific (Figure 1.10) and the Western Mediterranean (Figure 2.1) that the evolution of back-arc basins has two main stages. In the first and early stage of extension, the crust of the overriding plate is affected by extensional faulting forming a rift (see section 1.3.1.1) [e.g. Taylor, 1995; Parson and Wright, 1996;

Martinez et al., 2007]. During this phase an elongated depression bordered by faults, is created by tensional stresses. Then, in the second, more evolved extensional episode, the continental crust breaks off and spreading centers similar to those found at mid-ocean ridges are generated, forming new oceanic crust (see section 1.3.2.2) (Figure 1.9) [e.g. Taylor, 1995; Taylor et al., 1995; Benes et al., 1997; Martinez et al., 2007].

Additionally, formation of back-arc basins is accompanied by an important magmatic activity. Given that back-arc basins tend to initiate by rifting near the volcanic arc systems, the magmas that build up to construct the new back-arc crust are affected by two different sources: the hydrous flux melting that is associated to the dehydration of the subducted slab (pink area in Figure 1.9), and the pressure release melting that is produced by passive mantle decompression beneath spreading centers (red area in Figure 1.9) [e.g. Taylor, 1995; Martinez et al., 2007; Dunn and Martinez, 2011]. The influence of both sources is observed to be temporally and spatially juxtaposed in most back-arc basins, for example at the Lau basin (Figure 1.9 and 1.10) [Taylor, 1995; Martinez et al., 2007; Dunn and Martinez, 2011].

Regarding the kinematics of back-arc basins (Figure 1.9), their opening appear to be totally controlled by either proximal (Figure 1.9 left-hand panels) or far-field (Figure 1.9 right-hand panels) stresses [Martinez et al., 2007]. That implies that small changes in the whole subduction system results in significant variations on the opening of the basin. This can be clearly seen in the Philippine Sea (Figure 1.10) and in the Western Mediterranean region (see section 2.1). In the Philippine Sea, the Parece Vela and the Mariana Through back-arc basins are the result of the eastward rollback of the Pacific lithosphere. Despite sharing a common setting, both marginal basins display significant differences regarding their geometry (Figure 1.10). Extension in the Parece Vela basin appears to be rather symmetric (E-W), whereas the Mariana Trough displays an asymmetric degree of extension, being widest and hence more extended on its central part [Martinez et al., 1995]. Variations in the degree of extension and geometry of these basins are mainly attributed to changes on the trench geometry (i.e. subduction geometry) that results in important variations of the main stresses that control back-arc opening [Martinez et al., 1995, 2007].

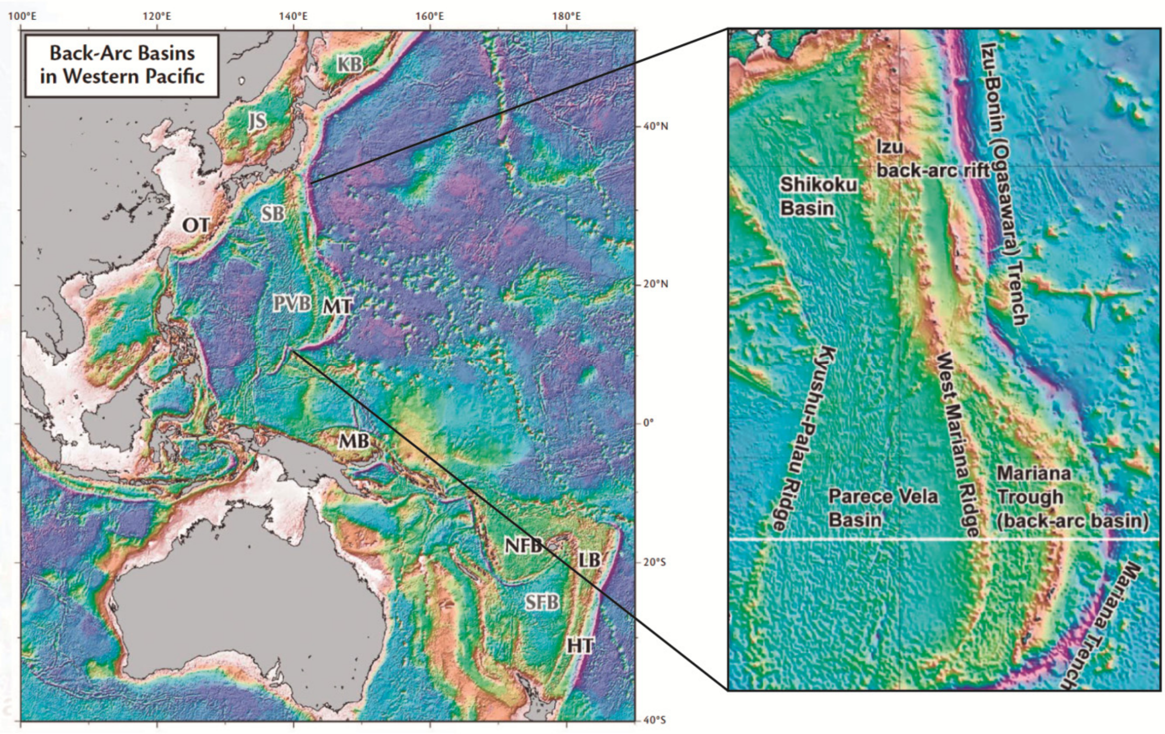
100°E
120°E
140°E
160°E
180°E
Back-Arc Basins
in Western Pacific
KB
JS
40°N
OT
SB
20°N
PVB
MT
0°
MB
NFB
LB
20°S
SFB
HT
40°S
Izu
back-arc rift
Shikoku
Basin
Izu-Bonin (Ogasawara) Trench
Kyushu-Palau Ridge
West Mariana Ridge
Parece Vela
Basin
Mariana
Trough
(back-arc basin)
Mariana Trench

Figure 1.10.- *Right-hand, distribution of the main back-arc basins in the western Pacific. HT= Havre Trough, JS = Japan Sea, KB = Kurile Basin, LB = Lau Basin, MB = Manus Basin, MT = Mariana Trough, NFB = North Fiji Basin, PVB = Parece Vela Basin, SB = Shikoku Basin, SFB = South Fiji Basin, and OT = Okinawa Trough. Left-hand, zoom of the Shikoku, Parece Vela, and Mariana Trough back-arc basins. Modified from Martinez et al. [2007].*

The Western Mediterranean basins also show this behavior, their geometry appears to be the result of changes in the subduction system configuration (Figure 2.1) [Rosenbaum et al., 2002; Jolivet et al., 2008; Schettino and Turco, 2011]. A more detailed description of these basins is presented in *chapter 2*.

1.3.2 Nature of the basement

Before introducing the concepts of this section, it is important to note the difference between lithosphere, crust and mantle, and to introduce the concept of basement. As stated before, the lithosphere is the rigid outermost shell of the Earth, and it is composed by the crust and uppermost mantle, being both chemically different (Figure 1.11). While the crust is constituted by a great variety of igneous, metamorphic and sedimentary rocks, the underlying rigid mantle is mainly formed by peridotite, a rock denser than those commonly found in the crust. The term **basement** is generally used to define those metamorphic or igneous rocks that underlie the sedimentary cover, although in petroleum geology it may also refer to the non-prospective rocks that lie below the strata of interest [Allaby, 2008].

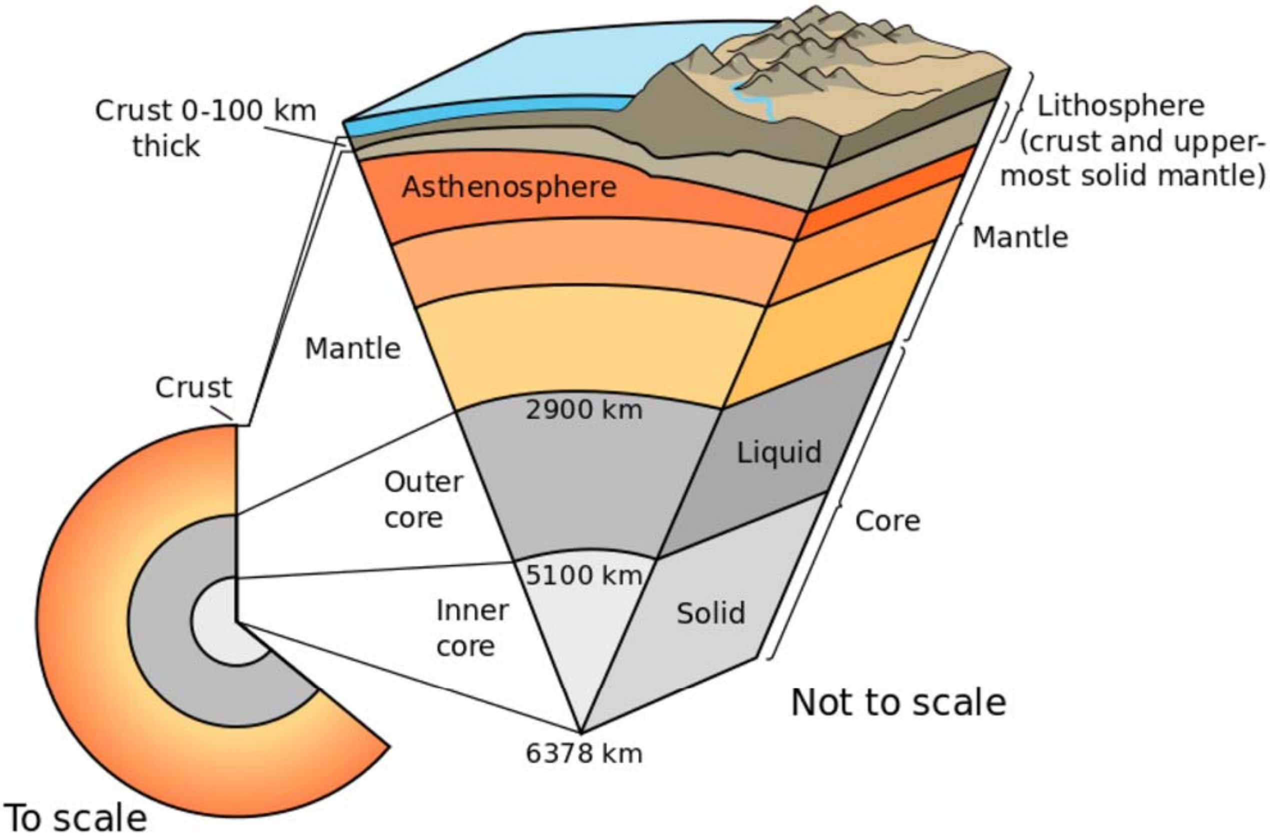
Crust 0-100 km thick
Asthenosphere
Lithosphere (crust and uppermost solid mantle)
Mantle
Mantle
Crust
2900 km
Liquid
Outer core
Core
5100 km
Inner core
Solid
Not to scale
6378 km
To scale

Figure 1.11.- *Earth's internal structure showing the distribution of the crust, mantle and core; the lithosphere and the asthenosphere are also represented in the not scaled drawn (right figure). Extracted from http://pubs.usgs.gov/gip/dynamic/inside.html*

The nature of the basement is defined by its rock's composition, which can be in turn determined by direct rock sampling and geochemical analysis. In the absence of rock samples, the composition can be also inferred using indirect geophysical methods, which allow inferring physical parameters that are characteristic of different rock types such as the seismic velocity, the rock density, or the gradients of these properties with depth. However, those properties are not univocal, meaning that many different rock types may have the same velocity or density values (e.g. Carlson and Herrick, 1990). A way to mitigate this issue is using empirical relationships that relate between them the physical properties for a given rock type. There exist a number of such relationships for seismic velocity and density for the most common oceanic and continental rock types [e.g. Carlson and Herrick, 1990; Christensen and Mooney, 1995]. Overall, an appropriate and realistic strategy to infer the nature of the basement in marine studies is to combine rock sampling information of the seabed from dredging or oceanic drilling with complementary geophysical information provided by methods such as wide-angle seismic (WAS) or gravity measurements (see chapters 3 and 4).

Based on geophysical and geological observations the most common affinities of the basement found in rifted margins and back-arc settings are: continental and oceanic crust, and exhumed mantle rocks [e.g. Boillot et al., 1980, 1987a; Beslier et al., 1993; Taylor et al., 1995; Benes et al., 1997]. In the following section I describe all of them in detail.

1.3.2.1 Continental crust

This type of crust is formed from mantle material over the geological time by a series multiple episodes of accretion, deformation, erosion, metamorphism, plutonism, and volcanism.

Based on the Wilson’s cycle (Figure 1.12), origin and growth of continental crust occurs at convergent plate boundaries. In subduction zones, arc volcanism provides new crustal material from slab-derived magmas making the overriding lithosphere thicker. Then, when subduction consumes all the oceanic lithosphere, both continental masses collide resulting in a complex orogenic belt like the Himalayas (Figure 1.12) [e.g. Taylor, 1967; Allaby, 2008].

Because of the numerous processes involved in its formation, the lithological composition of continental crust includes a wide variety of igneous, metamorphic, and sedimentary rocks. In general, continental crust presents a felsic bulk composition, which means that is relatively rich in elements that form feldspar and quartz (i.e. Si, Al, O, K, and Na).

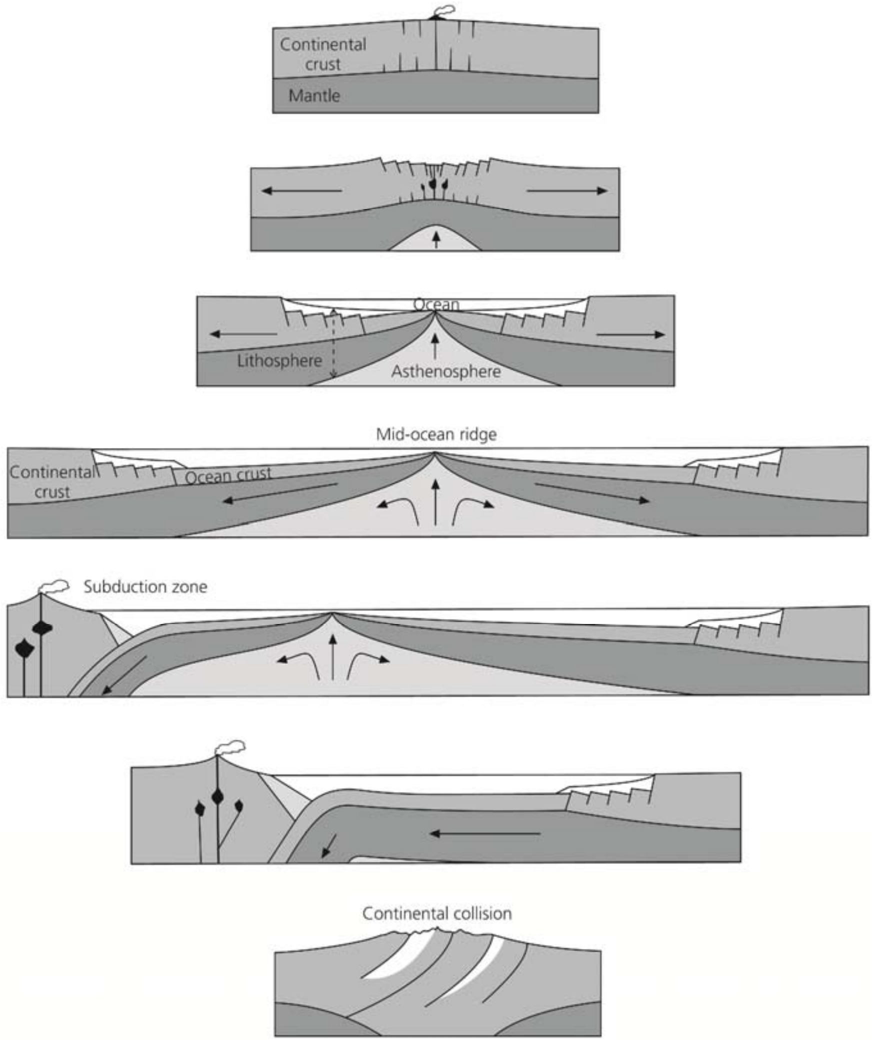
Continental crust
Mantle
Ocean
Lithosphere
Asthenosphere
Mid-ocean ridge
Continental crust
Ocean crust
Subduction zone
Continental collision

Figure 1.12.- *Schematic diagram of the Wilson's Cycle illustrating the evolution of continental crust, from rifting and formation of oceanic crust to subduction and continental collision. From http://www.earth.northwestern.edu/people/seth/202/new_2004/wilson_cycle.html*

Christensen and Mooney [1995] inferred an overall composition for continental crust by comparing results from a large number of WAS profiles, acquired in different tectonic provinces (Figure 1.13), with high-pressure laboratory measurements of P-wave seismic velocity of a wide range of rocks commonly found in continental crust. In summary, the authors conclude that in the upper crust, that is the first 10 km, P-wave seismic velocities usually range between 5.9-6.3 km/s (Figure 1.13), matching with granitic and low-grade metamorphic rocks. Beneath, in the middle and lower crust the average velocity increases and ranges between 6.5 and 6.8 km/s (Figure 1.13). These velocities match with metamorphic rocks like gneiss and amphibolites in the mid-crust, and gabbros at the lower crust. Therefore, the authors attribute the increase of velocity gradient to an increase in the metamorphic grade and a decrease in the silica content. Finally, the compositional difference between the felsic crust and the mantle peridotite is represented by sharp velocity contrast, where velocities jump from ~6.8 km/s to 8.0-8.2 km/s [Christensen and Mooney, 1995; Fowler, 2005]. Crustal density for this compositional model increases from 2.6 kg/cm^3 at surface to 3.1 kg/cm^3 at the base of the crust [Christensen and Mooney, 1995], which is in agreement with propositions that state that the average density for continental crust ranges between 2.7-3.0 kg/cm^3 [Allaby, 2008].

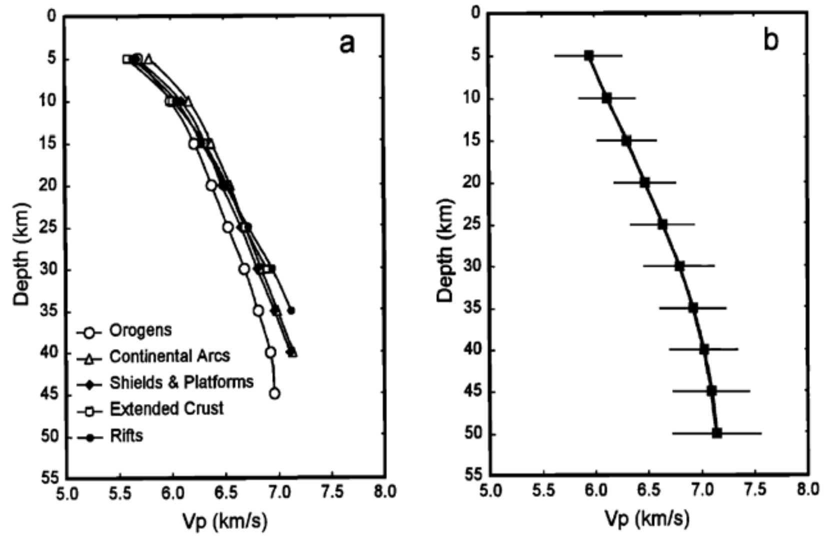

Figure 1.13.- *Average velocities versus depth of (a) five different tectonic provinces and (b) reference average crustal model compiled from weighted tectonic provinces at 5-km interval. Extracted from Christensen and Mooney [1995]*

The global average thickness for a continental crust ranges between 30 and 40 km [Christensen and Mooney, 1995; Fowler, 2005; Allaby, 2008]. However, continental crust may be affected by rifting, and become thinner due to tensional forces as described in section 1.3.1.1 (e.g. Great Rift Valley in Africa).

It is noteworthy that all of these features, seismic velocity, density, and thickness, may vary considerably depending on the tectonic framework that governs the continental crust. Figure 1.14 illustrates the general variations of velocity and thickness at different tectonic provinces. Lowermost crustal velocities of 7.0 km/s or higher that are observed in several settings such are arcs, rifts or rifted margins are commonly associated to magmatic underplating so they do not fit into the lithological classification referred to above.

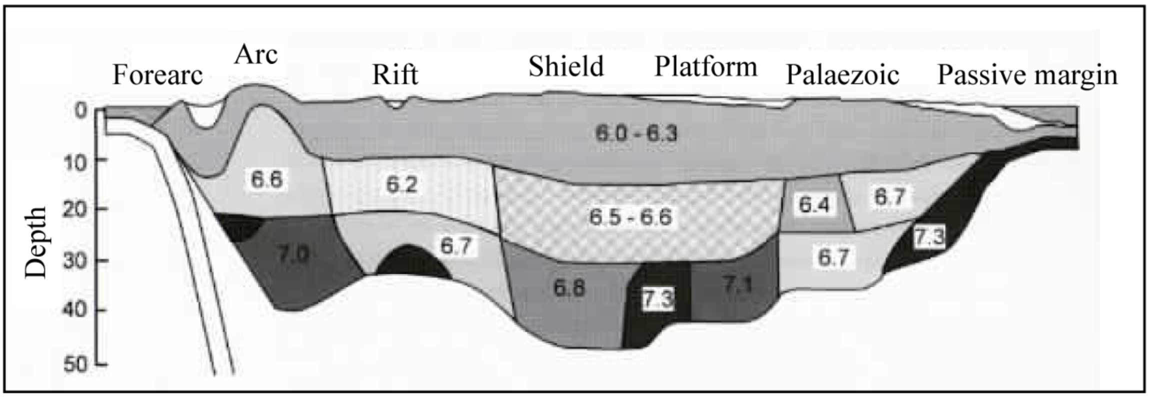

Figure 1.14.- *Cross section of an idealized continental crust showing the average P-wave velocity structure of different tectonic regions. Extracted from Fowler [2005].*

Transition between continental crust and oceanic crust, occurs in active margins and rifted continental margins (Figure 1.15). In active margins the crustal boundary between oceanic and continental crust is defined by active plate boundaries in convergent margins like subduction zones (see section 1.3.1.2 and Figure 1.6). In contrast, the continent-ocean boundary along rifted margins occurs along progressively rifted and extended continental crust that ultimately breaks apart and transitions to oceanic crust. Rifted margins are classified in two types depending on the degree of extension-related magmatism that is produced during the extension, that is: volcanic and non-volcanic rifted margins.

Volcanic margins are characterized by the generation of large amounts of magmas during their formation that are emplaced on top or at the base of the crust. The large amounts of magma produced in these types of margins cannot be explained only by decompression melting. Three primary hypothesis exist that account for this excessive magmatism, these are 1) mantle plume with elevated temperatures [White and McKenzie, 1989; White et al., 2008]; 2) small-scale convection at the base of the lithosphere [Mutter et al., 1988; King and Anderson, 1995]; and 3) heterogeneities in mantle source composition [Korenaga and Kelemen, 2000; Korenaga, 2004]. Independently of the process involved in the formation of the margin, volcanic margins are characterized by a narrow continent-ocean transition (COT) zone marked by the presence of lower crustal bodies interpreted as magmatic underplating [Geoffroy, 2005; Gernigon et al., 2006].

In contrast, non-volcanic rifted margins do not present such features. Instead, they are hyper-extended, characterized by polyphase and diachronous rifting, detachment faulting, and fault-bounded basement blocks that progressively thin towards the center of the basin [e.g. Reston et al., 1996; Louden and Chian, 1999; Tucholke et al., 2007]. In this case, the COT occurs more progressively along a wide (~100-200 km-long) region where the mantle can eventually be exhumed without any associated melting due to the progressive extension (see section 1.3.2.3) [e.g. Boillot et al., 1987b; Pérez-Gussinyé and Reston, 2001; Tucholke et al., 2007]. Figure 1.15 summarizes the overall crustal structure along volcanic and non-volcanic rifted margins.

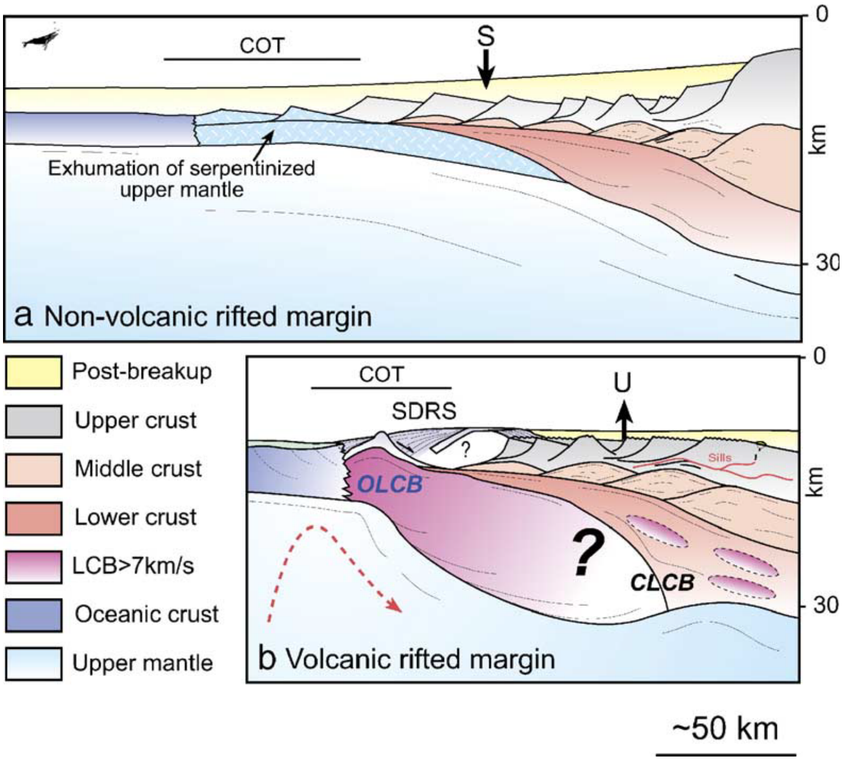
COT
S
Exhumation of serpentinized upper mantle
0
km
30
a Non-volcanic rifted margin
Post-breakup
Upper crust
Middle crust
Lower crust
LCB>7km/s
Oceanic crust
Upper mantle
COT
SDRS
U
?
OLCB
?
CLCB
Sills
0
km
30
b Volcanic rifted margin
~50 km

Figure 1.15.- *Conceptual sketch of (a) non-volcanic and (b) volcanic rifted or rifted continental margins structure showing the COT in both cases. CLCB: continental part of lower crustal body; OLCB: transitional–oceanic part of the lower crustal body; SDRS: seaward dipping reflectors. (S) Symbolizes the thermal subsidence of the non-volcanic margin; (U) represents the relative uplift recorded along the volcanic margin. From Gernigon et al. [2006]*

1.3.2.2 Oceanic crust

As explained in section 1.3.1.1, oceanic lithosphere, and hence, oceanic crust is formed at mid-ocean ridges along divergent boundaries. These structures are chains of undersea mountains with a total length of over 60.000 km [Fowler, 2005]. In contrast with subduction zones, mid-ocean ridges mark the constructive boundaries of plates. In these regions, hot melt produced by the passive decompression of mantle rocks rises from the asthenosphere along the axis of the ridge, and fills the space left by the separating plates; as this melt cools, it forms new oceanic crust (Figure 1.16).

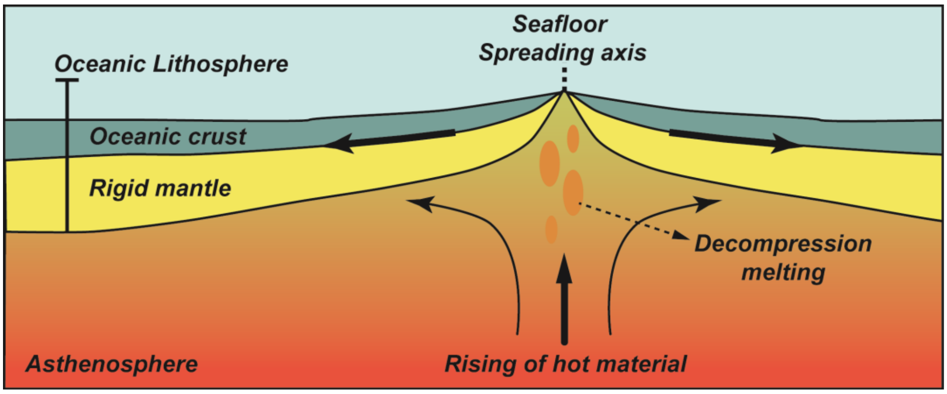
Seafloor
Spreading axis
Oceanic Lithosphere
Oceanic crust
Rigid mantle
Decompression melting
Asthenosphere
Rising of hot material

Figure 1.16.- *Basic sketch of the formation of oceanic crust in a mid-ocean ridge*

A large amount of WAS data correlated with rock sampling information provided by several surveys of the Ocean Drilling Program (ODP) and the Deep Sea Drilling Project (DSDP) among others, have determined that the oceanic crustal structure, lithology and composition are much more uniform than that of continental crust [Kennett, 1982; Bratt and Purdy, 1984; White et al., 1992].

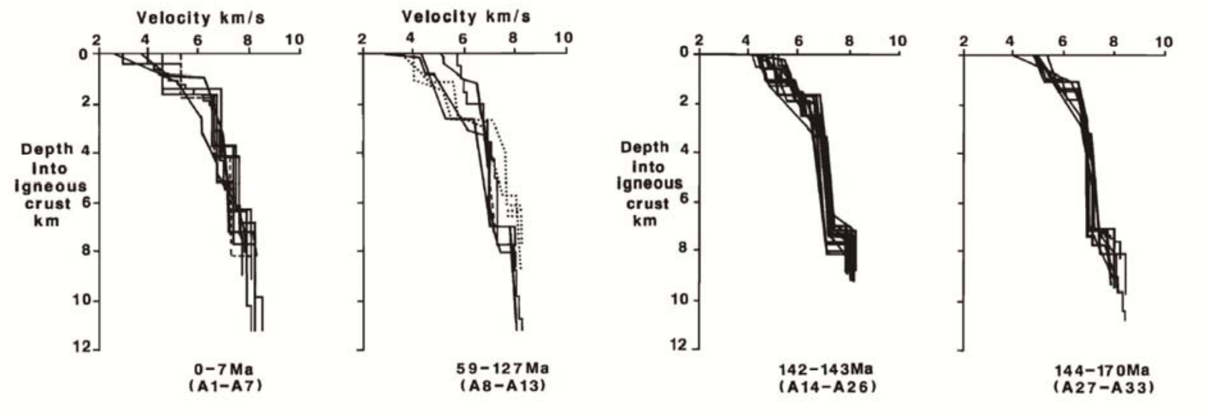

Figure 1.17.- *1D velocity-depth profiles from the North-Atlantic oceanic crust, grouped according to the age of the lithosphere. Extracted from White et al. [1992].*

White et al. [1992] compile a large number of velocity-depth profiles extracted from seismic lines acquired in the Atlantic and the Pacific, evidencing that despite some local differences, the general variation of seismic velocity with depth is fairly constant within each age zone (Figure 1.17).

This large amount of geological and geophysical data has allowed to identify a standard structure for oceanic crust (Figure 1.18). This structure includes from top to bottom:

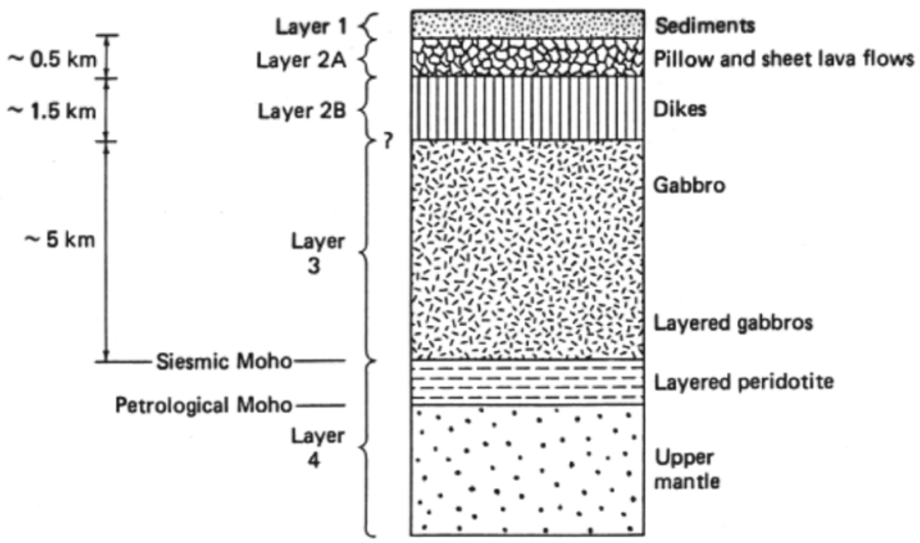
~ 0.5 km
~ 1.5 km
~ 5 km
Layer 1
Layer 2A
Layer 2B
?
Layer 3
Siesmic Moho
Petrological Moho
Layer 4
Sediments
Pillow and sheet lava flows
Dikes
Gabbro
Layered gabbros
Layered peridotite
Upper mantle

Figure 1.18.- *Basic sketch of the standard layered structure of oceanic crust, from Kennett [1982]*

Layer 1, the sedimentary layer. This layer varies in thickness from being absent over the oceanic ridge to 2-3 km near the continental shelves [Allaby, 2008]. P-wave velocity on top of this layer is close to water velocity (1.5 km/s) and increases steadily and rapidly with depth [White et al., 1992; Fowler, 2005]. The average density of this layer may vary depending on the type and degree of consolidation of sediments from ~1.6 to 2.3 kg/cm^3 [Hamilton, 1978].

Layer 2, this layer is usually called the *volcanic layer* and is subdivided in two layers: *Layer 2A* and *2B*. *Layer 2A* displays an average thickness of ~0.5 km and is represented by extrusive basaltic pillow and sheeted lavas. In contrast, *Layer 2B* is thicker than *2A* with an average thickness of 1.5 km and represented by basaltic dikes [Kennett, 1982] (Figure 1.18). Both layers define a region of the oceanic crust in which seismic velocity increases rapidly with depth, from ~3.5 km/s to ~6.2 km/s in ~ 2 km of crust (gradients of 1-2 s^{-1}) [White et al., 1992]. The rapid increase of seismic velocity is mainly attributed to: (1) lithological changes as a function of depth, and (2) the decrease on the degree of fracturing/porosity, and the related alteration of the rocks [Fowler, 2005]. Based on measured physical properties of core samples from the seafloor and from ophiolites (see below), the average density of *Layer 2* is estimated between 2.6-2.7 kg/cm^3 [Carlson and Herrick, 1990].

Layer 3 is the thickest oceanic layer, with an average thickness of 5 km [Allaby, 2008], although it is highly variable. Based on its physical properties and on onshore observations (i.e. ophiolites), it is assumed that Layer 3 is gabbroic in composition [e.g. Kennett, 1982; Fowler, 2005]. Seismic velocities in *Layer 3* range from ~6.5 km/s on top to ~7.2 km/s at the base of the crust, which means a velocity gradient of 0.1-0.2 s^{-1}, 10 times lower than *Layer 2* gradient (Figure 1.18). The average density of this layer is estimated between 2.9-3.0 kg/m^3 [Carlson and Herrick, 1990].

Layer 4 in Figure 1.18 corresponds to the uppermost mantle that underlies the oceanic crust, and therefore, it is not included in the oceanic crust structure.

Based on compilations of WAS data, it has been shown that oceanic crust is much thinner than continental crust, with a crustal thickness varying from 5.0 km and 8.5 km [White et al., 1992]. In some cases such as oceanic plateaus, originated under the influence of active mantle melting anomalies commonly identified as “hotspots”, oceanic crust can be much thicker, up to 30-40 km in some extreme cases such as Iceland, Galapagos Volcanic Province, or Ontong-Java [e.g. Gladczenko et al., 1997; Maclennan et al., 2001; Sallarès and Charvis, 2003]. However, here I will not refer to these anomalous cases.

Although this type of crust forms exclusively beneath the sea, it can be also found on land, since fragments of oceanic lithosphere were involved in convergent plate tectonics, being uplifted and exposed above sea level. These fragments, that not only include oceanic crust but also the uppermost section of the underlying mantle, are known as ophiolites and can be found in many region of the world like in Cyprus, in the Trodos complex [Christensen, 1978].

1.3.2.3 Exhumed mantle

At many rifted margins MCS and WAS data have evidenced how continental crust thins progressively as a result of the rotation of large continental blocks along high-angle normal faults (Figure 1.15) [e.g. Reid, 1994; Whitmarsh et al., 1996; Finlayson et al., 1998]. As thinning progresses, the highly stretched continental crust leads to the so-called continent-ocean transition (COT) zone (Figure 1.15). In some of these transition zones, ODP drillings have found that the basement was made of serpentinized mantle rocks [e.g. Boillot et al., 1980, 1987a; Whitmarsh and Wallace, 2001].

Serpentinization of mantle rocks occurs when seawater interacts directly with mantle at temperature < ~400°C. This interaction results in a metamorphic process that involves hydration of the ferromagnesian minerals of mantle rocks, mostly olivine. This process destroys the structure of this mineral by adding large amounts of waters into the crystalline structure giving as a result the transformation into serpentinite [Allaby, 2008].

The processes involved in exhumation of mantle rocks and serpentinization have been studied since the 80's and are still under discussion. Some of the first conceptual models of mantle serpentinization and exhumation were proposed by Boillot et al. [1987b]. Their model was based on a low-angle, normal faults setting in which mantle exhumation occurs from complex process of lithospheric necking and tectonic denudation of the underlying mantle (Figure 1.19). Later on, seismic studies in the West Iberia rifted margin evidenced the presence of serpentinized mantle beneath the rifted continental crust [Boillot, et al., 1989], implying that mantle serpentinization may occur beneath the stretched continental crust prior to exhumation in the COT zone. Assuming this, several laboratory and numerical models were performed to address fundamental questions on the rheological evolution of rifted margins and mantle exhumation [e.g. Brun and Beslier, 1996; Lavier and Manatschal, 2006; Pérez-Gusinyé and Reston, 2001; Pérez-Gussinyé et al., 2003]. These studies conclude that after significant extension the entire continental crust becomes brittle due to the progressive thinning and cooling (Figure 1.19). At this point, faulting cuts across the entire crust acting as seawater conduits to the mantle, where serpentinization occurs. Interestingly, mantle serpentinization not only changes the rock's chemistry but it also modifies its rheology from brittle to ductile regime [Escartín et al., 1997]. Thus, it is suggested that the serpentinized uppermost mantle acts as a decollement or detachment horizon [e.g. S reflector in Reston et al., 1996], accommodating large amounts of extension and leading to the full continental break-up and subsequent mantle exhumation (Figure 1.19) [e.g. Pérez-Gusinyé and Reston, 2001].

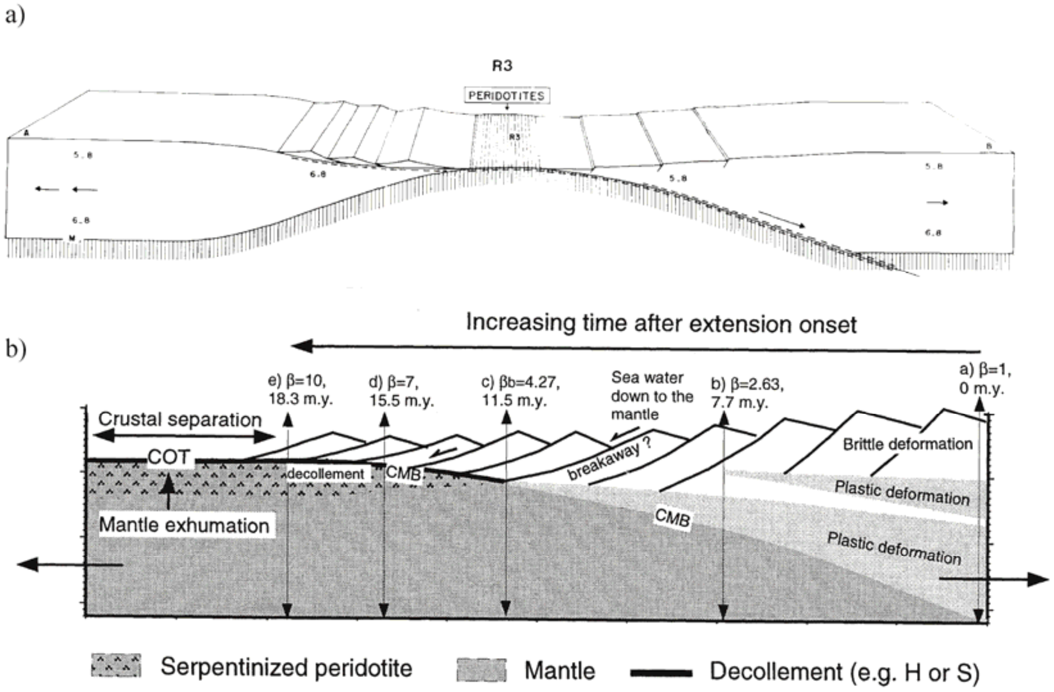
a)
R3
PERIDOTITES
5.8
6.8
b)
Increasing time after extension onset
e) β=10, 18.3 m.y.
d) β=7, 15.5 m.y.
c) βb=4.27, 11.5 m.y.
Sea water down to the mantle
b) β=2.63, 7.7 m.y.
a) β=1, 0 m.y.
Crustal separation
COT
decollement
CMB
breakaway ?
Brittle deformation
Plastic deformation
Plastic deformation
Mantle exhumation
Serpentinized peridotite
Mantle
Decollement (e.g. H or S)

Figure 1.19.- *(a) Low-angle, normal fault and tectonic denudation model presented by Boillot et al. [1987b] to explain mantle exhumation. (b) Basic sketch of the temporal evolution of a rifted margin, from the onset of the extension to the continental break-up and mantle exhumation. The sketch illustrates the onset of mantle serpentinization at the time that the entire continental crust becomes brittle (i.e. at β=4.27). At this stage the extension is accommodated by large decollements or detachment faults (black thick line). From Pérez-Gussinyé and Reston [2001].*

However, not only rheology plays an important role in mantle exhumation. As stated before, it is well known that the passive decompression of the astenospheric mantle results in large production of partial melting. Then, how can mantle be exhumed without producing melting? In mid-ocean ridges, it is well studied that the three parameters that control melting production from decompression of the mantle are velocity of extension, and temperature and composition of the underlying mantle [e.g. Klein et al., 1987; Reid and Jackson, 1987; Michael et al., 2003]. Based on this, dynamic models of rifting explored how these three parameters influence the formation the COT zone and mantle exhumation [Pérez-Gussinyé et al., 2006]. The results of these models conclude that in case that the mantle is cold enough, or extension is slow enough, or mantle source is depleted enough, extension could eventually lead to the exhumation of mantle rocks without producing significant amounts of melting [Pérez-Gussinyé et al., 2006].

Concerning the physical properties, serpentinization lowers both seismic velocity and density of mantle rocks, which originally display P-wave velocities of 8.1-8.2 km/s and density of ~3.3 kg/cm^3 [Birch, 1961; Allaby, 2008]. For that reason, exhumed mantle regions can be identified from seismic velocity and density models [e.g. Dean et al., 2000; Van Avendonk et al., 2006; Sibuet et al., 2007].

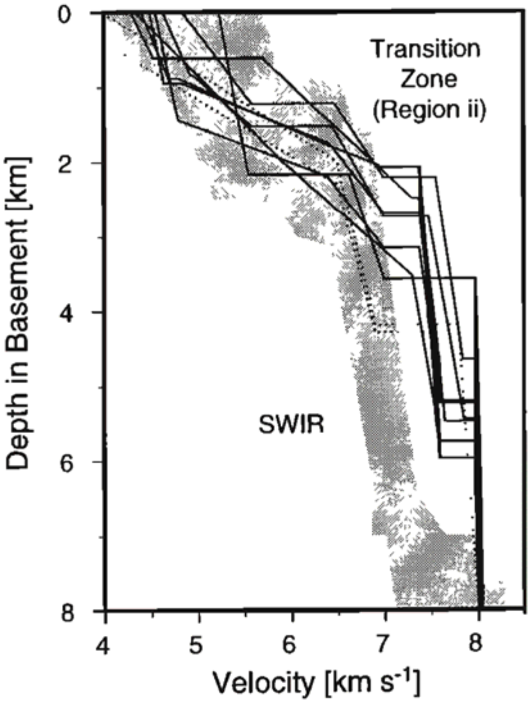

Figure 1.20.- *1D velocity-depth profiles (black thick lines) from the exhumed mantle zone in the southern Iberia Abyssal Plain overlaid with the reference velocity-depth profile of Atlantic oceanic crust (grey area) from White et al. [1992]. Extracted from Dean et al. [2000].*

The most relevant features concerning the seismic velocity structure of exhumed mantle regions are explained below and illustrated by Figure 1.20:

- In the uppermost 2-4 km of basement seismic velocities used to increase rapidly with gradients that can be even twice higher than those observed in oceanic *Layer 2*. This rapid increment is mostly attributed to a progressive decrease in peridotite serpentinization degree with depth due to the significant reduction of rock fracturing, and fluid percolation (Figure 1.20) [Chian et al., 1999; Dean et al., 2000; Sallarès et al., 2013a].

- Then, a moderate increment of seismic velocities underlies this fast transition zone, reflecting a less intense, more homogeneous serpentinization degree that would lead to unaltered mantle velocities (8.1-8.2 km/s) with depth (Figure 1.20) [Chian et al., 1999; Dean et al., 2000].

- Finally, no Moho discontinuity is defined, since there is no crust-mantle boundary [e.g. Dean et al., 2000].

Chapter 2: Geological & Geodynamic setting

2.1 The Western Mediterranean back-arc basins

The Western Mediterranean realm is characterized by the formation of back-arc basins associated to rollback of slabs and retreat of subduction fronts since Oligocene times [Dewey et al., 1989; Doglioni et al., 1997; Spakman and Wortel, 2004; Schettino and Turco, 2011]. As a result of of this setting, the morpho-tectonic structure of the Western Mediterranean is represented by an arcuate configuration of mountain belts [i.e. subduction fronts] that surrounds a system of back-arc basins formed by the Valencia Trough, the Liguro-Provençal, the South Balearic-Algerian, the Alborán, and the Tyrrhenian basins (Figure 2.1).

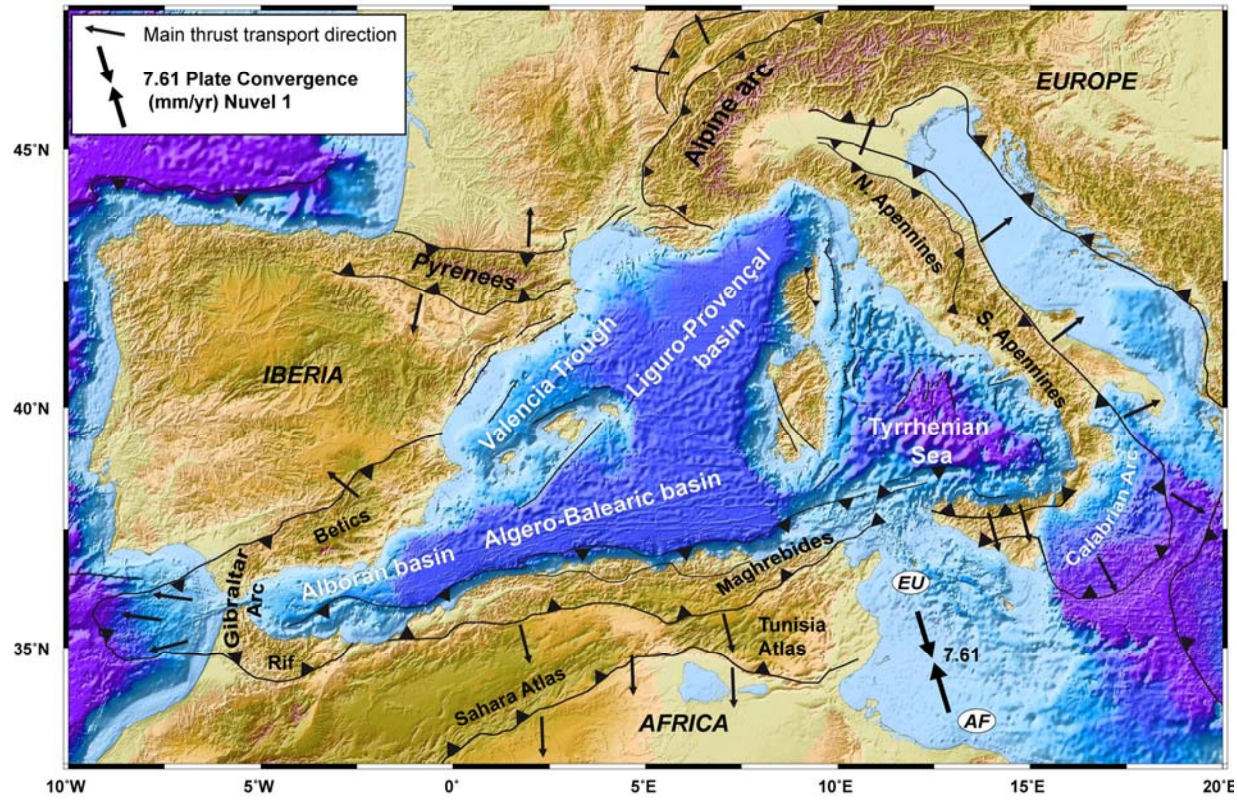
Main thrust transport direction
7.61 Plate Convergence (mm/yr) Nuvel 1
EUROPE
Alpine arc
N. Apennines
S. Apennines
Pyrenees
IBERIA
Valencia Trough
Liguro-Provençal basin
Tyrrhenian Sea
Calabrian Arc
Algero-Balearic basin
Betics
Alborán basin
Gibraltar Arc
Rif
Maghrebides
Tunisia Atlas
Sahara Atlas
AFRICA
EU
7.61
AF
45°N
40°N
35°N
10°W
5°W
0°
5°E
10°E
15°E
20°E

Figure 2.1.- *Bathymetric and topographic map showing the main tectonic features and the location of back-arc basins in the Western Mediterranean region, modified from Booth-Rea et al. [2007].*

The formation of this system of back-arc basins started ~33 Ma ago [Schettino and Turco, 2011] (Figure 2.1). In a first stage, migration of the trench zone related to the subduction of the old Ligurian Thetys lithosphere toward the east-northeast and south-

southeast caused the rotation of Sardinia, Corsica, the Balearic Islands, and the Kabylies leading to the opening of the Liguro-Provençal, the Valencia Trough, and the South Balearic-Algerian basins before ~20 Ma (Figure 2.2a). The opening of these basins was accompanied by continental rifting in the Valencia Trough [Pascal et al., 1992; Gallart et al., 1995], that evolved until full continental breakup and seafloor spreading in the South Balearic-Algerian basin [Booth-Rea et al., 2007] and the Liguro-Provençal basin [Rollet et al., 2002; Gailler et al., 2009].

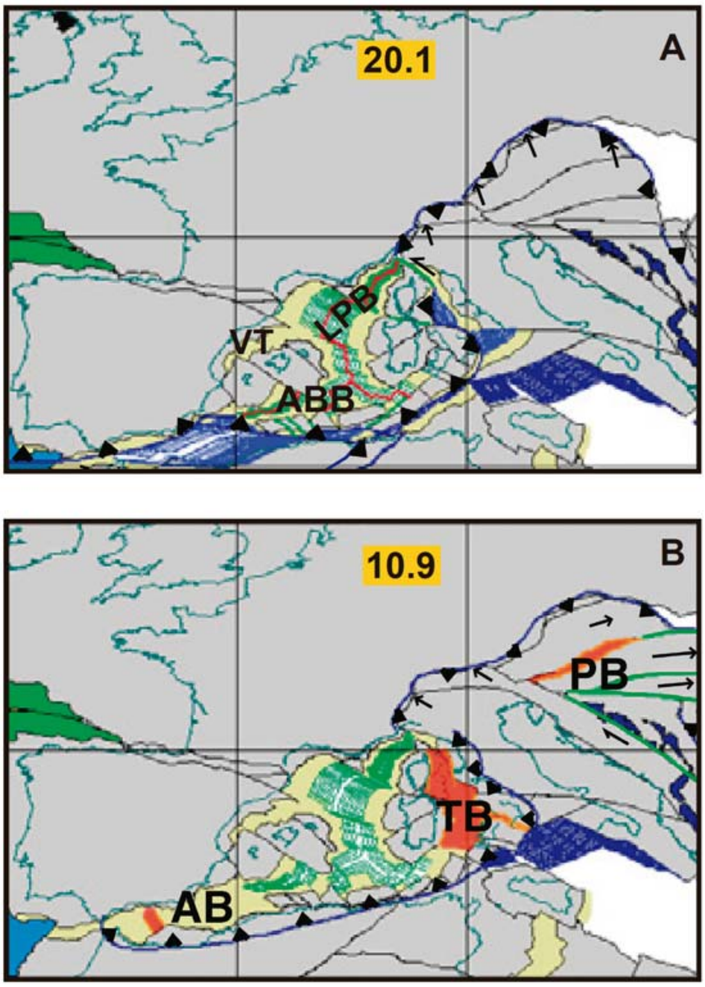

Figure 2.2.- *Plate reconstruction of Atlantic and Mediterranean regions from Schettino and Turco [2011], (A) at 20.1 Ma (chron C6n, early Burdigalian) and (B) at 10.9 Ma (early Tortonian). Red lines are spreading centers. Green and blue areas represent oceanic crust. The areas affected by the first rifting events are bounded by orange lines. Arrows represent direction and amount of relative motion. ABB: Algero-Balearic Basin; AB: Alboran Basin; LPB: Liguro-Provençal Basin; PB: Pannonian Basin; TB: Tyrrhenian Basin; VT: Valencia Trough.*

In a second stage, two subsequent episodes of trench retreat took place during the early Tortonian (10.9 Ma), leading to the formation of the Alborán basin, in a first stage, and the Tyrrhenian basin in a second stage [Schettino and Turco, 2011] (Figure 2.2b). The Alborán basin was generated by the westwards rollback of the subducting Alpine-Tethys oceanic lithosphere [Lonergan and White, 1997]. This subducted slab, which likely corresponds to the oceanic crust that floors the Gulf of Cadiz [Sallarès et al., 2011], has been imaged beneath the Gibraltar arc by means of global tomography [Spakman and Wortel, 2004]. Back-arc extension processes in the Alborán basin result in a thin continental crust later modified by arc magmatism [Booth-Rea et al., 2007].

Simultaneously to the opening of the Alborán basin, the eastward migration of the Apennines-Calabrian subduction system in the eastern part of the Western Mediterranean led to the opening of the Tyrrhenian basin (Figure 2.2b). The evolution and structure of this basin is presented more in detail in the next sections.

2.2 The Tyrrhenian back-arc basin

The Tyrrhenian is a Neogene, triangular shaped, back-arc basin, located at the easternmost region of the Western Mediterranean (Figure 2.1).

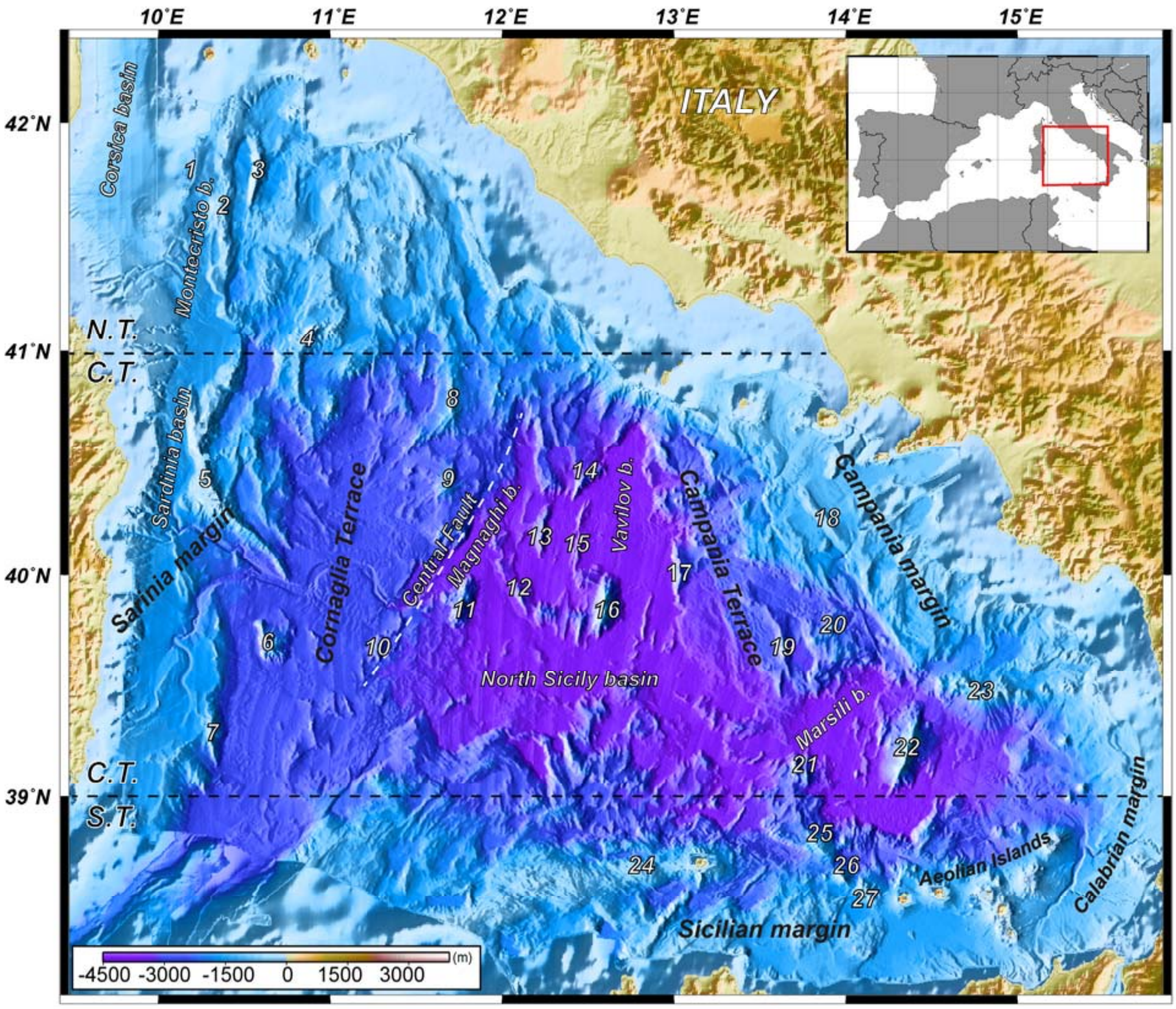
10°E
11°E
12°E
13°E
14°E
15°E
42°N
41°N
40°N
39°N
ITALY
Corsica basin
Montecristo b.
N.T.
C.T.
Sardinia basin
Sardinia margin
Cornaglia Terrace
Central Fault
Magnaghi b.
Vavilov b.
Campania Terrace
Campania margin
North Sicily basin
Marsili b.
C.T.
S.T.
Aeolian Islands
Calabrian margin
Sicilian margin
1
2
3
4
5
6
7
8
9
10
11
12
13
14
15
16
17
18
19
20
21
22
23
24
25
26
27
-4500 -3000 -1500 0 1500 3000
(m)

Figure 2.3.- *Bathymetric map of the Tyrrhenian basin. The location of the main sedimentary basins and morphological structures are included. N.T.: Northern Tyrrhenian, C.T.: Central Tyrrhenian, S.T.: Southern Tyrrhenian, 1: Pianosa Ridge, 2: Etruschi seamount, 3: Cialdi seamount, 4: Vercelli seamount, 5: Baronie seamount, 6: Cornaglia seamount, 7: Quirra seamount, 8: Cassini seamount, 9: Sechi seamount, 10: Major seamount, 11: Magnaghi seamount, 12: D'Ancona Ridge, 13: De Marchi seamount, 14: Farfalla seamount, 15: Gortani Ridge, 16: Vavilov seamount, 17: Flavio de Gioia seamount, 18: Monte delle Sirene, 19: Issel seamount, 20: Poseidone seamount, 21: Glauco seamount, 22: Marsili seamount, 23: Palinuro seamount, 24: Anchise seamount, 25: Sisifo seamount, 26: Enarela seamount, 27: Eolo seamount. The Central Fault after interpretation by Marani and Gamberi [2004].*

It is surrounded to the E and S by an arcuate orogenic system formed by the

Apennines in the Italian peninsula, the Calabrian Arc in southern Italy and the Maghrebides in Sicily and north-eastern Africa, and to the west by the Corsica-Sardinia block (Figure 2.1).

From a morpho-tectonic point of view, the Tyrrhenian basin can be subdivided in three different domains: the Northern (north of ~40º 45'N), which displays shallower seafloor and rough morphology; the Central (from ~40º 45'N to ~39ºN) with deeper seafloor and extended abyssal plains spotted with prominent volcanic and non-volcanic seamounts, and the Southern Tyrrhenian, where the active volcanic arc is represented by the Aeolian Islands in front of the Sicilian-Calabrian margin (Figure 2.3).

Since the Tyrrhenian basin is the setting of this study, a detailed description of its geodynamic evolution, tectonic, geology and volcanism is presented below based on the knowledge before the present work.

2.2.1 Geodynamic evolution of the Tyrrhenian basin region

The evolution of the Tyrrhenian basin together with the surrounding arcuate orogenic system is linked to the east-southeastward migration of the Apennines-Calabrian subduction front, which in turn is related to the slab rollback of the Thetyan oceanic lithosphere (Figure 2.4) [Malinverno and Ryan, 1986; Rehault et al., 1987; Faccena et al., 2001].

Before the opening of the Tyrrhenian basin, oceanic spreading occurred in the central part of the Liguro-Provençal basin in response to the 25º-30º counterclockwise rotation of the Corsica–Sardinia block at ~20-15 Ma [Gattacceca et al., 2007]. At that time rollback and hence back-arc extension slowed down and eventually stopped. It has been hypothesized that a possible cause for this slow down of extension was the arrival of the subducting slab at the 660 km-transition zone (upper-lower mantle transition) [Faccena et al., 2001].

Soon after, during the intra-Tortonian (~10-9 Ma) extension started in the Tyrrhenian region affecting a region occupied by the Alpine and the Apenninic orogenic belts. [Trincardi and Zitellini, 1987; Mascle and Rehault, 1990; Sartori et al., 1990, 2001]. Nevertheless, synrift deposits related to the last stages of opening of the Liguro-Provençal basin (~20 Ma) were found in the Corsica basin indicating that the westernmost section of the Northern Tyrrhenian basin undergone earlier extension

[Zitellini et al., 1986; Mauffret et al., 1999; Mauffret and Contrucci, 1999] (Figure 2.4a). From Tortonian to late Messinian the rapid eastward migration of the subduction front caused the roughly E-W contemporaneous back-arc extension in the Tyrrhenian region [Faccena et al., 2001; Rosenbaum and Lister, 2004] (Figure 2.4b).

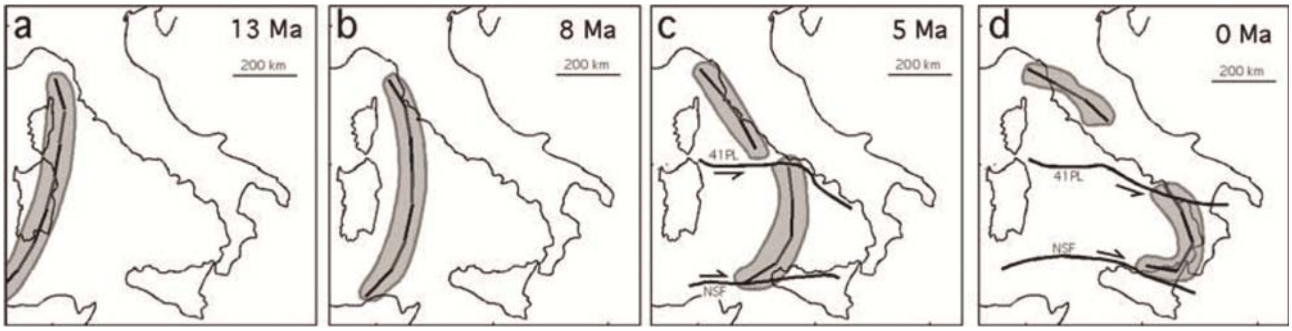

Figure 2.4.- *Schematic sequence of the Neogene and Quaternary evolution of the Apennines-Calabrian subduction front from Rosenbaum and Lister [2004].*

Between ~6-5 Ma the style of subduction rollback experienced major changes (Figure 2.4c). It is suggested that the under-thrusting of positively buoyant continental crust into the subduction system caused a progressive slow down of rollback in the Northern Tyrrhenian [Faccena et al., 2001]. Consequently, back-arc extension in the Northern Tyrrhenian also slowed down in the upper-Messinian and stopped during Pleistocene time [Bartole et al., 1995]. In contrast, the Central and Southern Tyrrhenian underwent larger amount of extension due to the rapid migration of the subduction front toward southeast [6 cm yr^{-1} in Faccena et al., 2004 and references therein], where it is currently consuming oceanic Ionian lithosphere beneath the Calabrian arc (Figure 2.4d) [Faccena et al., 2001; Chiarabba et al., 2008]. It has been suggested that extension in the Southern region may have led to continental break-up and oceanic crust formation in the Vavilov and Marsili basins (Figure 2.3) [Trincardi and Zitellini, 1987; Kastens and Mascle, 1990; Faccena et al., 2001; Rosenbaum and Lister, 2004]. The different degree of extension from north to south is believed to be accommodated by two major strike-slip systems located at 41ºN and along the north coast of Sicily, respectively (Figure 2.4c and d) [Bruno et al., 2000; Faccena et al., 2001; Rosenbaum and Lister, 2004].

2.2.2 Tectonic setting of the Tyrrhenian basin

Differences of extension from north to south caused by the rollback evolution in the Tyrrhenian basin, led to a complex tectonic structure and important crustal thickness variations (Figure 2.5) [Gvirtzman and Nur, 2001; Di Stefano et al., 2011].

Early interpretations of the tectonic structure of the Tyrrhenian basin were summarized by Funizello et al. [1981] in the Carta Tettonica d'Italia. Additional information has been also provided by seismic reflection data acquired since the 70's in the Tyrrhenian region by many authors [e.g. Zitellini et al., 1986; Trincardi and Zitellini, 1987; Kastens and Mascle, 1990; Mauffret et al., 1999; Mauffret and Contrucci, 1999; Sartori et al., 2004; Moeller et al., 2013] (Figures 2.6 and 2.7). The aim of this section is to integrate these data and present the most widely accepted aspects concerning the tectonic structure of the Tyrrhenian basin. I focus particularly in the Central part of the basin, which is the main area of interest of my work.

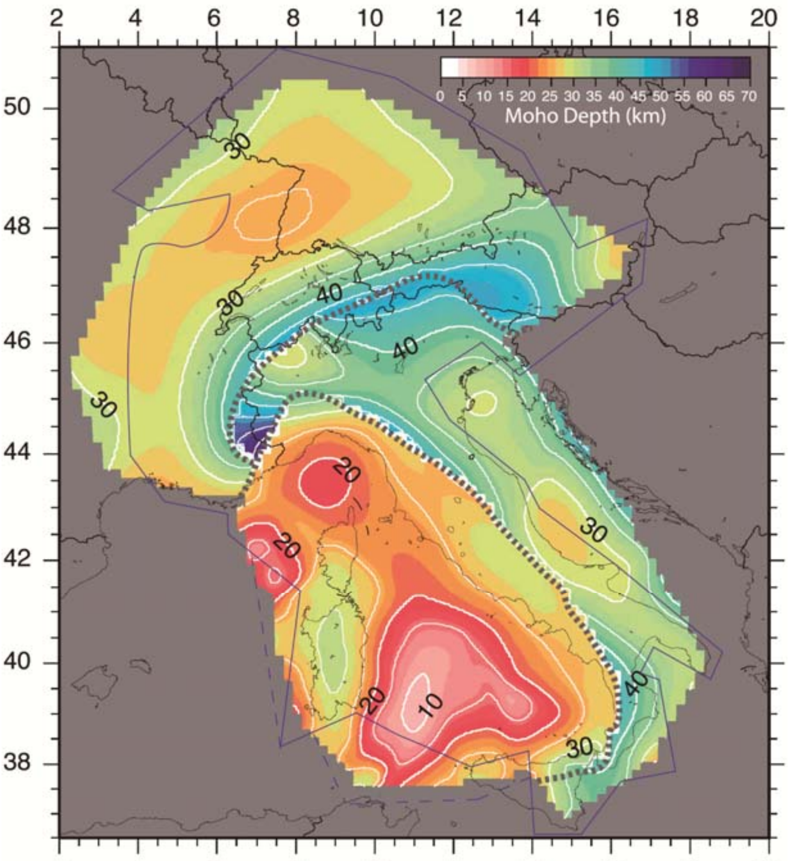

Figure 2.5.- *Map of the distribution of the Moho depth in the Alpine, Adriatic and Tyrrhenian regions, extracted from Di Steffano et al. [2011].*

Northern Tyrrhenian

The Northern Tyrrhenian displays a tectonic structure mainly formed by a roughly N-S-trending system of East-dipping normal faults that define a number of half-graben structures (Figure 2.6) [Zitellini et al., 1986; Mauffret and Contrucci, 1999; Mauffret et al., 1999; Moeller et al., 2013]. In the western region, the main tectonic feature is represented by the half-graben of the Corsica basin, which is >8.5 km-deep (Figures 2.3 and 2.6) [Mauffret et al., 1999; Moeller et al., 2013]. In the deepest part, this basin is filled by Oligocene-early Miocene synrift sediments [Zitellini et al., 1986; Mauffret et al., 1999] deposited during the counterclockwise rotation of Corsica and Sardinia. To the east of this basin the rifted crust exhibits a structure of tilted blocks rotated along eastward dipping normal faults [Moeller et al., 2013]. The resultant half-graben structure is filled by syn-tectonic deposits from late Tortonian, Messinian and Early-Pliocene times basin [Mauffret et al., 1999;], indicating that most of the normal faulting in this sector of the Northern Tyrrhenian was produced from Tortonian to mid-Pliocene time and hence during the opening of the Tyrrhenian. In response to this tectonic activity crustal thickness in the Northern Tyrrhenian thins from ~25 km to ~15 km thick from Corsica to the central parts of the basin along MEDOC WAS Line AB [Moeller et al., 2013] (Figure 2.6) and thickens toward the Italian peninsula where it is 25-30 km thick (Figure 2.5) [Di Stefano et al., 2011].

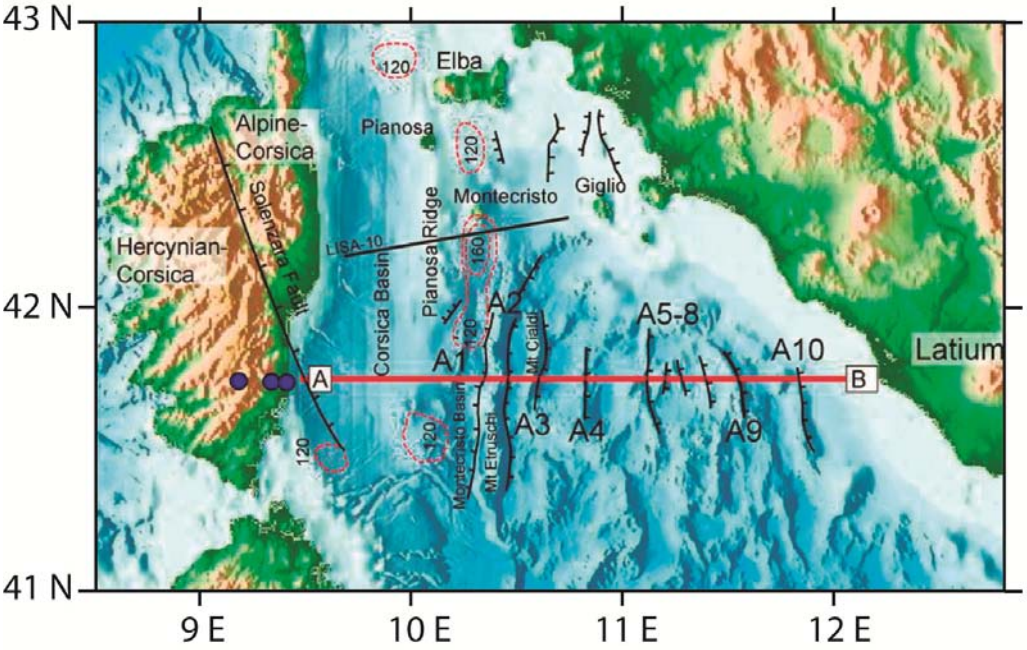
43 N
42 N
41 N
9 E
10 E
11 E
12 E
Elba
120
Alpine-
Corsica
Pianosa
120
Montecristo
Giglio
Solenzara Fault
Hercynian-
Corsica
LISA-10
Corsica Basin
Pianosa Ridge
160
120
A2
A1
Mt Cialdi
A5-8
A10
Latium
A
B
120
120
Montecristo Basin
Mt Etruschi
A3
A4
A9

Figure 2.6.- *Tectonic map of the Northern Tyrrhenian basin showing the location of the MEDOC WAS line AB, modified from Moeller et al. [2013].*

Central Tyrrhenian

To the south, the Tyrrhenian basin has been subjected to larger extension rates. The Central Tyrrhenian basin is bounded by the asymmetric conjugate margins of Sardinia and mainland Italy [Trincardi and Zitellini, 1987; Sartori et al., 2004] and by the Magnaghi, Vavilov and Marsili basins (Figure 2.3), which are interpreted to be oceanic [Kastens and Mascle, 1990]. In the Sardinia margin extensional faulting changes the trend from N-S to NE-SW eastward in response to changes of the subduction system during Messinian times (~6-5 Ma) [Faccena et al., 2001; Rosenbaum and Lister, 2004] (Figure2.4). Sartori et al. [2004] interpreted the tectonic structure of the ~180 km-wide Sardina margin, which they interpreted to include the Cornaglia Terrace (Figure 2.3), as an irregularly spaced system of tilted continental blocks rotated by East- and West-verging extensional faults (Figure 2.7). These authors interpreted MCS images to show that extensional faulting reaches the base of a ~10 km thick crust beneath the Cornaglia Terrace [Sartori et al., 2001; Carrara, 2002; Sartori et al., 2004]. Half-grabens in the Sardinia margin are filled with pre-rift deposits of Serravalian-Tortonian age and syn-rift deposits from late-Tortonian to intra-Pliocene age [Sartori et al., 2001; Carrara 2002; Sartori et al., 2004], which allows to constrain the duration of extension in this region. At the eastern edge, the east-dipping Central Fault, also known as the Selli Line, is interpreted to separate the Cornaglia Terrace from the Magnaghi and Vavilov basin (Figure 2.3) [Carrara, 2002; Sartori et al., 2004].

The tectonic structure of the Magnaghi and Vavilov basins has been proposed to be controlled by a N-S trending group of extensional listric faults (Figure 2.7) [Sartori et al., 2004]. In the Magnaghi basin the syn-extensional sequence was deposited during intra-Messinian to intra-Pliocene times [Kastens and Mascle, 1990; Sartori, 1990; Sartori et al., 2004], while in the Vavilov basin a sedimentary infill corresponding to the Pliocene-Quaternary appears undeformed directly covering the irregular topography of the basement [Sartori et al., 2004]. Another relevant feature of these basins is that both of them host large magmatic structures that are thought to be related with oceanic crustal accretion and intra-plate magmatism (Figure 2.10) (see section 2.2.3 and 2.2.4 for further details) [Savelli 2002]. Moho depth beneath Magnaghi and Vavilov basins has been inferred from topographical analyzes -based on isostatic equilibrium- and regional tomography at ~10 km of depth (Figure 2.5) [Gvirtzman and Nur, 2001; Di Stefano et al., 2011]. However, the seismic reflection profile presented in Sartori et al. [2004] does not image any Moho-like package of reflections beneath these basins (Figure 2.7).

The conjugated Italian margin of the Central Tyrrhenian is less extended than the conjugated margin of Sardinia [Trincardi and Zitellini, 1987; Sartori et al., 2004]. The

NW-SE-trending system of normal faults produced horst-and-graben structures parallel to the Apenninic chain (Figure 2.3). Some of these extensional structures appear to be currently inverted in response of a compressive episode that took place during upper-Pliocene-Quaternary times [Trincardi and Zitellini, 1987]. The syn-extensional sequences identified in the half-grabens infill indicate that rift-related faulting occurred during pre-Messinian times in this sector of the Italian margin [Trincardi and Zitellini, 1987]. Average Moho depth along the Italian margin has been estimated to be ~25-30 km (Figure 2.5) [Biella et al., 2007; Di Stefano et al., 2011].

The southeastern region of the Central Tyrrhenian is represented by the Marsili basin (Figure 2.3), where oceanic crust is interpreted to underlay the sediments [Trincardi and Zitellini, 1987; Kastens and Mascle, 1990]. This region is also the locus of the largest volcano in the Tyrrhenian basin, the so-called Marsili seamount, which is ~ 3000 m tall above the seafloor (Figure 2.3). Faulting in this basin presents a NNE-SSW direction implying a WNW-ESE extension [Kastens and Mascle, 1990]. The oldest sediments were deposited during early-Pleistocene times (~2 Ma) [Hieke et al., 1990].

Southern Tyrrhenian

The Southern Tyrrhenian basin is characterized by the Aeolian volcanic arc resulting of the subduction of the Ionian lithosphere (Figure 2.3). The tectonic structure of this region is represented by trans-tensional basins controlled by normal faults in response of a right-lateral transcurrent regime along WNW-ESE direction [Trincardi and Zitellini, 1987]. Additionally, the inversion of a number of basins reveals the occurrence of recent trans-pressional episodes in this area [Trincardi and Zitellini, 1987].

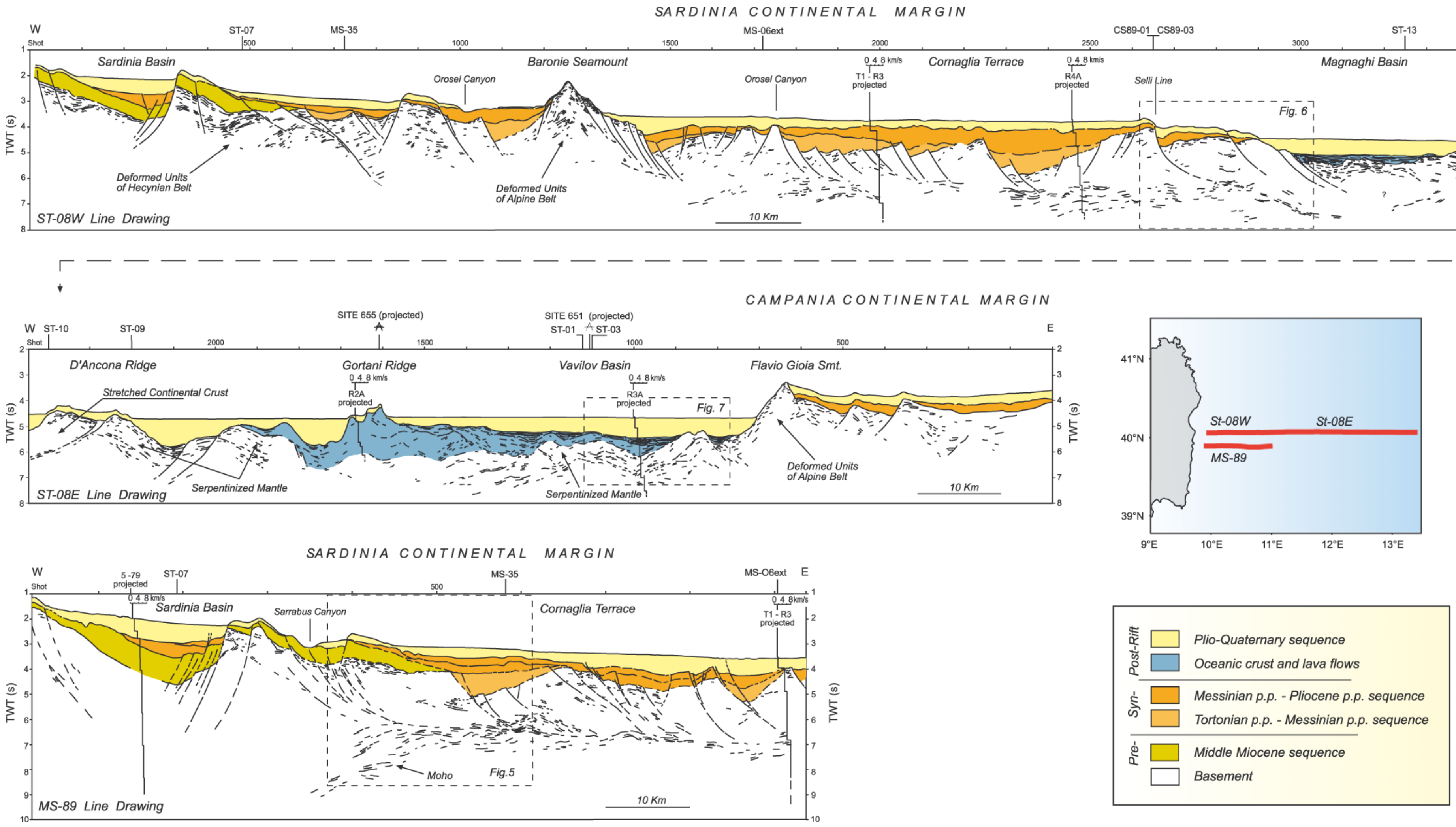
SARDINIA CONTINENTAL MARGIN
W
E
Shot
ST-07
MS-35
MS-06ext
CS89-01
CS89-03
ST-13
Sardinia Basin
Baronie Seamount
Orosei Canyon
Cornaglia Terrace
Magnaghi Basin
Selli Line
Fig. 6
T1 - R3 projected
R4A projected
0 4 8 km/s
Deformed Units of Hecynian Belt
Deformed Units of Alpine Belt
ST-08W Line Drawing
10 Km
TWT (s)
CAMPANIA CONTINENTAL MARGIN
ST-10
ST-09
SITE 655 (projected)
SITE 651 (projected)
ST-01
ST-03
D'Ancona Ridge
Gortani Ridge
Vavilov Basin
Flavio Gioia Smt.
Stretched Continental Crust
R2A projected
R3A projected
Fig. 7
Serpentinized Mantle
ST-08E Line Drawing
5 -79 projected
Sarrabus Canyon
Moho
Fig.5
MS-89 Line Drawing
41°N
40°N
39°N
9°E
10°E
11°E
12°E
13°E
St-08W
St-08E
MS-89
Post-Rift
Syn-
Pre-
Plio-Quaternary sequence
Oceanic crust and lava flows
Messinian p.p. - Pliocene p.p. sequence
Tortonian p.p. - Messinian p.p. sequence
Middle Miocene sequence
Basement

Figure 2.7.- *Geological and tectonic interpretation of the Central Tyrrhenian basin from line drawings of Lines ST-08W/E and MS-89 presented in Sartori et al. [2004].*

2.2.3 Previous work on the rock-type distribution of the Tyrrhenian basin

The first large compilation of information concerning the geology of the Tyrrhenian Sea date from the early 80's [Colantoni et al., 1981]. The map provided by these authors was drawn up on the basis of available data from the literature up to 1980 including samples from the Deep Sea Drilling Project (DSDP) Leg 42A [Keneth et al., 1978] (Figure 2.8). Later, the Ocean Drilling Program (ODP) Leg 107, provided, drilling sites 650 to 656, a considerable addition of lithological and stratigraphic information from the basin (Figures 2.8 and 2.9) [Kastens and Mascle, 1990]. In conjunction, all these data reflected for the first time the significant lithological and stratigraphic heterogeneity of the Tyrrhenian basin, suggesting a complex geological history.

Apart from samples acquired in the framework of the ODP and DSDP drilling, geophysical data has also been collected in the Tyrrhenian basin in the last decades [Fahlquist and Hersey, 1969; Nicolich, 1981; Recq et al., 1984; Duschenes et al., 1986; Kastens and Mascle, 1990; Sartori, 1990; Sartori et al., 2004; Cella et al., 2008] before the MEDOC experiment. All this information had allowed to improve the knowledge concerning the crustal structure and proposes the nature of the basement in the different parts of the basin. In this section I describe the main results of the most representative geophysical studies that in conjunction with the geological data have produced the most accepted geological interpretations of the basin proposed before this work.

Based on the lithological composition and the geological processes involved in their formation, three groups of rocks have been identified in the basin: ***igneous, metamorphic and granitic,*** and ***sedimentary rocks***.

Igneous rocks

This group includes lithologies linked with oceanic spreading and subduction processes, that is tholeiitic and alkali-olivinic basalts, related to oceanic spreading, calc-alkaline lavas, related to subduction, volcaniclastic rocks, and intrusive mafic and ultramafic rocks (e.g. serpentinites). Granitic rocks of continental affinity are presented in another group.

Basaltic rocks are mostly found in the Magnaghi, Vavilov and Marsili basins (Figure 2.3), and in very specific points of the Sardinia margin (e.g. ODP 654 in Figures 2.8 and 2.9). Basalts that have been associated to oceanic spreading processes are found in the Gortani ridge (ODP site 655 in Figures 2.8 and 2.9) [Beccaluva et al., 1990], the Vavilov basin (sites ODP 651 and DSDP 373 in Figures 2.8 and 2.9) [Barberi et al., 1978; Dietrich et al., 1977; Bertrand et al., 1990], and in both Marsili basin and seamount (ODP site 650 in Figures 2.8 and 2.9) [Colantoni et al., 1981; Beccaluva et al., 1990]. The overall, basic interpretation based on these data is that the Magnaghi, Vavilov and Marsili basins were formed by oceanic accretion [Kastens and Mascle, 1990; Faccena et al., 2001; Sarotri et al., 2004].

Comparatively low-resolution seismic refraction experiments carried out during the 60's-80's (Figure 2.9) provided local 1D velocity models that were interpreted as showing oceanic crust structure under the Magnaghi and Vavilov basins (Figure 2.3) [Fahlquist and Hersey, 1969; Nicolich, 1981; Recq et al., 1984; Duschenes et al., 1986]. Similarly, gravity and magnetic field anomalies observed beneath these sub-basins have been also interpreted as an indication for seafloor spreading [Cella et al., 2008]. An observation that has not been reconciled with this interpretation is the presence of serpentinized peridotites at the lowermost unit of site ODP 651 in the Vavilov basin (Figures 2.8 and 2.9) [Beccaluva et al., 1990; Bonatti et al., 1990]. Kastens and Mascle [1990] tentatively interpreted this occurrence as an isolated portion of continental crust that might contain a sliver of Thetyan ophiolite.

Further basaltic rocks have been found in the volcanic edifices of Magnaghi and Vavilov [Colantoni et al., 1981] (#11 and #16 in Figures 2.3, 2.8, and 2.9), but in this case the rocks have intra-plate and calc-alkaline (i.e. subduction-related) affinity [Robin et al., 1987; Savelli 2002]. Basaltic samples in the Sardinia margin, such as those found in ODP site 654 (Figures 2.8 and 2.9) also present an intra-plate affinity linked to post-extensional processes [Beccaluva et al., 1990].

Subduction-related calc-alkaline lavas are mostly concentrated in the Aeolian Island arc and related with the subduction of the Ionian slab (Figure 2.8). Volcaniclastic rocks, possibly linked with extension processes have been also identified in the Magnaghi and Vavilov basins, and locally in the Campania Margin [Colantoni et al., 1981] (Figures 2.3 and 2.8). For further details of the volcanic activity in the Tyrrhenian basin see section 2.2.4.

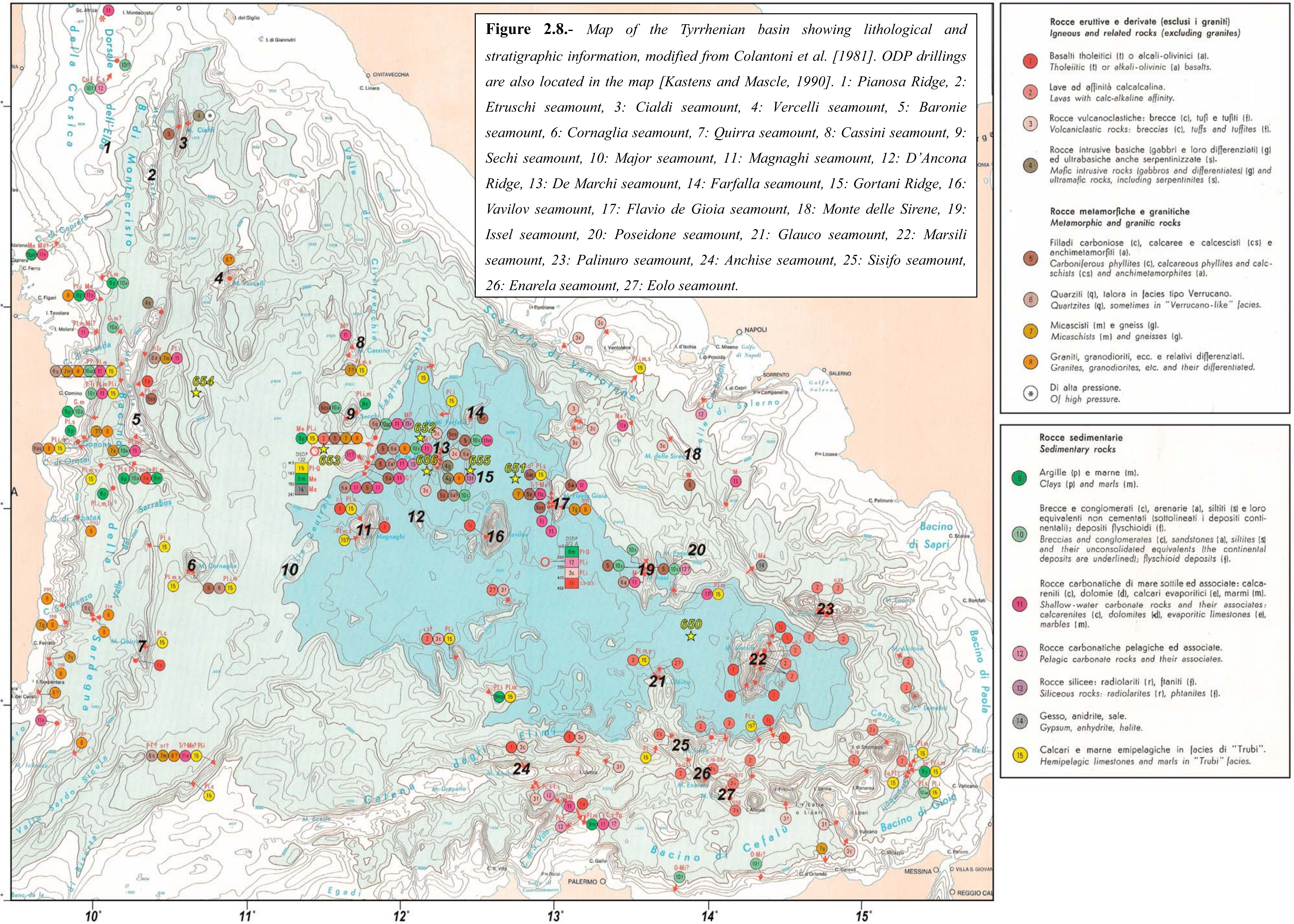

Figure 2.8.- *Map of the Tyrrhenian basin showing lithological and stratigraphic information, modified from Colantoni et al. [1981]. ODP drillings are also located in the map [Kastens and Mascle, 1990]. 1: Pianosa Ridge, 2: Etruschi seamount, 3: Cialdi seamount, 4: Vercelli seamount, 5: Baronie seamount, 6: Cornaglia seamount, 7: Quirra seamount, 8: Cassini seamount, 9: Sechi seamount, 10: Major seamount, 11: Magnaghi seamount, 12: D'Ancona Ridge, 13: De Marchi seamount, 14: Farfalla seamount, 15: Gortani Ridge, 16: Vavilov seamount, 17: Flavio de Gioia seamount, 18: Monte delle Sirene, 19: Issel seamount, 20: Poseidone seamount, 21: Glauco seamount, 22: Marsili seamount, 23: Palinuro seamount, 24: Anchise seamount, 25: Sisifo seamount, 26: Enarela seamount, 27: Eolo seamount.*

Rocce eruttive e derivate (esclusi i graniti)
Igneous and related rocks (excluding granites)
1 Basalti tholeitici (t) o alcali-olivinici (a). Tholeiitic (t) or alkali-olivinic (a) basalts.
2 Lave ad affinità calcalcalina. Lavas with calc-alkaline affinity.
3 Rocce vulcanoclastiche: brecce (c), tufi e tufiti (t). Volcaniclastic rocks: breccias (c), tuffs and tuffites (t).
4 Rocce intrusive basiche (gabbri e loro differenziati) (g) ed ultrabasiche anche serpentinizzate (s). Mafic intrusive rocks (gabbros and differentiates) (g) and ultramafic rocks, including serpentinites (s).
Rocce metamorfiche e granitiche
Metamorphic and granitic rocks
5 Filladi carboniose (c), calcaree e calcescisti (cs) e anchimetamorfiti (a). Carboniferous phyllites (c), calcareous phyllites and calc-schists (cs) and anchimetamorphites (a).
6 Quarziti (q), talora in facies tipo Verrucano. Quartzites (q), sometimes in "Verrucano-like" facies.
7 Micascisti (m) e gneiss (g). Micaschists (m) and gneisses (g).
8 Graniti, granodioriti, ecc. e relativi differenziati. Granites, granodiorites, etc. and their differentiated.
* Di alta pressione. Of high pressure.
Rocce sedimentarie
Sedimentary rocks
9 Argille (p) e marne (m). Clays (p) and marls (m).
10 Brecce e conglomerati (c), arenarie (a), siltiti (s) e loro equivalenti non cementati (sottolineati i depositi continentali); depositi flyschioidi (f). Breccias and conglomerates (c), sandstones (a), siltites (s) and their unconsolidated equivalents (the continental deposits are underlined); flyschioid deposits (f).
11 Rocce carbonatiche di mare sottile ed associate: calcareniti (c), dolomie (d), calcari evaporitici (e), marmi (m). Shallow-water carbonate rocks and their associates: calcarenites (c), dolomites (d), evaporitic limestones (e), marbles (m).
12 Rocce carbonatiche pelagiche ed associate. Pelagic carbonate rocks and their associates.
13 Rocce silicee: radiolariti (r), ftaniti (f). Siliceous rocks: radiolarites (r), phtanites (f).
14 Gesso, anidrite, sale. Gypsum, anhydrite, halite.
15 Calcari e marne emipelagiche in facies di "Trubi". Hemipelagic limestones and marls in "Trubi" facies.
42°
41°
40°
39°
38°
10°
11°
12°
13°
14°
15°
654
652
653
656
655
651
650
Dorsale dell'Elba
Bacino della Corsica
B. di Montecristo
Sardegna
Scarpata di Ventotene
Bacino di Sapri
Bacino di Paola
Bacino di Gioia
Bacino di Cefalù
Egadi
NAPOLI
SALERNO
PALERMO
MESSINA
CIVITAVECCHIA
I. Ustica
I. Stromboli
Golfo di Napoli
Golfo di Salerno

Metamorphic and granitic rocks

Metamorphic and granitic rocks of continental affinity have been also identified in the basin. The main lithologies of this group are phyllites, quartzites, micaschists, gneisses, and granites [Colantoni et al., 1981] (Figure 2.8).

Most of these rock types have been found in the Sardinia margin (Figure 2.3), confirming the continental nature of the basement there (e.g. Baronie seamount, #5 in Figures 2.3, 2.8, and 2.9). To the east, there is little lithological sampling information to define the lithology of the basement in the Cornaglia Terrace (Figures 2.3 and 2.8). The only point were the basement has been sampled is the top the Cornaglia seamount (#6 in Figures 2.3, 2.8, and 2.9), where Carboniferous metamorphic rocks have been recovered [Colantoni et al., 1981]. However this particular seamount may probably not be representative of the whole terrace, which has a more subdued bathymetric expression.

Several geophysical studies of the Cornaglia Terrace including old WAS [Nicolich, 1981; Duschenes et al., 1986] and relatively recent MCS studies [Carrara, 2002; Sartori et al., 2004], have been interpreted to indicate the existence of continental crust beneath the Cornaglia Terrace [Nicolich, 1981; Duschenes et al., 1986; Carrara, 2002; Sartori et al., 2004].

Continental-type rocks have been also found in the central parts of the basin, like in the Sechi seamount (#9 in Figures 2.3, 2.8, and 2.9) region and at the top of the Farfalla seamount (#14 in Figures 2.3, 2.8, and 2.9). In between the Magnaghi and Vavilov basins, metamorphic and granitic continental rocks have been also recovered in the structural high known as the De Marchi seamount [Colantoni et al., 1981] (#13 in Figures 2.3, 2.8, and 2.9). ODP site 656 (Figures 2.8 and 2.9) drilled Alpine-type rocks in the uppermost basement of this structural high, which was interpreted as an isolated fragment of continental crust emplaced in the oceanic region represented by the Magnaghi and Vavilov basins [Kastens and Mascle, 1990]. At the easternmost region of the Vavilov basin, Carboniferous granitic and metamorphic rocks were recovered in the prominent Flavio de Gioia seamount [Colantoni et al., 1981] (#17 in Figures 2.3, 2.8, and 2.9). Eastward of this structural high there are no basement samples from either DSDP or ODP. However, a continental nature has been suggested on the basis of different types of geophysical data, especially MCS images [Mascle and Rehault, 1990; Sartori, 1990; Sartori et al., 2004; Biella et al., 2007].

Finally, metamorphic and granitic rocks have been also found in the Cialdi, Verceli and Cassini seamounts located in the Northern Tyrrhenian (#3, #4, and #8, respectively in Figures 2.3, 2.8, and 2.9), where a recent study based on seismic tomography revealed the existence of continental crust likely intruded by mafic magmas at lower crustal levels [Moeller et al., 2013].

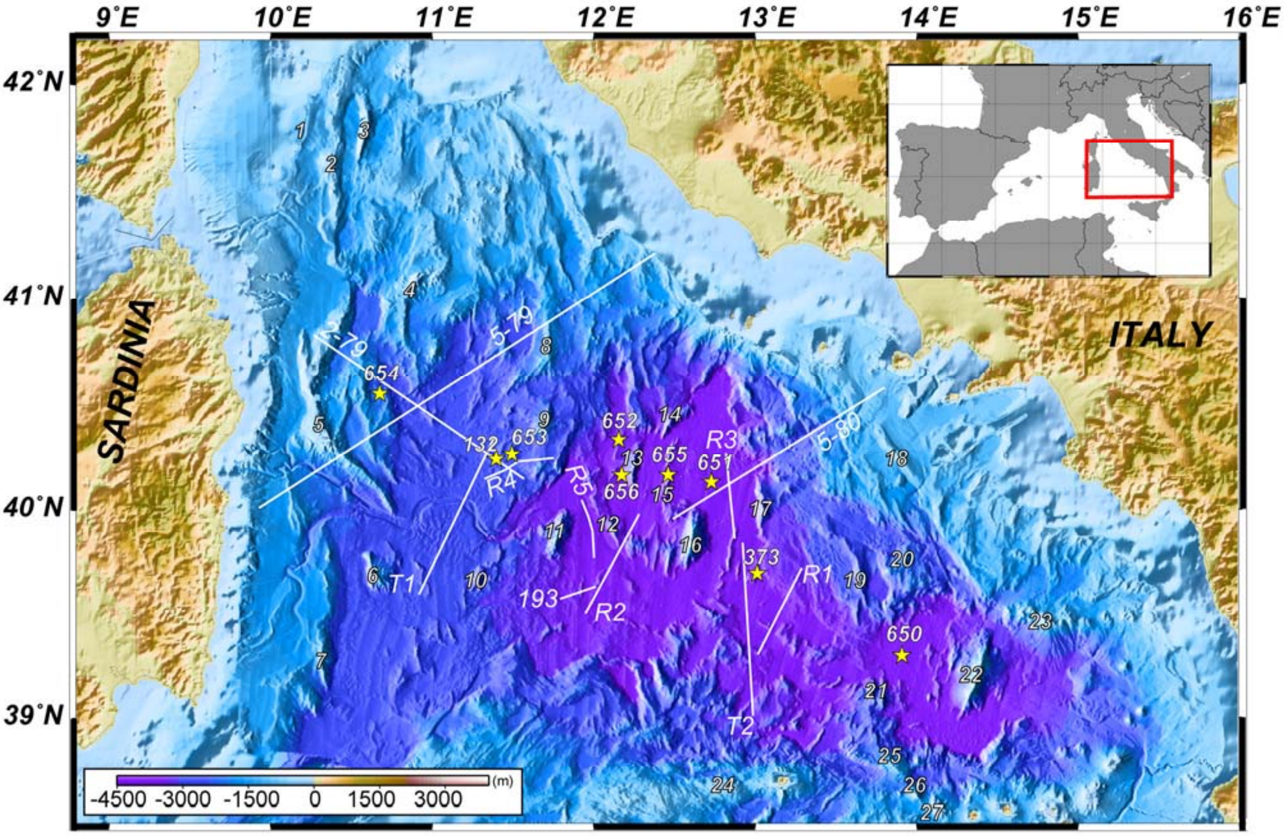
9˚E
10˚E
11˚E
12˚E
13˚E
14˚E
15˚E
16˚E
42˚N
41˚N
40˚N
39˚N
SARDINIA
ITALY
1
2
3
4
5
6
7
8
9
10
11
12
13
14
15
16
17
18
19
20
21
22
23
24
25
26
27
2-79
5-79
5-80
654
132
653
652
656
655
651
373
650
193
R1
R2
R3
R4
R5
T1
T2
-4500 -3000 -1500 0 1500 3000
(m)

Figure 2.9.- *Bathymetric and topographic map of the Tyrrhenian region showing the location of old WAS experiments carried out between the 60's and 80's (white lines) [Fahlquist and Hersey, 1969; Nicolich, 1981; Recq et al., 1984; Duschenes et al., 1986]. Yellow stars display the location of DSDP and ODP sites [Keneth et al., 1978; Kastens and Mascle, 1990]. 1: Pianosa Ridge, 2: Etruschi seamount, 3: Cialdi seamount, 4: Vercelli seamount, 5: Baronie seamount, 6: Cornaglia seamount, 7: Quirra seamount, 8: Cassini seamount, 9: Sechi seamount, 10: Major seamount, 11: Magnaghi seamount, 12: D'Ancona Ridge, 13: De Marchi seamount, 14: Farfalla seamount, 15: Gortani Ridge, 16: Vavilov seamount, 17: Flavio de Gioia seamount, 18: Monte delle Sirene, 19: Issel seamount, 20: Poseidone seamount, 21: Glauco seamount, 22: Marsili seamount, 23: Palinuro seamount, 24: Anchise seamount, 25: Sisifo seamount, 26: Enarela seamount, 27: Eolo seamount.*

Sedimentary rocks

This section presents a brief description of the sediments found in the ODP leg 107 [Kastens and Mascle, 1990] and DSDP leg 42 [Keneth et al., 1978].

ODP site 654 in the Sardinia margin (Figures 2.8 and 2.9) drilled a sequence that from top to bottom includes Pleistocene and Pliocene calcareous biogenic sediments, followed by Messinian evaporites and terrigenous sediments [Kastens and Mascle, 1990]. The lowermost unit of this site includes reddish conglomerate possibly indicating a continental depositional environment [Shipboard Scientific Party, 1987; Kastens and Mascle, 1990].

ODP site 653 is located next to DSDP 132 (Figures 2.8 and 2.9), both drillings present an upper sequence constituted by Pleistocene and Pliocene pelagic sediments that overlay a Messinian sequence of evaporites and terrigenous sediments [Keneth et al., 1978; Colantoni et al., 1981; Kastens and Mascle, 1990].

In the northernmost region of the Magnaghi basin (Figures 2.8 and 2.9), ODP site 652 displays an upper sequence of Pleistocene and Pliocene calcareous biogenic sediments followed by a Messinian unit formed by pelagic sediments interbedded with thin layers of gypsum and anhydrite [Kastens and Mascle, 1990]. Southward, ODP site 656 was drilled at the western side of a tilted fault block represented on surface by the continental De Marchi seamount (#13 in Figures 2.3 and 2.8). In this hole, calcareous biogenic and terrigenous sediments from the Pleistocene and Pliocene were found in the uppermost unit. The lowermost unit is constituted by red conglomerates, deposited in a continental environment, and derived from Alpine-type continental basement [Kastens and Mascle, 1990].

ODP site 655 was drilled on top of the Gortani Ridge, located in the Vavilov basin (Figures 2.8 and 2.9). Here a very thin Pleistocene and Pliocene sequence (< 100 m-thick) of calcareous biogenic and terrigenous sediments was found overlaying oceanic-type basalts that were proposed to form this ridge [Kastens and Mascle, 1990]. The sedimentary unit drilled in the Vavilov basin by ODP site 651 (Figures 2.8 and 2.9) shows ~350 m of Pleistocene and Pliocene pelagic, terrigenous and volcanogenic sediments. DSDP site 373 displays a rather similar sedimentary sequence [Keneth et al., 1978; Colantoni et al., 1981] (Figure 2.8).

ODP site 650 in the Marsili basin (Figures 2.8 and 2.9), found ~600 m of

Pleistocene and Pliocene terrigenous and volcanogenic sediments on top of vesicular basalts [Kastens and Mascle, 1990].ODP and DSDP data have reported the existence of Messinian deposits related to the salinity crisis in the Tyrrhenian basin (e.g. ODP site 653; DSDP site 132) [Keneth et al., 1978; Kastens and Mascle, 1990]. The spatial distribution of the main evaporitic deposits has provided important information that helped to reconstruct the main phases of opening of the Tyrrhenian basin [e.g. Rosenbaum and Lister, 2004].

2.2.4 Neogene-Quaternary Volcanism

The opening of the Tyrrhenian basin has been accompanied by an important volcanic activity, including the arc-type magmatism linked to the subduction of the Tethyan slab beneath the Apennines-Calabrian subduction front, the interpreted oceanic crust of the Vavilov and Marsilli basins, and the volcanic edifices of Vavilov, Marsilli and other large seamounts. Hence, the spatio-temporal distribution of magmatism (Figure 2.10) reflects a complex back-arc and arc igneous activity related to the retreat of the subduction front [Savelli, 2002; Lustrino 2011].

Magmatic rock types in the Tyrrhenian Sea basin present a wide variety of compositions ranging from subalkaline (tholeiitic and calc-alkaline) to alkaline (potassic), and ultra-alkaline (ultrapotassic) affinity [Lustrino et al., 2011] (Figure 2.10). Based on Savelli [2002], igneous activity in the Tyrrhenian region can be divided in 5 magmatic phases, being the oldest during Early-Mid Miocene times (~15-9 Ma), which concentrates in Corsica and Sardinia, and the youngest and most important during Pleistocene to present times (1.5-0 Ma), which concentrates in the Aeolian Islands (Figure 2.1).

Phase 1 [~15-9 Ma]:

The orogenic igneous activity related to this first phase took place soon after the last stages of the Liguro-Provençal opening [~20-15 Ma; Gattacceca et al., 2007] and the coetaneous Oligocene-Early Miocene volcanic activity located in Corsica and Sardinia (orange figures in Figure 2.10) [Savelli 2002]. Magmatic products related to this phase are found in Sardinia and in the Cornacya seamount, located in the southernmost part of the Cornaglia Terrace (easternmost inverted yellow triangle in Figure 2.10), and include calc-alkaline, high-K calc-alkaline and ultra-alkaline volcanics

[Savelli 2002]. Additionally, lamproitic rocks (ultrapotassic) were found in the northeastern sector of Corsica [Serri et al., 1993]. Isotopic composition analyses of these lithologies indicate a complex range of crustal contamination and possibly a component of slab-derived fluids and/or melts [Lustrino et al., 2011].

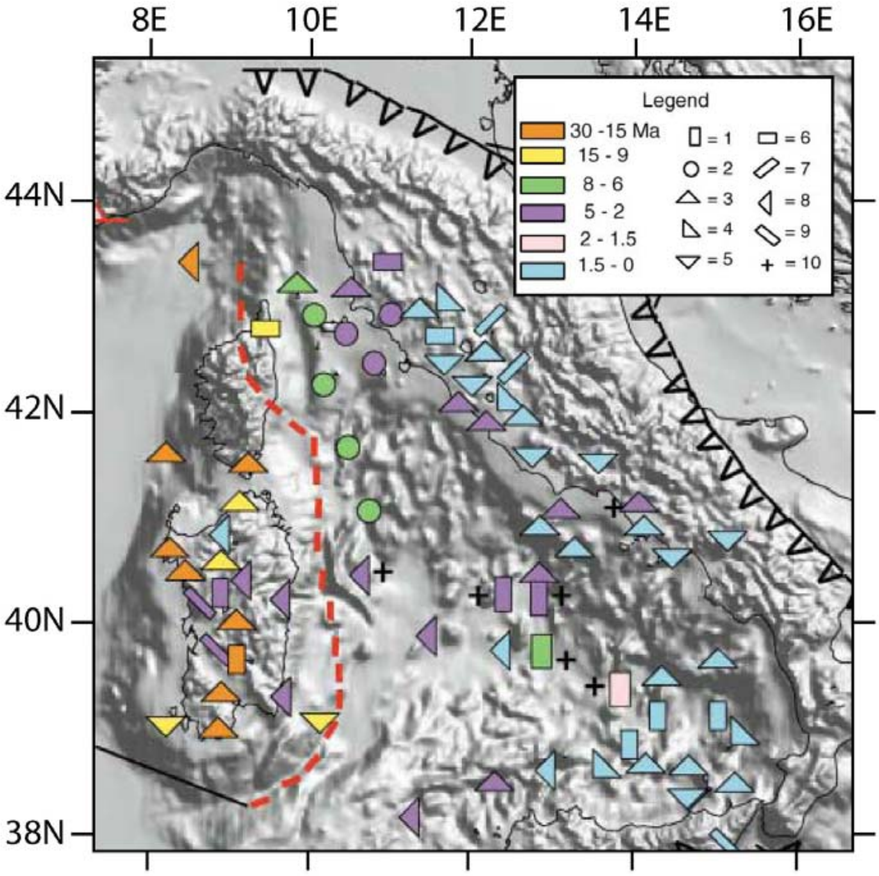

Figure 2.10.- *Map of the distribution of the magmatic activity in Sardinia, Corsica, and the Tyrrhenian and Apenninic regions from Oligocene to the present days, modified from Savelli [2002]. 1=tholeiites; 2=calcalkaline and high-K calcalkaline plutons; 3=calcalkaline and high-K calcalkaline volcanics; 4=shoshonites; 5=ultrapotassic volcanics; 6=lamproites; 7=carbonatites; 8=intra-plate volcanics; 9=rocks from intra-plate, large central volcanoes; 10=volcanics from deep drillings. Red dashed line shows the relict Alpine front as suggested by Savelli [2002].*

Phase 2 [8-6 Ma]:

During this phase the Tyrrhenian basin was already in advanced stages of extension [Kastens and Mascle, 1990]. In the northern Tyrrhenian basin granitoids were intruded in the stretched continental crust between 7.5 Ma and 6.5 Ma [Serri et al., 1993; Savelli, 2002]. At the same time in the southern basin the first tholeiitic basalts were erupted in the Vavilov basin [DSPD site 373, Dietrich et al., 1977] (site 373 in Figure 2.9).

Phase 3 [5-2 Ma]:

An important pulse of calc-alkaline and tholeiitic intra-plate volcanism (i.e. anorogenic) occurred in this phase [Savelli, 2002]. Evidences of this eruptive phase have been found in the island and margin of Sardinia (ODP site 654 in Figures 2.8 and 2.9) [Beccaluva et al., 1990; Savelli, 2002], and by volcanics in the Magnaghi (3-2.7 Ma) and the Vavilov (< 2.6 Ma) seamounts (#11 and #16 in Figures 2.3, 2.8, and 2.9) [Colantoni et al., 1978; Robin et al., 1987; Savelli 2002]. In addition, in the central part of the Tyrrhenian basin, enriched- and normal- mid ocean ridge basalts (E-/N-MORB) were emplaced in the Gortani Ridge at 4.3 Ma (ODP site 655 in Figures 2.8 and 2.9) and in the Vavilov basin basement at 2.6 Ma (ODP site 651 in Figures 2.8 and 2.9), respectively [Bertrand et al., 1990; Savelli, 2002]. However, basalts of this age in the Vavilov basin (ODP site 651 in Figures 2.8 and 2.9) also present a calc-alkaline affinity indicating the influence of slab-related products within the magmatic source [Bertrand et al., 1990]. During this phase calc-alkaline acidic volcanic and plutonic magmatism also occurred in the eastern sector of the Northern Tyrrhenian basin and western Apenninic chain [Savelli, 2002] (Figure 2.10). The isotopic composition of these magmas also revealed the influence of a slab [Lustrino et al., 2011].

Phase 4 [2-1.5 Ma]:

This is the shortest magmatic phase evidenced in the region and took place in the SE portion of the Tyrrhenian basin, probably during the formation of the Marsili basin (Figures 2.3, 2.8, and 2.9), where E-MORB and calc-alkaline basalts were generated during oceanic crustal accretion [ODP site 650 in Beccaluva et al., 1990].

Phase 5 [1.5-0 Ma]:

This is the most important magmatic phase of the Tyrrhenian region in terms of volume of volcanism [Savelli, 2002] (Figure 2.10). The Southern Tyrrhenian basin witnessed one of the most important episodes of volcanism of the late Pleistocene-Holocene age, which originated the current volcanic arc of the Aeolian Islands. These islands present a wide range of subduction-related volcanic rocks including calc-alkaline and ultrapotassic (Blue figures in Figure 2.10) [Savelli 2002]. Similarly, the large Marsili seamount was emplaced during this phase (#22 in Figures 2.3, 2.8, and

2.9) [< 0.7 Ma; Lustrino et al., 2011]. The composition of the Marsili seamount lavas varies from transitional- and E-type MORB to calc-alkaline basaltic and high-K andesitic type, suggesting that the source is also affected by slab-derived products [Lustrino et al., 2011]. Further to the north, in the Vavilov seamount the last intra-plate basalts erupted [~0.7- 0.1 Ma; Lustrino et al., 2011]. In the western margin of the Italian Peninsula, especially west of the northern Apenninic chain, magmatism was also widespread during this period of time [Serri et al., 1993; Savelli 2002] (Figure 2.10).

In summary, the magmatic activity of the Tyrrhenian region through time can be classified in two main groups:

i. A first group of slab-derived magmas linked to the evolution of subduction .

ii. A second group related to passive mantle decompression by lithospheric extension and/or other intra-plate processes (e.g. anorogenic volcanism in phase 3). Nevertheless, these rocks also show in their isotopic composition the influence of slab-derived fluids/melts [Lustrino et al., 2011].

Part II:

Methodology

Chapter 3: Acquisition & Modeling of Wide-Angle Seismics

3.1 Introduction

Wide-Angle Seismics (WAS) is an active seismic method that consists of acquiring and analyzing the seismic record of both refracted and wide-angle reflected waves that result from the propagation of elastic waves through the media at relatively long offsets between source an receiver. Modeling of these data provides information of the propagation velocity field through the medium of interest and on the geometry of geological discontinuities that have a contrast of impedance and produce laterally continuous reflected phases (e.g. the sediment-basement and Moho boundaries).

In this chapter I describe the acquisition system, processing, analysis, and modeling of marine WAS data for crustal-scale studies, which has been used often to study the structure and properties of active and passive margins, including different areas of the Western Mediterranean [e.g. Duschenes et al., 1986; Pascal et al., 1993; Contrucci et al., 2001; Gailler et al., 2009; Lêpretre et al., 2013].

3.2 Acquisition system

The marine WAS acquisition system consists of a seismic source, usually an array of air guns (Figure 3.1a), and a set of receivers that are deployed on the seabed (Figure 3.2). In our case the receivers are the so-called Ocean Bottom Hydrophones (OBH) (Figure 3.1c), which record pressure variations in the water using hydrophones, and Ocean Bottom Seismometers (OBS) (Figure 3.1b), that measure the three components of motion with a seismometer and also with a hydrophone. The whole system is attached to the seabed by an expendable anchor. When the experiment finishes the system is recovered by means of an acoustic releaser that liberates the instrument from the anchor that remains on the seafloor. Then the OBH/S rises by buoyancy to the sea surface where it is recovered from the vessel.

The design of a WAS experiment includes the source design (number, size, power, spatial distribution and depth of the guns), the firing interval, and the distance between receivers. These parameters are defined on the basis of the desired level of spatial and vertical resolution and the depth of the target to be sampled and modeled.

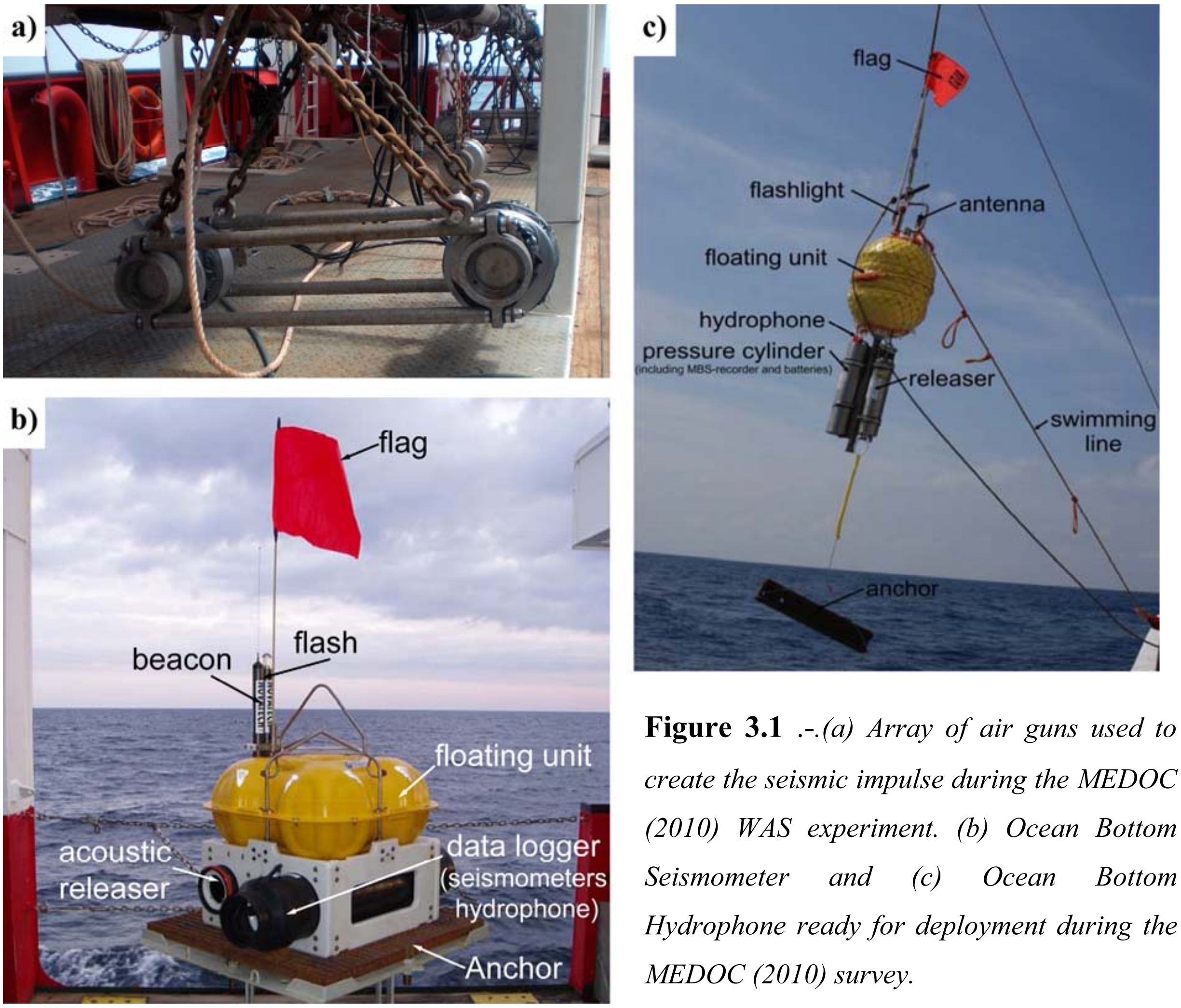
a)
b)
flag
beacon
flash
floating unit
acoustic releaser
data logger (seismometers hydrophone)
Anchor
c)
flag
flashlight
antenna
floating unit
hydrophone
pressure cylinder (including MBS-recorder and batteries)
releaser
swimming line
anchor

Figure 3.1 .-.*(a) Array of air guns used to create the seismic impulse during the MEDOC (2010) WAS experiment. (b) Ocean Bottom Seismometer and (c) Ocean Bottom Hydrophone ready for deployment during the MEDOC (2010) survey.*

The depth of the source controls the interference of primary and ghost pulses and thus the useful frequency bandwidth of the signal emitted by the source. In crustal-scale WAS experiments it is usually set deeper than in other seismic experiments (10-20 meters beneath the sea surface) to have lower frequencies in the source wavelet. Low frequencies attenuate less than higher ones as they propagate, reaching greater depth and longer offsets (e.g. source-receiver distance). Firing frequency or shot interval in WAS experiments is longer than in seismic reflection techniques because the shot point distance is aimed at minimizing the background noise by reducing wraparound noise from previous shots in the water layer. The typical shooting distance is 60-120 s or about 150-300 m. Receiver spacing helps improving the accuracy of the final velocity model, the smaller the receiver spacing, the higher is the redundancy of data, and hence the information provided by the data set in the modeling process is better constrained. The interval between receivers depends on many factors, such as the bathymetry or the number of available receivers, but for modern crustal-scale experiments it is typically set at 5-15 km spacing.

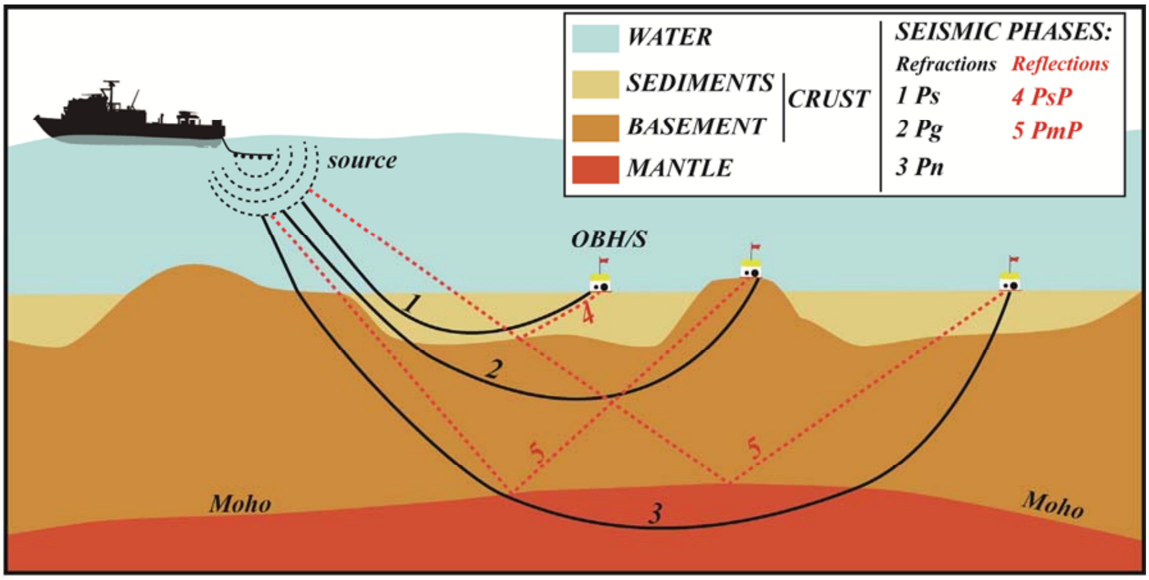

Figure 3.2 .-*Schematic representation of the WAS experiment and the propagation of the different P-waves seismic phases refracted through the sediments (PsP), crust (Pg), and mantle (Pn); and reflected at the sediment-basement boundary (PsP), and at the crust-mantle boundary (PmP).*

In this work, the R/V Sarmiento de Gamboa seismic source consisted of two arrays of 6 G-II airguns each, with a total capacity of 4600 in^3, fired at constant interval of 90s (~220m). Average receiver spacing for both WAS lines was ~10 km. WAS data along Line GH were recorded by 4 Spanish LC2000 4x4 OBSs deployed by the R/V Sarmiento de Gamboa, 22 German E-2PD and HTI-01-PCA OBHs and 5 Italian onshore Lennartz M24-LP-24 Bit seismometers installed in Sardinia. In the case of Line EF, WAS data were recorded by 5 Spanish LC2000 OBSs, 23 German E-2PD and HTI-01-PCA OBHs, and 5 Italian onshore Lennartz M24-LP-24 Bit seismometers installed in Sardinia (see Figure 1.1).

Once the experiment is designed according to the target to be resolved, the OBS/Hs are deployed on the seafloor and the seismic source is fired at constant interval, generating acoustic waves in the water column that propagate through the different layers of the subsurface. Out of the different phases recorded, those that are used for modeling are the body waves (i.e. either primary or P-waves, and secondary or S-waves) (Figure 3.2). In general those which are more commonly visible and thus generally used for modeling in WAS experiments are the P-waves (Figure 3.2). These seismic waves are reflected as a result of acoustic impedance contrasts across sharp geological interfaces and transmitted or refracted through the medium following Snell's law (Figure 3.3a).

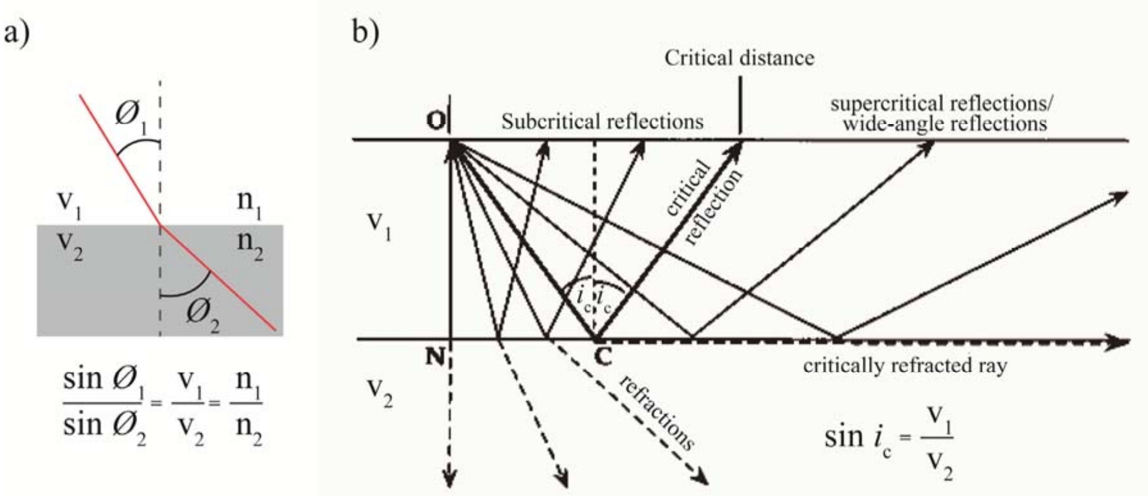
a)
Ø1
v1
n1
v2
n2
Ø2
sin Ø1 / sin Ø2 = v1 / v2 = n1 / n2
b)
Critical distance
O
Subcritical reflections
supercritical reflections/
wide-angle reflections
critical
reflection
V1
ic ic
N
C
critically refracted ray
V2
refractions
sin ic = V1 / V2

Figure 3.3 .-.*(a) Schematic representation of the Snell's law (left), showing how the ray path (red line) incides with angle* θ_1 *from a medium with velocity* v_1*, and refractive index* n_1 *to a lower medium with velocity* v_2*, and refractive index* n_2*;* $v_1 < v_2$*. As a result, the ray path is refracted with an angle* θ_2 *through the lower medium. The relationship between all this factors is represented by the Snell's law (right). (b) Schematic representation of the evolution of the reflections and refractions as the source-receiver distance increases. Note that after point C, the ray of the seismic wave incides with the critical angle* i_c *and critically refracts through the top of the lower layer. Reflections that occur after the critical distance are known as wide-angle reflections*

In theory, as the angle of incidence increases due to the increase of the source-receiver distance, the refracted rays experience a change of direction according to Snell's law (Figure 3.3a). When the source-receiver distance reaches the *critical distance* (Figure 3.3b), the ray encounter the boundary between geological layers with a *critical angle of incidence* (i_c in Figure 3.3b). At that point the ray is refracted with an angle of refraction of 90º and travels parallel to the boundary in the top of the lower layer with the faster velocity V_2. The critical angle i_c can be calculated by applying Snell's law (Figure 3.3b). At angles greater than the critical angle refraction is no longer possible. The energy from seismic rays that are incident more obliquely than the critical angle is entirely reflected. These reflections are known as *supercritical reflections*, or simply *wide-angle reflections*. They lose little energy to refractions and travel large distances providing information of boundaries like the sediment-basement boundary or the Moho [Lowrie, 2007].

The data recorded by an OBH/S consist of a continuous temporal trace that includes, at different offsets, the seismic events produced by the arrivals of the recorded waves corresponding to the different seismic phases. The sorting by offset of this seismic trace provides the so-called common receiver gather or record section that is commonly represented in an offset-time corrected diagram as shown in Figure 3.4. This representation makes easier the phase identification and interpretation.

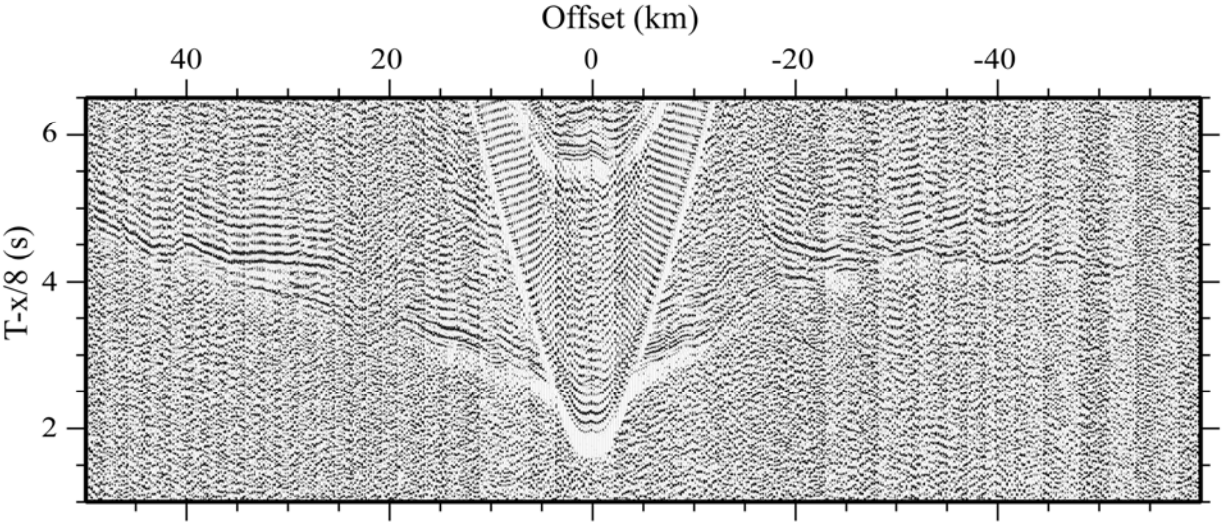

Figure 3.4 .-*Seismic record section obtained after sorting by offset the recorded seismic traces of an OBS/H. The vertical axis commonly represents a "reduced time", this is T-offset/**v**, where **v** is a reference velocity. This way, the slope of the different phases indicates if the propagation velocity is higher or lower than, or equal to, **v**. In the diagram above **v**= 8 km/s.*

3.3 Wide-Angle seismic data processing and seismic phase identification

WAS data are processed to enhance the signal-to-noise ratio and visually recognize better the lateral correlation of seismic phases in the record section. Processing of WAS data is considerably simpler than that applied to MCS data (see section 5.2), and typically includes:

- The relocation of the instrument in the seafloor. Oceanic currents may drift the receiver on its way to the seafloor causing significant variations in the original location of deployment.
- A processing sequence that generally consist of a predictive deconvolution (see section 5.3), a time- and offset-variant Butterworth (or other) bandpass filter and an amplitude balancing like an Automatic Gain Control (AGC) [e.g. Sallarès and Ranero, 2005; Moeller et al., 2013], although other processing steps may be applied to the data when necessary. In this work the WAS data processing has consisted of a Butterworth band-pass filter (5-15Hz) and an AGC for the OBSs of both lines, and a predictive deconvolution (see section 5.3), a Butterworth band-pass filtering (2-11Hz) and an AGC for the OBHs. For all the land receivers a Butterworth band-pass filtering (3-13Hz) was only applied.

Once data are processed the first step for phase identification is to determine the type of information that is available in the record section. In the case of refractions, the first arrivals are displayed as short segments of straight lines whose slope is proportional to the seismic velocity of the layer at which they turn out (e.g. Pg and Pn Figure 3.5). In this case, phases displaying slopes that are smaller than the correction velocity (see figure caption of Figure 3.4) must correspond to waves propagating at velocity lower than the correction velocity (e.g. Pg in Figure 3.5), whereas phases displaying slopes larger than the correction velocity must correspond to higher propagation velocity (e.g. Pn in Figure 3.5). In contrast, reflections are secondary arrivals represented by hyperbolic functions that are asymptotic to the corresponding refracted wave in the record sections. For example, PmP is asymptotic to Pg/Pn in the record section of Figure 3.5.

The analysis of WAS data consist in the identification of these seismic phases and the manual or automatic selection (picking) of their arrival times. The selected picks are used as initial data set for the next step: the modeling.

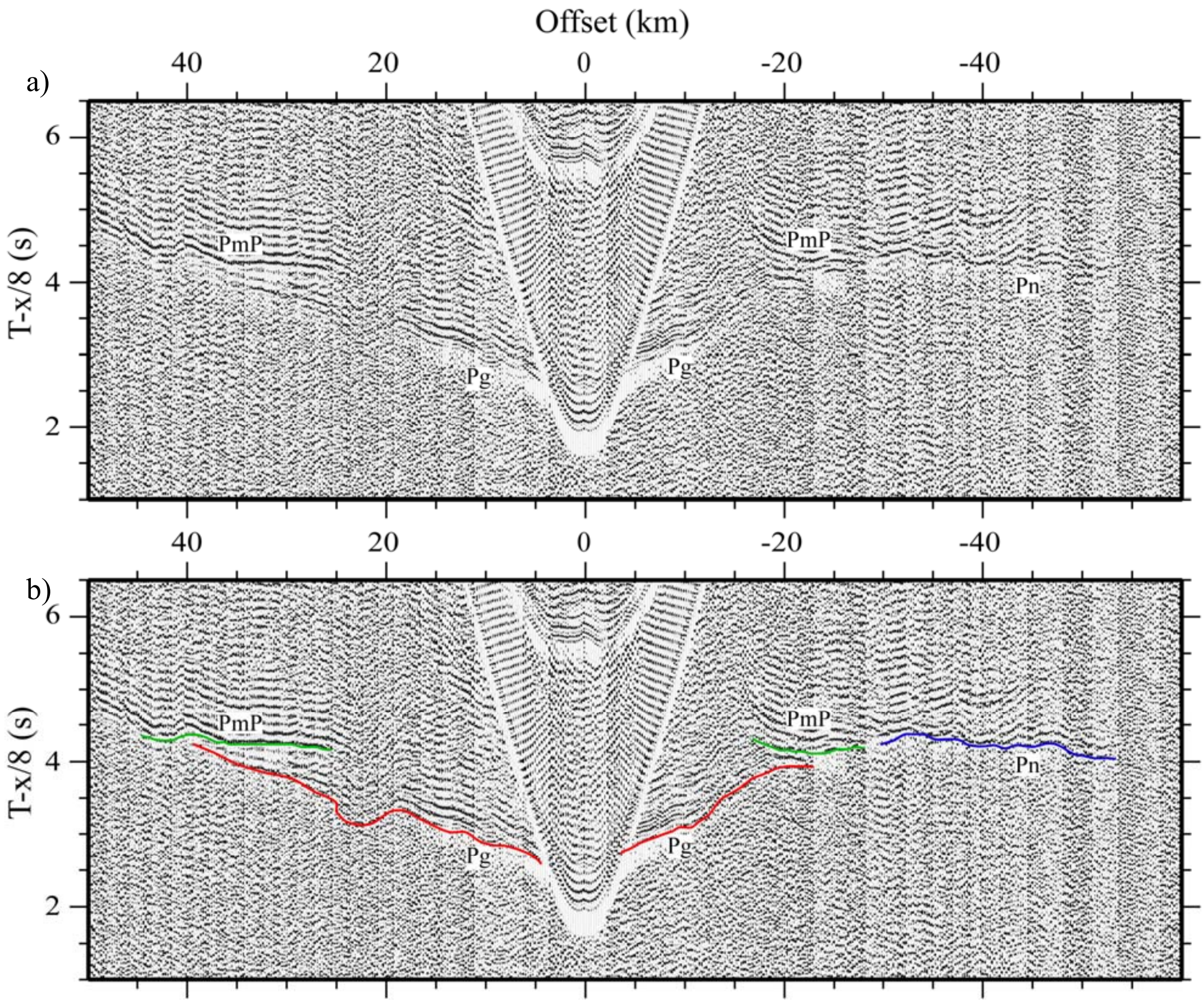

Figure 3.5 .-*(a) Record section shown in Figure 3.4 including three seismic phases of P-waves refracted through the crust (Pg) and mantle (Pn), and reflected at the Moho (PmP). Details of these phases are given in the text and in Figure 3.2. (b) Approximation of the hodochrone or travel time curves of the same seismic phases identified in (a). Note that the relation between the refracted Pg and the reflected PmP is asymptotic.*

3.4 Wide-Angle seismic modeling

Typically, there are two different ways to model the travel time data set and obtain a velocity model of the crust and uppermost mantle: forward modeling or inversion. Forward modelling implies that the velocity model and the geometry of the geological boundaries are manually built by an interpreter, and it is improved by trial-and-error until an acceptable fit between the observed and simulated data is obtained. The core tool to construct the velocity models is thus a ray-tracer algorithm [e.g. Zelt and Smith, 1992]. This method was widely used until the 90's and is still used in land experiments, where the number of sources/receivers is limited. However this approach has many limitations, the final solution is rather subjective, and it does not allow performing formal parameter uncertainty analysis. In addition, it becomes unfeasible when there is a large number of sources and receivers as is the case of modern 2D or 3D marine WAS experiments.

In contrast, the aim of inverse methods, also known as "tomographic" methods, is to determine the velocity model, as well as the geometry of the reflecting boundaries in the case that reflected phases are used, in an automatized manner [e.g. Toomey et al., 1994; Korenaga et al., 2000]. The tomographic problem can be divided in two parts. The first, which is known as forward problem, is the same that must be solved in the forward modeling techniques and consists of tracing the rays and calculating the synthetic travel-times. The second is the inverse problem. In this case the actual problem of travel-time calculation is approximated by a linear version, in which the travel time residuals for an initial (i.e. reference) model are related to the model changes by means of the matrix of partial derivatives (i.e. the Jacobian), which is also known as the sensitivity, or Fréchet, matrix. The inverse problem, which is solved iteratively, consists on inverting this matrix to get the model changes out from the travel time residuals for a reference model.

The WAS data in this work have been modeled using a joint refraction and reflection travel time inversion method, implemented in the code *tomo2d* [Korenaga et al., 2000]. This method allows obtaining a two-dimensional velocity model and also the geometry of a single floating reflector [Korenaga et al., 2000]. The velocity model is represented as a sheared mesh of velocity nodes hanging from the seafloor and/or land surface (Figure 3.6). The floating reflector is represented by an array of linear segments, whose nodal spacing is independent of that used in the velocity mesh [Korenaga et al., 2000]. The flow diagram of *tomo2d* is shown in Figure 3.7 and explained below.

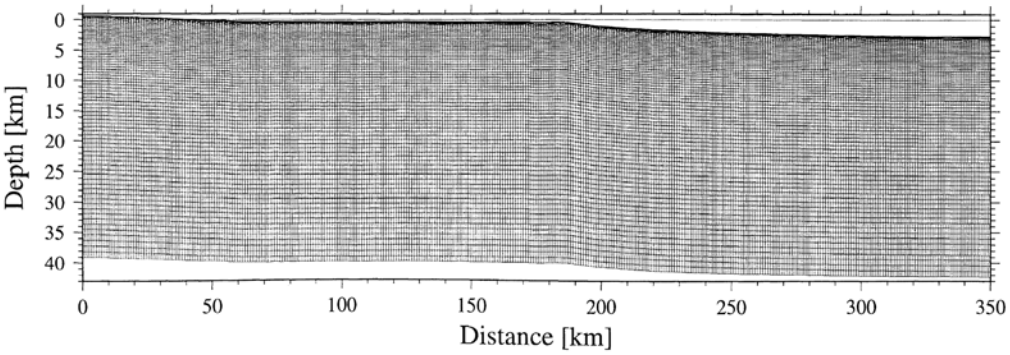
Depth [km]
0
5
10
15
20
25
30
35
40
0
50
100
150
200
250
300
350
Distance [km]

Figure 3.6 .- *Velocity mesh used by TOMO2D composed of cells of variable size hanging from seafloor. From Korenaga et al. [2000].*

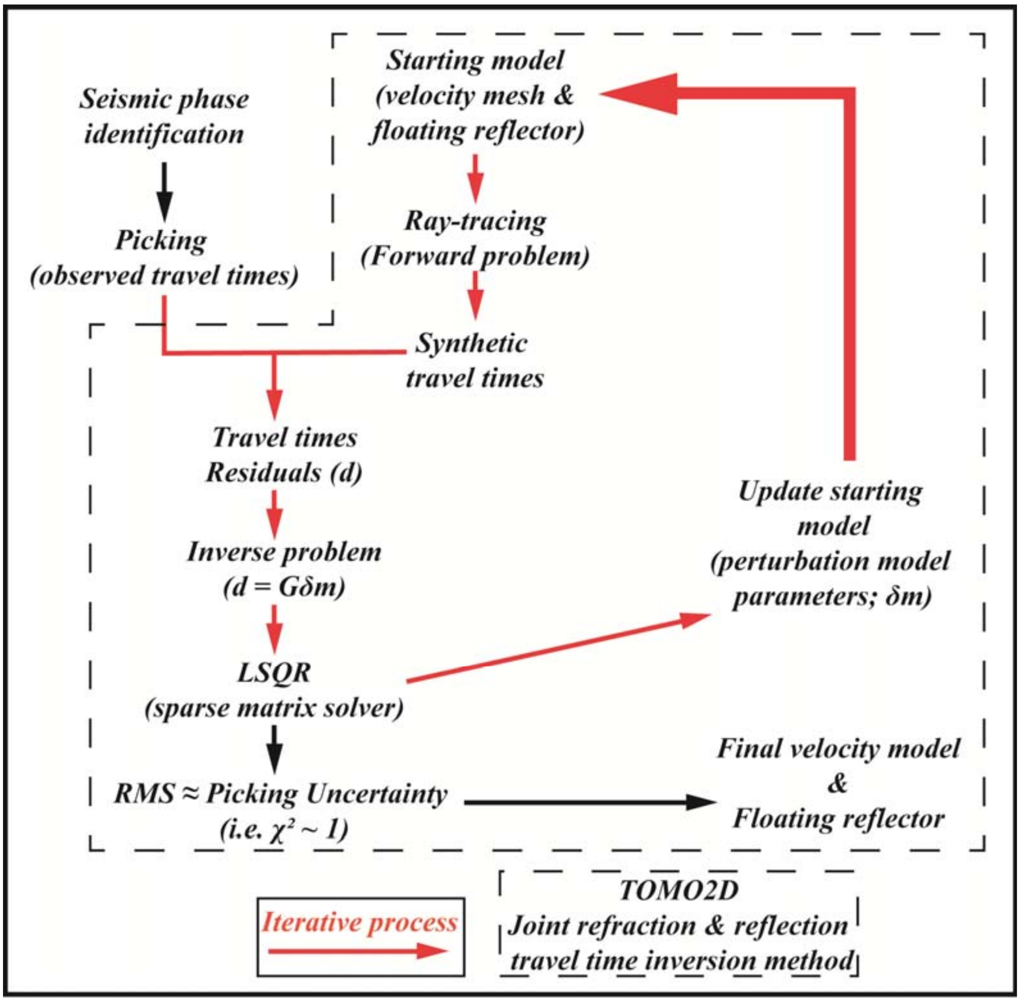
Seismic phase identification
Picking (observed travel times)
Starting model (velocity mesh & floating reflector)
Ray-tracing (Forward problem)
Synthetic travel times
Travel times Residuals (d)
Inverse problem (d = Gδm)
LSQR (sparse matrix solver)
RMS ≈ Picking Uncertainty (i.e. χ² ~ 1)
Update starting model (perturbation model parameters; δm)
Final velocity model & Floating reflector
Iterative process
TOMO2D Joint refraction & reflection travel time inversion method

Figure 3.7 .- *Flow diagram of the joint refraction and reflection travel time inversion method applied with TOMO2D [Korenaga et al., 2000].*

To solve the forward problem (Figure 3.7), this method uses a hybrid ray-tracing strategy that first calculates a polygonal ray trajectory using the graph method [Moser, 1991] that is subsequently refined using a ray-bending technique [Moser et al., 1992].

The optimal parameters for bending are calculated using the conjugate gradients method (Figure 3.8).

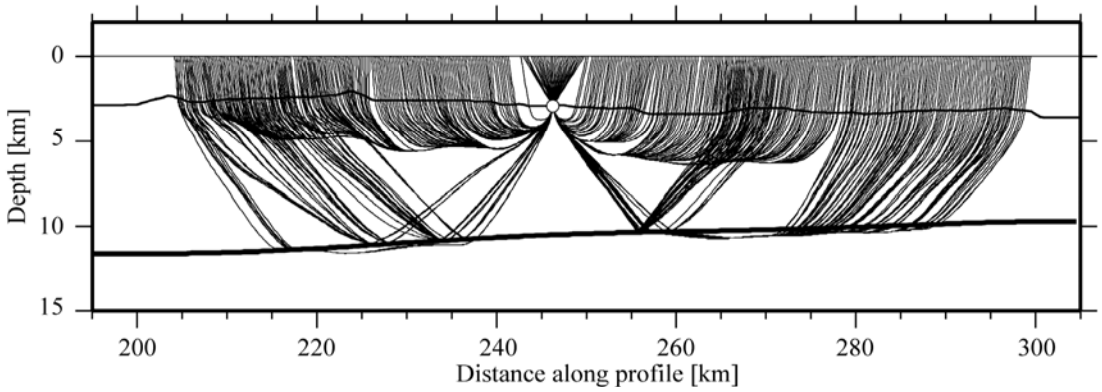

Figure 3.8 .- *Example of ray-tracing resulting from the combination of the graph and ray-bending methods for both refracted and reflected waves [Moser et al., 1992].*

Then, an inverse problem is set to solve equation 3.1, which represents the linear approximation of the forward problem around a reference model:

$$\mathbf{d} = \mathbf{G}\delta\mathbf{m} \quad . \tag{3.1}$$

In this case, ***d*** is the travel time residual vector, obtained from the difference between observed and synthetic data, ***G*** is the Fréchet derivative matrix (Jacobian matrix), that contains the velocity and depth derivatives of the residual travel times, and ***δm*** is the unknown model perturbation vector, which includes the velocity and floating reflector depth perturbations. Additionally, to control the degree of perturbation of the model parameters, smoothing constraints are applied to both velocity and reflector geometry, defining laterally- and vertically-variable correlation lengths. Damping constraints are also used to regularize the linear system and stabilize the inversion. Hence, with these weighting parameters added to the linear system, equation 3.1 can then be written as:

$$\begin{bmatrix} \mathbf{d} \\ \mathbf{0} \\ \mathbf{0} \\ \mathbf{0} \\ \mathbf{0} \\ \mathbf{0} \end{bmatrix} = \begin{bmatrix} \mathbf{G}_v & w\mathbf{G}_d \\ \lambda_v \mathbf{L}_{\mathrm{H}v} & \mathbf{0} \\ \lambda_v \mathbf{L}_{\mathrm{V}v} & \mathbf{0} \\ \mathbf{0} & w\lambda_d \mathbf{L}_d \\ \alpha_v \mathbf{D}_v & \mathbf{0} \\ \mathbf{0} & w\alpha_v \mathbf{D}_d \end{bmatrix} \begin{bmatrix} \delta\mathbf{m}_v \\ \frac{1}{w}\delta\mathbf{m}_d \end{bmatrix} \quad , \tag{3.2}$$

where, ***v*** and ***d*** subscripts denote the velocity and depth components. $\boldsymbol{L_{Hv}}$ and $\boldsymbol{L_{Vv}}$, correspond to the horizontal and vertical correlation length matrices for velocity, respectively, and $\boldsymbol{L_d}$ is the correlation length matrix for depth. $\boldsymbol{\lambda_v}$ and $\boldsymbol{\lambda_d}$ are control parameters of the smoothing constraints. The depth kernel weighting is represented by $\boldsymbol{w}$, which adjusts the depth sensitivity in the Fréchet matrix. Damping matrices for velocity and depth are represented by $\boldsymbol{D_v}$ and $\boldsymbol{D_d}$, respectively, and, $\boldsymbol{\alpha_v}$ and $\boldsymbol{\alpha_d}$ control the strength of the damping constraints.

Equation 3.2 is a sparse system, so it is efficiently solved using a sparse matrix solver. In the case of *tomo2d* the Fréchet matrix is inverted applying the *LSQR* solver [Paige and Saunders, 1982]. Given that the problem solved is a linear approximation of the real one, equation 3.2 must be applied iteratively using as input in each iteration the model parameters obtained in the previous one. This scheme is repeated until convergence is achieved (Figure 3.7). For that reason, the reference model is modified successively by $\boldsymbol{\delta m}$ until the root mean square (RMS) value of travel time equals approximately the uncertainty of the observed data (i.e. ~70-60 ms), or, what is the same, when the chi-squared (χ^2) value becomes ~1 (Figure 3.7). The linear sensitivity of the inversion, which is also a measure of the ray coverage throughout the model, is provided by the Derivative Weight Sum (DWS) [Toomey and Foulger, 1989] (Figure 3.9).

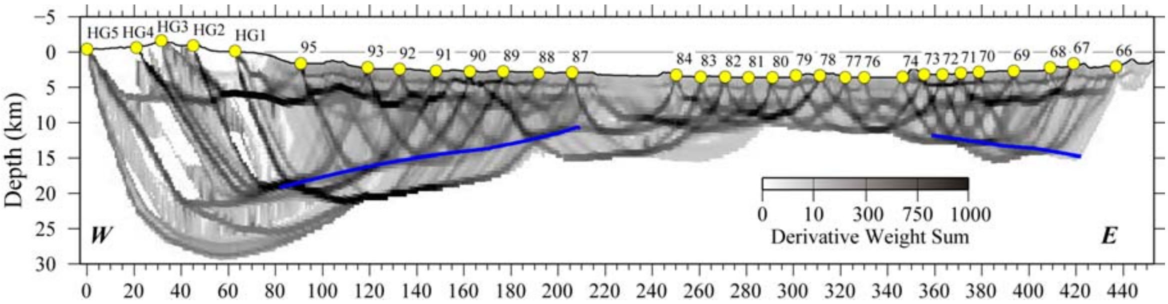

Figure 3.9 .- *Derivative weight sum for the velocity model of Line GH. The higher is the DWS, the higher is the ray coverage.*

In this work, the mesh of both models is 450 km wide and 35 km deep, with node spacing varying in the vertical component from 0.125 km at the seafloor to 1.5 km at the bottom, and a constant spacing of 0.5 km in the horizontal. Node spacing for the floating reflector is also 0.5 km and constant. In order to select the most appropriate set of regularization constraints, several combinations of correlation lengths, damping and smoothing parameters were tested. According to test results a horizontal correlation length of 2 km at the top and 8 km at the bottom, and a vertical correlation length of 0.2 km at the top and 1.5 km at the bottom were selected for Line GH model. For Line EF, a horizontal correlation length of 1 km at the top and 10 km at the bottom, and a vertical one of 0.2 km at the top and 1.5 km at the bottom were selected.

The final velocity model of Line GH (see Figure 6.2a) was obtained after 10 iterations with a RMS of 68 ms, and a χ^2 of 1.2. The RMS is 69 ms for the Pg, Pb and Pn phases and 59 ms for the PmP. In case of Line EF (see Figure 7.2a), the final model was obtained after 10 iterations with a RMS misfit of 68 ms, and a χ^2 of 1.3. The RMS for first arrivals (Pg and Pn phases) is 70 ms and 59 ms for PmP.

3.4.1 Layer-stripping strategy

As stated in the previous section, *tomo2d* just allows inverting a single reflector at a time, so it is necessary to define an iterative strategy in the case that different boundaries, or layers, have to be inverted. To solve this issue I followed a top-to-bottom layer-stripping strategy similar to that described in Sallarès et al. [2011; 2013a, b]. This multi-step inversion strategy consists of adding the data sequentially to the inversion, starting with shortest offsets (e.g. sediment phases) and finishing with the longest (e.g. mantle phases). This strategy permits to account for sharp geological contacts such as those occurring across the sediment/basement interface or the Moho [e.g. Sallarès et al., 2011].

The data of this work do not show clear sediment/basement boundary phases, so that the only reflector to be inverted is the Moho. Thus, I have followed a two-step layer-stripping strategy to invert first for the crustal phases and then for the upper mantle ones. Thus, in the first step the refracted phases through the crust (Pg) and basement (Pb) and reflected at the crust-mantle boundary (PmP) were jointly inverted to account for the entire crustal velocity field and the Moho reflector geometry (Figure 3.10).

In the second stage the crustal velocity model and Moho reflector obtained after the first step (Figure 3.10) were used as initial model whereas Pn phases were incorporated to the data set. To concentrate changes in those regions that are unresolved (i.e. below the crust-mantle boundary), the velocity nodes above the Moho reflector were over-damped by a factor of 100:1. As a result, the obtained velocity model displays a sharp velocity contact that coincides with the Moho location (Figure 3.11).

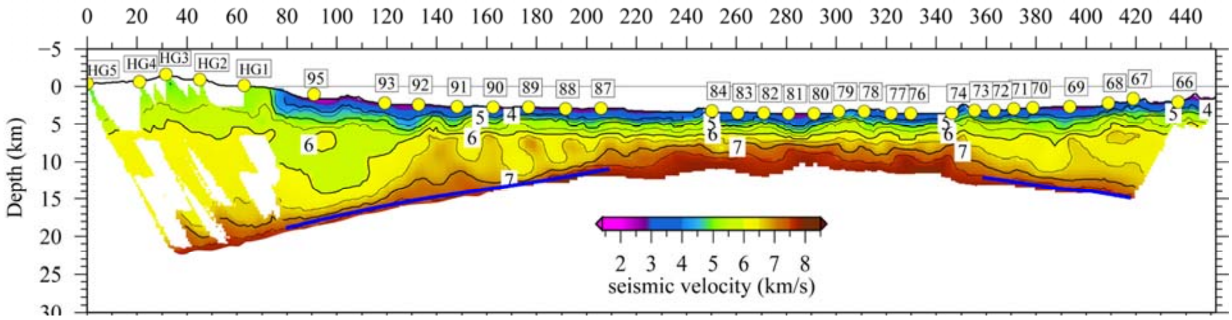

Figure 3.10 .- 2D *P-wave velocity model result of the first step of the layer stripping strategy. This tomographic model results from the inversion of Pg, Pb, and PmP phases. The tomographic model has been masked with the DWS values to show only those regions of the velocity mesh that are illuminated, and thus solved, during inversion.*

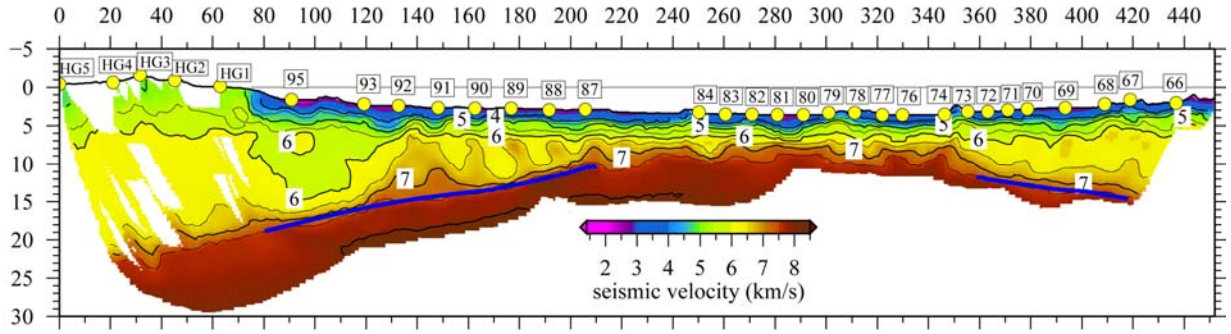

Figure 3.11 .- *P-wave velocity model result of the second step of the layer stripping strategy. This tomographic model results from the inversion of Pg, Pb, Pn and PmP phases.*

3.4.2 Uncertainty analysis

The uncertainty of the seismic velocity and other velocity-derived parameters such as density is fundamental for a reliable interpretation of basement affinity. Diverse deterministic techniques exist to estimate the parameter uncertainty based on the covariance matrix, but most of them only take into account the mathematical indetermination that is intrinsic to the approach and do not consider other sources of indetermination such as for example the dependence of the solution on the initial model used. In practical terms, the only methods to estimate the model uncertainty for a large-scale, non-linear inversions such as this one, are the stochastic, Monte Carlo-type ones [e.g., Tarantola and Valette, 1982; Tarantola, 1987]. In these methods, a set of data with random noisy travel-time sets with random initial models are inverted and the Monte Carlo realizations are constructed, with which the posteriori model covariance matrix can be estimated. By assuming that all the Monte Carlo realizations have the same probability, the mean deviation of all the solutions can be taken as a measure of the model parameter uncertainty [Tarantola, 1987]. The errors in the travel times are assigned based on Zhang and Toksöz [1998] approach, which suggest separating the picking errors on common shot errors (or receiver), common phase errors and individual picking errors. The amplitude of each of these errors depend on data quality but it is typically 15-30 ms each for a total of 45-90 ms. The highly correlated nature of travel time pick errors can be taken into account by this data randomization. Therefore to estimate model parameters uncertainty due to combinations of picking errors and starting velocity model a nonlinear Monte Carlo-type error analysis has been performed. This method is similar to that used in Sallarès and Ranero [2005], which is a modified version of that used in Korenaga et al. [2000]. The flow diagram of the analysis made is shown in Figure 3.12.

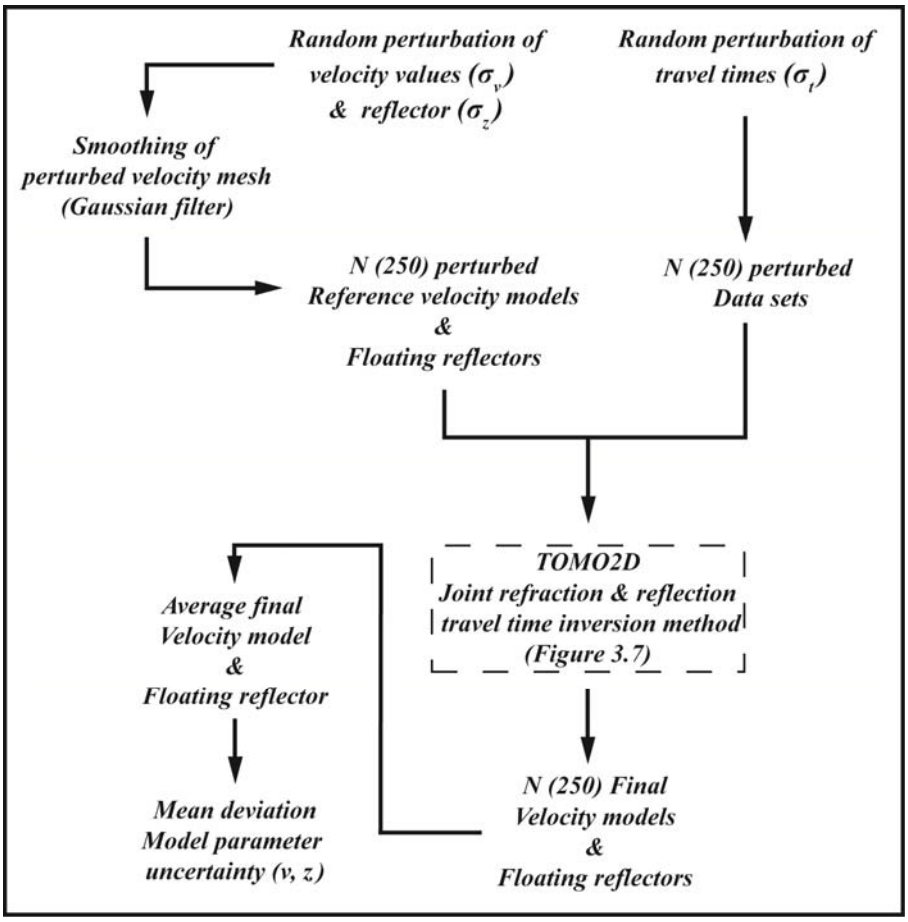
Random perturbation of velocity values (σ_v) & reflector (σ_z)
Random perturbation of travel times (σ_t)
Smoothing of perturbed velocity mesh (Gaussian filter)
N (250) perturbed Reference velocity models & Floating reflectors
N (250) perturbed Data sets
TOMO2D Joint refraction & reflection travel time inversion method (Figure 3.7)
Average final Velocity model & Floating reflector
N (250) Final Velocity models & Floating reflectors
Mean deviation Model parameter uncertainty (v, z)

Figure 3.12 .- *Flow diagram of the Monte Carlo Uncertainty approach applied to travel time inversion.*

This approach consist of randomly perturbing the velocity values of the initial model and the depth of the Moho reflector using a Gaussian distribution with a reasonable variance taking into account a priori information (σ_V=0.75 km/s and σ_Z=2 km). This way, we create a set of 250 2D reference models and their modified reference Moho reflectors. A Gaussian filter is applied to the reference velocity mesh to avoid abrupt changes of velocity within the model caused by the perturbation step. Additionally, 250 noisy travel time data sets were constructed by adding a Gaussian distribution for timing errors (σ_t=65ms), which includes the potential influence of common phase errors (±25ms), common receiver errors (±25ms) and individual picking errors (±15ms). Then, randomly selected pairs of perturbed reference models and reflectors, and noisy data sets are inverted. The average mean deviation of all inversion solutions is taken as a measure of the model parameters (velocity and reflector's geometry) uncertainty [Tarantola, 1987]. Details of the results obtained with this analysis are given in chapters 6 and 7.

Chapter 4: Gravity

4.1. Introduction

Gravitational attraction measurements and hence gravity anomalies are routinely used in many crustal-scale studies to complement WAS-derived information such as crustal thickness and velocity, and hence to further constrain the petrological nature of the rocks [e.g. Todd and Reid, 1989; Reid and Jackson, 1997].

Gravity is directly proportional to the distribution of the masses in the Earth, so it is directly related with density (ρ). Additionally, there is also empirical evidence showing that in most cases approximately linear relationships exist between the density of rocks and their P-wave velocity (Vp) [e.g. Christensen and Mooney, 1995; Carlson and Miller, 2003]. Thus, it is possible to convert modeled Vp values to ρ using the existing Vp-ρ empirical relationships for different rock types and model the density distribution to check whether it is compatible with the observed gravity data. This chapter explains the fundamentals of the acquisition and modeling of gravity data, and presents the Vp-ρ relationships used in this work.

4.2 Data acquisition and corrections

Gravity data are acquired with a gravimeter (Figure 4.1), which measures variations of the downward gravity acceleration. The units of these measurements are *milligals* (mGal) (10^{-3} mgal = 10^{-5} m s^{-2}). Since these instruments are extremely sensitive to vibrations, gravimeters in marine experiments are habitually stabilized on a platform that isolates the sensor from the influence of the movements of the ship (Figure 4.1).

Marine gravity measurements are affected by sea level changes, and variations on heading, speed and gyro of vessel. Besides, neither the shape of Earth nor its density distribution are uniform, there are deviations in the direction and magnitude of the gravity across its surface. Therefore, data must be corrected by sea level, Eötvös effect, which is the change in perceived gravitational force caused by the eastbound or westbound velocity, and drift corrections to obtain the Free Air Gravity Anomaly, which according with the Geodetic Reference System of 1980 in Moritz [2000], is calculated with equation 4.1.

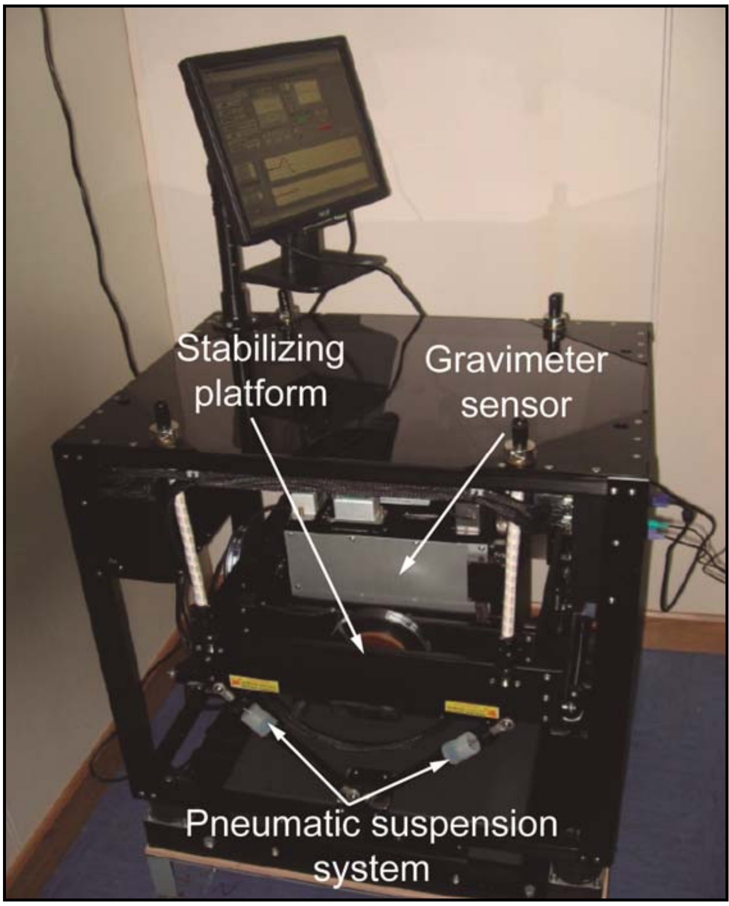

e

Figure 4.1 .- *Marine gravimeter Lacoste & Romberg installed onboard the R/V Sarmiento de Gamboa and used to acquire the gravity data during the MEDOC experiment.*

$$\text{Free Air Anomaly} = Gm + Eot - drift - Gt; \qquad (4.1)$$

$$Eot = 7.5038*v*\sin(\alpha)*\cos(\lambda)+0.04154*v2; \qquad (4.2)$$

$$Gt = 978.0327*(1.0+0.0053024*(\sin(\lambda))2-0.0000058*\sin(\lambda))2). \qquad (4.3)$$

Where, ***Gm*** is the measured gravity data, and *Eot* the Eötvös correction (Equation 4.2), which depends on the velocity (***v***) and the gyro (***α***) of the vessel, and on the latitude (***λ***). ***Gt*** is the theoretical gravity value, which depends exclusively on ***λ*** (Equation 4.3). Once these corrections are applied, the observed gravity data can be used as a reference value during the gravity modeling (section 4.4).

4.3 Empirical relationships between compressional-wave velocity (Vp) and density (ρ)

In this work, gravity modeling has been used to complement the information provided by WAS. To do this, I have converted the WAS-derived Vp models to ρ models using different empirical Vp-ρ relationships for each geological layer and domain assuming a given lithological composition. The idea behind this approach is to see whether it is possible to discern between interpretations of the nature of basement rocks based on seismic velocity exclusively [Korenaga et al., 2001; Sallarès et al., 2001; Sallarès and Ranero, 2005]. However, there are several aspects that must be taken into account to properly address this issue. Vp-ρ relationships may present significant uncertainty because of the compositional and porosity effects of the rock. Similarly, velocity models always have data-associated uncertainty. The cumulative effect of such uncertainties causes the non-uniqueness of the velocity-derived density distribution, and hence includes a subjective interpretation in the construction of the density model that is used to explain the gravity anomaly [Korenaga et al., 2001]. Therefore, it is important to determine how well constrained is the velocity model and to translate its uncertainty to the derived-density model. To address these requirements I have used the results obtained from the Monte Carlo uncertainty analysis of the velocity model (section 3.4.2) to infer the corresponding uncertainty of the derived density model and synthetic gravity response.

The selection of the proper Vp-ρ relationships is essentially based on previous velocity analysis and geological interpretations of the velocity model. This, in turn, allows the definition of the regions or domains where the selected Vp-ρ relationships will be applied (Figure 4.2).

Vp-ρ relationships of interest in this work include the Hamilton's [1978] conversion law for the sedimentary layer (Figure 4.3), which is a result of a compilation of large amount of DSDP data, and reflection and refraction measurements of sound velocity in marine sediments. For the basement I have tested Vp-ρ relationships for three different affinities, including continental, oceanic and exhumed mantle rocks. For continental igneous and metamorphic rocks I used the relationship from Christensen and Mooney's [1995] [Figure 4.3]. For oceanic crust basalts and gabbros of Layer 2 and 3 the Carlson and Herrick's [1990] conversion law was used (Figure 4.3). Finally, for low-T partially serpentinized peridotites I used Carlson and Miller's [2003] relationship (Figure 4.3).

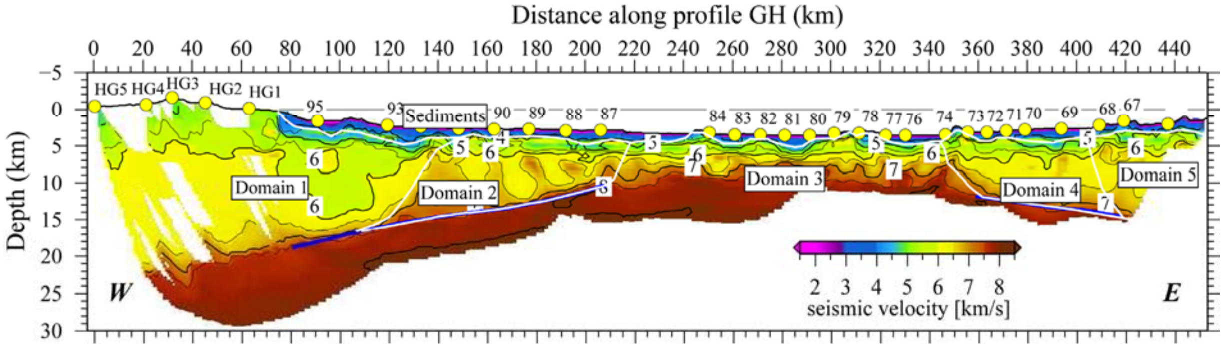

Figure 4.2.- *Definition of geological domains (white lines) in the tomographic model of Line GH as a previous step to the application of Vp-ρ relationships.*

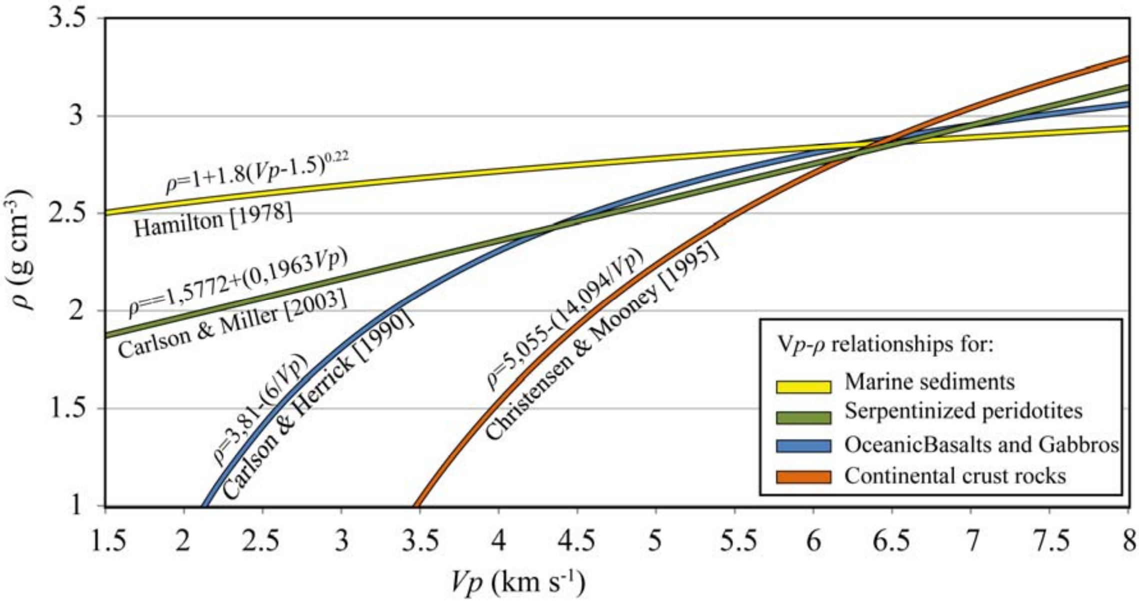

Figure 4.3.- *Graphical representation of all the Vp-ρ relationships used in this work. Empirical formulas and corresponding references are shown above and below each relationship, respectively.*

The Vp-ρ conversion laws shown in figure 4.3 have been estimated in laboratory conditions, so that to convert in situ ρ from in situ Vp, temperature and pressure derivatives of velocity and density must be taken into account in the conversion process to correct from in situ to laboratory conditions, and *vice-versa* [Korenaga et al., 2001]. Hence, using these derivatives, the conversion of in situ Vp to in situ ρ can be expressed with the following equations:

$$V_r(p_r,T_r) = V(p,T) + \frac{\partial V}{\partial p}(p_r - p) + \frac{\partial V}{\partial T}(T_r - T), \tag{4.4}$$

$$\rho_r(p_r,T_r) = f[V_r(p_r,T_r)], \tag{4.5}$$

$$\rho(p,T) = \rho_r(p_r,T_r) + \frac{\partial \rho}{\partial p}(p - p_r) + \frac{\partial \rho}{\partial T}(T - T_r), \tag{4.6}$$

where, $\boldsymbol{V_r}$ is the converted-to-laboratory conditions velocity or velocity of reference, $\boldsymbol{V}$ is the in situ velocity (i.e. that from the velocity model), and $\boldsymbol{\rho_r}$ and $\mathbf{T_r}$ the reference pressure and temperature values (e.g. 1000 MPa and 25ºC), respectively. Additionally, in situ values of pressure (p) and temperature ($\boldsymbol{T}$) are inferred from both thermal (33ºC km^{-1}) and lithostatic (33.3MPa km^{-1}) gradients [Korenaga et al., 2001]. With $\boldsymbol{V_r}$ calculated by equation 4.4, Vp-ρ empirical reletionships can be then applied to obtain $\boldsymbol{\rho_r}$ from $\boldsymbol{V_r}$ (i.e. Equation 4.5). Subsequently, in situ $\boldsymbol{\rho}$ are calculated from $\boldsymbol{\rho_r}$ using expression 4.6 that includes pressure and temperature derivatives of ρ, obtaining thereby, the velocity-derived density model.

Pressure and temperature derivatives of velocity and density in this work were applied for the oceanic crust [Korenaga et al., 2001] and mantle rocks relationships [Kern and Tubia, 1993]. The derivative values employed in each case are shown in Table 4.1:

	d*Vp*/d*P* *(km s^{-1} MPa^{-1})*	d*Vp*/dT *(km s^{-1} ºC^{-1})*	d***ρ***/d*P* *(g cm^{-3} MPa^{-1})*	d***ρ***/d*T* *(g cm^{-3} ºC^{-1})*
Oceanic crust	**2x10^{-4}**	**-4x10^{-4}**	**0.01x10^{-3}**	**-0.03x10^{-3}**
Serpentinized peridotites	**3.94x10^{-4}**	**-8.21x10^{-4}**	**0.069x10^{-3}**	**-0.028x10^{-3}**

Table 4.1.- *Pressure and temperature derivatives of velocity and density for oceanic crust [Korenaga et al., 2001] and serpentinized peridotites [Kern and Tubia, 1993].*

4.4 Gravity modeling

The 2D gravity modeling is performed using Parker's [1972] spectral method as modified by Korenaga et al. [2001]. It calculates the free air gravity anomaly produced by the density model. In this approach, the 2-D gravity anomaly g_z caused by a 1-D density variation $\rho(x)$ bounded by two limits $z=z1(x)$ and $z=z2(x)$ (Figure 4.4) is expressed in the Fourier domain as a function of the density distribution between these two limits as Equation 4.7 [Parker, 1972]:

$$F[g_z] = -2\pi G \exp(|k|z_0) \cdot \sum_{n=1}^{\infty} \frac{(-|k|)^{n-1}}{n!} F[\rho(z_1^n - z_2^n)], \tag{4.7}$$

where **F**[] represents the 1-D Fourier transform with respect to the horizontal coordinate, and G, z_0,and k are the universal gravity constant, the vertical coordinate of the observation plane, and the horizontal wavenumber, respectively. This approximation includes usually a restriction to constant thickness to separate the **F**[ρ] term from other higher-order terms with topography variations and to construct an iterative inversion formula for the density inversion.

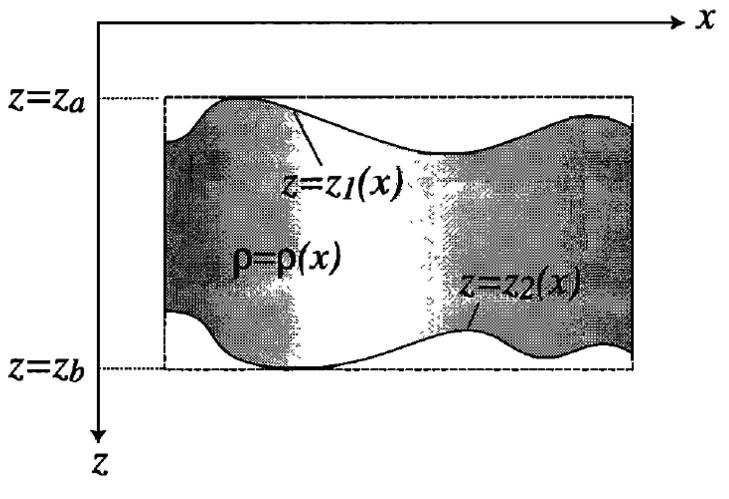

Figure 4.4.- *Schematic diagram showing the 2D density model geometry, with the presence of upper and bottom topography. After Korenaga et al. [2001]*

This limitation to constant thickness is easily solved noting that the 1D density variation between the two boundaries can be also expressed as a layer of constant thickness with topographic variations [Korenaga et al., 2000]. Equation 4.7 can then be written as equation 4.8:

$$\frac{F[g_z]}{2\pi G e^{|k|z_0}} = \frac{1}{|k|}\left(e^{-|k|z_a} - e^{-|k|z_b}\right)F[\rho] + \sum_{n=1}^{\infty}\frac{(-|k|)^{n-1}}{n!} \cdot \{e^{-|k|z_{r1}} F[\rho((z_a - z_{r1})^n - (z_1 - z_{r1})^n)] + e^{-|k|z_{r2}} F[\rho((z_2 - z_{r2})^n - (z_b - z_{r2})^n)]\}, \tag{4.8}$$

in which, z_a***=min(z1),*** z_b***=max(z2),*** z_{r1}***=(za+max(z1))/2*** and z_{r2}***=(zb+min(z2))/2***; because the convergence of the infinite series summation is fastest when the reference plane is located between the top and bottom boundaries of the target area ***(z1, z2)*** [Parker, 1972]. Equation 4.8 is that used to calculate the gravity anomaly of the different models tested in this work, using the code grav2d [Korenaga et al., 2001].

Worth to be mentioned is that the measured gravity anomaly is affected by surrounding bodies that may be out of the modeled structure, like deeper mantle or distant large crustal bodies that usually results in long-wavelength variations of the gravity field. This influence is not included in the velocity-derived density model, and hence in the synthetic gravity anomaly. Consequently, the synthetic anomaly is habitually affected by a systematic shift respect the observed anomaly that must be corrected to properly compare both anomalies.

Chapter 5: Acquisition, Analysis & Processing of Multichannel Seismics

5.1 Introduction

As WAS, MCS data can be also classified as an active seismic method. In this case, however, it is based on the acquisition and processing of seismic data resulting from near-vertical reflections of elastic waves at the different interfaces of the medium. Moreover, in contrast with WAS that aims to explains the great-scale structure of the crust and uppermost mantle from velocity models, MCS allows to characterize (small-scale) geological structures of the crust directly from 2D/3D high resolution images of the subsurface resulting from a thorough processing of the recorded seismic data. Although this methodology is often applied on land, this chapter deals with offshore applications.

Marine MCS data has been widely used in oil explorations since the 60's to map in detail sedimentary structures. Additionally, it has been also very useful to obtain new information about the geometry of rifted continental margins, and to investigate the mechanisms involved in their formation [e.g. Pérez-Gussinyé et al., 2003; Ranero and Pérez-Gussinyé, 2010]. To explain this method in detail, this chapter focuses on the offshore acquisition system and the data processing required to obtain the final seismic image of the subsurface.

5.2 Acquisition system and geometry of the experiment

In MCS marine experiments, the acquisition system consist of an array of air guns as seismic source (Figure 5.1a), similar to WAS experiments, and a set of hydrophones as receivers, distributed along a cable or streamer (Figure 5.1b). Apart from hydrophones, the streamer also includes several devices like compasses (Figure 5.1c), that record the magnetic heading at several points of the streamer allowing to control its shape, the birds (Figure 5.1d), that control the streamer depth during the experiment, and the tail buoy (Figure 5.1e), attached to the tail of the streamer with a Global Positioning System (GPS) that sends the signal via UHF and/or through the streamer to know its location. The length and depth of the streamer, the number and spacing of channels (formed by several hydrophones), and the source configuration depends on the objectives of the experiment.

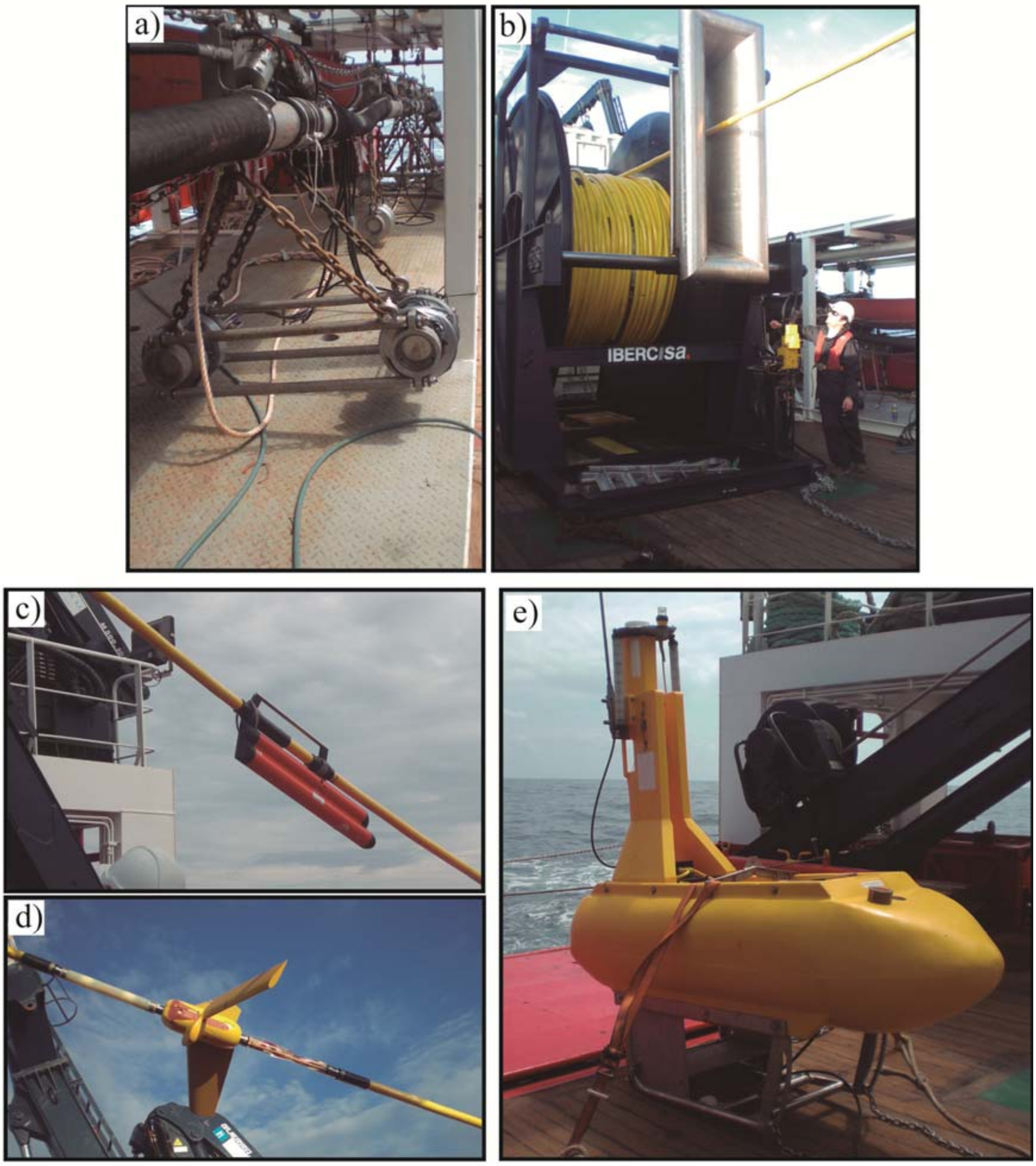

Figure 5.1.- *Acquisition system during the MEDOC (2010) MCS experiment. It includes the (a) array of air guns as the seismic source, (b) the ~3.5 km long streamer, which in turn is composed by the hydrophones, (c) the compasses, (d) the birds, and (e) the tail buoy.*

In contrast with WAS experiments where receivers (i.e. OBS/H) remain in the seabed (Figure 3.2), in MCS the seismic source and receivers (i.e. streamer) are both towed of the stern of the vessel along a profile (Figure 5.2). The array of air guns is submerged at depths of 3-15 m below sea level, and fired at constant distance interval (i.e. shot spacing) along the profile, generating a constructive interference of the acoustic signal (3-70 Hz), that create an energetic pulse (wavefront) closer to the theoretic Dirac delta. Then, once this energetic pulse interacts with the subsurface, part of it is reflected at the different interfaces of the crust as a result of changes in the acoustic impedance of the medium and returned back to the surface where it is recorded by the hydrophones of the streamer as seismic traces (Figure 5.2).

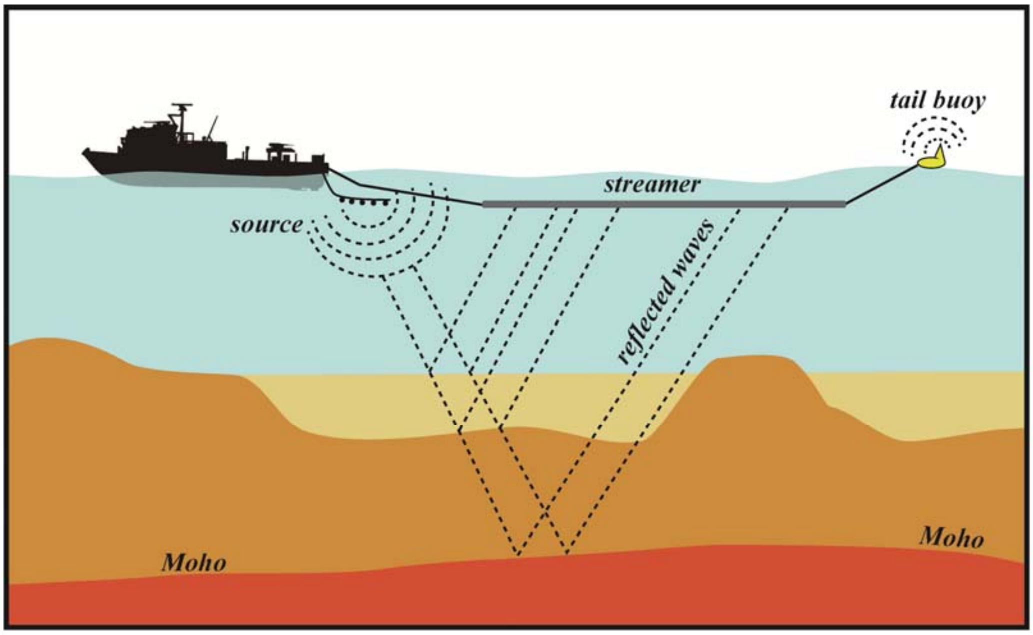

Figure 5.2 .-*Schematic representation of the MCS experiment and the propagation of the reflected waves at each interface of the subsurface.*

The geometry of this acquisition system allows that several wave fronts reflect in a same interface's location or depth point (Figure 5.3). All the traces reflecting in the same point in depth make up a Common Depth Point (CDP) gather (Figure 5.3), and the maximum number of traces in the CDP gathers is the **fold**. The larger the fold per CDP, the larger is the redundancy of data per CDP. The fold (***F***) of the experiment depends essentially on the number of channels (α), the spacing between them ($\boldsymbol{x}$), and the shot frequency of the source (μ) (equation 5.1).

$$\boldsymbol{F = (\alpha x)/2\mu} \qquad (5.1)$$

Hence, the longer the streamer, the larger is the CDP fold. In the MEDOC experiment, the streamer was 3450 m long with 276 channels separated each 12.5 m, and the shot spacing was set to 50 m (~20s at 4.8 knots) to achieve a fold of ~35 traces per CDP. Figure 5.3 shows a schematic representation of this multifold, or multichannel, system:

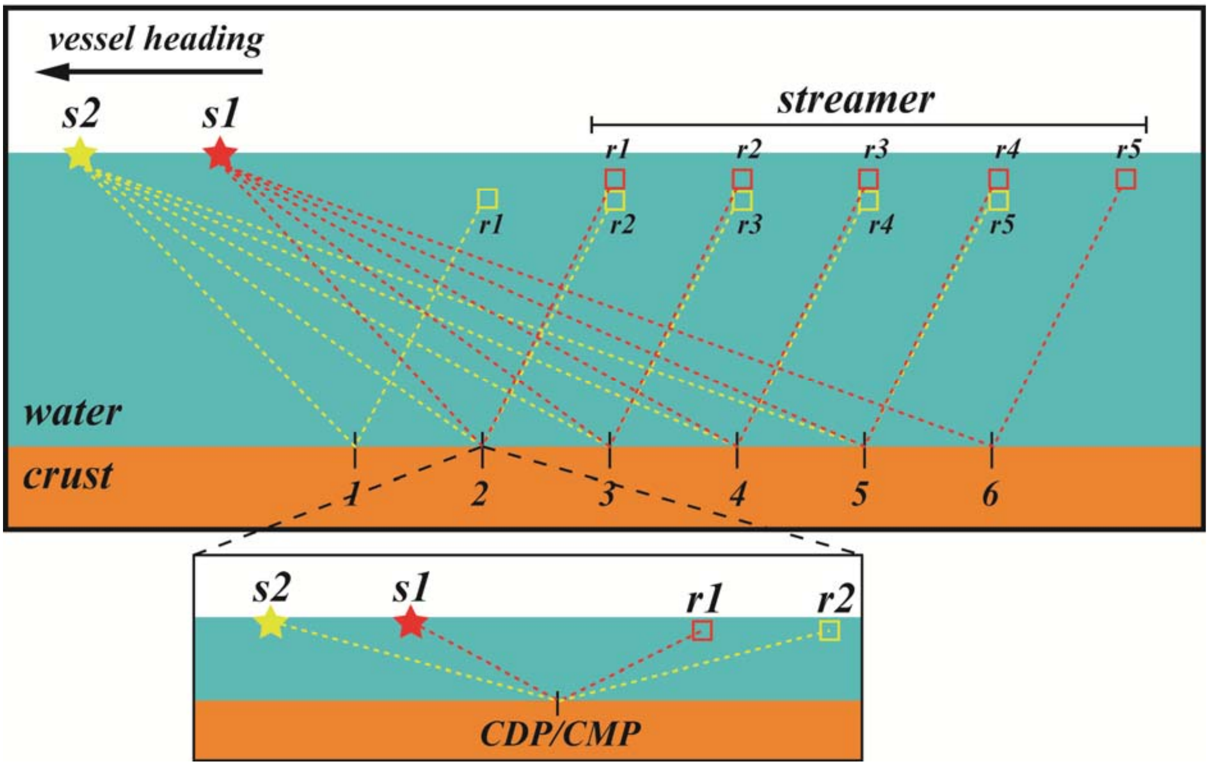

Figure 5.3 .-*Schematic representation of the multichannel acquisition system used in marine MCS (top), and the resultant geometry of a CDP (bottom). S1 and S2 represent two consecutive shots, and r1, 2, 3, 4, and 5 show the hydrophones location along the streamer at the each time of firing (i.e. s1 and s2). Yellow and red dashed lines represent the reflected waves at each point of the seafloor interface (numbers). The resultant CDP is shown for number 2, although numbers 3, 4, and 5 have been also recorded by several receivers at different offset. Fold value of this schematic CDP is 2, since only two reflections have been displayed in this sketch (i.e. those recorded by r1 and r2).*

Note that when reflections illuminate a flat interface, the CDP is equivalent to the midpoint between source and receiver, therefore it is also known as Common Mid Point (CMP) (Figure 5.3).

In conclusion, the great strength of the MCS system is data redundancy, because it takes multiple images of the same point in depth in the form of CDP/CMP gathers assuring data redundancy, which consequently will increase the signal-to-noise ratio of the data. To get the full potential of these data it is necessary to properly process them in order to attenuate/eliminate the noise (random and coherent) inherent to the data recording. This process sequence is detailed in the next section.

5.3 Data processing

MCS data processing aims to eliminate or attenuate the inherent noise of the signal in order to increase the signal-to-noise ratio and improve the quality of the data. Additionally, it also aims to properly sort MCS data to finally obtain a seismic section of the subsurface that provides realistic geological information. Although I present in this work two MCS profiles, MEDOC4 and MEDOC6, I have only performed the processing of MEDOC 4. Here I explain the main processing steps followed to obtain the final seismic section of MEDOC4, which were accomplished using Globe Claritas software. The evolution of the data during processing is shown in section A.2.2.1 of the Annex.

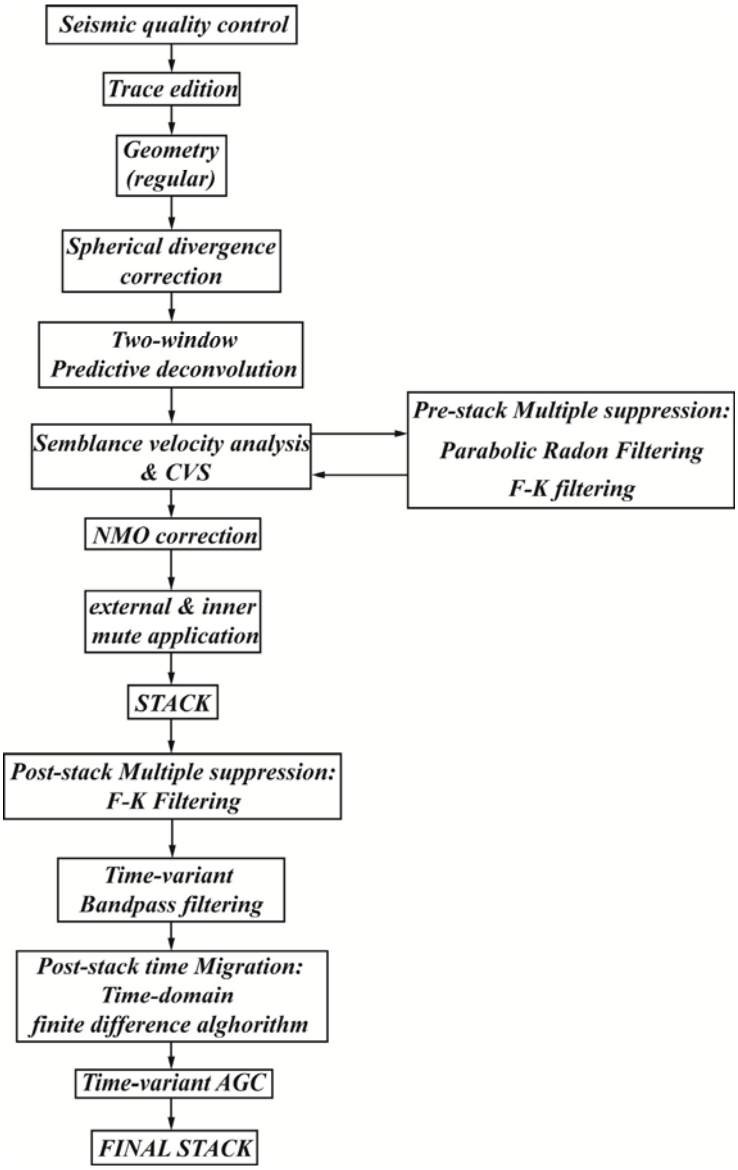
Seismic quality control
Trace edition
Geometry (regular)
Spherical divergence correction
Two-window Predictive deconvolution
Semblance velocity analysis & CVS
Pre-stack Multiple suppression: Parabolic Radon Filtering F-K filtering
NMO correction
external & inner mute application
STACK
Post-stack Multiple suppression: F-K Filtering
Time-variant Bandpass filtering
Post-stack time Migration: Time-domain finite difference alghorithm
Time-variant AGC
FINAL STACK

Figure 5.4 .-. *Generic processing flow followed to process MCS data of profile MEDOC4.*

Seismic quality control and trace edition:

During the acquisition of MCS data several factors like the malfunction of channels or the interference of signal due to marine traffic may occur, causing incoherent noise on the registered signal. It is important, then, to control the quality of the data before starting with a more exhaustive processing. Hence, it is necessary to careful visualize all shot/CMP gathers (Figure 5.5), and treat and/or remove noisy traces when necessary.

Geometry

The geometry of the experiment has to be defined in order to correctly identify and place each trace of the seismic dataset. Geometry information like number of streamers, number of channels, shot distance, channel distance, shot location, channel location, near offset, etc. is then setup in the header of each trace. Once the traces are identified and located, CDP gathers can be created when assembling the traces that illuminate the same point in depth. Figure 5.5 illustrates how the trace order changes within a shot gather and a CDP gather.

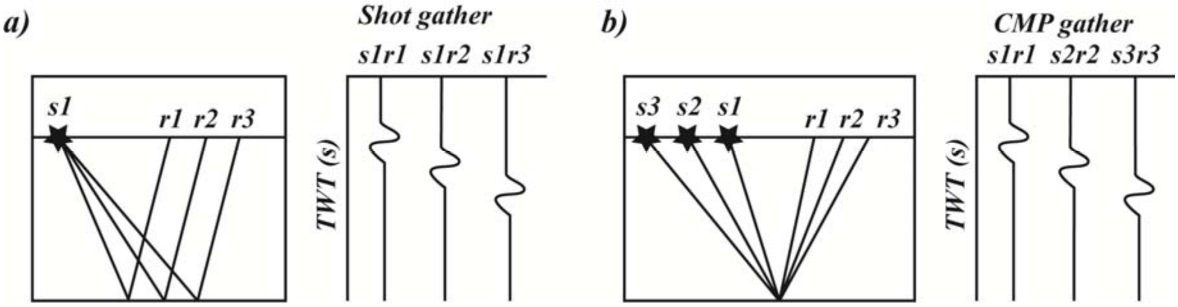

Figure 5.5 .- *Trace visualization of a (a) Shot gather and (c) CMP gather. Modified from Bartolome [2002]*

During the experiment, the streamer is most likely affected by sea perturbations like waves or currents that modify the geometry of the experiment along the profile. Hence, detailed information of the xyz-location of the streamer at every shot should be introduced to set up a realistic geometry. However, in regional MCS experiments, whose main purpose is to investigate large structures (i.e. crustal scale), it is usual to apply a marine regular geometry, which assumes that the streamer is towed of the vessel along a straight and constant course, and shots are fired at a constant distance. This assumption in regional studies provides enough resolution to accomplish data processing and interpretation of crustal structures. For that reason, in this work, a regular geometry has been defined and set in traces headers.

Spherical divergence correction

Spherical divergence is the attenuation of seismic wave amplitude due to energy dissipation and geometrical spreading of the wavefront as it interacts with the different layers of the subsurface. The loss of energy of the seismic wave causes that the amplitude of the seismic signal becomes lower with depth (time). Hence, it is necessary to compensate this loss and recover the best resolution of the seismic trace in time before applying further processing. Assuming an earth model with increasing velocity with depth, the amplitude decay can be represented as:

$$\mathbf{1/tV^2}, \qquad (5.2)$$

where, ***V*** is the velocity of propagation and ***t*** the two-way travel time [Newman, 1973]. Therefore, to apply a spherical divergence correction is necessary to have a first estimation of the velocity propagation of the medium or V(t). The correction of amplitude decay, then, is done by multiplying the samples of the trace by a time variant scalar function that enhances the signal of the trace, increasing its temporal resolution.

Deconvolution

The seismic trace is the result of convolution of the seismic wave created by the source or seismic wavelet, and the Earth's impulse as a response to the interaction of the seismic wavelet with the different layer boundaries of the subsurface (acoustic impedance). The aim of the deconvolution is to remove the effect of the source waveform from the trace, and enhance the signal corresponding to the Earth's response.

Mathematically, as its names suggests, deconvolution is the inverse process of convolution. The conventional convolution model of a seismogram may be represented by Equation 5.3, where ***x(t)*** is the recorded seismogram, ***w(t)*** the source wavelet, ***e(t)*** the Earth's impulse response, ***n(t)*** the random ambient noise, and * signifies convolution (Figure 5.6) [Yilmaz, 2001].

$$x(t) = w(t) * e(t) + n(t), \qquad (5.3)$$

The aim of deconvolution, then, is to recover ***e(t)*** from ***x(t)***. However, all that normally is known in equation 5.3 is only ***x(t)*** (recorded seismogram), since ***e(t)*** must be estimated, and ***w(t)*** is normally unknown, although in some cases, however, it can be inferred from measurements of the signature of the air-gun. Finally, there is no prior information of the ambient noise ***n(t)***. Then, to efficiently solve equation 5.3 ***n(t)*** is usually assumed to be zero. Thus, equation 5.3 can, then, be written as equation 5.4 [Yilmaz, 2001].

$$x(t) = w(t) * e(t), \qquad (5.4)$$

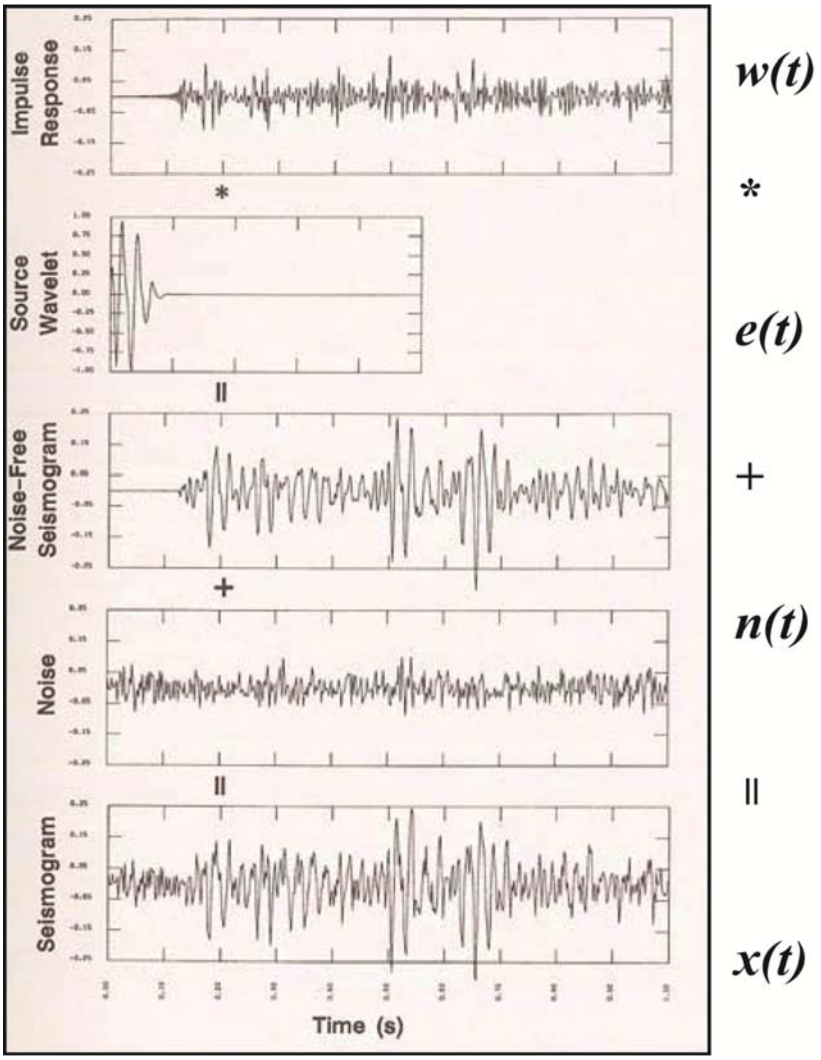

Figure 5.6 .- *Graphical representation of the convolution model explained by Equation 5.3. After Yilamz [2001].*

Convolution in time domain (*) is represented by a rather complex mathematic operation, whereas in the frequency domain it becomes a simple multiplication. Thus, the recorded time signal is converted to the frequency domain using the Fourier transform to easily resolve the deconvolution problem. Thus, equation 5.4 is now written as equation 5.5 [Yilmaz, 2001].

$$A_x(\mu) = A_w(\mu)A_e(\mu), \qquad (5.5)$$

where, $A_x(\mu)$, $A_w(\mu)$, and $A_e(\mu)$ are the amplitude spectra of ***x(t)***, ***w(t)***, and ***e(t)***, respectively. Now, if the source wavelet ***w(t)*** or $A_w(\mu)$ is known (record of the source signature), the solution to the deconvolution problem is fundamentally deterministic. However, the seismic wavelet is usually unknown, hence, ***e(t)*** or $A_e(\mu)$ must be determined from a statistical methods.

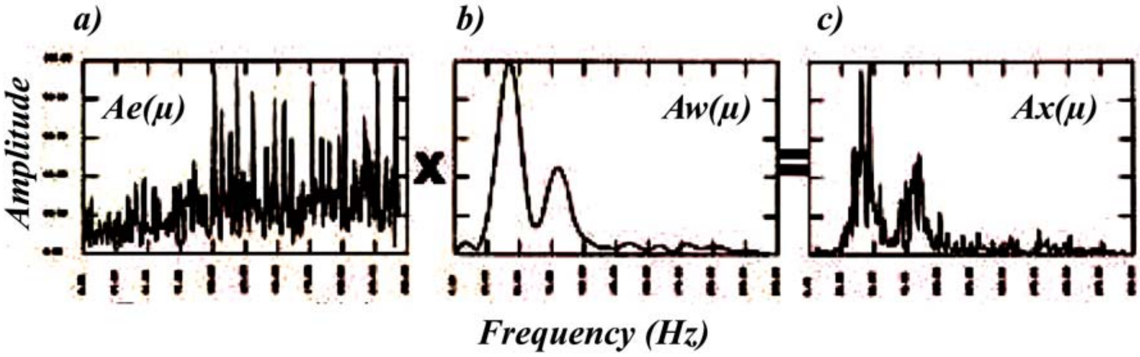

Figure 5.7 .- *Frequency spectrum of the seismogram $A_x(\mu)$ as a result of the multiplication of the seismic wavelet $A_w(\mu)$, and the Earth's impulse response $A_e(\mu)$. After Yilamz [2001]*

In Figure 5.7, it can be observed that the similarity in the overall shape between the amplitude spectrum of the wavelet (Figure 5.7b) and that of the seismogram (Figure 5.7c) is apparent. In fact, it is generally believed that the rapid fluctuations observed in the amplitude spectrum of a seismogram (Figure 5.7c) are manifestation of the earth's impulse response (Figure 5.7a), while the basic shape is associated fundamentally with the source wavelet (Figure 5.7b). This occurrence is also observed in the autocorrelation functions of the three signals (Figure 5.8)

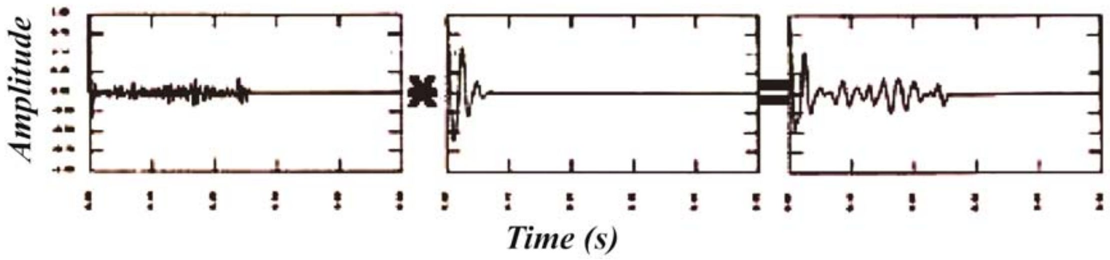

Figure 5.8 .- *Autocorrelation functions of the three signals shown in Figure 5.7. Modified from Yilamz [2001].*

Thus, the source wavelet can be statistically estimated from a recorded seismogram by computing its amplitude spectrum and autocorrelation function. This is the foundation of the statistical deconvolution.

Hence, statistical predictive deconvolution in practice consists of design a time windows in the CMP gathers from which the autocorrelation functions of the seismogram is computed to estimate the amplitude and phase spectra of the seismic wavelet. Then, given a length of the trace (operator length), a Wiener filter is designed (operator). This type of filter is also known as predictive filter, since it predicts coherent energy (seismic wavelet) from a signal and subtracts it from the waveform [Peacock and Treitel, 1969]. The operator is, then, applied within a time window (application window) to filter the effect of the source from the recorded signal increasing temporal resolution and subsurface reflectivity.

In this work, two design windows are used accounting for the different seismic facies and the loss of energy of the seismic wavelet with depth. Hence, a first window was designed for the shallow sediments and a second for the lower sediments and basement. The operator length for the first window was 300 ms while for the second was 360 ms. The gap of both windows was set at 24 ms (see Figure A.2.2.2).

Velocity analysis and NMO correction

As observed before in Figure 5.5b, reflectors represented in a single CMP describe a hyperbolic function (Figure 5.5 and 5.9). This reflects the relationship between arrival times and source-receiver offset (Figure 5.9). The time difference between travel times at a given offset and at zero offset is called *normal moveout* (NMO) (Figure 5.9). This time difference must be corrected previously to sum and stack traces in CMPs applying the hyperbolic moveout equation (Equation 5.5):

$$t_n=[t^2-(4h^2/v^2_n)]^{1/2}, \qquad (5.5)$$

where t_n is the time after NMO correction, h the depth of the reflector, and t the recorded travel time of the reflector. The v_n value is the velocity function required to correct the NMO, also known as the NMO velocity, which is equal to the velocity of the medium above the reflector [Yilmaz, 2001]. Nevertheless, the velocity that can be inferred from seismic data is known as stacking velocity and presents differences with the NMO velocity: stacking velocity is based on the hyperbola that best fits data over the entire spread length, whereas NMO velocity is only based on a small-spread hyperbolic travel time [Yilmaz, 2001]. However, stacking and NMO velocities are generally assumed to be equal.

To properly perform the NMO correction, a velocity analysis has to be made for each CMP to find the mentioned velocity of correction. There are several ways to perform this analysis, those used in this work are: the semblance analysis and the constant-velocity stack (CVS) analysis. The semblance analysis consists of stacking traces of a given CMP at different hyperbolic trajectories or velocities, obtaining thereby, its *velocity spectrum* (Figure 5.10). Then, from this velocity spectrum one may identify those velocities corresponding to the best lateral coherency or semblance of the signal at time. The picking of the maximum levels of lateral coherency at different travel times will provide the best stacking velocity function of the CMP (Figure 5.10).

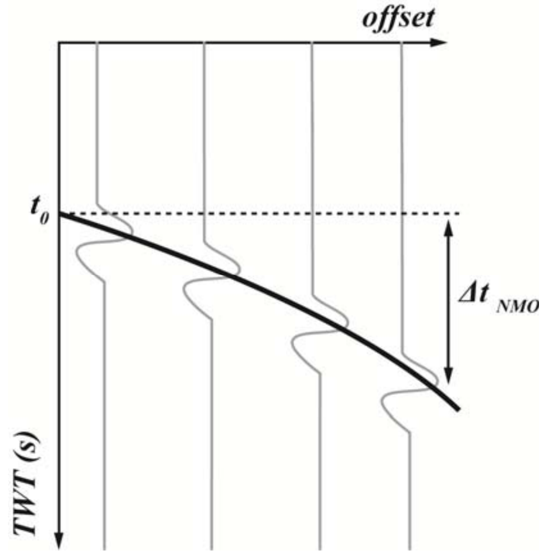

Figure 5.9.- *Basic sketch of the NMO time difference (Δt_{NMO}) between traces of a single CMP gather.*

Alternatively to the semblance analysis, a small portion of a line can be stacked with a range of constant velocity values obtaining the CVS, which can be plotted in the form panel. Stacking velocities that yield the desired stack then can be picked from the CVS panel. Both analyzes are performed more than once, since the temporal resolution of the signal is incremented after multiple removal (see below). Hence, velocity spectrum changes after multiple suppression allowing the identification of new events in depth (time).

Before stacking velocities using the selected velocity functions, however, and external mute is recommended to be applied. Muting is an elementary processing technique that removes those undesired sections of the trace. External muting is mainly applied at shallow levels to far-offset traces to avoid *stretching* deformations (Figure 5.11). This effect is a frequency distortion undergone by far-offset traces due to the NMO correction that must be excluded from stacking.

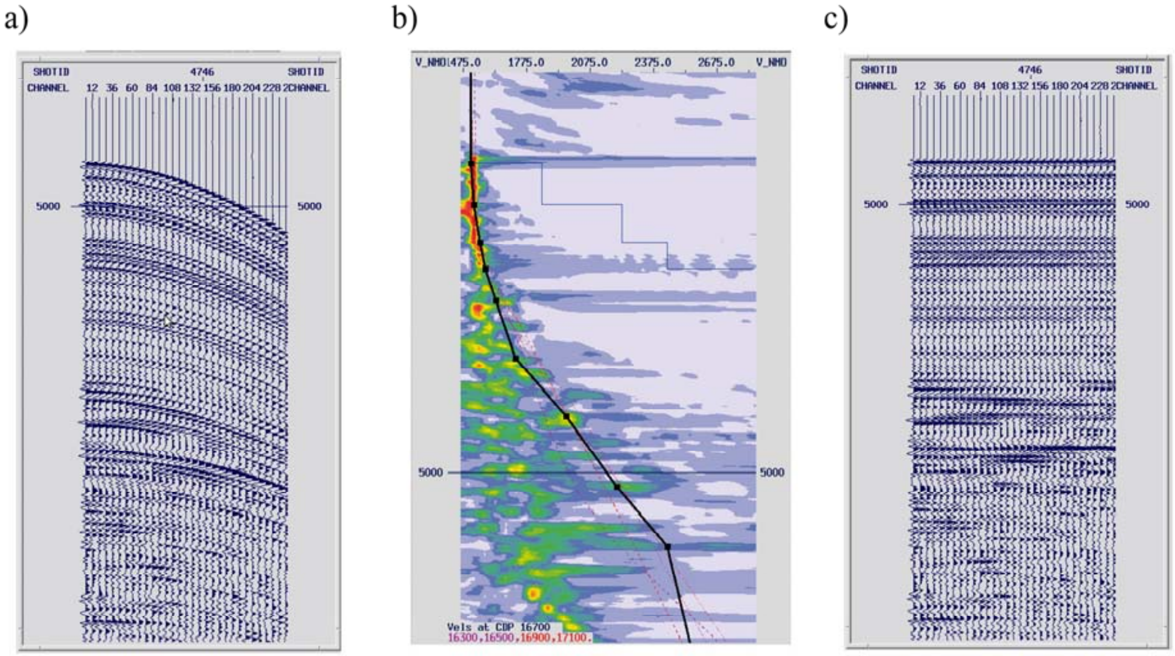

Figure 5.10 .- *(a) CMP 37500 of profile MEDOC-4 without NMO correction. (b) Semblance velocity spectrum of CMP 37500. The velocity function (black line) has been selected on the basis of the events with highest coherency (red). (c) CMP 37500 with NMO correction.*

Multiple suppression

This sequence of the processing aims to attenuate the signal of multiple or secondary reflections in order to unmask real primary reflections. The multiple signal is a coherent noise generated when the seismic energy produce more than one reflection during its travel path. Depending on their time delay from the primary event, multiples are classified as shot-path (or peg-leg) when are located closed to the primary, or long-path when they appear as a separate event. In marine data acquisition, multiple reflections of the seafloor are typically registered due to a portion of seismic energy reverberating in the water layer. These multiple reflections strongly affect the quality of the data as they usually mask real low-amplitude reflections. This kind of noise cannot be treated with a simple bandpass filter since it presents frequencies similar to primary reflections. In this work, the multiple suppression consist of applying **a parabolic radon transform** demultiple process that attenuates most of the multiple seafloor reflection, followed by **a pre- and post-stack frequency-wavenumber (F-K) filter** that eliminates residual multiple in the far-offset, and an **inner mute** for residual multiple in the near-offset.

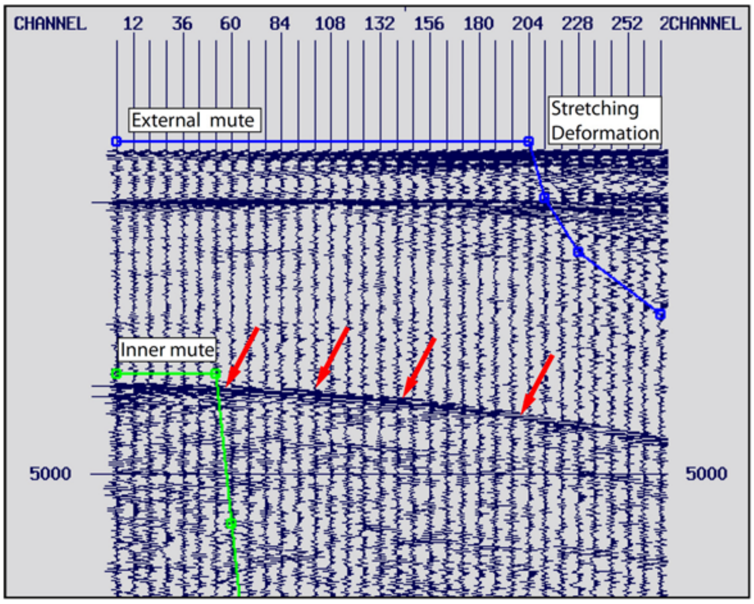

Figure 5.11 .- *External and inner mutes manually picked in the NMO-corrected CDP 2500 of MEDOC4. Red arrows depict the multiple signal*

Parabolic Radon transform

The parabolic Radon transform decomposes the input data of a CMP gather into the parabolic Radon domain (Figure 5.12), where the dipping events of the CMP are observed as parabolas or hyperbolas, while flat events are visualized as points. This allows to better discriminate multiples and primaries reflections and attenuate the multiples.

To apply the parabolic Radon transform, then, the NMO correction is first applied to the CMP gathers, using equation 5.5. Thus, primary reflections in this NMO-corrected CMP gather are represented as flat events, while multiple arrivals are undercorrected events (e.g. left panel in Figure 5.13). These NMO-corrected CMP gathers are transformed into the parabolic Radon domain. Then, the parameters of the parabolic moveout for primaries and multiples arrivals are defined. These parameters refer to the amount of parabolic moveout at far offset, and are the main criteria used by the Radon filter to suppress those parabolas corresponding to the multiple. To remove as much as possible multiple arrivals without modifying primaries, several trials of these parameters have been performed before choosing that applied in this work of 0.85. Once the Radon filter is applied, the NMO correction is undone to get the demultipled CMP gathers (see Figure A.2.2.3).

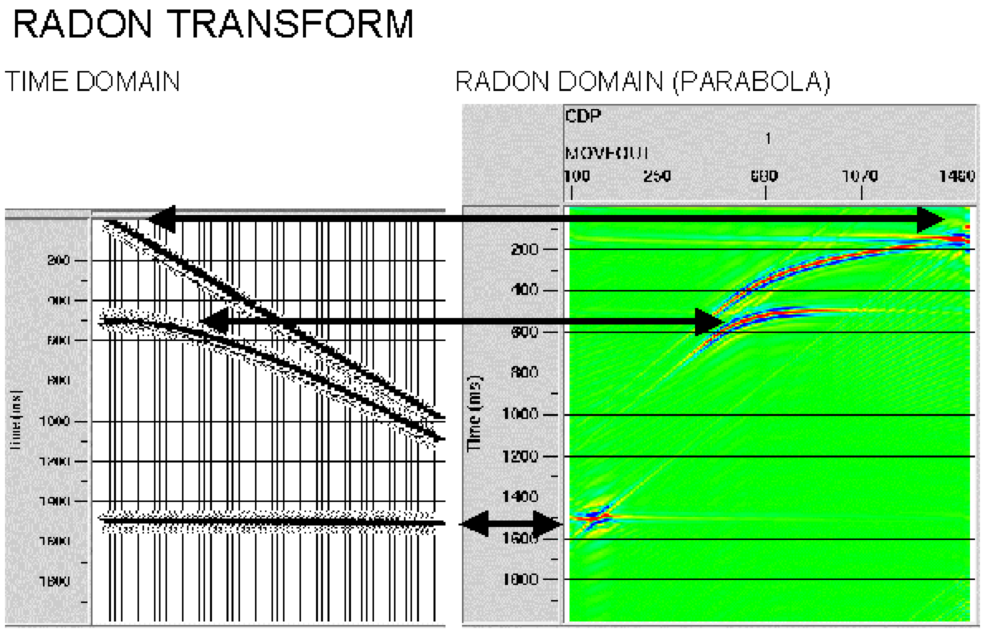

Figure 5.12 .- *Illustration of the Radon transform. In the Radon domain dipping event of the CDP gather become parabolas while flat events become punctual events. From http://www.xsgeo.com/course/basic.htm#radon*

In this work, Radon demultipling was performed in ***super-CMP*** gathers (8 CMP gathers to form one super-CMP, in this experiment) in order to have all offsets of the geometry, this is a trace distance of 12.5 m instead of 100 m as is usual in a conventional CMP gather. This increment of the offset resolution improves the parabolic Randon demultipling by reducing spatial aliasing caused by the long offset between traces within a normal CMP gather.

F-K filtering

An efficient way to remove the remaining multiple energy that left after applying the Radon transform is to apply a F-K filter. The F-K filter is based on the F-K transform, which decomposes the input data in the F-K domain, where the coherent linear events of the time-space (T-X) domain are separated by their dips (Figure 5.13). Therefore, a range of dips in time can be identified in FK domain and suppressed by muting (Figure 5.14)

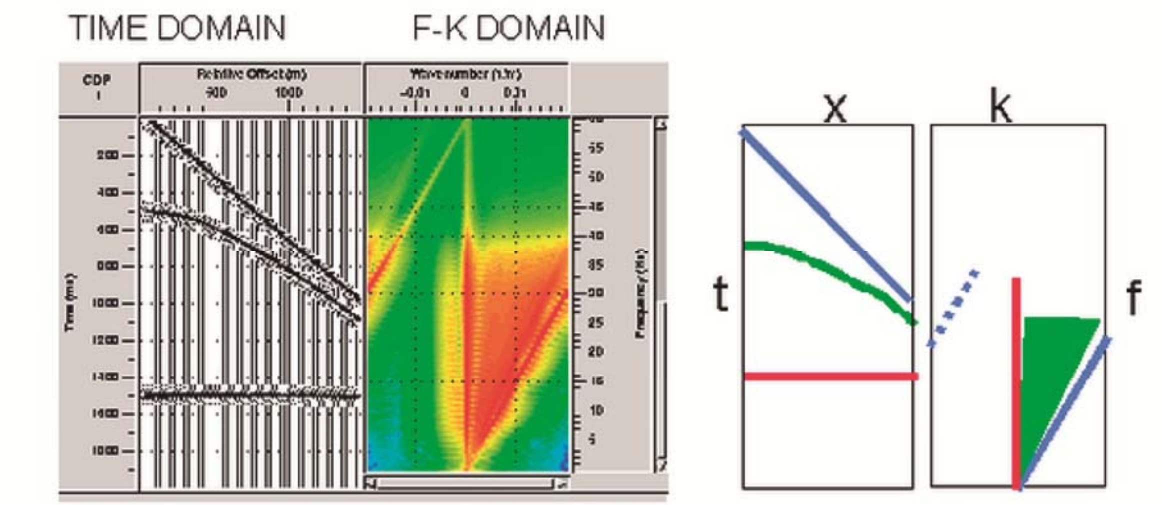

Figure 5.13 .- *Example of the F-K transform. Dipping and flat events of the time domain can be discriminated in the F-K domain. From http://www.xsgeo.com/course/basic.htm#fk*

Hence, multiple suppression from CMP gathers (pre-stack) using F-K filtering is achieved by applying them the 2D Fourier transform o the NMO-corrected CMP gathers, and obtaining the 2D F-K amplitude spectrum. Then, the region corresponding to the multiple energy is selected to be muted (Figure 5.14). Finally, the 2-D inverse Fourier transform is applied to the filtered data to return to the T-X domain.

Inner mute

The inner mute is used to remove multiples in the near offset traces, where their slope resembles to that of primaries (Figure 5.11), and hence, neither the F-K filtering nor the parabolic Radon transform work properly.

Stack

Once accomplished the above processing traces in each CMP are ready to be added together and summed to provide a stack section (Figure 5.15). Stacking traces from a CMP gather reduces noise and improves the overall quality of the data. In a stack section, however, a zero-offset is assumed for each stack trace, that means that the source-receiver distance is zero and that the stacked trace corresponds to a normal-incidence trace at the CMP gather location (Figure 5.16b).

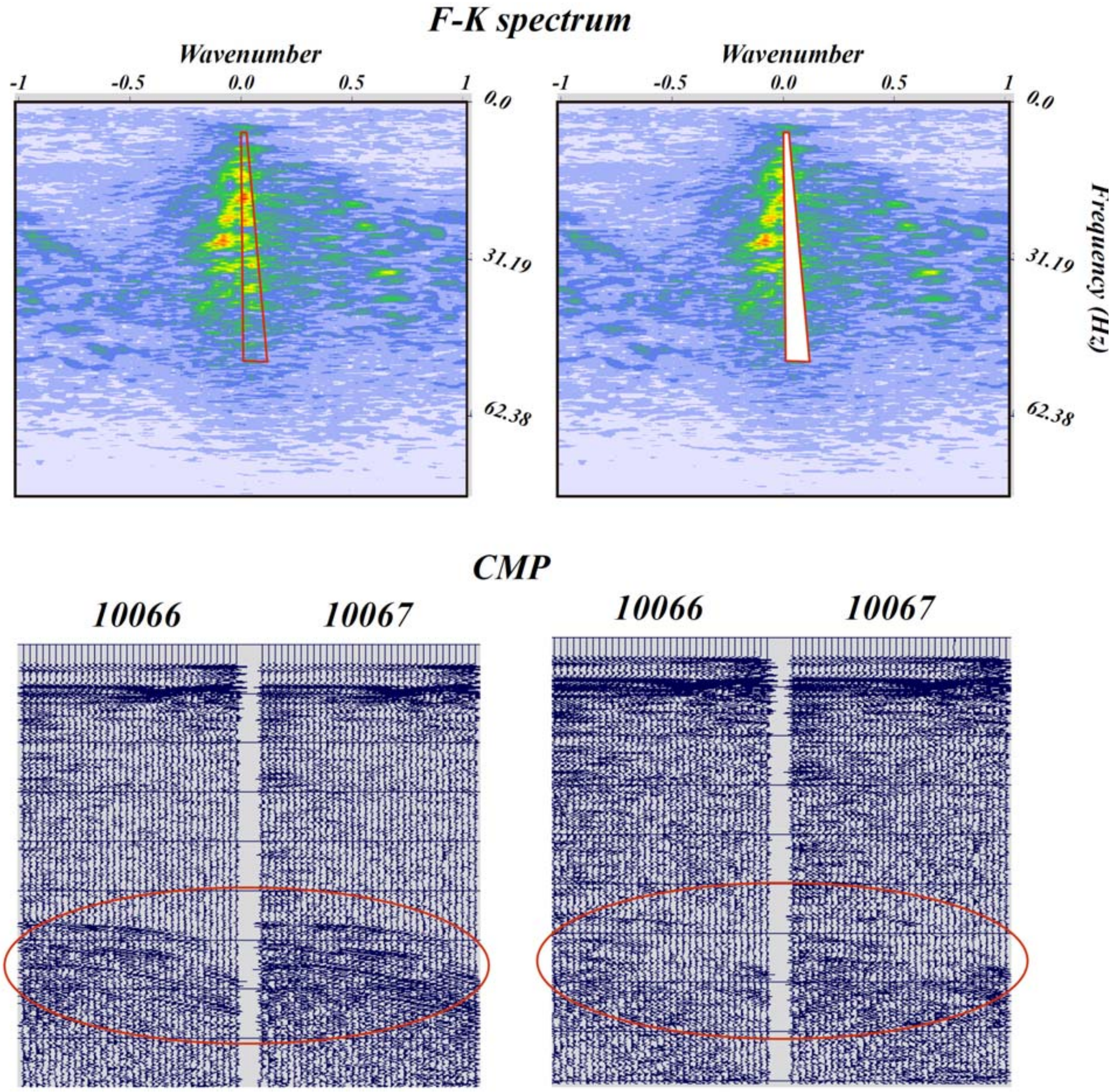

Figure 5.14 .- *Representation of the F-K filtering sequence. CDPs are NMO corrected (left) in order to differentiate between dipping (multiple) and flat (primaries) events in the F-K domain (upper panels). The multiple is attenuated in the CMPs (right) by muting the signal enclosed by the red box in the F-K spectrum (upper right).*

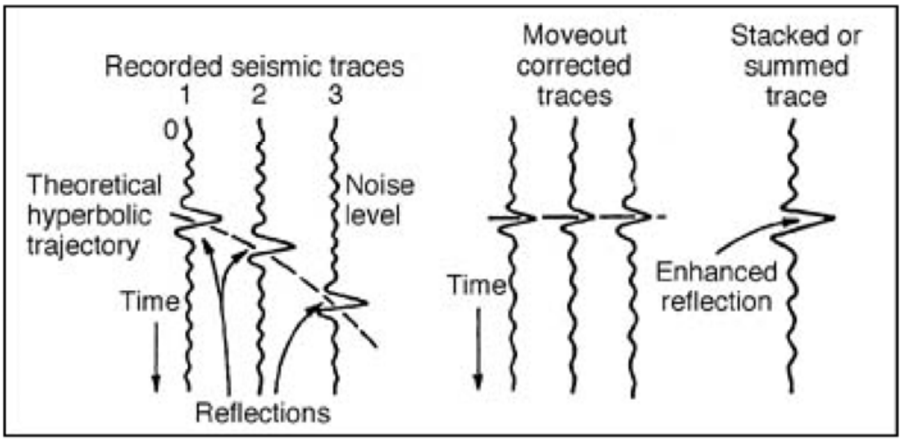

Figure 5.15 .- *(Left) Seismic traces of a CMP gather uncorrected. (Mid) Traces of a CDP gather with NMO correction. (Right) Stacked trace result of the sum of all traces within a CDP gather. From http://www.glossary.oilfield.slb.com/en/Terms/s/stack.aspx*

Since this assumption is only valid for flat events or geological layers, dipping reflectors in a stack section are not at their true location (Figure 5.16) resulting in diffractions of seismic waves that have to be properly processed before interpretation. This issue is addressed with the migration - explained below -, which moves dipping reflectors from their apparent locations to their true location providing the proper geometry of the geological layers in the seismic section.

Post-stack filtering

Before applying the migration to the seismic stack section, in this work I have applied a post-stack filtering to attenuate those undesired frequencies from the stack. The filter consisted of a time variant band-pass filter built up with three windows manually picked based on geological structure:

- 1st window: was designed from the top of the seafloor to the base of the sediments, with filter frequencies of 4-6-60-80 Hz.
- 2nd window: that goes from the top of the sediment to almost the crust-mantle boundary, with frequencies of 2-5-45-60 Hz
- 3rd window: designed from the crust-mantle boundary to the end of the bottom of the seismic section, with frequencies of 1-2-35-45 Hz

Post-stack time migration

As aforementioned the stack of CMP gathers produces a zero source-receiver offset, which implies a normal-incidence of the ray path to the reflecting interface

(Figure 5.16b and 5.17a). This assumption is obviously not realistic, since the subsurface reflectors are not always horizontal and hence ray path do not reflect always with a normal incidence (Figure 5.16a). As a result, dipping events in the stack section are not at their true location. Migration moves these dipping reflectors to their true subsurface and collapse diffractions using an interval velocity function. Interval velocity corresponds to the constant velocity of a single layer and can be approximately calculated from DIX equation (Equation 5.6) [Allaby, 2008]:

$$v_{\mathrm{int}} = [(t_2 v_{\mathrm{rms2}}^2 - t_1 v_{\mathrm{rmsl}}^2)/(t_2 - t_1)]^{1/2} \qquad (5.6)$$

Where, t_1 and t_2 are the travel-time of the upper and lower reflectors that define the interval or layer, respectively; and V_{rms1} and V_{rms2} are the root-mean square velocities of the upper and lower reflectors, respectively. The root-mean square velocity is picked in the seismic section based on geological observations (e.g. geometry of sedimentary basin, top of basement, crust-mantle boundary, etc.).

In summary, migration of stack sections increases spatial resolution and yields a section that more closely resembles the geologic cross-section of the profile [Yilmaz, 2001] (Figure 5.16c and 5.17b).

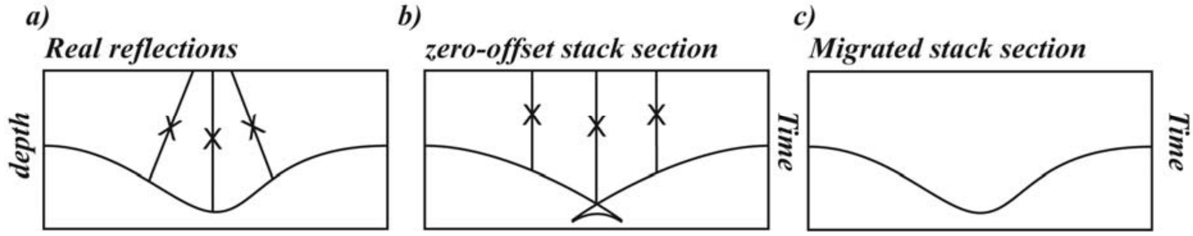

Figure 5.16 .- *Basic sketch of the effect of migration. (a) Shows the real reflections on a synclinal structure, while (b) shows a stacked section of this structure assuming zero-offset reflections, and (c) time migrated section displaying the real location of the synclinal reflector.*

Migrated sections are commonly presented in time (Figure 5.17b), since the velocity estimated from seismic data by conventional methods is limited in accuracy. Hence, depth conversion is not accurate. The migration process that produces a migrated time section is called *time migration*, whereas if the final result is a depth section is called *depth migration.* In this work, the migration step has been performed by applying a post-stack time migration based on a finite difference algorithm that works on the T-X domain and allows migration of 45º-60º dipping events. To migrate section MEDOC4 I have used a dip of 0.55 which is optimal to migrate events dipping up to ~56º.

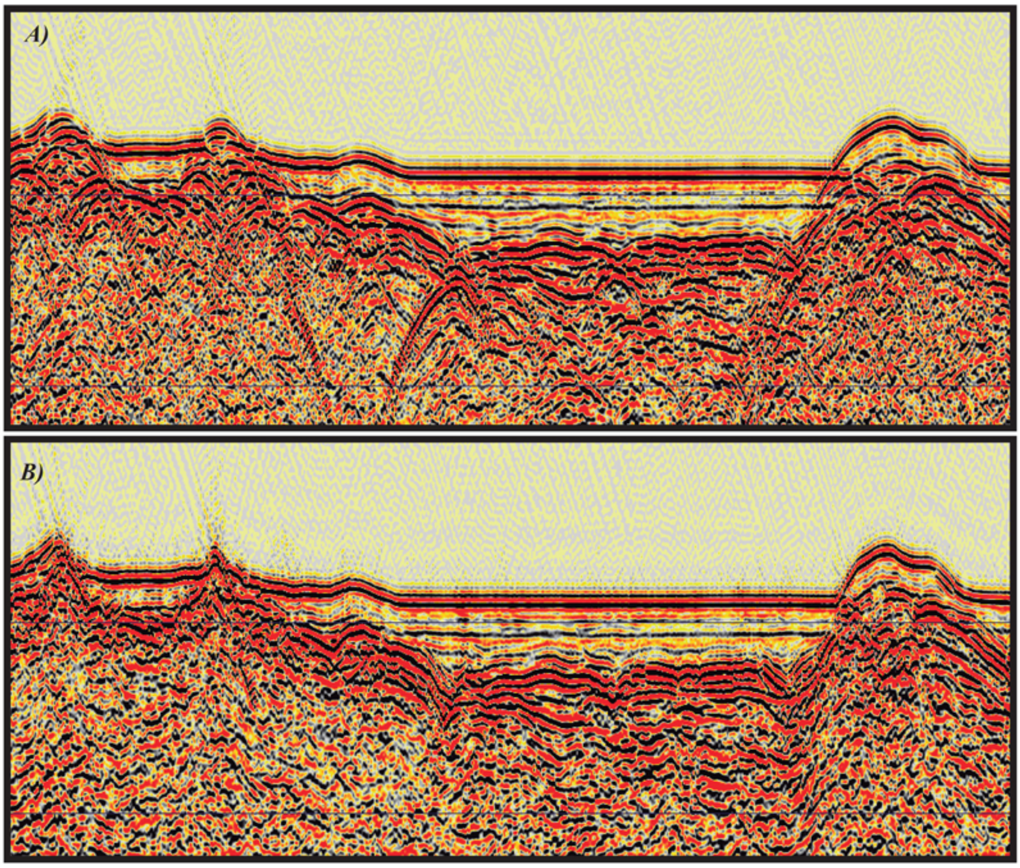

Figure 5.17 .- *Comparison between a stacked time section of profile MEDOC 4 without migration (A) and with time migration (B) applied. Note that diffractions in (A) appeared collapsed in (B), where the reflector geometry becomes geologically more realistic.*

The velocity model used to assess the time migration has to be designed carefully since low velocities do not entirely collapse reflectors, and high velocities may create overcorrected artifacts or smiles (Figure 5.18). The velocity model used in this work varies in time and space. It was firstly designed on the basis of the geometry of the main reflections, which were interpreted as the main geological boundaries that limit layers with changes of seismic velocity.

After the migration a time-variant Automatic Gain Control (AGC) was applied to the time-migrated stack section to obtain the final MCS image profile MEDOC 4 (see section 7.2.2).

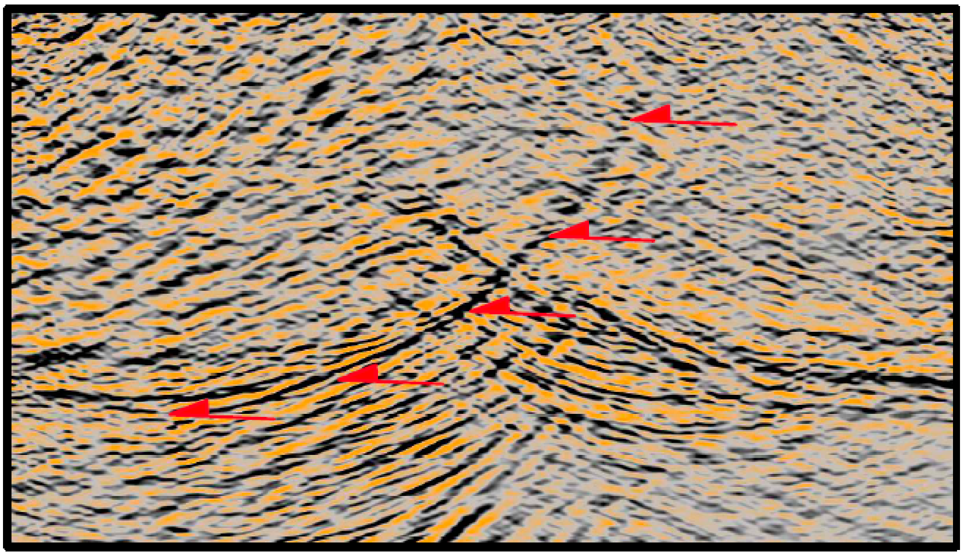

Figure 5.18 .- *Smile structure (red arrows) result of the overmigration of a multiple reflection during time migration of profile MEDOC4.*

Part III:

Results & Discussion

Chapter 6: Line GH/MEDOC-6

The results and discussion presented in this chapter have been included in the manuscript *"Seismic structure of the Central Tyrrhenian basin: geophysical constraints on the nature of the main crustal domains"* that has been recently accepted for publication in the Journal of Geophysical Research – Solid Earth, and of which I am first author.

6.1 Data analysis

Line GH (Figure 6.1) extends from Sardinia to the Campania margin across the deepest parts of the Tyrrhenian basin (Magnaghi and Vavilov basins) (Figure 6.1). In this section I present the WAS data of this line and the different seismic phases selected for modeling.

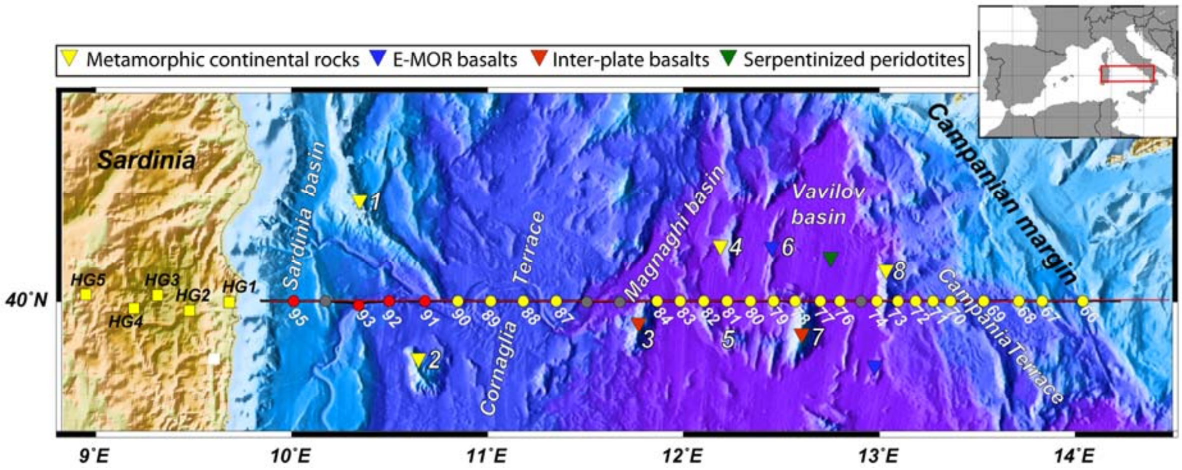
▼ Metamorphic continental rocks ▼ E-MOR basalts ▼ Inter-plate basalts ▼ Serpentinized peridotites
Sardinia
Sardinia basin
Cornaglia Terrace
Magnaghi basin
Vavilov basin
Campanian margin
Campania Terrace
HG5
HG3
HG2
HG1
HG4
1
2
3
4
5
6
7
8
95
93
92
91
90
89
88
87
84
83
82
81
80
79
78
77
76
74
73
72
71
70
69
68
67
66
40°N
9°E
10°E
11°E
12°E
13°E
14°E

Figure 6.1.- *Bathymetric and topographic map of the Tyrrhenian Sea region showing the location of Line GH/MEDOC-6 and the location of the main morphological features. The Land-stations (yellow squares), OBSs (red circles) and OBHs (yellow circles) used to obtain the tomographic model of Line GH (Figure 6.2a) are also depicted in the image. Grey circles correspond to both OBSs and OBHs that came out without valid data. Colored triangles represent the petrological nature of the basement at those points of interest for this section [Dietrich et al., 1977; Colantoni et al., 1981; Kastens and Mascle, 1990; Sartori et al., 2004] 1: Baronie seamount, 2: Cornaglia Seamount, 3: Magnaghi seamount, 4 De Marchi seamount, 5: D'Ancona Ridge, 6: Gortani Ridge, 7: Vavilov seamount, and 8: Flavio de Gioia seamount.*

6.1.1 Wide-Angle seismic Data

Four types of seismic phases have been interpreted in the record sections (Figures A.1.1.1 to A.1.1.31 in section A.1.1 of the Annex); three refraction phases within the crust (Pg), the basement (Pb) and uppermost mantle (Pn), and a crust-mantle boundary reflection (PmP). In average, land-stations display a ~40 km-long Pg phase with apparent velocities ranging from 6.0-6.5 km/s (Figures A.1.1.1 to A.1.1.5), a Pn phase from km ~40 to ~110 with a mantle-like apparent velocity of >7 km/s, and energetic PmP reflections (Figure A.1.1.1 to A.1.1.5). The same phases are observed in OBS 95 to OBH 87 located in the Sardinia margin and the Cornaglia Terrace (Figure A.1.1.6 to A.1.1.13). These OBS/H stations show Pg arrivals in 40-50 km offset range with 6.0-6.5km/s apparent velocities, and faster Pn phases with >7 km/s apparent velocity. Most of these record sections display a secondary arrival corresponding to PmP reflections, indicating an abrupt crust-mantle velocity boundary. Conversely, OBHs 84 to 74 located in the central part of the basin under the Magnaghi and Vavilov basins, display no PmP phase (Figure A.1.1.14 to A.1.1.23) (Figure 6.1). Here a single refracted phase through the basement (Pb) is interpreted, because it is not evident how to distinguish between crustal and upper mantle refractions. This Pb phase is observed up to 90 km offset with unusually high apparent velocity of > 7 km/s at short offsets in most OBH records. In this region, only OBH 77, 78 and 79 (Figures A.1.1.19 to A.1.1.21), show Pb phases with slower 5-6 km/s apparent velocities along their ~30 near-offset km, located across the Gortani Ridge and Vavilov seamount (Figure 6.1). From OBH 73 to 66 (Figures A.1.1.22 to A.1.1.31) across the Campania Terrace and margin (Figure 6.1), seismic phases changes displaying a configuration that resembles to that of the conjugate Sardinia margin, with moderate-velocity Pg phases in the ~40km offset range, mantle-like velocity Pn phases, and clear, high-amplitude PmP phases (Figure A.1.1.31).

A total of 14403 first arrivals (Pg, Pb and Pn) and 1877 PmP reflections were manually picked combining all the record sections. A picking error of one half of the dominant period in the data (~8 Hz) was assumed for refracted phases, and slightly larger for reflected phase arrivals, accounting for a possible systematic shift in arrival identification. Taken this into account, picking uncertainty was between 40-50 ms for Pg, Pb and Pn and 60ms for PmP.

6.2 Results

In the following section I present the main results obtained from the modeling and processing of Line GH/MEDOC-6 WAS, MCS, and gravity data. These results provide the velocity, tectonic, and density structure of the crust and uppermost mantle along this transect.

6.2.1 Velocity structure

The main characteristics of the velocity model in Figure 6.2a are the laterally variable marine sediment layer, the heterogeneous basement velocity structure showing a strong vertical velocity gradient at its upper part, and the progressive crustal thinning toward the center of the basin. Based on the velocity structure I propose the presence of 5 different domains.

Domain 1 extends from 0 to ~125 km (Figure 6.2a) and includes mainland Sardinia (0-80 km), and the Sardinia margin (80-125 km). Here the model displays the 2.0-2.5 km-deep Sardinia basin (Figures 6.2a), with Vp of ~1.8 km/s at the top to 3.5-4.0 km/s at the base (Figure 6.6). Under the sedimentary basin, the upper 2-3 kms of the basement are characterized by a strong velocity gradient of ~0.5 s^{-1}, underlain by a lower velocity gradient with velocity at mid- and lower-crustal levels of 5.5-6.5 km/s. The Moho of Domain 1 is well constrained by PmP reflections between km ~80 to ~125 km along the profile in Figure 6.2a, showing a significant shoaling from 20-21 km depth at ~80 km to ~15 km depth at ~125 km along profile, defining a significant crustal thinning (Figure 6.2a).

Domain 2 extends from ~125 to ~210 km, (Figure 6.2a), and corresponds to the Cornaglia Terrace (Figure 6.1). Similarly to Domain 1, the underlying uppermost 2-3 km of basement have a vertical velocity gradient of ~0.5 s^{-1}, whereas mid-and lower-crustal velocities are higher than in Domain 1, ranging between 6.5 km/s at the top to 7.1-7.2 km/s at the bottom (Figure 6.2a). The Moho is well-constrained by clear PmP phases in WAS data and it is also visible in the MCS line (Figures 6.4 and 6.5). It shoals from ~15 km to 10 km depth between ~125 to ~210 km along profile (Figure 6.2a). The basement velocity structure also displays abrupt lateral contrasts of about 0.5 km/s that delineate four 10-15 km-wide, sub-vertical structures with velocity ranging between 6.0 km/s and 6.5 km/s (between OBH 91 and 87 in Figure 6.2a).

Domain 3 extends from km ~210 to ~345 along profile (Figure 6.2a). This region is characterized by the absence of wide-angle Moho reflections (no PmP between OBH 84 and OBH74). Similarly, the MCS images that show Moho reflections in other domains, do not display clear reflections at the expected Moho TWT in Domain 3 (Figure 6.4 and 6.6). The Vp model displays here the strongest vertical velocity gradient ($\geq 1\ s^{-1}$), twice as strong as in any other domains. The base of the 1-2 km-thick sediment cover of Magnaghi and Vavilov basins, well imaged on MCS data (Figure 6.4), corresponds to the 3.5-4.0 km/s contours (Figure 6.6). The basement is not bounded at its base by PmP reflections and it is well-resolved by the dense coverage of Pb phases in Figure 6.2b. The velocity structure shows a gradual increase from ~4.0-4.5 km/s near the top of basement to 8 km/s at the deepest well-resolved part of the model at ~7-10 km depth, i.e. 4-5 km below the top of the basement. In average, the vertical velocity gradient in these uppermost ~5 km of the basement is twice stronger than in Domain 2, and even more compared with that of Domain 1. Coinciding with the bathymetric highs of Magnaghi seamount, and the profile intersections with the D'Ancona and Gortani Ridges and the Vavilov seamount (Figure 6.1 and 6.2a), the model shows four velocity anomalies extending from the top of the basement to about 10 km depth (r1-r4 in Figure 6.10). Compared to the rest of Domain 3, these anomalies have gentler vertical velocity gradient, faster velocity at shallow levels, and slower velocity at deep levels. These local anomalies are better displayed by comparing vertical velocity gradients rather than absolute velocities (Figure 6.10b) (see section 6.3.4 for details).

Domain 4 encompasses the Campania Terrace, from ~350 to 410 km (Figures 6.1 and 6.2a). Here, PmP reflections are clear in the record sections (Figure A.1.1.24 to A.1.1.28), constraining well the Moho geometry. Crustal thickness increases from ~7 to ~10 km from km 355 to ~410 along profile (Figure 6.2a). The basement velocity structure is similar to Domain 2, with Vp increasing from 4.0-4.5 km/s at the top to 7.1-7.2 km/s at the base of the crust. However, the velocity distribution of Domain 4 is more homogeneous laterally, without the sub-vertical velocity structures observed in Domain 2 (Figure 6.2a).

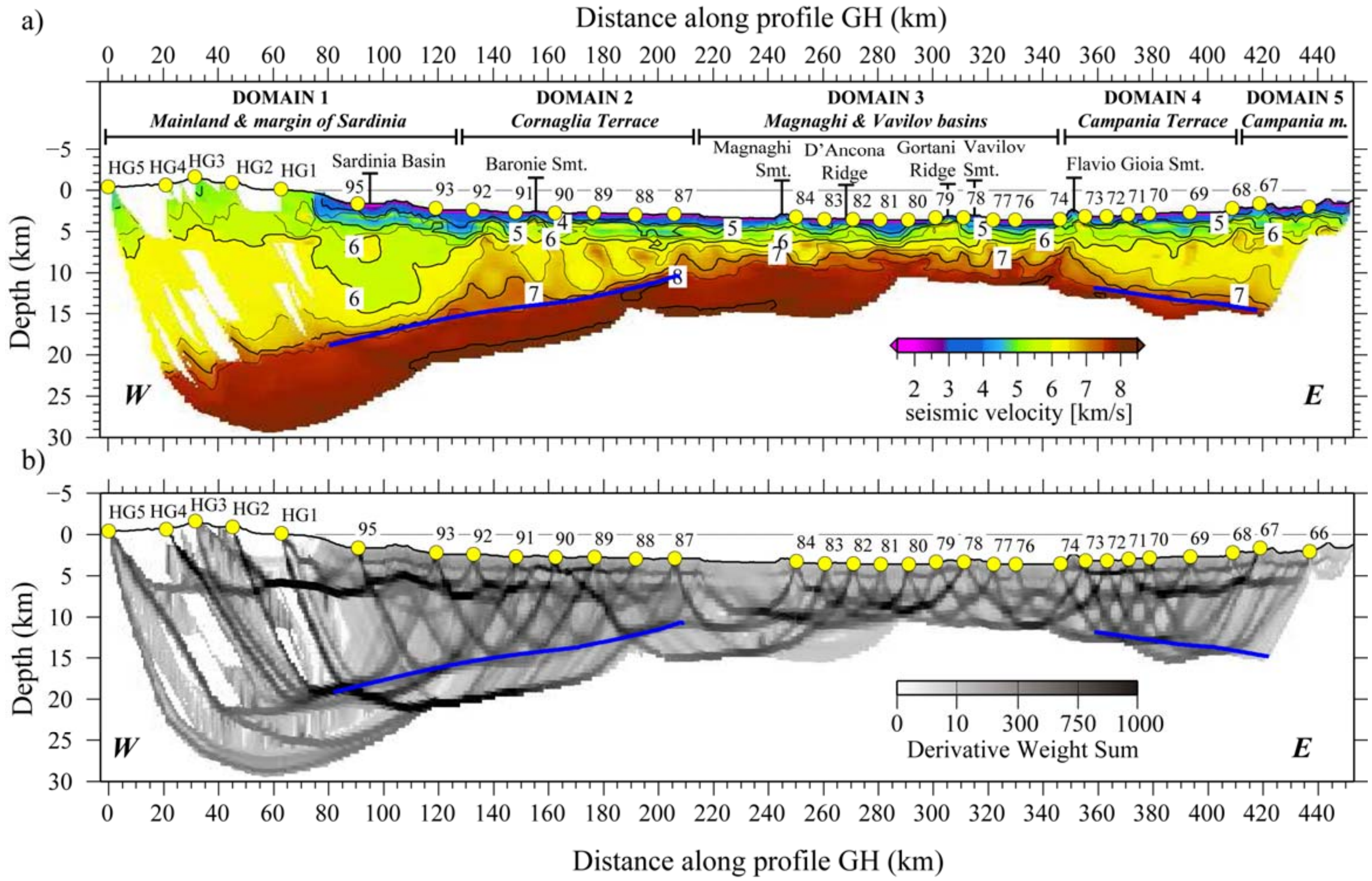

Figure 6.2.- *(a) Final P-wave velocity model of the crust, uppermost mantle and Moho geometry along the WAS Line GH.. Campania m.: Campania margin. (b) Derivative Weight Sum (DWS) values of the above tomographic model (a). Blue line in both panels, (a) and (b), is the inverted Moho geometry Yellow circles are the Land-stations, OBHs, and OBSs used in this thesis.*

Domain 5 runs across the Campania margin (i.e. last 30-40 km of profile in Figure 6.2a). Here the crustal structure is just moderately well-resolved because the ray-coverage is poorer (Figure 6.2b). However, the reduction in crustal velocities and the increment of crustal thickness complemented with a significant change of the bathymetry relief suggest that it may represent a change in crustal structure, hence a fifth domain is interpreted.

Mantle velocity structure is well resolved along the entire line. Beneath mainland and Sardinia margin (Domain 1) long-offset Pn phases recorded in the land-stations dive 5-10 km into the mantle (Figure 6.2a). Clear Pn phases on OBH and OBS records along Domains 2 and 3 (Figures A.1.1.6 to A.1.1.13) constrain well the mantle velocity, whereas the Campania margin (Domain 4) has limited ray coverage so that mantle velocity is less well resolved (Figure 6.2b). Overall, velocity under the Moho increases with depth from ~7.6 km/s just under the crust-mantle boundary to ~8.0 km/s ~5 km below, indicating low uppermost mantle velocity in all Domains (Figure 6.2a).

6.2.1.1 Uncertainty analysis

Crustal velocity and Moho depth uncertainty of the velocity model in Figure 6.2a is displayed in Figure 6.3.

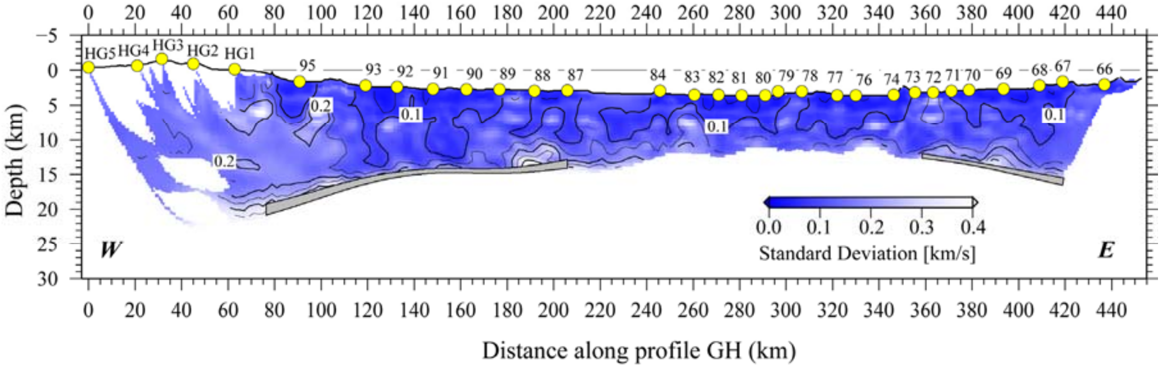

Figure 6.3.- *Final standard deviation values for the P-wave velocity values and the Moho geometry (grey band), as a result of the statistical uncertainty analysis. Note that in this analysis the mantle is not included. Details of the calculation are given in section 3.4.2 in chapter 3. Yellow circles display the location of the Land-stations, OBHs, and OBSs used in this thesis.*

Uncertainty values range between ±0.1 km/s and ±0.2 km/s in most of the model, except under Sardinia, where velocity uncertainty is between ±0.2 km/s and ±0.3

km/s due to low ray coverage (Figure 6.2b). Velocity uncertainty is also >±0.2 km/s at some locations with strong velocity gradient or contrast, like at ~15 km depth between OBH 87 and 88, and below OBH 69 (Figure 6.3). This effect has been observed in other studies [Sallarès et al., 2011, 2013a] around the sediment-basement boundary where there is a sharp velocity contrast. Depth uncertainty for the Moho is small, ranging between ±0.2 km where crustal velocity is constrained by Pg and Pb phases, and ±1.3 km where crustal velocity is primarily controlled by PmP phases only and the depth-velocity trade-off is higher (Figure 6.3).

6.2.2 Tectonic structure

As stated before, although I have not processed the MCS profile MEDOC-6, I have interpreted it and included it in my thesis to complement the information of the coincident WAS model of Line GH (Figure 6.2a). Particularly, the post-stack time migration image of MEDOC-6 was used to define the tectonic structure and to map the presence/absence of Moho in the near-vertical seismic reflection image (Figure 6.4). The MCS profile displays well the sediment cover, the top of basement (TOB), and locally groups of reflections from the lower crust that possibly delineate the transition to the Moho at their base (Figure 6.4 and 6.5). The Vp model has been converted to two-way time (TWT) and overlain on the seismic image to directly compare the structure obtained by the two methods (Figure 6.6). Overall, there is a regional good correspondence between structures in both images, but the two methods appear to have mapped some structures in different ways, which may give information on the nature of rocks forming the domains.

The crust-mantle boundary has been mapped in Domain 1 only with PmP wide-angle reflections because MCS data is contaminated with multiple energy at Moho arrival time predicted by WAS modeling (blue line in Figures 6.4 and 6.6). In Domains 2 and 4 both methods have detected the crust-mantle boundary and provide complementary information. The interpreted crust-mantle boundary appears in MCS image typically as a band of reflections that is ~0.2-0.5 s TWT thick, formed by individual events that are ~0.5-2 km long (Figure 6.5) and locally as sub-horizontal reflections that may indicate a more abrupt boundary (e.g. CMPs 44000-45000). The band of reflections may be interpreted to represent a layered transition from crust to mantle rocks. In some areas the sub-horizontal reflections forms the base of a reflectivity package where gently dipping mid-crustal reflections merge downdip (e.g. CMPs 47000-42000 and 17000-14000 in Figure 6.5).

The crust along domains 2 and 4 displays a 7-9 km laterally rather constant thickness (Figure 6.2a) that is displayed as a 2.5 to 2.9 s TWT thick crust in seismic images (Figure 6.5). Similar crustal structure and lower crustal reflectivity has been described in oceanic back-arc crust in the South Balearic basin [Booth-Rea et al., 2007] and in –slightly thinner- oceanic crust formed at fast-spreading rates [Ranero et al., 1997]. In these two settings the lower crustal structure has been interpreted as formed by either a lithological layering formed in a lower-crustal magma chamber or a deformation fabric of such a lithological layering that has been transposed by ductile flow.

The crust-mantle boundary location obtained by WAS modeling and converted to TWT systematically shows the Moho somewhat shallower than the base of the reflectivity band in MCS images (Figures 6.4, 6.5 and 6.6). This observation has two potential explanations: 1) the package of reflections in MCS images represents a layering with overall mantle velocities and the crust to mantle velocity transition is at its top, observed as the Moho location in the WAS, 2) alternatively, the TWT mismatch of Moho location in both data sets is due to seismic anisotropy [e.g. Sallares et al., 2013b]. This situation may arise when subhorizontal-propagating WAS waves travel faster than near-vertical MCS waves. Domain 3 shows neither wide-angle PmP reflections nor MCS images of the crust-mantle boundary, which strongly indicates that the increase from Vp<8km/s to Vp>8km/s is not an abrupt lithological boundary, but a gradual transition possibly over hundreds of meters that is expressed by the strong vertical velocity gradient (Figure 6.7).

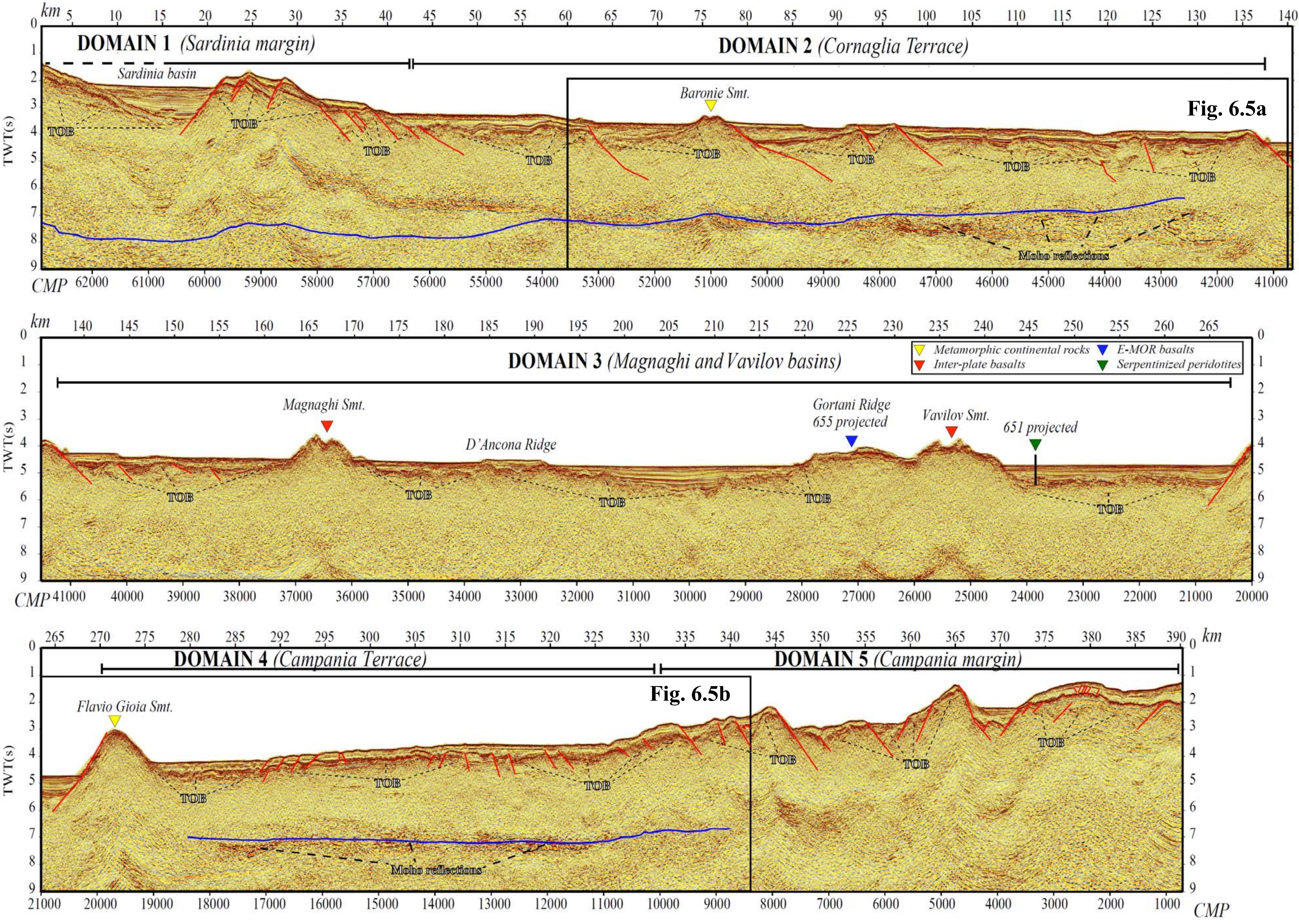
km
DOMAIN 1 (Sardinia margin)
DOMAIN 2 (Cornaglia Terrace)
Sardinia basin
Baronie Smt.
Fig. 6.5a
TOB
Moho reflections
TWT(s)
CMP
DOMAIN 3 (Magnaghi and Vavilov basins)
Metamorphic continental rocks
Inter-plate basalts
E-MOR basalts
Serpentinized peridotites
Magnaghi Smt.
D'Ancona Ridge
Gortani Ridge
655 projected
Vavilov Smt.
651 projected
DOMAIN 4 (Campania Terrace)
DOMAIN 5 (Campania margin)
Fig. 6.5b
Flavio Gioia Smt.

Figure 6.4.- *Post-stack time migration of profile MEDOC-6. The tectonic structure of the curst along this section is mainly represented by landward and seaward normal faults (red lines). Noted the excellent correlation between the interpreted Moho along the MCS profile and that obtained by the inversion of PmP phases (blue line). Colored triangles are the same used in Figure 6.1 to indicate the nature of the basement inferred from rock sampling [Dietrich et al., 1977; Colantoni et al., 1981; Kastens and Mascle, 1990; Sartori et al., 2004]. TOB: top of basement.*

Domain 2 displays a tectonic structure fundamentally different compared to that of Domain 1. It is characterized by comparatively wider spacing between fault blocks that in Domain 1, indicating that faulting was less important during extension of Domain 2. In Domain 2 there are 6 main fault blocks with a maximum relief of a few hundreds of meters, bounded by eastward dipping normal faults (Figure 6.5). The largest and only fault block that crops out of the seafloor is the southernmost extension of the Baronie seamount (Fig 6.1). The Baronie fault-block forms over 1 km of top-of-basement relief, and dredging indicates a continental origin [Sartori et al., 2004] so that is probably similar to blocks in Domain 1. The rest of the fault blocks of Domain 2 are considerably smaller in dimensions.

Domain 3 across the Magnaghi and Vavilov basins is bounded on either end by two set of major faults that dip with opposite directions on either side. However, the ~130 km-wide Domain 3 displays basically no evidence of high-angle normal faulting causing significant basement relief (Figure 6.4 and 6.6). The large relief in the map (Fig 6.1) corresponds to the 1-4 km tall basaltic Magnaghi and Vavilov seamounts (Figure 6.1), and D'Ancona and Gortani Ridges. The deeper, smooth basement top of the Vavilov basin was drilled during ODP 651 near line MEDOC-6. Drilling recovered a few tens of meters of basalt overlying mantle peridotite [Kastens and Mascle, 1990] (Figure 6.1). Domain 3 has neither Moho reflections in the MCS images nor PmP phases from Moho in the WAS records, which may indicate a different nature for the basement of this Domain (Figure 6.4 and 6.6).

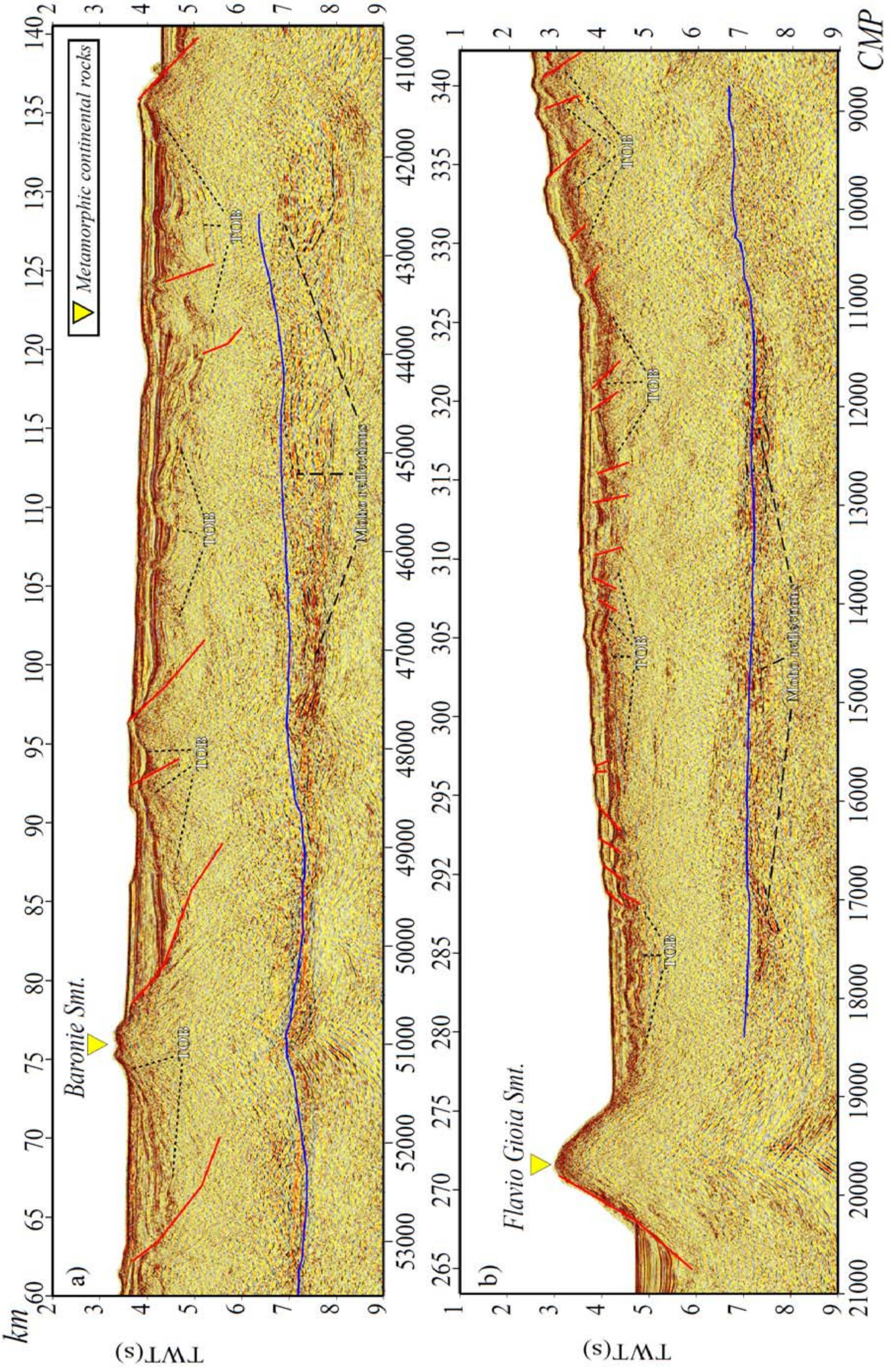
a)
b)
km
TWT(s)
CMP
Metamorphic continental rocks
Baronie Smt.
Flavio Gioia Smt.
TOB
Moho reflections
60
65
70
75
80
85
90
95
100
105
110
115
120
125
130
135
140
53000
52000
51000
50000
49000
48000
47000
46000
45000
44000
43000
42000
41000
265
270
275
280
285
292
295
300
305
310
315
320
325
330
335
340
21000
20000
19000
18000
17000
16000
15000
14000
13000
12000
11000
10000
9000
1
2
3
4
5
6
7
8
9

Figure 6.5.- *(a) Close-up of the MCS profile in Figure 6.4 along the Cornaglia Terrace. The main features of this region include the coincident absence of both, the inverted Moho (blue line) and the interpreted one along the MCS profile at ~ 135km of the profile MEDOC-6, and the presence of seaward normal faults (red lines). The yellow triangle represents the petrological nature of the Baronie seamount [Kastens and Mascle, 1990; Sartori et al., 2004]. (b) Close-up of Figure 6.4 along the Terrace and margin of Campania. As in the Cornaglia Terrace in (a), the location of the Moho interpreted along this region of the MCS profile and that obtained by the inversion (blue line) coincide remarkably well. The yellow triangle indicates the continental nature of the Flavio Gioa seamount [Colantoni et al., 1981; Kastens and Mascle, 1990]. TOB: top of basement*

Domain 4 extends from ~275 to 330 km along the MCS profile, with a structure in the MCS image that resembles the structure of Domain 2, but contains fewer, smaller-offset faults (Figures 6.4, 6.5 and 6.6). The image shows a fairly smooth top of the basement, indicating minor tectonic extension during the creation of this region of the basin. The well-imaged lower-crustal packages of reflections in the MCS data (Figure 6.5) and the spatially coincident PmP WAS reflections (Figure 6.6) clearly delineate the base of the crust as an abrupt seismic boundary for Domain 4, which is in contrast to Domain 3 but similarly to Domain 2. The pattern of eastward-dipping lower-crustal reflections that merge with the base of the crust reflections in the MCS image is also similar to the structure of Domain 2 (CMP 16000 to 14000 in Figure 6.5).

The MCS image extends further eastward that the WAS recordings and provides a wider coverage of Domain 5 (Figure 6.2). The seismic image of Domain 5 displays a progressive shoaling of the top of basement corresponding to a gradual landward thickening of the crust, as indicated by the WAS model (Figures 6.4 and 6.6). The crust is cut by numerous faults, including several large-offset normal faults that produce considerable top of basement relief. The tectonic structure of half and full grabens of few hundreds of meter to about 1 km deep indicates that extension by faulting was a comparatively important process during the opening of Domain 5, similarly to Domain 1 and in contrast to Domains 2-4.

.

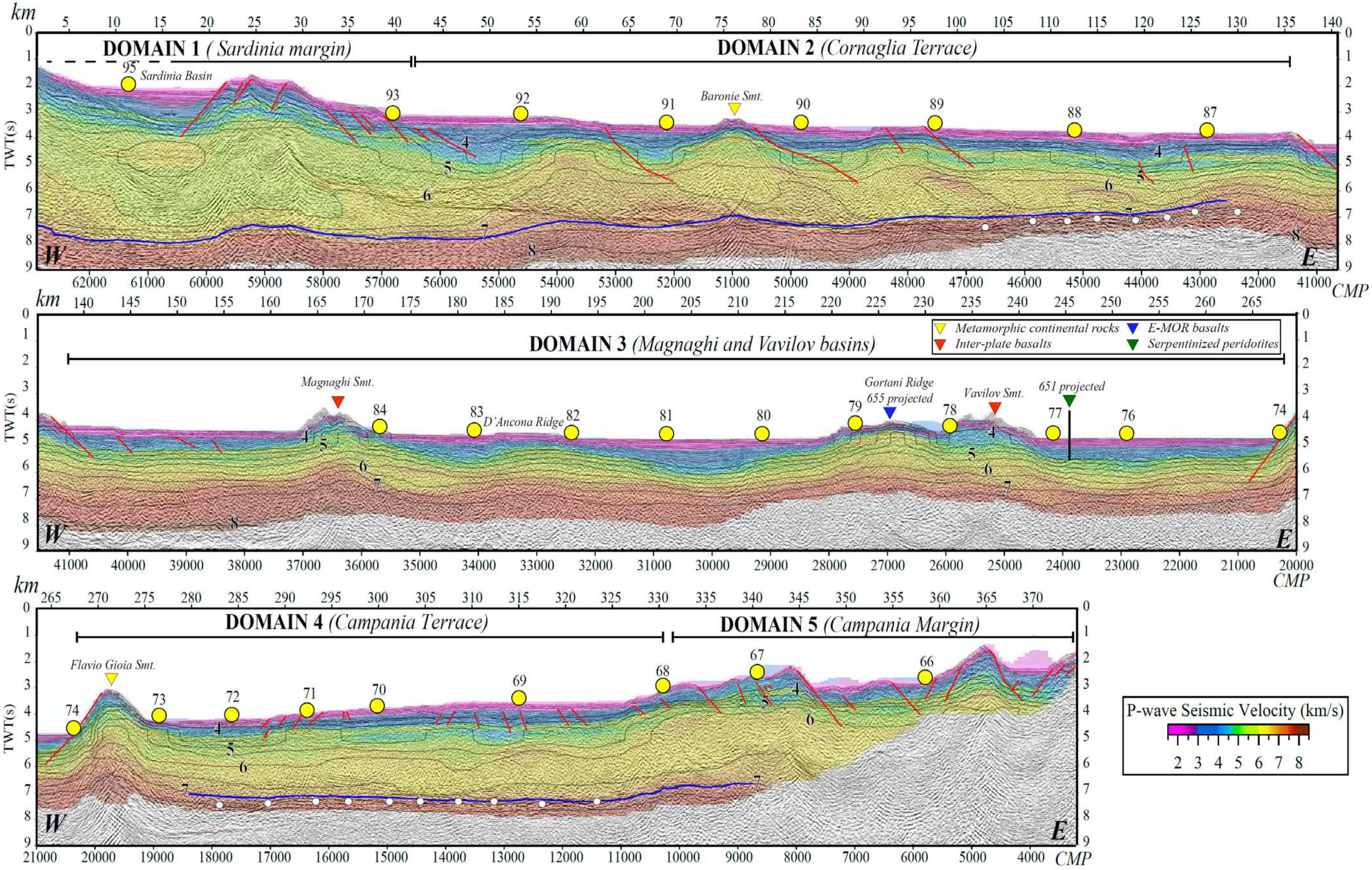
DOMAIN 1 (Sardinia margin)
DOMAIN 2 (Cornaglia Terrace)
DOMAIN 3 (Magnaghi and Vavilov basins)
DOMAIN 4 (Campania Terrace)
DOMAIN 5 (Campania Margin)
Sardinia Basin
Baronie Smt.
Magnaghi Smt.
D'Ancona Ridge
Gortani Ridge
655 projected
Vavilov Smt.
651 projected
Flavio Gioia Smt.
Metamorphic continental rocks
E-MOR basalts
Inter-plate basalts
Serpentinized peridotites
P-wave Seismic Velocity (km/s)
2 3 4 5 6 7 8
km
TWT(s)
CMP
W
E

Figure 6.6.- *Post-stack time migration of profile MEDOC-6 with the same tectonic interpretation as in Figure 6.4 and overlaid with the TWT converted version of the P-wave seismic velocity model (Figure 6.2a). Yellow circles display the location of the OBSs and OBHs along the profile. Colored triangles are the same used in Figure 6.4 [Dietrich et al., 1977; Colantoni et al., 1981; Kastens and Mascle, 1990; Sartori et al., 2004]. White circles display the location of those reflections interpreted as the crust-mantle boundary. Note that in Domains 2 and 4, the tomographic model presents an inversion of seismic velocities from 5km/s to 4km/s. This inversion could be related to the existing salt deposits of the Cornaglia Terrace (CMP 46000-42000) and the Campania Terrace (CMP 16000-11000).*

6.2.3 Automatized interpretation of basement affinity based on P-wave depth-velocity profiles

To reduce interpretation subjectivity from the conventional velocity analysis (Figure 6.7), I have developed an independent method for the automatic classification of the petrological affinity of the structural domains based on velocity-depth relationships. The method consists of comparing 1-D velocity-depth profiles extracted from the 2-D tomographic model (Figure 6.2a) with compilations made for continental crust [Christensen and Mooney, 1995], oceanic crust [White et al., 1992] and exhumed mantle [Sallarès et al., 2013a] (Figure 6.8). As a result, the RMS difference between 1-D velocity models along the 2-D profile (1-D profiles are calculated from 5-km-wide averages of the 2D velocity model) with the average of each of the three velocity-depth references is calculated [White et al., 1992; Christensen and Mooney, 1995; Sallarès et al., 2013a], allowing to assign the petrological affinity corresponding to the smallest RMS. The results obtained from the comparison with continental crust, oceanic crust and exhumed mantle are depicted in Figure 6.8a.

The smallest RMS at any point along the line automatically determines the basement affinity (Figure 6.8b). This method clearly separates basement type in the five domains previously discussed in section 6.2.1. In Domain 1, the reference model that best fits the velocity-depth profile is that of continental crust (Figure 6.8a and 6.8b). Domains 2 and 4, including the Cornaglia Terrace and the conjugate Campania Terrace have velocities that fit better with the reference model of oceanic crust (Figure 6.8). However, in these two domains the lower crust has velocities that are systematically lower than typical, Atlantic-like, 0-7 Ma old oceanic crust [White et al., 1992] (Figure

6.7). The easternmost ~10 km of the profile matches better the continental crust reference, suggesting that the nature of Domain 5 could be continental. This interpretation must be carefully taken since this region is poorly constrained by the WAS data. However Biella et al. [2007] shows that at about 90 km eastward OBH 66 the basement displays continental features. Interestingly, a narrow continental-affinity segment is discerned in Domain 2, coinciding with the location of the Baronie seamount of known continental nature [Sartori et al., 2004] (Figure 6.8c). In Domain 3 the velocity-depth profiles that match best clearly correspond to that of partially serpentinized peridotite (Figure 6.7 and 6.8b), with the exception of two narrow segments just below the Gortani Ridge and the Vavilov seamount, which are better explained by an oceanic crustal affinity (Figures 6.3a and 6.8b). These two seamounts have been previously described as basaltic edifices [Robin et al., 1978; Beccaluva et al., 1990; Bertrand et al., 1990; Savelli, 2002], possibly intruding a basement made of serpentinized mantle rocks.

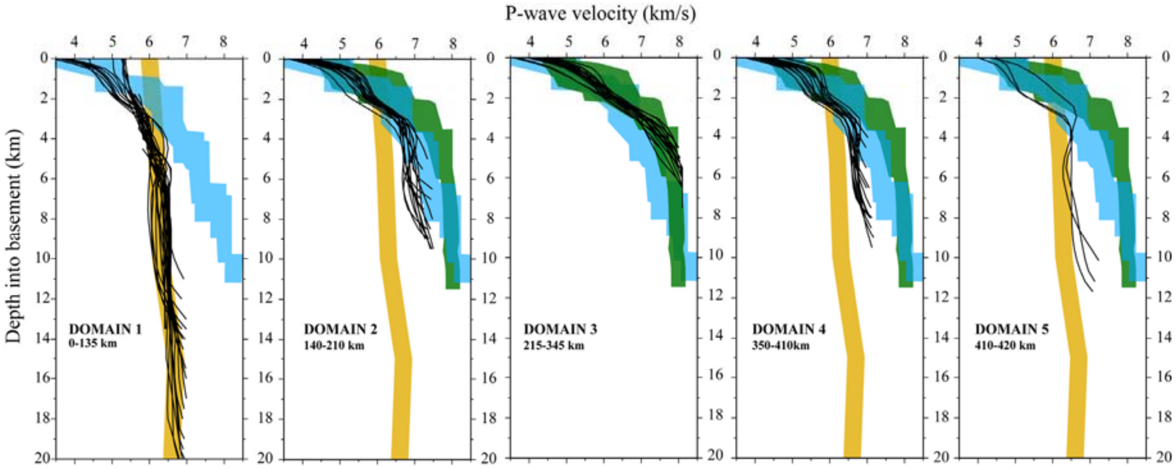

Figure 6.7.- *1D P-wave velocity-depth profiles of the five differentiated domains along the tomographic model (Figure 6.2a). Black lines represent the 5 km-laterally-averaged 1D velocity-depth profiles extracted from the tomographic model. 1D velocity-depth profiles of reference include a 20 km–thick continental crust (orange band) [Christensen and Mooney, 1995], 0-7 Ma Atlantic oceanic crust (blue band) [White et al., 1992], and a compilation of the exhumed mantle regions found West Iberia (green band) [Dean et al., 2000; Sallarès et al., 2013].*

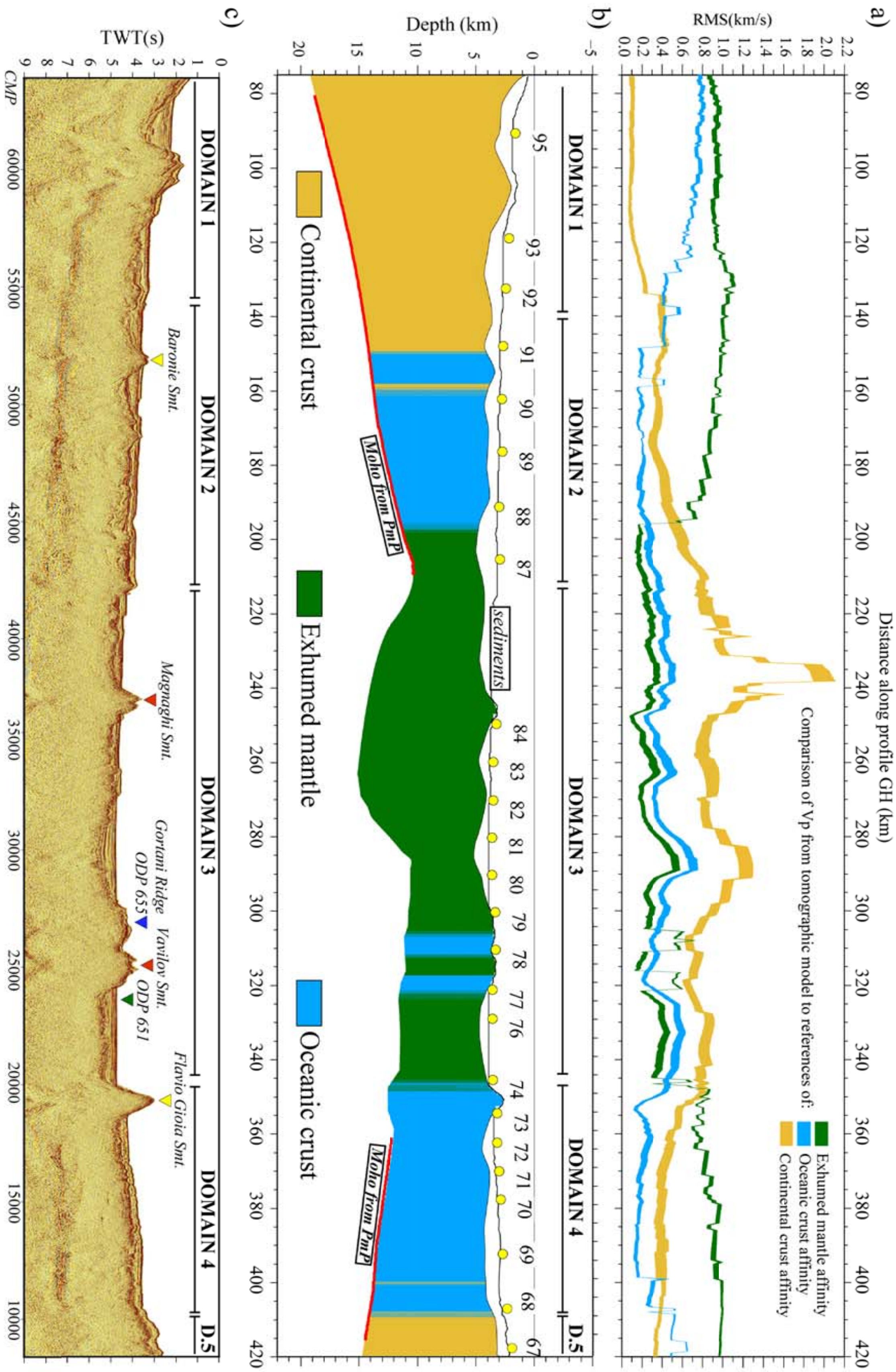
a)
Distance along profile GH (km)
RMS(km/s)
Comparison of Vp from tomographic model to references of:
Exhumed mantle affinity
Oceanic crust affinity
Continental crust affinity
b)
Depth (km)
DOMAIN 1
DOMAIN 2
DOMAIN 3
DOMAIN 4
D.5
sediments
Moho from PmP
Continental crust
Exhumed mantle
Oceanic crust
c)
TWT(s)
CMP
Baronie Smt.
Magnaghi Smt.
Gortani Ridge
ODP 655
Vavilov Smt.
ODP 651
Flavio Gioia Smt.

Figure 6.8.- *(a) Velocity RMS values for the three models referred in the text as a function of the distance along the tomographic model (Figure 6.2a), result of the automatic basement classification analysis (see section 6.2.3). The orange band corresponds to the comparison of each 1D velocity-depth profile of the tomographic model and the continental crust 1D velocity-depth reference [Christensen and Mooney, 1995]. Similarly, the blue and green bands corresponds to the comparison with a young (0-7 Ma) Atlantic oceanic crust [White et al., 1992] and an exhumed mantle region [Sallarès et al., 2013], respectively. Details of the calculation are given in the text (see section 6.2.3). The thickness of each RMS line corresponds to the error bar obtained in the uncertainty analysis explained in section 3.4.2. (b) Basement affinity model corresponding to the automatic basement classification shown in (a). The inverted Moho geometry (thick red line) and the location of the OBSs and OBHs (yellow circles) are also shown in the image. (c) MCS profile MEDOC-6 with the main morphological structures identified along the profile (e.g. Vavilov seamount), and the projections of ODP sites 655 and 651 [Kastens and Mascle, 1990]. The petrological nature of the basement is also represented by the same colored triangles as in Figure 6.1 (see legend in Figures 6.1, 6.4 or 6.6) [Dietrich et al., 1977; Colantoni et al., 1981; Kastens and Mascle, 1990; Sartori et al., 2004]. Vertical scale is exaggerated.*

6.2.4 Density structure

In order to challenge the petrological interpretation described in the previous section (Figure 6.7 and 6.8), the velocities of the tomographic model (Figure 6.2a) have been converted into densities using the Vp-ρ relationships corresponding to the petrological affinities assigned by the automatized velocity analysis and mentioned in section 4.3 in chapter 4 (Figure 6.8). Hence, the Christensen and Mooney's [1995] Vp-ρ relationship for continental rocks was used in Domains 1 and 5, Carlson and Herrick's [1990] conversion law for oceanic crust in Domains 2 and 4, and Carlson and Miller [2003] Vp-ρ relationship for partially serpentinized peridotites in Domain 3.

The gravity response of the resulting density model (Figure 6.9a) presents a slight mismatch of 18mGal with the observed free-air gravity anomaly. A possible explanation for this mismatch is the anomalous lower crustal velocity in Domains 2 and 4, which is systematically lower than a typical 0-7 Ma-old oceanic crust [White et al., 1992], possibly reflecting a different petrological composition. To correct this effect, crustal densities have been decreased by 1-2% in these two domains (Figure 6.9b). The obtained model fits remarkably well the observed gravity anomaly with an RMS of 8 mGal (Figure 6.9a).

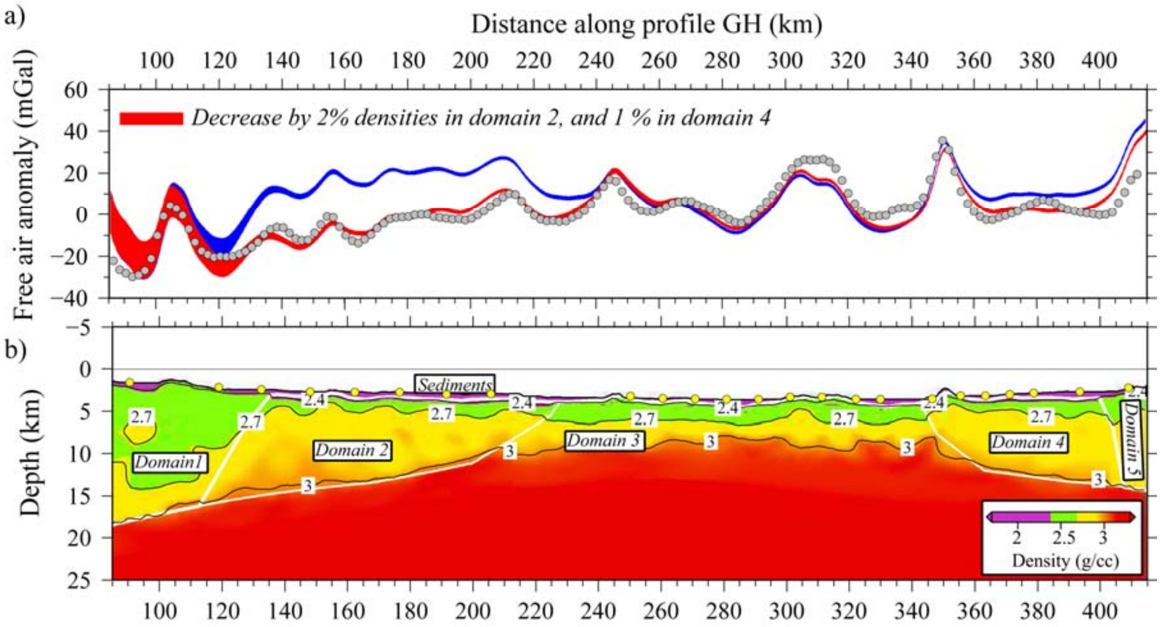

Figure 6.9.- *(a) Observed free-air gravity anomaly (grey circles) recorded during the MEDOC survey. Blue band corresponds to the gravity anomaly calculated from the velocity-derived density model obtained using Hamilton's [1978] relationship for the sediment layer, Christensen and Mooney's [1995] relationship for continental crust in Domain 1 and 5, Carlson and Herrick's [1990] relationship for oceanic crust in Domains 2 and 4, and Carlson and Miller's [2003] conversion law for partially serpentinized peridotites in Domain 3. The RMS value for this case is 18 mGal. Red band corresponds to the gravity anomaly calculated from the density model obtained by using the same conversion laws as in the first case, but decreasing by 2 % and 1 % densities in Domains 2 and 4, respectively. The RMS value is 8 mGal. (b) Velocity-derived density model corresponding to the best fit (red band). Yellow circles show the location of the OBS and OBH.*

6.3 Characterization of geological domains along Line GH/MEDOC-6

In this section, the results obtained from the WAS model, MCS image, and the gravity modeling are integrated in order to interpret the nature of the basement beneath the Sardinia margin (Domain 1), Cornaglia Terrace (Domain 2), Vavilov and Magnaghi basins (Domain 3), Campania Terrace (Domain 4) and Campania margin (Domain 5).

6.3.1 The continental margins of Sardinia (Domain 1) and Campania (Domain 5)

The Sardinia Island and its margin (Domain 1 in Figures 6.2a, 6.4 and 6.6) have a continental velocity and density structure (Figure 6.7 and 6.8). This interpretation is also consistent with regional geology. Field observations indicate that Sardinia basement is mainly formed by Paleozoic, locally Mesozoic and Eocene rocks from the European continental lithosphere, overlaid by -from bottom to top- continental-to-marine sediment sequence related to Oligocene-Miocene rifting [Cherchi and Montadert, 1982]. Similarly, dredged basement rocks of the Sardinia margin (Figure 6.1, 6.4 and 6.5) include Late Paleozoic (~300 Ma) granitoids (e.g. Baronie seamount in Figures 6.2a, 6.5, 6.6 and 6.7) of the Variscan orogeny [Mascle and Rehault, 1990; Sartori et al., 2004], covered by Serravallian-early Tortonian to Pliocene-Pleistocene sediment [Mascle and Rehault, 1990; Sartori, 1990; Sartori et al., 2004].

The WAS data do not constrain well crustal thickness beneath the island, but complementary gravity modeling indicates a ≤24 km thickness, in agreement with previous seismic estimations [Di Stefano et al., 2011]. Other WAS profiles acquired during the MEDOC-2010 experiment in the northern Tyrrhenian basin, across Corsica and offshore to the east, suggests a similar thickness beneath the island [Moeller et al., 2013]. The crystalline crust thins from ~15 km thick under the coastline (km 80, Figure 6.2a) to 9 km at Domain 1 edge, implying a stretching factor (ß) of ~3 (km 125, Figure 6.2a). However, the transition between continental Domains 1 and 2 along the transect is probably relatively abrupt as the automatic classification seems to indicate and a Continent to Ocean Transition (COT) has not been found (Figure 6.8b).

Domain 5 (Campania margin) is less well characterized with WAS data because the line has mapped only the outer segment (Figure 6.2a) although it is also classified as continental (Figure 6.8). However, the MCS image extends further East and shows 60 km of a terrain characterized by significant extensional tectonics during formation. The structure of Domain 5, with a rough, eastward shoaling relief, indicating a gradual eastward thickening of the crust, (also mapped in the segment covered with the WAS line) is clearly differentiated from Domain 4. No basement samples from the margin have been reported in literature, and I interpret this segment as an extension of the continental crust of Italy mainland.

6.3.2 Magmatic crust under the Cornaglia Terrace (Domain 2) and Campania Terrace (Domain 4)

In Domains 2 and 4 there are two anomalously tall seafloor highs, the Baronie and Flavio Gioia seamounts, respectively, where dredging recovered continental rocks (Figures 6.1). These highs are narrow and only Baronie shows well as continental in the automatized classification (Figure 6.8b). However, the rest of Domains 2 and 4 do not appear as continental in the automatized classification. Under the Cornaglia Terrace (Domain 2) and Campania Terrace (Domain 4) (Figures 6.1, 6.2a, 6.4, 6.5 and 6.6) the basement presents a two-layer seismic structure characterized by different vertical velocity gradients that resemble oceanic crust layer 2 and layer 3 typical structure but with somewhat slower velocity in the lower crust (Figure 6.7). Under the Cornaglia Terrace the velocity model shows East-dipping crustal-scale velocity anomalies perhaps linked to east-dipping crustal-scale faults observed in the upper crust in the MCS line (Figures 6.2a and 6.5). This might indicate that these faults may be reaching close to the crust-mantle boundary. In contrast, faulting in the Campania Terrace has smaller offset.

The limited amount of extension by faulting in the Campania Terrace is accompanied by a velocity structure somewhat more homogeneous than in the Cornaglia Terrace (Figure 6.2a), although it displays similar velocity-depth profiles (Figure 6.7). Most lower crust velocity-depth profiles of both domains display velocities ranging between 6.5 and ~7.0 km/s, so they are between typical continental and oceanic [Christensen and Mooney, 1995; White et al., 1992] (Figure 6.8a), with a few exceptions in Domain 2 that may reach 7.1-7.2 km/s in the lowermost crust.

Thus, in general the velocity-depth relationships in Domains 2 and 4 agree better with that of oceanic crust (Figures 6.7 and 6.8). However, the crust in these two domains is slightly thicker than typical oceanic crust [White et al., 1992], ranging between 7-9 km and locally reaching 12 km (Figure 6.2a). In addition, to obtain a good fit of the gravity data in these two domains (Figure 6.9a) it is necessary to decrease the crustal densities obtained with the Carlson and Herrick's [1990] Vp-ρ relationship for oceanic crust by 1-2% (Figure 6.9). This suggests a departure in mineral composition from typical mid-ocean ridge oceanic crust.

A two-layer seismic structure with similarly slow lower crustal velocity and crustal thickness has been described in other back-arc extensional settings, such as Ligurian basin [Gailler et al., 2009] and Lau basin [Turner et al., 1999]. In Lau the seismic structure is attributed to volcanic intrusions into the lower crust during crustal extension [Turner et al., 1999] and to oceanic crust in the Ligurian [Gailler et al., 2009]. Additionally, it is important to note that it has been suggested that the interaction between subduction-related hydrous flux melting and decompression melts under a back-arc spreading center system produce a rock composition more felsic than typical mid-ocean ridge basalts [Dunn and Martinez, 2011].

Therefore, a plausible hypothesis is that the two-layer seismic structure under the Cornaglia Terrace and Campania Terrace (Figures 6.3a and 6.7) could have formed during the first phases of back-arc spreading at a distance of the volcanic arc close enough that there was an important contribution of subduction-related magmatism during crustal accretion [Martinez et al., 2007].

6.3.3 Exhumed mantle-rock basement at the Magnaghi and Vavilov basins (Domain3)

The Magnaghi and Vavilov basins (Domain 3) are the segments that do not display Moho reflections in either MCS (Figures 6.4 and 6.6) or WAS data (Figures A.1.1.14 to A.1.1.23), and show the strongest vertical velocity gradients (Figure 6.7). The basement classification based on velocity-depth profiles indicate that the seismic structure is analogous to the continental-ocean transition of the West Iberia margin where the basement appears to be made of mantle rocks with no overlay of crustal-type rocks [Dean et al., 2000; Sallarès et al., 2013a]. The velocity uncertainty is small enough to discard that it might correspond to 0-7 Ma old-oceanic crust [White et al., 1992] (Figure 6.7). These results, together with the corroboration by the good fit of the gravity data using Carlson and Miller's [2003] conversion law for partially serpentinized peridotites (Figure 6.9), strongly indicate that the basement is made of mantle rocks with no detectable igneous crust carapace.

In contrast with this interpretation, 1D P-wave velocity models obtained by forward modeling from WAS data recorded by deep-ocean geophones and seismographs between the 60's and the 80's [Fahlquist and Hersey, 1969; Nicolich, 1981; Recq et al., 1984; Duschenes et al., 1986] (see Figure 2.9), were interpreted as indicating that the Magnaghi and Vavilov basins are floored by oceanic crust. Nonetheless, the spatial density of deep-ocean receivers in these studies (~5 receivers per 100 km of profile) was much lower than in the MEDOC experiment (Figures 6.1 and 6.2a), and shot-spacing was 10 times larger than in the MEDOC WAS lines [Duschenes et al., 1986], so that the resolution and velocity control in our models is far better as demonstrated by the uncertainty analysis.

Additionally, there is some evidence of igneous rocks in the basin that include the E-MOR basalts drilled on top of the Gortani Ridge (ODP site 655) and at the basement of the Vavilov basin (ODP site 651) [Beccaluva et al., 1990; Bertrand et al., 1990; Savelli, 2002] (Figures 6.1, 6.4 and 6.6). The Gortani Ridge is intersected by the tomographic model (between OBH79 and 80 in Figures 6.1 and 6.2a) and consequently imaged in depth (at ~300 km in Figure 6.2a). The velocity model shows that its crustal structure is anomalous and local (Figure 6.10) and it is not representative of the nature of the whole domain. The interpretation on its nature and origin is discussed in the next section.

Concerning the oceanic-like nature of rocks of the Vavilov basin, E-MOR basalts drilled in this region are underlain by serpentinized peridotites, being this the lithological composition of the last unit in the borehole (ODP site 651 in Figures 6.1, 6.4 and 6.6) [Bonatti et al., 1990; Kastens and Mascle, 1990]. Other magmatic intrusions are present along this domain (i.e. Magnaghi and Vavilov Smts.) (Figures 6.2a and 6.10), however, based on their affinity (alkaline) and age (3-0.1 Ma), I conclude that they are not representative of oceanic accretion related to the opening of the Magnaghi and the Vavilov basins [Robin et al., 1978; Savelli, 2002], but they likely represent later episodes of magmatic activity that intruded the original basement made of mantle rocks.

On the basis of these observations, the basement beneath Domain 3 is interpreted to be mainly constituted by serpentinized peridotites locally intruded and overlaid by ocean-like basalts (i.e E-MOR basalts). The strong vertical velocity gradient in the uppermost 3-4 km of the basement (> 1s^{-1}), the smoother velocity gradient just beneath, the velocities lower than those characteristic of unaltered mantle (< 8.2 km/s), and the absence of the Moho (Figure 6.2a and 6.6) are common features that have also been observed off Western Iberia [Pinheiro et al., 1992; Chian et al., 1999; Dean et al., 2000; Sallarès et al., 2013a]. In that region, the strong velocity gradient of the uppermost 3-4 km of the basement is attributed to an abrupt decrease in degree of serpentinization with depth (e.g. from >80 % of serpentinization to 30-20% in less than 2 km), whereas the underlying smoother velocity gradient would correspond to a weakly serpentinized mantle [Sallarès et al., 2013a]. The similar velocity and velocity gradient encountered in the Central Tyrrhenian basin allows me to suggest that the case is also very similar.

6.3.4 Volcanic intrusions in mantle-rock basement

Throughout Domain 3, and coinciding with the location of the magmatic edifices of the Magnaghi and Vavilov seamounts, the D'Ancona Ridge and the southernmost part of the Gortani Ridge, the tomographic model displays several vertically-elongated velocity anomalies characterized by a gentler vertical velocity gradient as compared with the rest of this domain (e.g. at ~300 km in Figures 6.10a). In order to improve the definition of these velocity anomalies, the vertical velocity gradient model obtained from the tomographic model (Figure 6.2a) has been compared with a laterally-smoothed version of the vertical velocity gradient model, excluding the sedimentary layer. As a result, I have obtained anomalies where the vertical gradient is smoother than the background gradient. As can be seen in Figure 6.10b, these anomalies concentrate under the volcanic centers (r1, r2, r3, r4 in Figure 6.10b).

The sub-vertical anomaly r1 (Figure 6.10b), one of the strongest anomalies in the tomographic model (<-0.3s^{-1}), is interpreted as the root of the magmatic body corresponding to the Magnaghi seamount, which has been sampled and dated at 3.0-2.7 Ma [Savelli, 2002].

Anomaly r2 (Figure 6.10b) occurs under the intersection of the D'Ancona Ridge with the WAS line (Figures 6.1 and 6.10). This ridge, which has not been sampled, has been generally interpreted as a faulted continental block, although a possible magmatic origin has also been suggested [Marani and Gamberi, 2004; Sartori et al., 2004]. On the basis of its location and given that the velocity gradient below is rather high in comparison to that of a continental block (e.g. Baronie Smt at 150 km of profile in Figure 6.2a); it might also correspond to a basaltic intrusion into the mantle basement forming the root of a volcanic edifice.

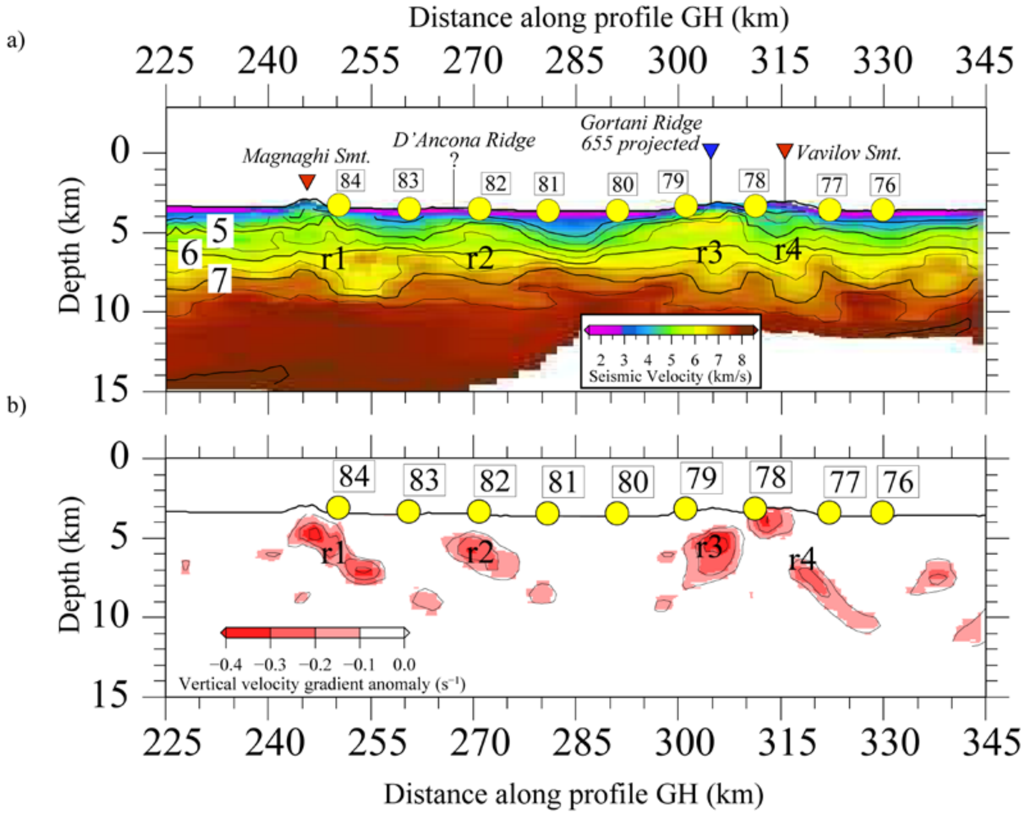

Figure 6.10.- *(a) Close-up of the tomographic model (Figure 6.2a) along the Magnaghi and Vavilov basins with the main morphological elements identified. The same colored triangles used in Figure 6.1 are also used in this image [Dietrich et al., 1977; Colantoni et al., 1981; Kastens and Mascle, 1990]. (b) Map of the vertical velocity gradient anomalies along the tomographic model, which has been obtained by comparing the vertical velocity gradient model, corresponding to the tomographic model (Figure 6.2a), with a laterally-smoothed version of the same gradient model. The smoothing was done by applying a Gaussian filter with a horizontal correlation length of 15 km and a vertical one of 0.5 km. The goal of this method is to determine the dimensions of those velocity anomalies observed along the tomographic model (Figure 6.2a), which in this case might be representing the tomographic signature of the structure in depth of the Magnaghi seamount. (r1), D'Ancona (r2) and Gortani (r3) Ridges, and the Vavilov seamount (r4).*

Anomaly r3 (Figure 6.10b) is interpreted as the root of the Gortani Ridge. This ridge is composed by E-MOR basalts (ODP site 655) dated at 4.3 Ma [Beccaluva et al., 1990; Bertrand et al., 1990; Savelli, 2002], being the oldest magmatic body imaged in the central basin, but younger than the opening of the Vavilov basin where it intrudes.

Anomaly r4 (Figure 6.10b) is located below the northernmost intersection of Vavilov seamount, likely representing a related intrusion. Similarly to Magnaghi seamount, Vavilov seamount is related to intra-plate magmatism created at 2.6-0.1 Ma after the end of extension in the central basin [Robin et al., 1978; Savelli, 2002].

Chapter 7: Line EF/MEDOC-4

As in chapter 6, the results and discussion of this chapter, together with the discussion in section 8.1 are included in the paper *"3D definition of geological domains in the Central Tyrrhenian basin based on crustal properties"* to be submitted for publication to Geochemistry, Geophysics, Geosystems (G^3), and of which I am first author.

7.1 Wide-Angle seismic Data analysis

The ~400 km-long Wide-Angle seismic (WAS) Line EF (Figure 7.1) extends from Sardinia to the Campania margin (Figure 6.1), ~55 km to the north of line GH (Figure 7.1). As in section 6.1, I present here the WAS data of this line and the different seismic phases selected for modeling.

7.1.1 Wide-Angle seismic Data

Three types of seismic phases were identified in the record sections (Figures in Annex A.1.2). Two of them were interpreted as refractions throughout the crust (Pg) and the mantle (Pn), and the other as a reflected phase into the crust-mantle boundary (PmP). As in the case of the GH line, and due to the thickness of the sedimentary layer, sedimentary phases were not identified. In Sardinia most land-stations display a ~40 km-long Pg phase with an apparent velocity of 6.0-6.5km/s, except land-station EF1 (Figure A.1.2.5), which presents > 70 km-long Pg phase. Only in land-stations EF1 and EF4 a 90-100 km offset Pn phase with an apparent velocity of ~8 km/s is identified (Figure A.1.2.5). The only PmP phase in land-stations is identified in receiver EF1 (Figure A.1.2.5). The same distribution of seismic phases is observed from OBS 36 to OBH 55 (Figures A.1.2.6 to A.1.2.24). In these receivers the Pg phase presents an apparent velocity of 6.0-6.5 km/s at offsets ranging from ~50 km beneath the Sardinia margin (Figure A.1.2.6) to ~30 km below the Cornaglia Terrace (Figure A.1.2.12) and Sechi and Farfalla segments (Figures A.1.2.15 and A.1.2.21) to the point where Pn phases arise.

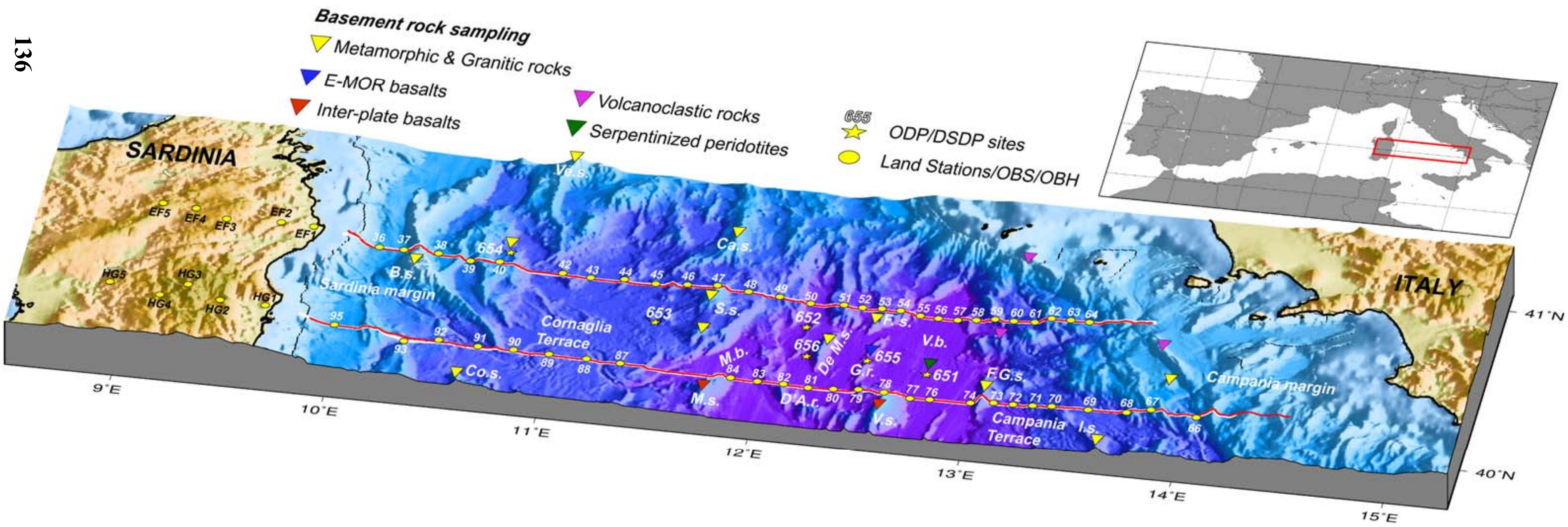
Basement rock sampling
Metamorphic & Granitic rocks
E-MOR basalts
Inter-plate basalts
Volcanoclastic rocks
Serpentinized peridotites
655
ODP/DSDP sites
Land Stations/OBS/OBH
SARDINIA
ITALY
Sardinia margin
Cornaglia Terrace
Campania margin
Campania Terrace
B.s.
Ca.s.
Co.s.
Ve.s.
S.s.
F.s.
V.b.
M.b.
M.s.
De M.s.
G.r.
D'A.r.
V.s.
F.G.s.
I.s.
654
653
652
656
655
651
EF1
EF2
EF3
EF4
EF5
HG1
HG2
HG3
HG4
HG5
9°E
10°E
11°E
12°E
13°E
14°E
15°E
40°N
41°N

Figure 7.1.- *Bathymetric and topographic map of the Central Tyrrhenian region, with petrological information and location of Lines EF/MEDOC-4 (northern line) and LineGH/MEDOC-6 (southern line). Red solid lines correspond to WAS profiles and white thick lines represent MCS lines. Yellow circles correspond to Land-stations, OBSs and OBHs used to record WAS data in both profiles. Yellow stars display the location of ODP sites [Kastens and Mascle, 1990]. Colored triangles represent the lithological nature of the basement [Dietrich et al., 1977; Colantoni et al., 1981; Kastens and Mascle, 1990]. B.s.: Baronie Seamount, Ca.s.: Cassini seamount, Co.s.: Cornaglia Seamount, D'A.r.: D'Ancona Ridge, De M. s.: De Marchi Seamount, F.s.: Farfalla Seamount, F.G.s.: Flavio Gioia Seamount, G.r.: Gortani Ridge, I.s: Isel seamount, M.s.: Magnaghi Seamount, M.b.: Magnaghi Basin, S.s.: Sechi Seamount, Ve: Vercelli seamount, V.b.: Vavilov Basin, V.s.: Vavilov Seamount.*

This variation in length of the Pg phases indicates a substantial crustal thinning towards the East. Pn phases are clearly observed in most OBHs displaying an apparent velocity of ~8 km/s (Figures A.1.2.6 to A.1.2.24). Reflections from the crust-mantle boundary (i.e. PmPs) are also identified in most of these receivers (i.e. from OBS 36 to OBH 55) (Figures A.1.2.6 to A.1.2.24). Eastward, the seismic record of OBH 56, located in the northernmost part of the Vavilov basin (Figure 7.1), displays striking differences with the aforementioned receiver records, showing a Pg phase extending ~40 km from the receiver with a rather fast apparent velocity of ~7 km/s which followed by a faster, Pn-like phase (Figure A.1.2.25). Similarly, Pg phases observed at the eastern wing of the record section of OBH 55 (Figure A.1.2.24) and the western wing of OBH 57 (Figure A.1.2.26) also display fast apparent velocities of >7km/s immediately below the sediments. It is worth noting that PmP-like reflections have been identified in the western wing of OBH 57 (Figure A.1.2.26), but not in the eastern wing of OBH 55 or in OBH 56 (Figure A.1.2.24 and A.1.2.25).

Record sections of OBH 57 to OBH 64 located in the northern Campania Terrace and margin (Figure 7.1), show clear Pg phases with a moderate velocity of ~6.0-6.5 km/s, similar to those observed in stations located on the Sardinia margin (Figure A.1.6). The maximum offset at which Pg phases are observed increase toward the continent (Figures A.1.2.26 to A.1.2.33). For offset longer than Pg, a prominent Pn phase is observed in most receivers up to 70 km offset, displaying apparent velocities of >7 km/s (Figures A.1.2.26 to A.1.2.33). PmP reflections are also identified in some receivers at offsets that increase toward the East, in accordance with the expected crustal thickening towards the continent (Figures A.1.2.26 to A.1.2.33).

Overall, a total of 14557 first arrivals corresponding to refracted waves (Pg, Pb, and Pn) and 2477 corresponding to reflections at the crust-mantle boundary (PmP) were manually picked in the 33 record sections that are shown in Annex A.1.2. The uncertainty for the different seismic phases, which corresponds to half a period of the dominant wavelength of the seismic source, was 40-50 ms for Pg and Pn, and 60 ms for PmP.

7.2 Results

The following section presents the main results obtained from modeling and processing of WAS, MCS, and gravity data corresponding to Line EF/MEDOC-4. As in Line GH/MEDOC-6, these results provide the velocity, tectonic, and density structure of the crust and uppermost mantle along the profile.

7.2.1 Velocity structure

The velocity model of profile EF (Figure 7.2a) shows the velocity structure of the crust and uppermost mantle together with the Moho geometry. As in the case of profile GH (Figure 6.2), the model displays marked lateral velocity variations in both sediments and basement, a strong vertical velocity gradient between these units, and a significant crustal thinning toward the central part of profile (Figure 7.2a). On the basis of these observations 5 domains are identified along 7 regions of the profile, these are 1a, 1b, 2a, 2b, 3, 4, and 5. Their location along the model corresponds to the distribution to the north of the five velocity domains described in Line GH (Figure 6.2).

Domain 1a (Figure 7.2a), corresponds to the island and continental margin of Sardinia. Crustal velocities beneath the island range between 6.0 and 6.5 km/s, similar to those obtained in Line GH under the island (Figure 6.2). The margin of Sardinia (OBS 36 to 40 in Figure 7.2a) has velocity contours outlining the 2.0-2.5 km-deep Sardinia basin, which displays velocities varying from 1.8 km/s at the top to ~3.5 km/s at the base. To the east, the basin is limited by the continental Baronie seamount (Figures 7.1 and 7.2a). The basement beneath the sedimentary layer of the Sardinia margin presents a steep velocity gradient (~0.5 s^{-1}) in its uppermost 2-3 km, and turns gentler below. Mid- and lower-crustal velocities range between 6.0 and 6.5 km/s (Figure 7.2a). In this domain the crust thins from ~20 km at 100 km of profile to ~10 km-thick at ~145 km (Figure 7.2a).

Domain 2a includes the northernmost part of Cornaglia Terrace, from ~145 km to 200 km along the profile (Figure 7.2a). As in Line GH, this domain has lower crustal velocities that range from 6.5 to 7.5 km/s, being ~10% higher than velocity in Domain 1a (Figure 7.2a). The crust under Cornaglia Terrace thins from ~11 to 8 km from 145 to ~170 km along profile, and remains fairly constant to the edge of Domain 2 (Figure 7.2a).

Eastward, Domain 1b has been named Sechi segment since it intersects the Sechi seamount. This domain extends from 200 to 270 km along the profile (Figure 7.2a) and presents a velocity distribution of the sedimentary layer and uppermost 2-3 km of the basement similar to Domain 2a (Figure 7.2a). However, mid- and lower-crustal velocities are lower, ranging between 5.5 km/s to 6.5 km/s, similar to Domain 1a of Sardinia margin (Figure 7.2a). The crust is 8-7 km-thick along the entire domain with an almost flat Moho geometry (Figure 7.2a).

Domain 2b has been named the Farfalla segment, which extends from km 280 to ~300 along the profile (Figure 7.2a). Here, lower crustal velocities sharply increase toward Vavilov basin (Figures 7.1 and 7.2a), reaching values that range between 6.5 to 7.5 km/s at a depth of ~2-3 km below the top of basement. In this domain, the crust thins from ~7 km to ~6 km (Figure 7.2a).

Domain 3 extends across the northernmost part of Vavilov basin (Figure 7.1 and 7.2a). As in Line GH, the basement in this region presents the steepest vertical velocity gradient of the tomographic model ($>0.8\ s^{-1}$) (Figure 7.2a). The lack of PmP reflections in the OBHs deployed in this short segment in the central part of the domain implies that the crust-mantle boundary is absent there or, at least, that it does not represent a sharp, first-order transition as is the case of the rest of the profile (Figure 7.2a).

To the East, Domain 4 includes the northernmost extension of Campania Terrace (Figure 7.1), and extends from km ~320 to ~350 along profile (Figure 7.1 and 7.2a). The crustal velocity distribution is similar to that of Domain 2b, with lower crustal velocities that decrease away from Vavilov basin (Figure 7.2a). The crustal thickness increases from ~6 km to 9 km in ~30 km of profile bounded by a well-defined Moho boundary(Figure 7.2a).

Finally, Domain 5 extends from km ~350 to the end of the profile along the Campania margin (Figure 7.2a). Here, mid- and lower-crustal velocities decrease compared to Domain 4, to 5.5-6.5 km/s (Figure 7.2a), and are similar to velocities of Domain 1a and 1b. The lack of land-stations and reversal shooting make the PmP ray-coverage limited under this domain, so that Moho is worse constrained than in the rest of domains (Figure 7.3). However, the progressive crustal thickening toward the continent, 10 to 14 km in less than 20 km, is well constrained (Figure 7.2a).

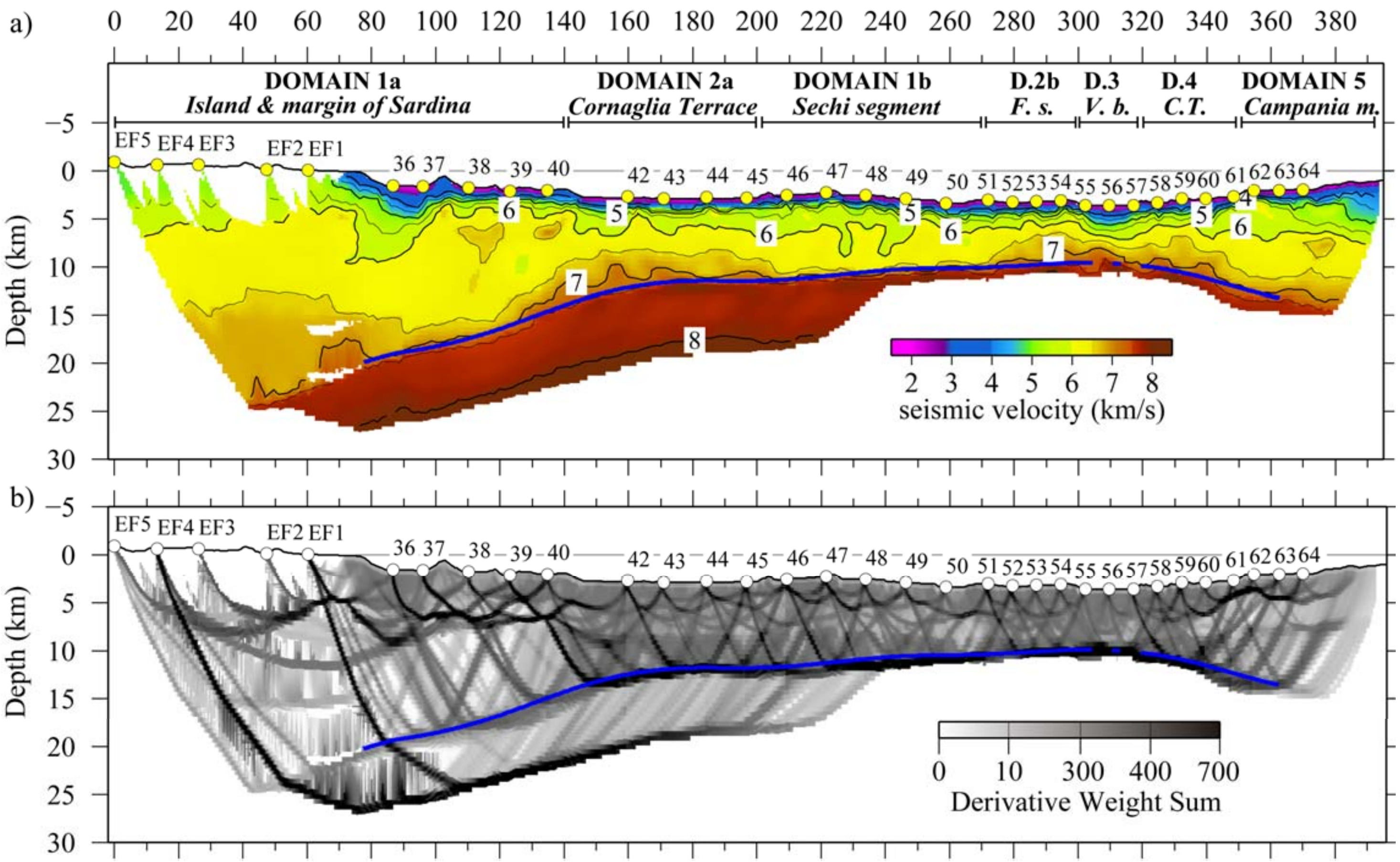

Figure 7.2.- *(a) Final 2D P-wave tomographic model of the crust, uppermost mantle and geometry of the Moho obtained from the inversion of Pg, Pn and PmP phases along Line EF. Yellow circles and blue line display the receiver location and the inverted Moho geometry, respectively. (b) Derivative Weight Sum (DWS) of tomographic model in (a).*

The uppermost mantle velocity structure is well-resolved up to ~6 km beneath the Moho reflector with good coverage of Pn phases (Figure 7.2b) in the western section of the model under domains 1a and 2a (Figure 7.2a). In contrast, the other domains have Pn phases diving less than ~1 km deep below the Moho into the mantle (Figure 7.2a). Mantle velocity ranges between 7.5 to 8.0 km/s, which is lower than the ~8.1-8.2 km/s typically associated to non-altered uppermost mantle peridotites [Christensen, 1978; Carlson and Miller, 2003].

7.2.1.1 Uncertainty analysis

The results of the statistical uncertainty analysis for the crustal velocity structure and the Moho geometry along Line EF are shown in Figure 7.3:

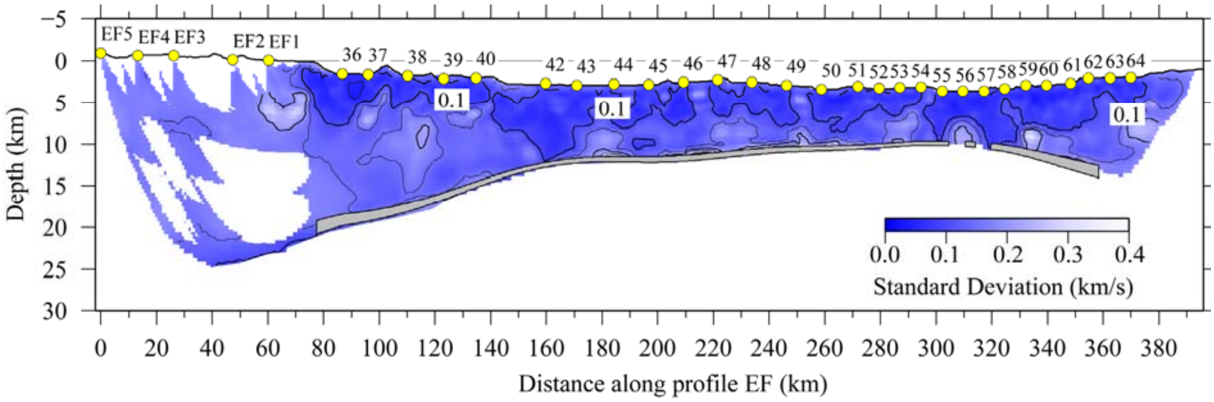

Figure 7.3.- *Final standard deviation values for the P-wave velocity values and the Moho geometry (grey band), as a result of the statistical uncertainty analysis. Contours lines are every 0.1 km/s. Note that in this analysis the mantle is not included. Details of the calculation are given in section 3.4.2 in chapter 3. Yellow circles display the location of the Land-stations, OBHs, and OBSs used in this profile.*

The P-wave velocity uncertainty is lower than ±0.1 km/s in the uppermost parts of the model, where the ray coverage of Pg phases is the best (Figure 7.3), and increases to ±0.2 km/s in regions where the ray coverage of Pg phases is poorer so crustal velocity is constrained based on PmP phases alone, for instance beneath the continent and the Sardinia margin (Figure 7.2b). Moho depth uncertainty ranges from ±0.25 km in regions well covered by both Pg and PmP phases (for example between OBH 45 and 54), and almost ±1 km in sections of the model poorly covered by PmP reflections (e.g. beneath the Campania margin) (Figure 7.2b), and in areas where Pg phases are lacking so crustal velocity structure is mainly controlled by PmPs, and hence the depth-velocity trade-off is larger (i.e. western part of the Sardinia margin in Figure 3c).

7.2.2 Tectonic structure

The post-stack time migrated profile MEDOC 4 (Figure 7.4) shows the sedimentary blanket, the tectonic fabric, and bright and continuous lower crustal reflectivity likely attributed to some form of lower crustal layering and Moho reflections. Following the same steps as in section 6.2.2, the velocity model and the PmP-inverted Moho reflector were converted to two-way time (TWT) and overlaid on the MCS image to compare the information of both data sets (Figure 7.5). It is worth noting the remarkable correlation between the WAS Moho reflector and the Moho reflections interpreted in the MCS profile (Figure 7.5).

The crust-mantle boundary is clearly observed in Domains 2a, 1b, 2b and 4 (Figures 7.4 and 7.5). In Domain 2a and 1b (i.e. under Cornaglia Terrace and Sechi segment), laterally continuous packages of reflections are observed between 7.0-7.5 s TWT, likely indicating the Moho location at their base (Figure 7.4). The PmP-inverted Moho reflector coincides rather well with this reflectivity along both domains except between CMP 25000 and 26500, where the reflectivity package appears to be slightly deeper than the inverted Moho in the velocity model (Figure 7.4 and 7.5). This misfit between both reflectors is similar to that observed in the comparison of WAS-Line GH and the MCS profile MEDOC-6 (see Figure 6.4 and 6.6). As explained in section 6.2.2, it can be attributed to velocity anisotropy between vertical and sub-horizontal propagation [Sallarès et al., 2013b], or, alternatively, it can indicate that the band of reflectivity in MCS image occurs in the uppermost mantle and that the crust-mantle boundary is located at its top, thus coinciding with the location of the Moho in the velocity model. In Domain 2b (i.e. Farfalla segment), less clear lower crustal reflections shoal from 7.0 to ~6.5 s TWT (Figures 7.4 and 7.5). Similarly to Domain 1b, there is a slight mismatch with respect to the location of the inverted Moho between CMP 34500 and 35000 (Figures 7.4 and 7.5). Domain 4 presents a package of strong reflectivity between CMP 40000 and 42000, being again slightly deeper than the Moho obtained by the inversion of PmP (Figures 7.4 and 7.5). In contrast with all previously discussed domains, lower crustal reflections in Domains 1a and 5 are masked by the remaining energy of the water-layer multiple, and therefore it is difficult to discern the location of the Moho reflections (Figure 7.4). In Domain 3, there are not clear lower crustal reflections that could be associated with the crust-mantle boundary (Figures 7.4 and 7.5).

Concerning the tectonic structure, Domain 1a (Figure 7.4) presents at its westernmost part a large tilted fault-block that includes the half-graben of the Sardinia basin. The major fault that controls this basin appears to be deeply rooted into the basement dipping to the west (Figure 7.4). Additionally, other minor westward and eastward dipping normal faults cut the strata of the basin, which presents an important sedimentary infill of >2 s TWT with ~ 1.5 s TWT of syn-tectonic sequence (Figure 7.4). To the east, the horst of the continental Baronie seamount [Colantoni et al., 1981; Sartori et al., 2004] (Figure 7.4) is bounded by two major normal faults and affected by minor faulting at its top (Figure 7.4). The rest of Domain 1a (from 35 km to ~70 km in Figure 7.4), is represented by 3 tilted fault-blocks that bound 3 half-grabens. The sedimentary infill, which is ≤1 s TWT-thick, display a number of major, east-dipping faults. The morpho-tectonic features of this region, which are displayed in the bathymetry (Figure 7.1), suggest that these structures together with the Baronie seamount are related to a major continental block that have collapsed during extension.

The transition between Domain 1a and 2b appears to happen with no significant structural changes (Figure 7.4). The tectonic structure of Domain 2a in the Cornaglia Terrace is totally different from that of Domain 1a. Beneath the sedimentary blanket, which is ≤1s TWT-thick, the top of the basement is affected by some minor faulting, but overall it appears to be fairly uniform laterally (Figure 7.4). Some sub-horizontal intra-crustal reflectors (between CMP 13000-16000 in Figure 7.4) are observed across this 8-10 km-thick crustal domain (Figure 7.2a and 7.4).

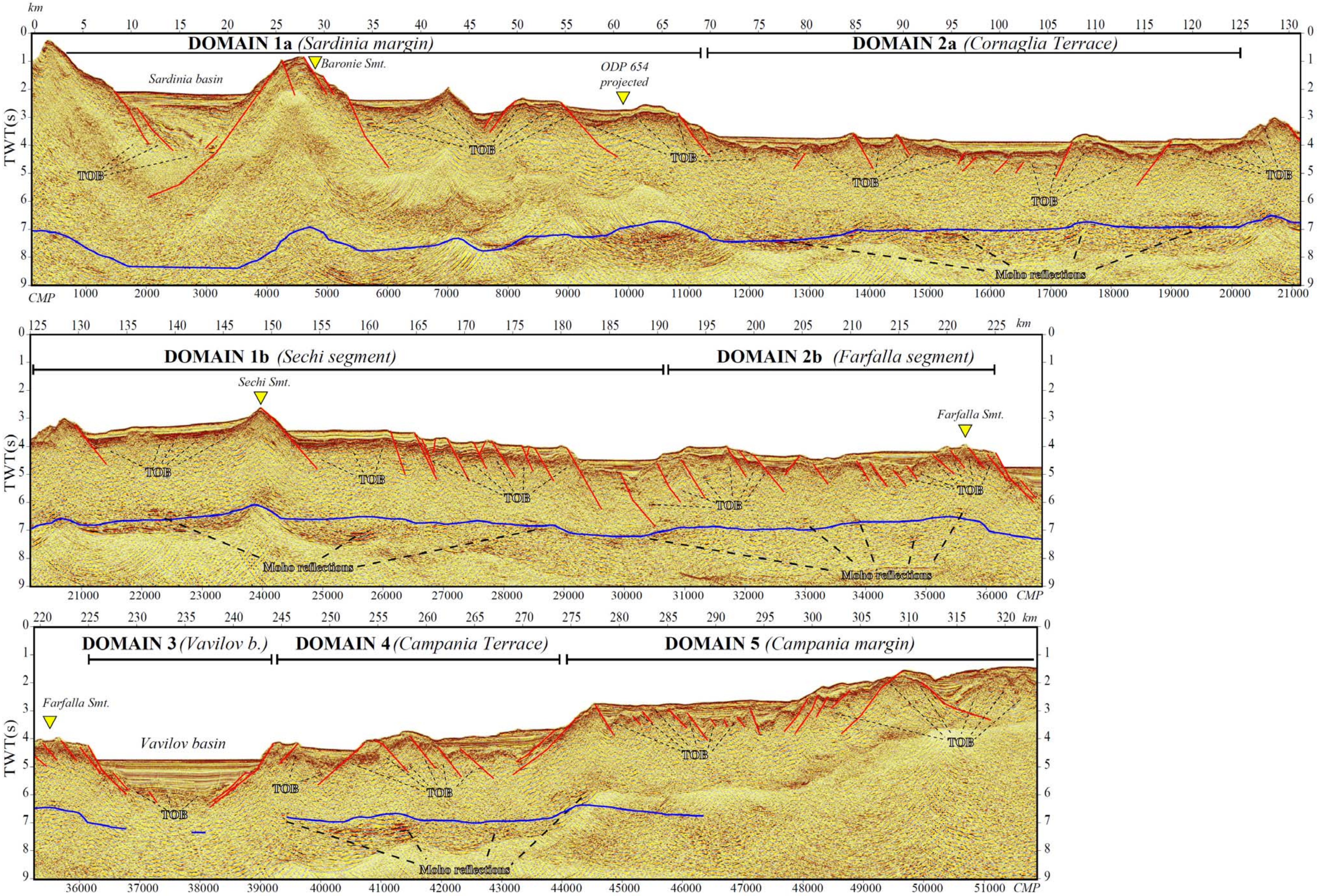
km
TWT(s)
CMP
DOMAIN 1a (Sardinia margin)
DOMAIN 2a (Cornaglia Terrace)
Sardinia basin
Baronie Smt.
ODP 654 projected
TOB
Moho reflections
DOMAIN 1b (Sechi segment)
DOMAIN 2b (Farfalla segment)
Sechi Smt.
Farfalla Smt.
DOMAIN 3 (Vavilov b.)
DOMAIN 4 (Campania Terrace)
DOMAIN 5 (Campania margin)
Vavilov basin

Figure 7.4.- *Post-stack time migration image of profile MEDOC-4 overlaid with the tectonic interpretation (red lines). Blue line represents the PmP-inverted Moho geometry. As in Figure 7.1, inverted triangles are colored according to the nature of basement inferred from seabed rock sampling (see legend in Figure 1) [Colantoni et al., 1981; Kastens and Mascle, 1990]. TOB: Top of basement.*

The tectonic structure of Domain 1b (i.e. Sechi segment) varies significantly from West to East. The western sector (from 125 to 155 km along profile in Figure 7.4) is mainly characterized by two structural highs bounded to the east by two major normal faults and a small basin with a ~1 s TWT-thick sedimentary infill between them. The Sechi seamount (Figure 7.1), which is known to be continental in nature [Colantoni et al., 1981], corresponds to the easternmost structural high of this domain (from 155 to 190 km in Figure 7.4). Eastward, the domain is affected by pervasive eastward-dipping normal faulting. The variations in the tectonic setting are also reflected in crustal thickness variations. The crust is thicker beneath the Sechi seamount (8-9 km) and thinner in the eastern sector (~7 km) (Figure 7.2a and 7.4). The transition between Domains 1b and 2b occurs rather sharply at 185-190 km along the profile (Figure 7.4), where some sub-vertical lower crustal reflections appear to reach the crust-mantle boundary (CMP 30000-31000 in Figure 7.4).

Domain 2b runs across the so-called Farfalla segment and, as in the eastern part of Domain 1b (the Sechi segment), normal faulting appears to cut deep into crust, indicating that a significant tectonic activity took place during its formation (Figure 7.4). The most representative structure of this domain is the tilted continental fault-block of the Farfalla seamount (Figure 7.1) [Colantoni et al., 1981], which is located at the easternmost region. Crustal thickness decreases from ~7 km to 6 km thick along this domain (Figure 7.2a).

The Vavilov basin in Domain 3 is filled by a ~1.5 s TWT-thick sequence of sediments and is bounded at either side by major faults. The strata is horizontally continuous without significant faulting, however, as in profile MEDOC-6 (Figure 6.4), the uppermost parts of the basement appear to be locally affected by minor faulting (Figure 7.4).

Domain 4 includes the northern segment of the Campania Terrace (from 250 to 280 km along profile in Figure 7.4). This domain presents similarities with Domain 2b (i.e Farfalla segment) concerning the tectonic structure. However, the package of reflectivity attributed to the crust-mantle boundary is thicker in this domain (Figure 7.4). Transition between Domains 4 and 5 is characterized by a significant thickening of the crust toward the continent, which is expressed at the surface by a bathymetric shoaling (Figures 7.1 and 7.4). The tectonic and bathymetric structure of Domain 5 displays differences from west to east. The western region of this domain (from 280 km to 305 km in Figure 7.4) presents a fairly flat topography and a pervasive minor normal faulting, whereas the eastern region (from ~305 km to the end of profile in Figure 7.4) presents a bathymetric shoaling and several major faults that appear to cut deep into the crust (Figure 7.4).

.

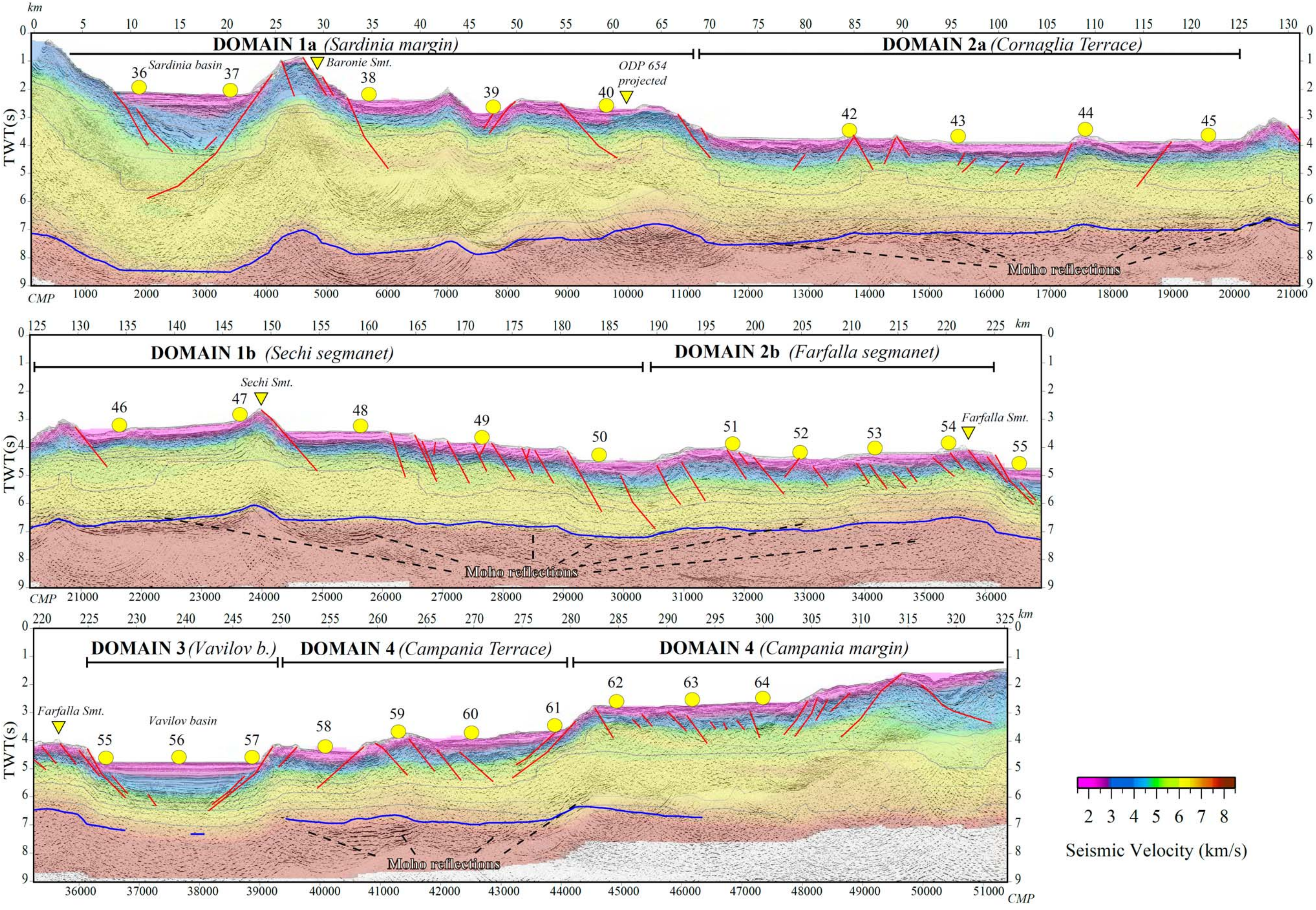
km
TWT(s)
CMP
DOMAIN 1a (Sardinia margin)
DOMAIN 2a (Cornaglia Terrace)
Sardinia basin
Baronie Smt.
ODP 654 projected
36
37
38
39
40
42
43
44
45
Moho reflections
DOMAIN 1b (Sechi segmanet)
DOMAIN 2b (Farfalla segmanet)
Sechi Smt.
Farfalla Smt.
46
47
48
49
50
51
52
53
54
55
Moho reflections
DOMAIN 3 (Vavilov b.)
DOMAIN 4 (Campania Terrace)
DOMAIN 4 (Campania margin)
Farfalla Smt.
Vavilov basin
55
56
57
58
59
60
61
62
63
64
Moho reflections
2 3 4 5 6 7 8
Seismic Velocity (km/s)

Figure 7.5.- *MCS image of profile MEDOC-4 overlaid with the P-wave velocity model shown in Figure 7.2a converted to TWT. Yellow circles and blue line represent the OBS/H location and geometry of the PmP-inverted Moho, respectively. Colored triangles are the same used in Figure 4 to indicate the continental nature of the basement [Colantoni et al., 1981; Kastens and Mascle, 1990].*

7.2.3 Automatized interpretation of the basement affinity based on P-wave depth-velocity profiles

In this section I have used the same approach as in Line GH to automatically classify the petrological affinity of the basement based on the vertical velocity structure of the model along line EF (Figure 7.2a). The approach is described in section 6.2.3 in chapter 6.

The results obtained using this technique as well as those obtained in the conventional velocity analysis have allowed to define the possible petrological affinity of the different domains described in previous sections (Figures 7.6 and 7.7). The affinity that best explains the velocity-depth structure in Domains 1a, 1b and 5 (Figures 7.6 and 7.7) is that of continental crust [Christensen and Mooney, 1995]; whereas Domains 2a, 2b, 3, and 4 agree better with the velocity-depth profile representative of oceanic crust (Figures 7.6 and 7.7) [White et al., 1992]. However, it must be noted, as in Line GH, that the lower crustal velocities in these domains, especially under the Cornaglia Terrace (Domain 2a in Figure 7.2a, 7.6 and 7.7), are lower than those expected in a young (0-7 Ma) oceanic crust [White et al., 1992] (Figure 7.6). In Domain 3, in the northernmost tip of the Vavilov basin (Figures 7.1 and 7.2a) the velocity profiles are also consistent with oceanic crust, although some of them display stronger velocity gradients characteristic of exhumed mantle (Figure 7.6) [Dean et al., 2000; Sallarès et al., 2013a]. This observation is less clear and more confined to a limited region (i.e., between OBH 55and 56 in Figures 7.2a and 7.7) than in the case of the Line GH, where most of the basement beneath the Vavilov basin has been classified as exhumed mantle based on the velocity-depth profiles (see Figure 6.8).

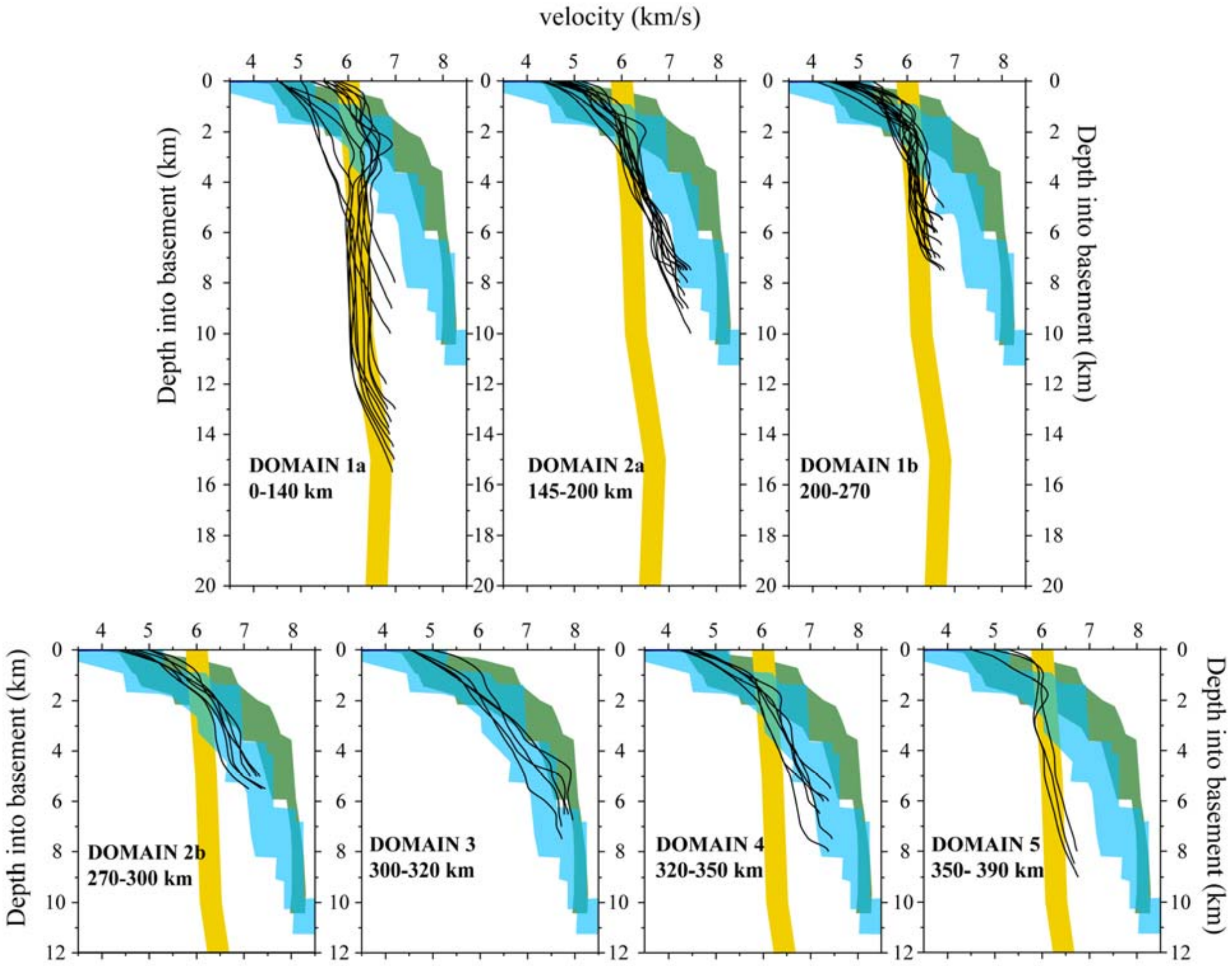

Figure 7.6.- *1D P-wave velocity-depth profiles corresponding to the seven regions identified in the tomographic model (Figure 7.2a) (black lines). 1D velocity-depth reference profiles include the 20 km-thick continental crust from Christensen and Mooney [1995] (orange band), 0-7 Ma Atlantic oceanic crust from White et al. [1992] (blue band), and a exhumed mantle compilation made from Dean et al. [2000] and Sallarès et al. [2013a], both works focused on the western Iberia margin (green band).*

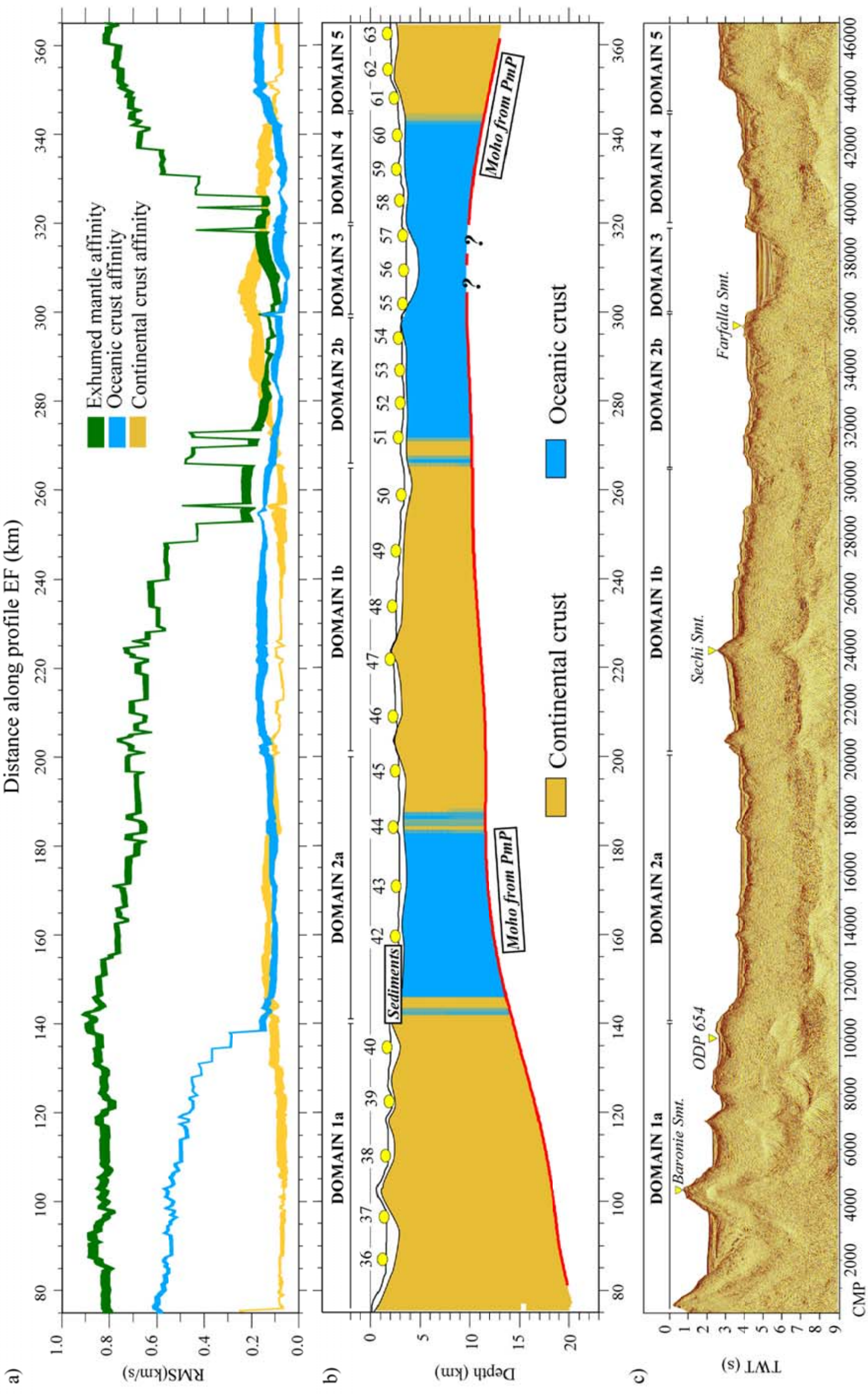
a)
b)
c)
Distance along profile EF (km)
80
100
120
140
160
180
200
220
240
260
280
300
320
340
360
RMS(km/s)
1.0
0.8
0.6
0.4
0.2
0.0
Exhumed mantle affinity
Oceanic crust affinity
Continental crust affinity
Depth (km)
0
5
10
15
20
DOMAIN 1a
DOMAIN 2a
DOMAIN 1b
DOMAIN 2b
DOMAIN 3
DOMAIN 4
DOMAIN 5
36
37
38
39
40
42
43
44
45
46
47
48
49
50
51
52
53
54
55
56
57
58
59
60
61
62
63
Sediments
Moho from PmP
Moho from PmP
?
?
Continental crust
Oceanic crust
TWT (s)
0
1
2
3
4
5
6
7
8
9
Baronie Smt.
ODP 654
Sechi Smt.
Farfalla Smt.
CMP
2000
4000
6000
8000
10000
12000
14000
16000
18000
20000
22000
24000
26000
28000
30000
32000
34000
36000
38000
40000
42000
44000
46000

Figure 7.7.- *(a) Final result corresponding to the same automatic classification of the basement affinity used section 6.2.3. RMS velocity values are obtained from the comparison of the basement vertical velocity structure of the tomographic model (Figure 7.2a)* **-***1-D profiles are extracted from 5-km-wide average of the velocity model***-** *with references of continental crust (orange band) [Christensen and Mooney, 1995], oceanic crust (blue band) [White et al., 1992], and exhumed mantle (green band) [Sallarès et al., 2013a]. (b) Resulting basement affinity model corresponding to the automatic classification shown in (a). Yellow Circles correspond to the OBS/H location. (c) MCS post-stack time migrated image of profile MEDOC 4 with the same colored triangles shown in Figures 7.1, 7.4 and 7.5 [Colantoni et al., 1981; Kastens and Mascle, 1990]. Vertical scale is exaggerated.*

7.2.4 Density structure

As in Line GH, in order to verify the results of the automatic basement affinity classification (Figure 7.7), I converted the velocity model into densities using Vp-ρ relationships according to the inferred compositions (Figure 7.7) and I checked the fit between the calculated gravity response and the observed one (Figure 7.8). The relationships used for sediments, continental and oceanic crustal rocks, and exhumed mantle rocks are those already presented in section 4.3 and used to perform the density modeling in section 6.2.4.

The fit using these relationships is rather good overall but presents a significant misfit that is concentrated in Domain 2. Similarly to what is observed in the same area along Line GH, the calculated anomaly in this domain is 10-15 mGal higher than the observed one, so the density should be reduced by 2 % to match well the observed gravity anomaly (Figure 7.8b). With this correction, the RMS misfit between the observed and calculated anomalies is only of 6.9 mGal (Figure 7.8b). Additionally, it is important to note that using Carlson and Miller's [2003] Vp-ρ relationship for partially serpentinized peridotites in Domain 3 (i.e. Vavilov basin) instead of Carlson and Herrick's [1990] conversion law for oceanic basalts and gabbros the results are rather similar.

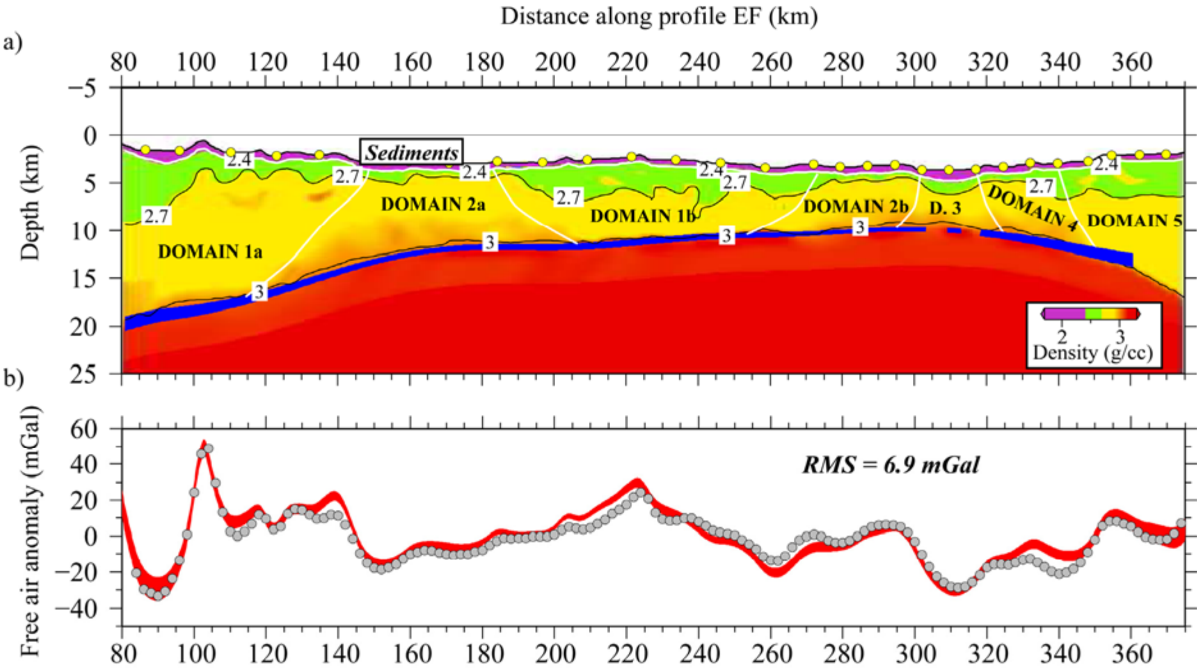

Figure 7.8.- *(a) Velocity-derived density model obtained using Christensen and Mooney's [1995] Vp-ρ relationship for continental rocks in Domains 1a, 1b, and 5, and Carlson and Herrick's [1990] conversion law for oceanic crustal rocks in Domains 2a, 2b., 3, and 4. Hamilton's [1978] Vp–ρ relationship for sediments was used for the sedimentary layer. Densities in Domain 2a were decreased by 2% to fit the observed gravity anomaly. Blue band represents the uncertainty values of the inverted Moho geometry. (b) Observed (grey circles) and calculated (red band) free-air gravity anomaly corresponding to the velocity-derived density model shown in (a).*

7.3 Characterization of geological domains along Line EF/MEDOC-4

This section integrates all the results provided by the WAS-derived model, the MCS profile and the gravity modeling to discuss the nature and spatial distribution of the different geological domains identified along LineEF/MEDOC-4 (Figure 7.2a).

7.3.1 Continental crust in the Sardinia and Campania margins and the Sechi segment (Domains 1a, 1b and 5)

As in Line GH, the continental affinity of Domain 1a is supported by basement samples in Sardinia [e.g. Cherchi and Montadert, 1982], and on top of the Baronie Seamount (Figure 7.1) [Colantoni et al., 1981; Mascle and Rehault, 1990; Sartori et al., 2004]. In addition, pre-Tortonian reddish conglomerates were drilled in ODP site 654, in the last unit of the hole (Figure 7.1) [unit VI of site 654 in Shipboard Scientific Party, 1987], indicating that they were most likely deposited in a continental environment [Shipboard Scientific Party, 1987]. Crustal thickness beneath Sardinia has been inferred from gravity modeling at ~25 km-deep, being in agreement with what is estimated in Line GH and also with results from active and passive seismic tomographic models in the area [Di Stefano et al., 2011; Moeller et al., 2013]. In the western edge of Domain 1, beneath the Sardinia margin (at 140 km in Figure 7.2a), crustal thickness has decreased to ~10 km thick, implying a stretching factor (β) of ~2.5.

In Domain 1b, the Sechi segment, crustal thickness is fairly constant (~8 km) resulting in a high stretching factor (β >3) (Figure 7.2a). The continental affinity determined by the gravity and velocity analyses is supported by dredging samples of calcareous phyllites and calcschists on top of the Sechi seamount [Colantoni et al., 1981] (Figures 7.1 and 7.4). These samples are lithologically alike to those sampled on top of the continental De Marchi seamount (Figure 7.1) [Colantoni et al., 1981; Mascle and Rehault, 1990; Sartori 1990]. These observations, together with those made from the tectonic structure (Figure 7.4) support the interpretation that the Sechi segment corresponds to a highly stretched continental crust.

As in Line GH (see section 6.3.1), the conjugated Campania margin (Domain 5 in Figures 7.2a and 7.4) is interpreted as the westernmost extension of the Italian continent. Crustal thickness of this domain has been also inferred from gravity modeling, increasing from 7.5 km to ~15 km-thick ~25 km landward (Figure 7.8).

7.3.2. Magmatic back-arc crust in the Cornaglia and Campania Terraces (Domain 2a and 4), and in the Farfalla segment (Domain 2b)

As in the southern Line GH, the Cornaglia Terrace (Domain 2a) in Line EF presents a velocity structure that is close to that of young oceanic crust [White et al., 1992] (Figures 7.6 and 7.7), but with a crustal velocity gradient in Layer 3 twice weaker than the gradient of a typical oceanic crust (Figure 7.6) [White et al., 1992]. In addition, results from the gravity modeling suggest that there is a difference in the petrological composition with respect to "normal" mid-ocean ridge oceanic crust (Figure 7.8), similarly to what has been obtained in Line GH (see section 6.3.2). Therefore, following the same arguments presented in section 6.3.2, this domain is interpreted as formed by back-arc rift and/or spreading near the volcanic arc, so that it would be significantly influenced during its formation by subduction-related magmatism [Martinez et al., 2007; Dunn and Martinez, 2011].

In the Farfalla segment (Domain 2b) and in the conjugated Campania Terrace (Domain 4) (Figure 7.2a) mid and lower crustal velocities increase toward the Vavilov basin (Domain 3). The velocity analysis has determined that both domains present a crustal velocity structure that resembles to that of oceanic crust [White et al., 1992] (Figures 7.6 and 7.7). However, drillings on top of the Farfalla seamount in Domain 2.2 have found Carboniferous phyllites [Colantoni et al., 1981] indicating continental affinity. In contrast, lower crustal velocities beneath this seamount and just above the Moho are >7.0 km/s, considerably larger for lower continental crust velocities, typically found at 6.5-6.8 km/s (Figure 7.2a and 7.6) [Christensen and Mooney, 1995].

A similar seismic structure and crustal thickness is observed at the transition between the continental crust of the Sardinia margin and the magmatic crust of the Cornaglia Terrace in both Line EF (Figure 7.2a) and GH (Figure 6.2a). These similarities may suggest that both domains correspond to a highly stretched continental crust that has been progressively affected by underplating of igneous rocks as they were extended. The existence of volcanoclastic rocks in the region could support this hypothesis (Figure 7.1) [Colantoni et al., 1981]. Alternatively, high velocities of the lower crust might also correspond to mantle material serpentinized by fluid flow through faults in the crust. In this case, the PmP reflections observed in the OBH records would correspond to the base of the serpentinization front. This has been proposed in the Liguro-Provençal basin [e.g., Pascal et al., 1993; Chamot-Rooke et al., 1999; Gailler et al., 2009], and in the Iberian and Canadian margins [Dean et al., 2000; Funk et al., 2004] to explain similar high velocities beneath the stretched continental crust.

In any case, the lack of petrological information in both domains makes difficult the confirmation of these hypotheses.

7.3.3. Possible presence of exhumed mantle rocks at the northernmost Vavilov basin (Domain 3)

In contrast with results obtained in Line GH (Figure 6.8), the nature of the northern Vavilov basins seems to be less clear. Although the velocity structure seems to fit better with an oceanic-like gradient (Figure 7.6 and 7.7), the density modeling has shown that the gravity fit is rather similar whether using the oceanic crust conversion law of Carlson and Herrick [1990] or that for serpentinized mantle rocks of Carlson and Miller [2003].

The presence of oceanic crust beneath this region of the Vavilov basin is unlikely; since no Moho reflections are evidenced in the MCS profile nor in most of the WAS records (Figures 7.4, 7.5, and A.1.2.25). Only few reflections have been evidenced in OBH 57 (Figure A.1.2.26 in the Annex) and might also correspond to another type of contrast, like the base of a serpentinization front, for instance.

Therefore, assuming that the Vavilov basin has been the locus of mantle rocks exhumation (Figure 6.7 and 6.8), and that this exhumation has been accompanied by large basaltic intrusions, as evidenced by Figure 6.10 and samples from the ODP site 655 and 651 (Figure 7.1) [Beccaluva et al., 1990]; the lower velocity gradient of this region might be caused by the influence of basaltic sills or dikes in the exhumed mantle basement. Nevertheless, this hypothesis needs to be confirmed with further petrological and geophysical information.

Chapter 8: Geological domains of the Central Tyrrhenian: Geodynamic implications

8.1 Distribution of the geological domains in the Central Tyrrhenian basin

In this section I discuss the distribution of the geological domains in the central Tyrrhenian basin based on the results obtained in Line GH (chapter 6) and Line EF (Chapter 7) (Figure 8.1).

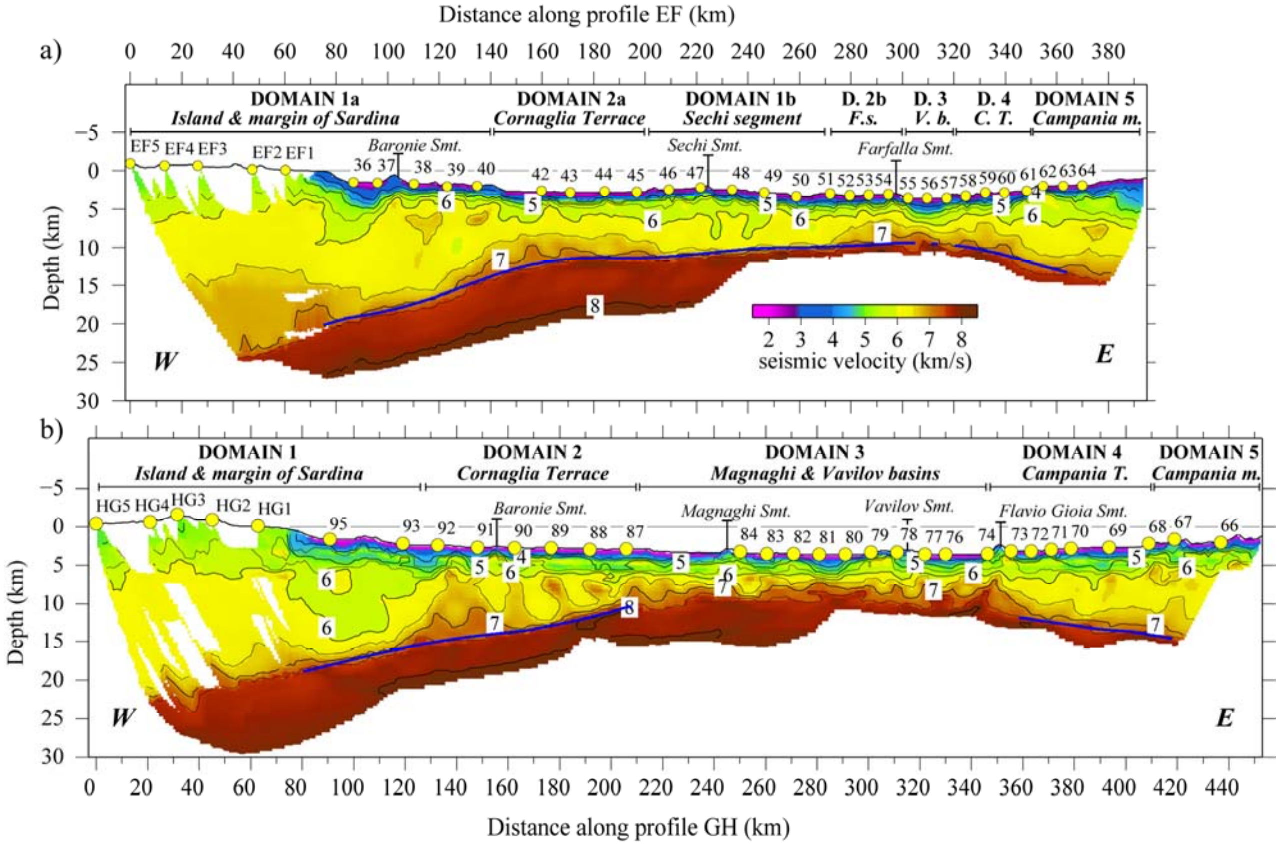

Figure 8.1.- *P-wave velocity models of Lines EF (a) and GH (b). Yellow circles display location of land-stations, and OBS/H along both profiles. Blue lines represent the PmP-inverted Moho geometry.*

The goal is to integrate all available data to spatially define the distribution of continental crust, magmatic back-arc oceanic crust, and exhumed mantle in the study region. The geophysical models and seismic images have been combined with rock sampling information and seafloor morphology (Figure 7.1), to interpret the spatial configuration of the Central Tyrrhenian domain (see Figure 8.5).

8.1.1 Continental crust

As indicated in the previous two chapters, continental crust in the Central Tyrrhenian basin is identified in Domains 1 and 5 in both lines (Figures 8.1).

Domain 1 in both profiles includes the Island and the upper margin of Sardinia, and the region defined as the Sechi segment (Domain 1b) (Figures 8.1). In the Sardinia Margin (Domain 1 and 1a), lateral changes in crustal thickness are similar in both profiles displaying a thinning of the crust from ~20 km-thick beneath the coast line to 14-13 km-thick under the eastern limit of the continental margin (Figure 8.2).

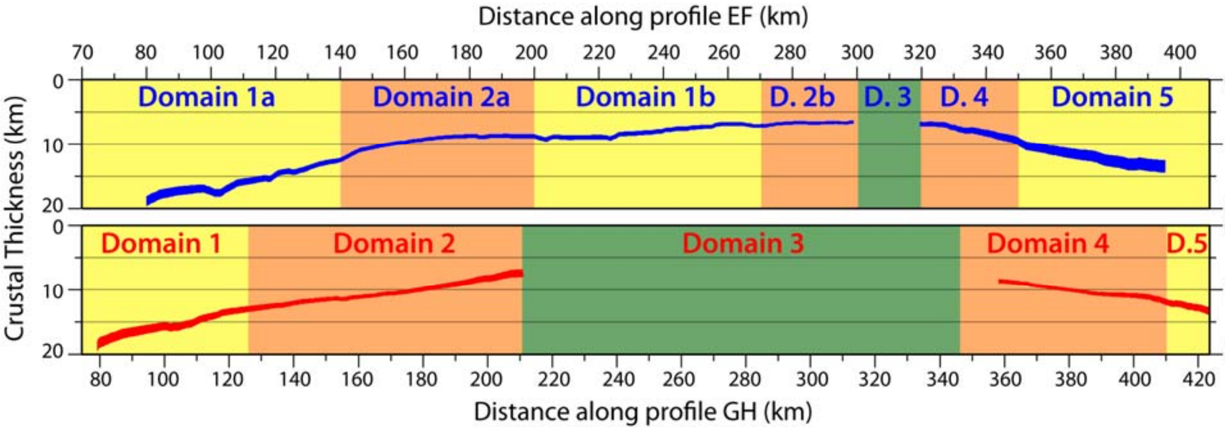

Figure 8.2.- *Crustal thickness along Line EF (blue) and GH (red) inferred from the PmP-inverted Moho.*

In contrast, the crustal velocity structure beneath the Sardinia margin presents some differences from north (Domain 1a) to south (Domain 1). Along Line EF crustal velocities (~6.0-6.3 km/s) are slightly higher than in profile GH (~5.8-6.0 km/s) (Figures 8.1 and 8.3a). This may be explained by lithological changes [Christensen and Mooney, 1995]. This hypothesis is supported by the wide variety of lithologies (e.g. basaltic, granitic, and metamorphic) found by dredging in the Sardinia margin [Colantoni et al., 1981].

The Sechi segment in Line EF (Domain 1b) is interpreted as a stretched portion of continental crust (β > 3) (Figures 7.7, 8.2a, and 8.4). The tectonic structure interpreted from the bathymetric map supports that this domain is formed by a 30-40 km long southward extension of the same continental crust defined further north [Moeller et al., 2013] (Figure 8.5).

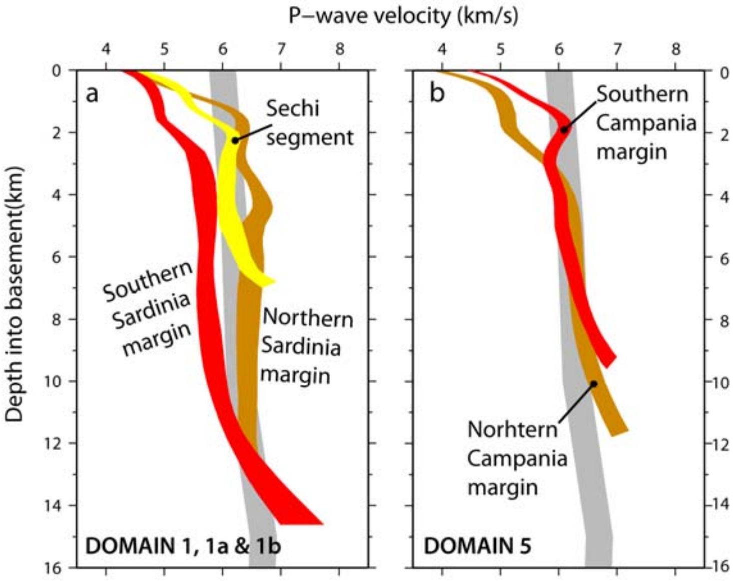

Figure 8.3.- *1D P-wave velocity-depth profiles corresponding to (a) domains 1, 1a, 1b, and (b) domain 5. Grey band represents the 1D velocity-depth reference for a 20 km-thick continental crust from Christensen and Mooney [1995].*

The Campania margin (Domain 5) is mapped by both WAS lines (Figures 8.1, 8.3, 8.4, and 8.5) and interpreted as the westernmost extension of the Italian continent (Figure 8.5). The short segments mapped with WAS and gravity data indicate no important variations in crustal thickness or crustal velocity structure from north to south along the margin (Figures 8.2 and 8.3b).

The basement of the northern Tyrrhenian basin has been poorly sampled, but the available information indicates a continental affinity (Figure 8.5) [Colantoni et al., 1981]. In agreement, WAS tomographic models reveal the presence of continental crust likely affected by possibly minor magmatism [Moeller et al., 2013]. Hence, the continental crust domains mapped with the WAS lines have been extended in Figure 8.5 toward the Northern Tyrrhenian region.

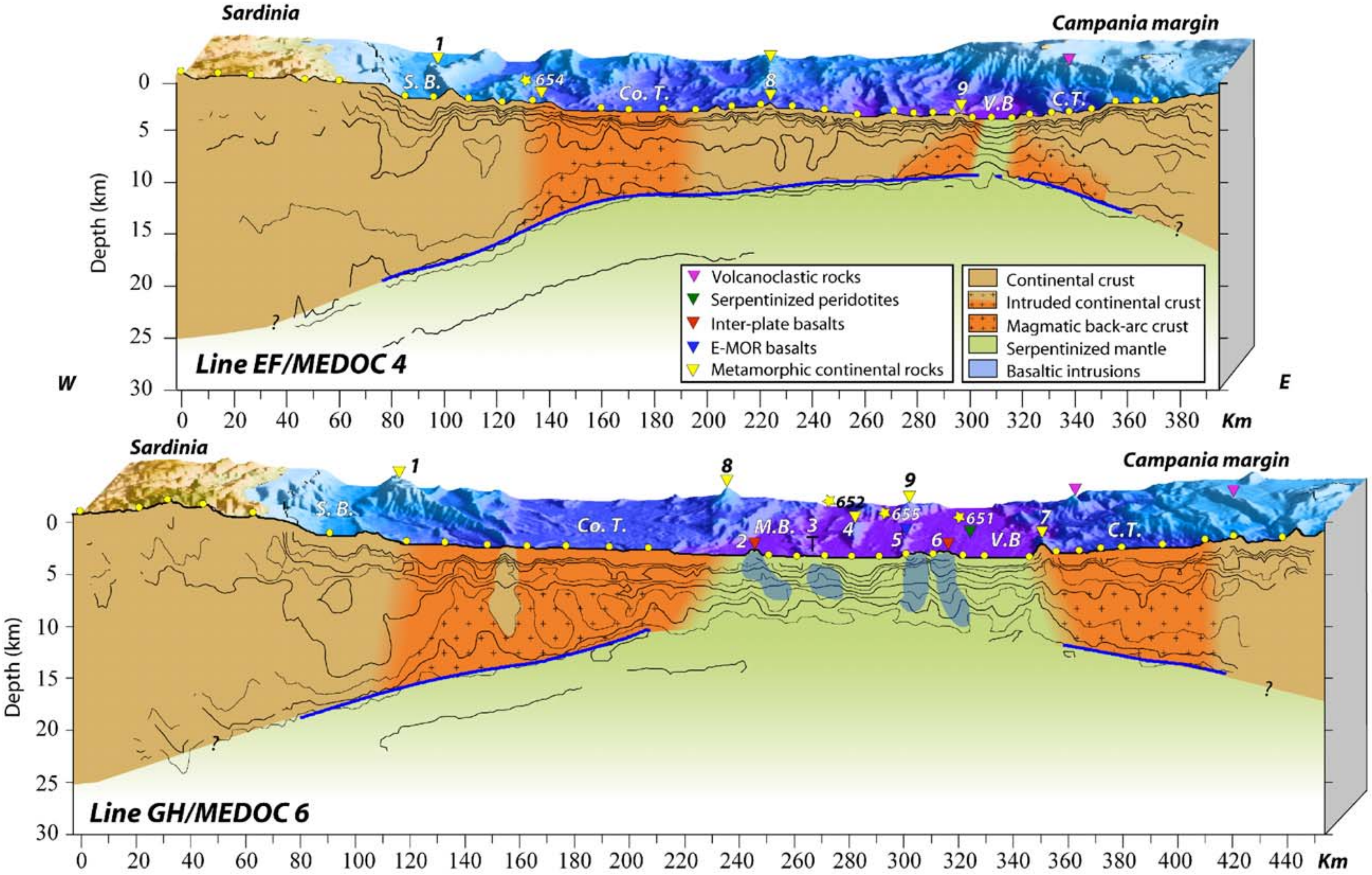
Sardinia
Campania margin
1
654
S. B.
Co. T.
8
9
V.B
C.T.
Depth (km)
0
5
10
15
20
25
30
W
E
Line EF/MEDOC 4
?
▼ Volcanoclastic rocks
▼ Serpentinized peridotites
▼ Inter-plate basalts
▼ E-MOR basalts
▼ Metamorphic continental rocks
Continental crust
Intruded continental crust
Magmatic back-arc crust
Serpentinized mantle
Basaltic intrusions
0 20 40 60 80 100 120 140 160 180 200 220 240 260 280 300 320 340 360 380 Km
Sardinia
Campania margin
1
S. B.
Co. T.
8
9
652
655
651
M.B.
2
3
4
5
6
7
V.B
C.T.
Depth (km)
0
5
10
15
20
25
30
Line GH/MEDOC 6
?
0 20 40 60 80 100 120 140 160 180 200 220 240 260 280 300 320 340 360 380 400 420 440 Km

Figure 8.4.- *Interpretative cross sections of tomographic models EF (a) and GH (b) correlated with the bathymetry of the Central Tyrrhenian basin. Yellow circles and blue lines correspond to receiver location and geometry of the Moho, respectively. C.T.: Campania Terrace, Co.T.: Cornaglia Terrace, M.B.: Magnaghi Basin, S.B.: Sardinia Basin, V.B.: Vavilov Basin, 1: Baronie seamount, 2: Magnaghi seamount, 3: D'Ancona Ridge, 4: De Marchi seamount, 5: Gortani Ridge, 6: Vavilov seamount, 7: Flavio de Gioia, 8: Sechi seamount, 9: Farfalla seamount*

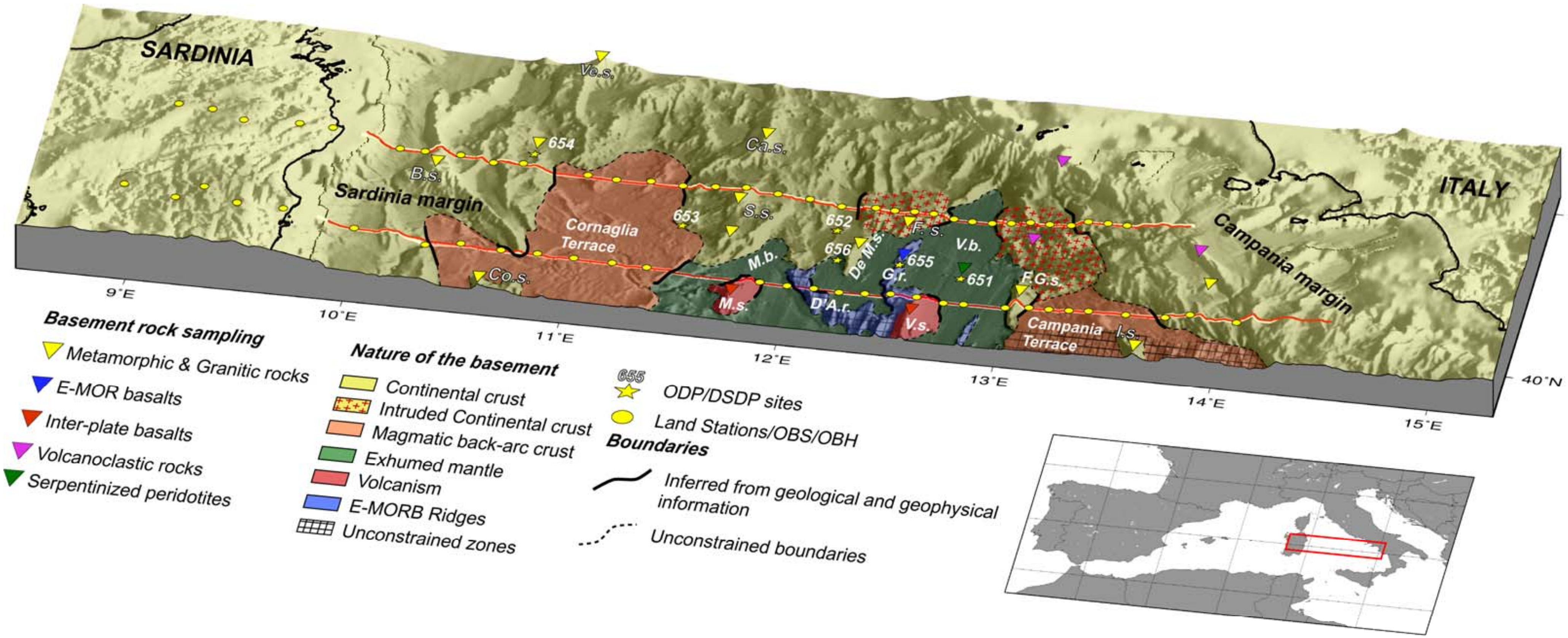
SARDINIA
ITALY
Sardinia margin
Campania margin
Cornaglia Terrace
Campania Terrace
Ve.s.
Ca.s.
B.s.
S.s.
Co.s.
654
653
652
656
655
651
De M.s.
F. s.
V.b.
M.b.
G.r.
F.G.s.
M.s.
D'A.r.
V.s.
I.s.
9°E
10°E
11°E
12°E
13°E
14°E
15°E
41°N
40°N
Basement rock sampling
Metamorphic & Granitic rocks
E-MOR basalts
Inter-plate basalts
Volcanoclastic rocks
Serpentinized peridotites
Nature of the basement
Continental crust
Intruded Continental crust
Magmatic back-arc crust
Exhumed mantle
Volcanism
E-MORB Ridges
Unconstrained zones
ODP/DSDP sites
Land Stations/OBS/OBH
Boundaries
Inferred from geological and geophysical information
Unconstrained boundaries

Figure 8.5.- *Bathymetric and topographic map of the Central Tyrrhenian region shown in Figure 7.1, displaying the plan view distribution of the main basement domains. The interpretation of this map is based on geophysical information of both WAS (red line) and MCS (white line) transects (white and red lines), rock sampling [Colantoni et al., 1981; Kastens and Mascle, 1990], and from geomorphological observations. B.s.: Baronie Seamount, Ca.s.: Cassini seamount, Co.s.: Cornaglia Seamount, D'A.r.: D'Ancona Ridge, De M. s.: De Marchi Seamount, F.s.: Farfalla Seamount, F.G.s.: Flavio Gioia Seamount, G.r.: Gortani Ridge, I.s: Isel seamount, M.s.: Magnaghi Seamount, M.b.: Magnaghi Basin, S.s.: Sechi Seamount, Ve: Vercelli seamount, V.b.: Vavilov Basin, V.s.: Vavilov Seamount.*

8.1.2 Magmatic back-arc crust

Anomalous magmatic-type crust with a 2 layer structure that departs from typical oceanic crust has been identified in Domains 2 and 4 in both lines (Figures 8.1, 8.4, and 8.5).

Domain 2 extends along the Cornaglia Terrace from south (Domain 2) to north (Domain 2a) (Figures 8.1, 8.4, 8.5, and 8.6a) showing variability in tectonic and velocity structure of the crust.

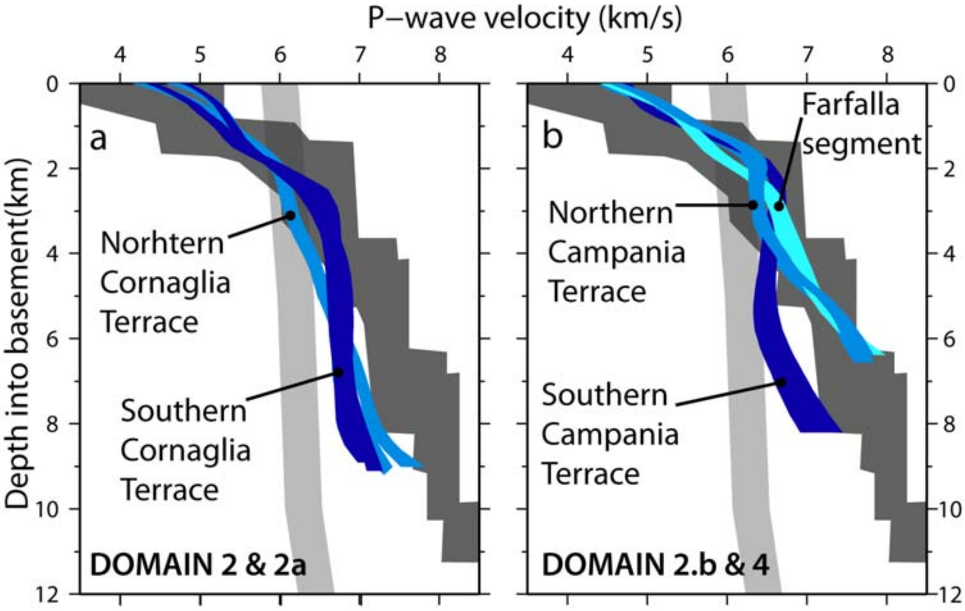

Figure 8.6.- *1D P-wave velocity-depth profiles corresponding to (a) Domain 2, 2a ,and (b) Domains 2b and 4. Light grey band represents the 1D velocity-depth reference for a 20 km-thick continental crust from Christensen and Mooney [1995], whereas the dark grey band is the 1D velocity-depth reference for a 0-7 Ma Atlantic-type oceanic crust of White et al. [1992].*

The tectonic structure of the southern segment (Domain 2) is characterized by large tilted fault-blocks, controlled by eastward dipping normal faults that appear to be deeply-rooted into the crust (Figure 6.5a), whereas faulting in the northern segment (Domain 2a) is less important (Figure 7.4). These tectonic variations are accompanied by differences in the velocity structure (Figure 8.1 and 8.6a). The southern segment of the Cornaglia Terrace (Domain 2) has a laterally comparatively heterogeneous velocity structure marked by 4 sub-vertical velocity anomalies of 6.0-6.5 km/s (Figure 8.1b), whereas the velocity field of the northern segment is comparatively more homogeneous (Figure 8.1a). Additionally, the velocity gradient of the crust in the northern region (Domain 2a) appears to be gentler than in the south that shows a 2 layer structure

(Figure 8.6a). All these differences suggest a lower amount of extension and possibly a less important effect of magmatism during extension in the northern region of the Cornaglia Terrace (Domain 2a).

The Farfalla segment (Domain 2b) is intersected by Line EF (Figure 8.1a, 8.4, and 8.5). Dredging of metamorphic continental rocks on top of the Farfalla seamount suggests that it may likely correspond to stretched continental crust similar to that identified in Domain 1b in the Sechi segment (Figure 8.1a, 8.3 and 8.5). However, the oceanic-like velocity structure, and particularly the high lower crust velocity of this domain (Figure 8.6b) may suggest that it is affected by either magmatic intrusions or that the high lower crust velocity may in fact represent serpentinized mantle rocks [e.g. Chamot-Rooke et al., 1999; Dean et al., 2000; Funk et al., 2004].

To the east, the Campania Terrace (Domain 4) is mapped by both WAS lines showing from north to south differences in crustal velocity structure (Figure 8.6b), and in the tectonic expression (Figures 6.4, 7.4, and 8.1, 8.6b). Faulting in the northern segment is more important than in the southern segment, where faulting appears to be less important, only affecting the uppermost part of the basement (Figures 6.4 and 7.4). In addition, in the northern segment the crust thickens eastward 3-4 km in ~30 km of profile, while in the southern segment a similar variation occurs in ~60 km of profile (Figure 8.2). These tectonic differences are also evidenced in the bathymetry (Figures 7.1 and 8.5), which shows a rough fault-controlled topography in the north, and a subdued relief in the southern region. A similar variation in bathymetry occurs between the Sardinia margin (Domain 1) and the Cornaglia Terrace (Domain 2) (Figures 8.4and 8.5).

Based on these observations, the northern region of the Campania Terrace (Domain 4 in Line EF) might be similar to the Farfalla segment (Domain 2b), representing a continental crust heavily intruded by rift-related magmatism or serpentinized mantle, while the southern section of the terrace (Domain 4 in Line GH) possibly corresponds to a back-arc oceanic crust similarly to Cornaglia Terrace (Domain 2 and 2a) (Figures 8.4 and 8.5).

8.1.3 Exhumed mantle

In both lines, the basement of Domain 3 is interpreted to be mainly formed by exhumed mantle rocks (Figures 8.1, 8.4, and 8.5).

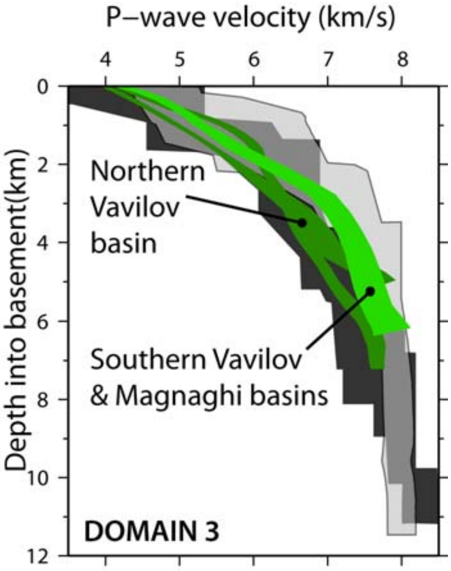

Figure 8.7.- *1D P-wave velocity-depth profiles corresponding to Domain 3. Light grey band represents the 1D velocity-depth reference for exhumed mantle regions [Dean et l., 2000; Sallarès et al., 2013], whereas the dark grey envelop represents oceanic crust reference as in Figure 8.6 from White et al. [1992].*

In Line GH, this domain extends more than 120 km across the Magnaghi and Vavilov basins, in the Vavilov basin it is 20 km-wide along Line EF, mimicking the V-shaped morphology of deepest seafloor (Figures 8.1, 8.4, and 8.5).

This domain contains basaltic edifices possibly related to oceanic crustal accretion [i.e. Sites 655 and 651 in Figures 8.5] [Beccaluva et al., 1990] and to inter-plate volcanism (i.e. Magnaghi and Vavilov seamounts in Figures 8.4 and 8.5) [Robin et al., 1978; Savelli, 2002]. Some of these structures are intersected by Line GH and mapped at depth as low velocity anomalies that indicate locally-intruded bodies (Figure 6.10). Line EF, in contrast, does not show evidence of basaltic structures at crustal depths. However, the lower velocity gradient of the basement, compared to that of the southern line GH (Figure 8.7) suggests that the exhumed mantle rock basement could be locally intruded by basaltic sills or dikes.

8.2 Implications of the new geological domains defined in the Central Tyrrhenian Sea

The interpretation of the velocity, density and tectonic structure obtained with the MEDOC experiment WAS, gravity and MCS data, has led to a radically new definition of geological domains in the Central Tyrrhenian basin (Figures 8.4 and 8.5) compared to what has been previously accepted.

Previous interpretations of the Cornaglia (Domain 2 and 2a) and the new-defined Campania Terraces (Domain 4) assumed a basement formed by stretched continental crust (Figure 7.1 and 8.5) [e.g. Duschenes et al., 1986; Sartori et al., 2004]. However, the two-layer velocity structure in those two regions fits better with that of oceanic-type crust, or what is called magmatic back-arc crust. The depth-velocity distribution indicates that the lower crust velocity is slightly slower than typical oceanic Layer 3. The interpretation is that this oceanic-type crust structure formed in a back-arc spreading setting influenced by flux melting related with the dehydration of the subducted Ionian slab, similar to what has been described in other back-arc basins in the Pacific [Martinez et al., 2007; Dunn and Martinez, 2011]. In this context, it is likely that the crust was build at the approximate location of the volcanic arc, so its anomalous velocity and density structure might reflect the combined effect of the original volcanic arc crust, developed on top of a continental crust, and later affected by magmatism during the extensional phase.

Previous interpretations of the Magnaghi and the Vavilov basins assumed that they were floored by oceanic crust [Kastens and Mascle, 1990; Sartori et al., 2004; Cella et al., 2008] and that the serpentinized peridoties cored in ODP site 651 (Figure 7.1 and 8.5) might correspond to an isolated continental block that contain a sliver of Tethyan ophiolite [Kastens and Mascle, 1990]. As a result most maps from the region typically display ocean crust in the basins. In contrast, the results of this thesis suggest that the basement of the Magnaghi and Vavilov basins is fundamentally composed of mantle peridotites serpentinized to 5-6 km depth under the sediment cover. The new interpretation is that these altered mantle rocks are locally intruded by basaltic magmas that form the root of volcanic constructions of the Magnaghi and Vavilov seamounts, and D'Ancona and Gortani Ridges (Figure 6.10).

Results obtained along this transect of the MEDOC experiment show that the Sardinia and Campania conjugate margins are formed by extended continental crust of overall crustal and tectonic asymmetric structure. The joint analysis of velocities and densities with observations of the tectonic structure show how both continental margins rather abruptly transition to what has been interpreted as magmatic back-arc crust in the Cornaglia (Domain 2 and 2a) and Campania (Domain 4) Terraces. Finally, in contrast to what has been previously proposed, the back-arc crust under both terraces give up in the center of the basin to exhumed mantle rocks of the Magnaghi and Vavilov basins (Domain 3).

The structure defined with the data set of this thesis indicates a spatial distribution of rock types that implies a temporal basin evolution from an extending continental crust to back-arc oceanic crust formation and to mantle exhumation. This spatial distribution of crust types and the inferred temporal evolution are in stark contrast to current models of lithospheric extension and rifting in systems where mantle unroofing is interpreted to have occurred (e.g. North Atlantic rifted margin). Commonly accepted models studying the continent to ocean transition (involving mantle unroofing) typically postulate a continuum from continental crust extension, mantle exhumation and eventual oceanic crust formation by gradual instauration of a decompression melt system [e.g. Pérez-Gussinyé et al., 2006]. To explain this peculiar configuration of the basement, in the following section I examine the potential mechanisms that may have led to the formation of these domains in the Central Tyrrhenian basin.

8.3 Conceptual model of the basement formation in the Central Tyrrhenian basin

The main purpose of this section is to discuss the processes that may have led to the formation of the different types of basement identified in the Central Tyrrhenian and propose a model to explain the opening of the basin.

As explained in chapter 2, the opening of the Tyrrhenian basin, as is also the case of the rest of Western Mediterranean basins, has been governed by slab rollback and back-arc extensional processes. In this setting, it is well-studied, particularly in the western Pacific basins, that back-arc extension tends to initiate near the weakest zone of the overriding plate, which is the volcanic arc (see Figure 1.9 in section 1.3.1.2.2) [Mollnar and Atwater, 1978; Martinez et al., 2007; Dunn and Martinez, 2011]. Consequently, back-arc rifting and the initial stages of oceanic spreading are influenced by both pressure-release melting (i.e. that related to the extension) and subduction-derived hydrous flux melting (Figure 8.8a) [Martinez et al., 2007; Dunn and Martinez, 2011]. The simultaneous influence of these processes tends to generate a magmatic crust in which composition and hence physical properties are between extended arc-type and oceanic-type crust [Dunn and Martinez, 2011]. Therefore, it is very difficult to discern the relative input of both magmatic sources.

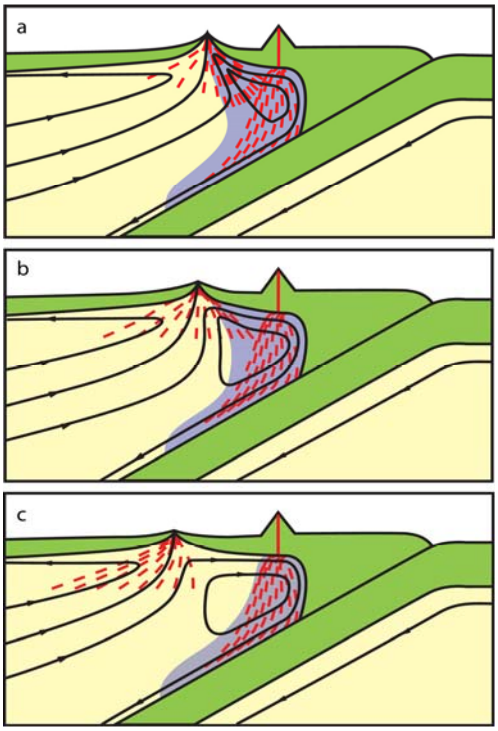

Figure 8.8.- *Vertical sections of a subduction zone showing the spatio-temporal evolution of a back-arc spreading system. As the subduction front and the volcanic arc migrate trenchward due to slab rollback, the influence of hydrous flux melting (grey area) at the mid-ocean ridge decreases. In the last stage (3) magma supply at the spreading center is mainly generated by passive decompression of the underlying mantle. Consequently, the crust formed in this system would transition from arc-like composition to a normal oceanic crust. The green area depicts lithospheric plates and red dashes are melt flow. From Dunn and Martinez [2011]*

As rollback proceeds and hence extension increases, the spreading center physically separates from the volcanic arc and from the influence of hydrous flux melting, so that the main production of magma at the ridge results from pressure-release melting (Figure 8.8b) [Martinez et al., 2007; Dunn and Martinez, 2011]. Consequently, a typical oceanic crust starts to be formed in the spreading center (Figure 8.8c). However, the results of this thesis suggest that there is no “typical” oceanic crust in the Central Tyrrhenian basin formed as a result of the extension. Instead of that, mantle appears to have been exhumed without significant melting in the central parts of the basin.

As explained in section 1.3.2.3, the exhumation of the mantle prior to the generation of melting depends on the parameters that control production of magma at the spreading center, that is: extension velocity, temperature and mantle composition [Klein et al., 1987; Reid et al., 1987; Michael et al., 2003; Pérez-Gussinyé et al., 2006].

Numerical experiments indicate that for extension velocities <0.6 cm yr^{-1} mantle exhumation may occur prior to melt production, preventing to form a well-developed oceanic crust [Pérez Gussinyé et al., 2006]. However, extension rates in the Central Tyrrhenian are thought to be ten times faster [5-6 cm yr^{-1} according to Faccena et al., 2001], which would have triggered the production of large amounts of pressure-release melting, and so the formation of a typical oceanic crust, if the mantle would have been under regular conditions, that is, at a potential temperature of ~1300ºC and with a fertile, pyrolitic-type composition [e.g. Korenaga and Kelemen, 2000; Koreanga, 2004]. Therefore, extension velocity cannot explain mantle exhumation without crustal generation in the Central Tyrrhenian.

Regarding the thermal structure, it has been found that for extension rates as low as of 1 cm yr^{-1}, a sub-lithospheric mantle temperature of ~1200 ºC is needed to promote mantle exhumation prior to melting [Pérez-Gussinyé et al., 2006]. As the Central Tyrrhenian has opened at velocities six times faster [Faccenta et al., 2001], the temperature of the mantle should be considerably lower than 1200 ºC to exhume mantle without production of pressure-release melting. It is really difficult to conceive a process that could cold the mantle to such low temperatures, especially in the mantle wedge above a subducting slab where temperature is typically well above 1200 ºC [e.g. Peacock, 1996; Syracuse et al., 2010]. Additionally, the investigation of the thermal structure of the mantle beneath the Liguro-Provençal basin at the time of the spreading phase concludes that the potential mantle temperature should be around 1280 ºC [Chamot-Rooke et al., 1999], which makes even more unlikely that the potential mantle temperature at the time of opening of the Tyrrhenian basin was below 1200ºC.

The last parameter that may explain mantle exhumation prior to melting is the composition of the mantle source. A more depleted composition of the mantle leads to lower melting degrees beneath the spreading center [e.g. Michael et al., 2003; Pérez-Gussinyé et al., 2006]. Geochemical analyses of the peridotites drilled in the Vavilov basin (site 651 in Figure 8.4) concluded that they are highly depleted in composition, and attribute this depletion to partial melting under hydrous conditions (slab-derived melts) [Bonatti et al., 1990].

Therefore, the depletion of the mantle seems to be a priori the most likely cause that could explain mantle unroofing in the Central Tyrrhenian. Based on the geochemical analysis of the peridotites from ODP 651 in the Vavilov basin, a possible explanation to this is that subduction and back-arc processes in the Western Mediterranean have triggered the production of large amounts of melting, for example during the opening of the Liguro-Provençal basin just before the opening of the Tyrrhenian one. This cumulative process may have led to the progressive depletion of the underlying mantle. Therefore, since the Tyrrhenian is the youngest back-arc basin formed in this setting, and given that it opened just after the Liguro-Provençal basin, the hypothesis that the mantle beneath this region could be considerably depleted is rather plausible.

Based on this hypothesis, I propose a conceptual model characterized by a depleted mantle setting in which production of pressure-release melting is limited, so the melt production is dominated by hydrous flux melting from the subducted slab. The model displays 5 stages of opening: **(I)** a normal subduction scenario followed by **(II)** development of the back-arc rift, **(III)** initiation of back-arc spreading, **(IV)** mantle exhumation, and finally **(V)** a last stage in which large volcanic edifices are emplaced in the central part of the basin (Figure 8.9)

The **Stage I** shows previous phase to back-arc extension, in which bending-related faulting promotes hydration of the subducting lithosphere [Ranero et al., 2003]. When the appropriate pressure/temperature conditions are met (typically at a depth of 100-150 km), the subducting lithosphere releases these fluids into the overlying mantle, triggering the generation of hydrous flux melting in the mantle wedge. This slab-derived melting originates arc volcanism (Figure 8.9a). Note that the mantle beneath the overriding plate is illustrated as depleted in composition following the arguments stated above. This stage might correspond to the latest phases of opening of the Liguro-Provençal basin at ~20-15 Ma [Gattacceca et al., 2007].

In **Stage II** back-arc rifting was already initiated due to the migration of the subduction front toward the oceanic plate as a result of the slab rollback (black arrows in Figure 8.9b). During this stage, back-arc extension triggers the decompression of the underlying mantle that rises passively beneath the spreading center. As stated above, this process would promote the formation of pressure-release melts if the mantle would be under normal conditions. However, we assume that the mantle is depleted enough to limit the production of this type of magmatism considerably. In contrast, since back-arc rifting occurs near the volcanic arc, a large amount of hydrous flux melting would be accreted forming thereby a new magmatic crust, in which both composition and crustal structure would differ from those of normal oceanic crust [Martinez et al., 2007; Dunn and Martinez, 2011]. This process could explain the "anomalous" characteristics of the crust that we found in domains 2, 2a and 4 (Figure 8.1, and 8.6), which would correspond to "a mixture" between the original continental crust, the volcanic arc that was emplaced on top of it during subduction, and the final influence of subduction-related magmatism. Stage II, then, illustrates the Tyrrhenian basin at some point between the last phases of rifting and the initiation of the spreading center. At that period both rifted continental crusts reported in the Sardinia and the Campania margins (Domain 1,1a and 5) and in the called Sechi segment (Domain 1b) would have formed (see Figure 8.9b).

Thus, between **Stage II** and **Stage III** a new magmatic back-arc crust is formed due to the accretion of large amounts of hydrous flux melting (grey crust in Figure 8.9c). This magmatic back-arc crust would correspond to that found beneath the Cornaglia (Domain 2 and 2a) and Campania (Domain 4) Terraces (Figures 8.4 and 8.5). As observed in previous sections the seismic velocity structure of this type of crust closely resembles to an oceanic crust (e.g. Atlantic oceanic crust) [White et al., 1990] but with lower velocity gradient in the L3 region. Gravity modeling indicates that this crust presents a departure in composition with normal oceanic crust. However, without further geochemical information it is not possible to confirm if this process is compatible with the composition of the basement rocks.

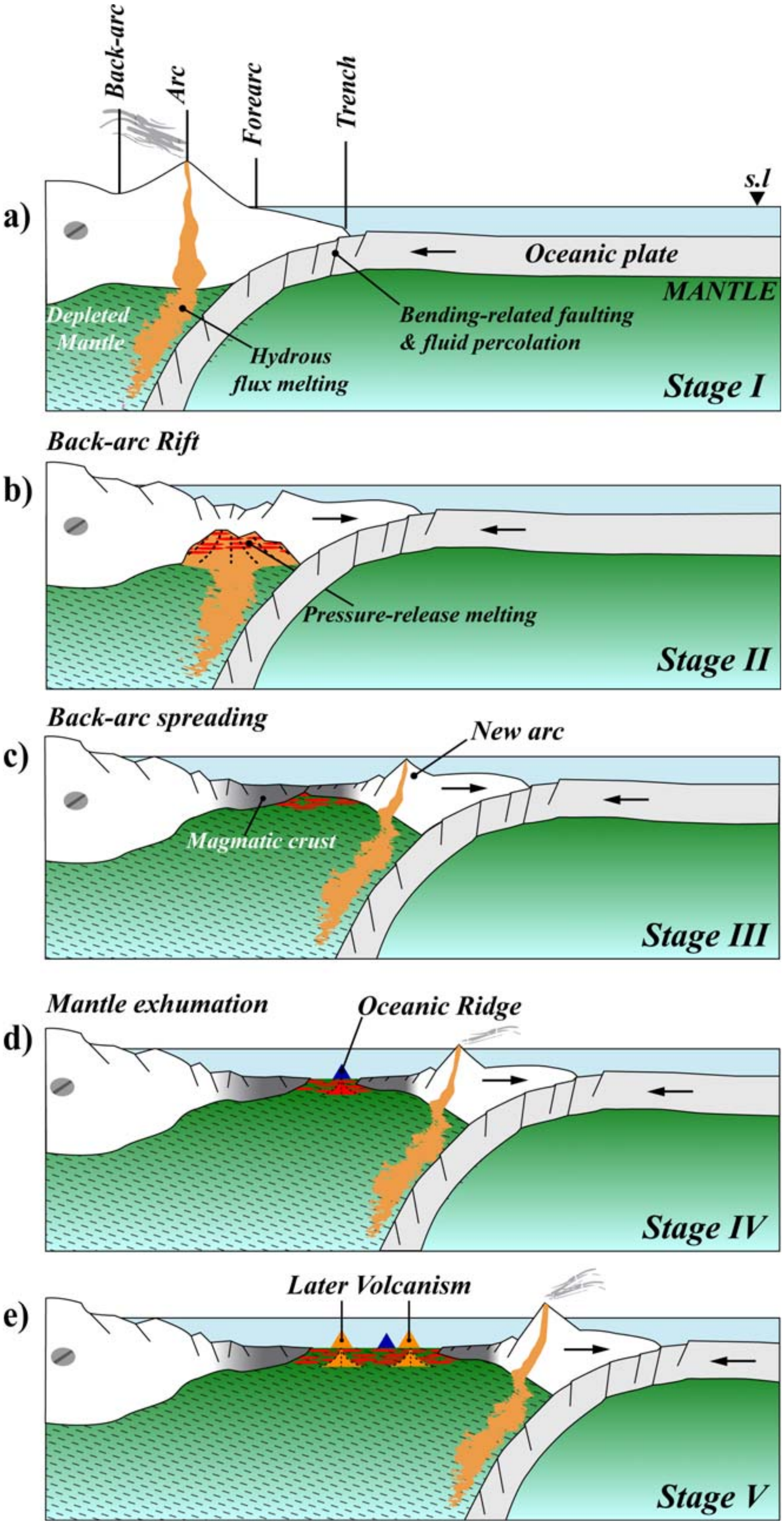
Back-arc
Arc
Forearc
Trench
s.l
a)
Oceanic plate
MANTLE
Depleted Mantle
Hydrous flux melting
Bending-related faulting & fluid percolation
Stage I
Back-arc Rift
b)
Pressure-release melting
Stage II
Back-arc spreading
c)
New arc
Magmatic crust
Stage III
Mantle exhumation
Oceanic Ridge
d)
Stage IV
Later Volcanism
e)
Stage V

Figure 8.9.- *Formation model of the Central Tyrrhenian basin in a slab rollback and depleted mantle setting. Note that the overriding plate is screwed and thus fixed.*

In **Stage III** back-arc rift has evolved until full continental break up and back-arc spreading has initiated (Figure 8.9c). In this stage, as hydrous flux melting migrates with subduction front trenchward, magma supply in the spreading center must diminish considerably because the depleted mantle is not able to produce large amounts of melting by itself. In this case, the limited amounts of melt are not emplaced as a crust but as intrusive bodies forming sills and dikes as has been observed in the ODP site 651 [Beccaluva et al., 1990]. Therefore, in **Stage IV** (Figure 8.9d), extension leads to the exhumation of mantle rocks, while the little amount of pressure-release melting forms isolated oceanic ridges like the Gortani Ridge [4.3 Ma] (ODP 655 in Figure 8.5) [Beccaluva et al., 1990; Bertrand et al., 1990]. This stage would illustrate the formation of the basement that floors the Magnaghi and Vavilov basins (Domain 3) (Figure 8.5).

Finally, as stated in section 2.2.4 the Tyrrhenian basin was subjected to an important pulse of anorogenic volcanism [Savelli, 2002]. **Stage V** (Figure 8.9e) illustrates the emplacement of important volcanic edifices in the Magnaghi and the Vavilov basins as a result of this sporadic magmatic episode dated at 3-0.1 Ma (i.e. posterior to the exhumation of the mantle) and attributed to an intermittent episode of intra-plate magmatism [Robin et al., 1978; Savelli, 2002].

In summary, the presented model, speculates on formation of the Central Tyrrhenian basin in a regional setting that is constrained by the presence of a depleted mantle source. However, it is clear that the hypothesis of a depleted mantle should be tested and confirmed by geochemical analysis of the exhumed peridotites in combination with petrological mantle melting models. In addition, rock sampling and further geochemical information of the basement in the magmatic back-arc crust region would allow to better constrain the affinity of the basement, and to infer the processes related with its formation. In Chapter 10 I propose some potential studies that would provide this valuable information and would help to better understand the geological structure of the Central Tyrrhenian.

Part IV:

Conclusions

Chapter 9: Conclusions

9.1 Geophysical cross-sections

The results obtained from WAS and gravity modeling, together with observations based on the MCS profiles MEDOC-4 and 6 reveal three different basement affinities in the Central Tyrrhenian basin, that is, continental crust, magmatic back-arc crust and exhumed mantle. In addition, combination of these results with morpho-tectonic observations from bathymetry, and geological information from rock sampling and drilling [Colantoni et al., 1981; Kastens and Mascle, 1990] has allowed to interpret the plan view distribution of these domains (Figure 8.5). This section presents the main conclusions concerning the distribution of continental crust, magmatic back-arc crust, and exhumed mantle in the Central Tyrrhenian basin.

Continental crust

In Line GH this type of crust is observed in Domain 1 and 5 (Figure 8.1b and 8.4b). Domain 1 is formed by the continental crust of Sardinia and its margin, which is characterized by landward and seaward normal faults and crustal thinning from ~22 km to ~13 km-thick. The conjugate margin of Campania (Domain 5) might represent the westernmost part of the Italian continental crust.

Similarly, in Line EF continental crust is also observed beneath the Island and margin of Sardinia in Domain 1a, characterized by a significant crustal thinning from ~25 to ~10 km-thick. However, the northern and southern geophysical segments of the Sardinia margin display differences in crustal velocity structure (Figure 8.3a) that might be attributed to differences in the petrological composition (e.g. granitic, basaltic, metamorphic). To the east, the continental Domain 1b is identified along the Sechi segment as a highly stretched portion of continental crust ($\beta>3$) (Figure 8.1a and 8.4a). This domain appears to belong to a major continental structure that extends northward and southward but does not reach Line GH (Figure 8.5). Finally, in Line EF the conjugated Campania margin (Domain 5) is also intersected and interpreted to represent the westernmost extension of the Italian continental landmass (Figure 8.5).

Continental crust is extended toward the Northern Tyrrhenian (Figure 8.5), where it is believed that is partially intruded by magmas at lower crustal levels [Moeller et al., 2013].

Magmatic back-arc crust

In Line GH it is represented by the Cornaglia Terrace (Domain 2) and the Campania Terrace (Domain 4) (Figures 8.1b and 8.4b). The transition between continental and magmatic crust is only observed by a marked, abrupt increase of velocities (> 7 km/s) in the lower crust (at ~125 km in Figure 8.1b). Large-scale normal faulting has affected the Cornaglia Terrace (Figure 6.5a), whereas in the Campania Terrace, normal faulting is less important (Figures 6.5b). The crustal structure in both regions is represented by velocities slightly lower than those found in a 0-7 Ma-old-oceanic crust [White et al., 1992]. This has been discussed and finally interpreted as indicative of back-arc spreading close to the active volcanic arc [Martinez et al., 2007].

In Line EF, this type of crust is encountered in Domains 2a, 2b, and 4 (Figure 8.1a). Domain 2a is represented by the northern region of the Cornaglia Terrace showing lower crustal velocities >7 km/s and a rather homogeneous velocity (Figure 8.6a) and tectonic (Figure 7.4) structure compared to that of Line GH in the south (Domain 2) (Figure 6.5a). Eastward of Line EF, lower crustal velocities > 7 km/s are also observed in Domains 2b and 4 in the Farfalla segment and the northern Campania Terrace, respectively (Figures 8.1a and 8.4a). The Farfalla segment (Domain 2b) does not present any counterpart in Line GH (Figure 8.1 and 8.5), and it is interpreted as a continental crust affected by magmatic underplaiting or either serpentinized mantle rocks at the base of the crust [e.g. Chamot-Rooke et al., 1999; Dean et al., 2000; Funk et al., 2004]. In contrast, the Campania Terrace is intersected by Line GH in the south (Figure 8.1, 8.4, and 8.5), displaying crustal velocity, tectonic, and bathymetric variations from north to south (Figures 6.4, 7.4, and 8.1, 8.6b). These differences suggest that the northern terrace might correspond to a stretched continental crust heavily intruded by rift-related magmas, while the southern terrace might correspond to a magmatic back-arc crust, similar to that of the Cornglia Terrace (Domain 2 and 2a).

However, drilling in the Cornaglia and Campania Terraces has only evidenced the presence of isolated continental blocks (e.g. Flavio de Gioia seamount in Figure

8.1b, 8.4b, and 8.5) [Colantoni et al., 1981]. Hence, further rock sampling and geochemical information of the basement in these two terraces is necessary to better constrain its petrological nature.

Exhumed mantle

In Line GH, the presence of a basement made of exhumed mantle rocks is evidenced in Domain 3, which intersects both V-shaped Magnaghi and Vavilov basins (Figure 8.1b, 8.4, and 8.5). The main characteristics of this domain are the lack of Moho reflections in both WAS and MCS data and a vertical velocity structure characterized by a strong velocity gradient in the topmost 3-4 km similarly to other regions where basement is interpreted to be made of serpentinized mantle [Reid, 1994; Dean et al., 2000; Van Anvendonk et al., 2006; Sallarès et al., 2013a].

In Line EF, the presence of a mantle rock basement is less clear, since the velocity gradient is lower than the velocity-depth references of exhumed mantle, and hence fits better with that of oceanic crust (Figure 8.7). However, the lack of Moho reflections in the MCS data and in most of the WAS receivers of this region supports the exhumation of mantle (Figures 7.4, 7.5, and A.1.2.25). Thus, I tentatively suggest that the lower velocity gradient of the exhumed mantle basement might be attributed to the influence of basaltic intrusions like sills and dicks. Nevertheless, more petrological information of the basement is needed to confirm this interpretation.

Additionally, this domain hosts large basaltic edifices related to oceanic crustal accretion (i.e. Sites 655 and 651 in Figures 8.5) [Beccaluva et al., 1990] and to inter-plate volcanism (i.e. Magnaghi and Vavilov seamounts in Figures 8.4 and 8.5) [Robin et al., 1978; Savelli, 2002]. Some of these structures are intersected by Line GH and imaged in depth showing that they are local and hence not representative of the entire basement nature (Figure 6.10).

The overall differences in the seismic velocity structure and the tectonic signature between domains of the northern Line EF and the southern Line GH are most likely attributed to the southward increase of extension that characterizes the Tyrrhenian basin [e.g. Faccena et al., 2001; Sartori et al., 2004].

The analysis of these new geophysical data has led to a radically new definition of geological domains in the Central Tyrrhenian. According to the presented distribution of the basement, rifting in the Central Tyrrhenian basin would have started with continental crust extension, continued with back-arc spreading leading to generation of magmatic back-arc crust, followed by mantle exhumation and subsequent magmatic intrusions.

9.2 Basement formation model

To explain the formation of the basement in the Central Tyrrhenian basin I propose a new conceptual model for the opening of the basin (Figure 8.9). This model is based on those previously proposed to explain back-arc extension and formation of the Western Pacific basins in slab rollback settings [Martinez et al., 2007; Dunn and Martinez, 2011].

The most relevant observation concerning the evolution of the basin is the presence of a wide exhumed mantle band in the Central Tyrrhenian despite the fast spreading rates (5-6 cm/yr) and the apparently “normal” mantle temperatures at the time of extension. This makes that the most likely cause for the lack of substantial magmatism at the spreading, and hence formation of typical oceanic crust, is the presence of a depleted mantle source.

In summary, the presented model is based on 5 stages of opening in which a depleted mantle setting constrains the production of pressure-release magmas, and thus, back-arc crustal accretion is mainly explained by the influence of subduction-related melts (i.e. hydrous flux melting in Figure 8.9). The main features of these stages are briefly exposed below:

I. The first stage consists of a normal subduction scenario, in which slab-derived melting originates arc volcanism (Figure 8.9a). The mantle beneath the overriding plate is assumed to be depleted in composition. This stage may likely illustrate the latest phases of opening of the Liguro-Provençal basin at ~20-15 Ma [Gattacceca et al., 2007].

II. In the second stage back-arc rift forms as a result of the slab rollback (Figure 8.9b). In this stage, extension causes the passive decompression of the underlying asthenospheric mantle, which in turn results in the production of pressure-release melts. However, since the mantle is assumed to be depleted, this production is rather limited. In contrast, since rifting occurs near the volcanic arc a large amount of hydrous flux melting is accreted in the lower crust forming thereby a new magmatic crust. The composition and crustal structure of this new magmatic crust would differ from those of normal oceanic crust [Martinez et al., 2007; Dunn and Martinez, 2011]. Stage II, then, illustrates the formation of both magmatic crusts interpreted beneath the Cornaglia and the Campania Terrace (Domains 2, 2a, and 4) (grey crust in Figure 8.9c).

III. In the third stage back-arc spreading is initiated (Figure 8.9c). However, as hydrous flux melting migrates with subduction front trenchward, magma supply in the spreading center diminish considerably because the depleted mantle source is not able to produce large amounts of melting by itself. Consequently, no oceanic crust is generated, but the limited amount of melt is emplaced as intrusive bodies forming sills and dikes, as suggested by the ODP site 651 (Figure 8.5) [Beccaluva et al., 1990], and isolated oceanic ridges like the Gortani Ridge [4.3 Ma] (ODP 655 in Figure 8.5) [Beccaluva et al., 1990; Bertrand et al., 1990].

IV. In the fourth stage (Figure 8.9d) extension leads to the exhumation of mantle rocks, while the little amount of pressure-release melting continues forming isolated oceanic ridges. This stage would illustrate the formation of the basement that floors the Magnaghi and Vavilov basins (Figure 8.5).

V. Finally, the last stage illustrates the emplacement of large volcanic edifices in the central part of the basin, as a result of the sporadic magmatism dated at 3-0.1 Ma (i.e. posterior to the exhumation of the mantle) and attributed to an intermittent episode of intra-plate magmatism (e.g. Vavilov seamount in Figure 8.5) (Figure 8.9e) [Robin et al., 1978; Savelli, 2002].

Chapter 10: Outlook

The results of this Thesis provide novel information concerning the petrological nature of the geological domains and their distribution in the Central Tyrrhenian basin with unprecedented accuracy and detail. The spatial distribution of these domains has been discussed, as along with a conceptual model that attempts to explain how extension leads to the formation of stretched continental crust, magmatic back-arc crust, and mantle exhumation in the Central Tyrrhenian. However, as stated in previous chapters additional geological, geophysical, and geochemical information is needed to address the open questions arising with these new findings. Therefore, in this chapter I propose the acquisition of new geophysical data, the location of several sites for drilling and dredging, and the investigation of the formation of these types of basement from numerical modeling that would help to answer those open questions.

10.1 Geophysical transects

The distribution of the geological domains made in this thesis has been inferred with only two geophysical profiles that are separated ~55km one from each other. Additionally the available rock sampling information [e.g. Colantoni et al., 1981] is useful to identify local structures, but not to define the overall nature of the different domains. Consequently, most of the boundaries in the basement distribution map remain unconstrained (Figure 8.5). To solve this issue and constrain the distribution of the main geological domains, I recommend to complement the existing data with new WAS, gravity, and MCS profiles, which will also provide new information on the crustal structure of the Northern Sicilian margin and on the transition between the Vavilov and the Marsili basins (see Figure 2.3). The proposed experiment includes 6 long geophysical transects along which WAS, gravity, and MCS data would be acquired (Figure 10.1):

- Profile **P1** cuts from north to south the Cornaglia Terrace crossing roughly perpendicular the MEDOC lines of this thesis (Figure 10.1). The data of profile P1 would provide information on the north-south variations of the crustal structure, and on the transition between the magmatic back-arc crust of the Cornaglia Terrace and the continental crust identified in the Northern Tyrrhenian.

- Profiles **P2** and **P3** are parallel between them and perpendicular to the lines presented in this thesis. The proposed profiles cut from north to south the Magnaghi and Vavilov basin, and end in the Northern Sicilian margin (see Figure 2.3). Geophysical data along P2 and P3 would help to constrain the northern and southern boundaries of the exhumed mantle domain, and would provide valuable information on the nature of the basement beneath the northern margin of Sicily and its relationship with the volcanic arc (Figure 10.1). Additionally, both profiles are designed to cut several ODP sites, which would allow the correlation of the MCS data with the main seismo-stratigraphic units.

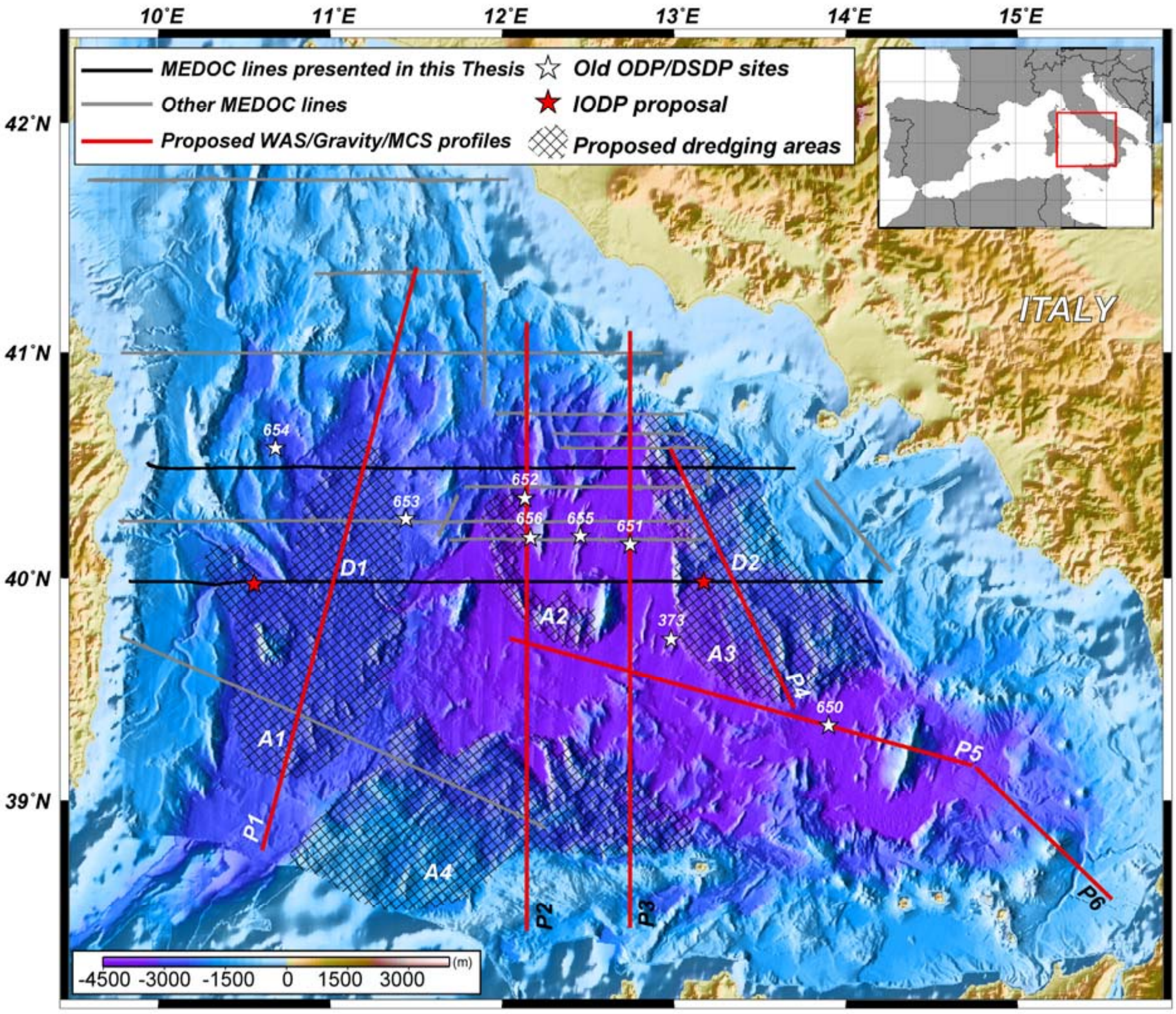
10°E
11°E
12°E
13°E
14°E
15°E
42°N
41°N
40°N
39°N
MEDOC lines presented in this Thesis
Other MEDOC lines
Proposed WAS/Gravity/MCS profiles
☆ Old ODP/DSDP sites
★ IODP proposal
Proposed dredging areas
ITALY
654
653
652
656
655
651
373
650
D1
D2
A1
A2
A3
A4
P1
P2
P3
P4
P5
P6
-4500 -3000 -1500 0 1500 3000
(m)

Figure 10.1.- *Geophysical, drilling, and dredging survey proposal.*

- Profile **P4** runs along the Campania Terrace, crossing Line EF and GH (Figure 10.1). Similarly to P1, this profile is designed to investigate the north-south crustal variations, and to constrain better the crustal structure along the Campania Terrace.

- Profile **P5** is proposed to provide new insights on the crustal transition between the Vavilov and the Marsili basin. This profile would also reveal the crustal structure and nature of the Marsili basin. Hopefully, it would also image the magmatic chamber beneath the Marsili seamount (see #22 in Figure 2.3). Moreover, profile P5 cuts P2 and P3 providing more constrains concerning the 3D distribution of the geological domains.

- Profile **P6** is a continuation of profile P5 towards the southeast (Figure 10.1). This profile would cross the Aeolian Islands and the Calabrian margin (see Figure 2.3) in order to provide valuable information of the crustal structure beneath the arc. In addition, it would be interesting to extend the line further to the southeast, crossing the Calabrian arc, to investigate the whole subduction system including the incoming and upper plates at seismogenic depths.

10.2 Drilling and dredging

One of the most relevant points in this thesis is the definition of magmatic back-arc crust beneath the Cornaglia and the Campania Terraces. However, this observation is constrained only with crustal velocity and density information. To better constrain the petrological nature of these domains it is necessary to drill in these two areas and perform geochemical analysis of the samples. For that reason, I propose **D1** and **D2** as two potential locations for IODP (Integrated Ocean Discovery Program) drilling sites (Figure 10.1). The location of these two perforation sites is based on the information provided by MCS images and the seismic velocity models obtained in this work.

Interestingly, it turns out that in the last years several proposals for drilling in the Mediterranean Sea have been presented to the IODP [e.g. GOLD project, DREAM project]. One of the main goals of these projects is to drill below the thick Messinian salt layer and provide information on the Mediterranean basin history. Since the Tyrrhenian basin is also the locus of Messinian salt deposits, particularly in the Cornaglia Terrace [e.g. Fabbri and Curzi, 1981; Sartori et al., 2004], I believe that drilling in the Cornaglia and Campania Terraces would not only provide petrological information of the basement, but it would also grant invaluable geological information on the Messinian geological record, and hence, on the evolution of the opening of the basin.

Because of drilling is rather expensive and it requires extensive ship time to accomplish the objectives, I additionally propose four areas for rock dredging (Figure 10.1):

- Area **A1** is located in the Cornaglia Terrace because of the lack of rock sampling in this region . The main goal of this proposal is to ground-truth the interpretation of magmatism related with the formation of the aforementioned back-arc crust.
- Area **A2**, where dredging would give petrological information about the nature of the D'Ancona Ridge which is still a matter of discussion [Marani and Gamberi, 2004].
- Dredging in area **A3** would be conducted to investigate the presence of magmatism during the formation of this region, similarly to dredging A1. Additionally, it would put an end to the lack of petrological information in the Campania Terrace providing important information on the nature of some structural highs in this terrace.
- Finally, I suggest dredging in area **A4,** in the Northern Sicilian margin (Figure 10.1) to ground-truth the geophysical data acquired in that region with petrological information obtained from rock sampling of the seabed.

The geological data collected from dredging would also be subjected to an exhaustive geochemical analysis in order to shed some light upon the formation of the basement beneath the selected regions.

10.3 Numerical modeling

As stated above further investigations of the parameters that control back-arc extension and mantle exhumation are necessary to constrain the conceptual model of section 8.3 (Figure 8.9). Therefore, in addition to the acquisition of new geophysical and geological data in the Tyrrhenian basin, that would also help to address this issue, I suggest the investigation of the mechanisms involved in back-arc extension and mantle exhumation from numerical modeling. Dynamic models of extension such as those presented by Pérez-Gussinyé et al. [2006] would allow to explore how extension velocity, mantle composition and temperature influence the evolution of the entire system as well as the formation the different domains observed in the Central Tyrrhenian basin.

Part V:

References

The results and discussion of Chapter 6 are part of the following paper that has been recently accepted by the Journal of Geophysical Research – Solid Earth:

Prada, M., V. Sallares, C.R. Ranero, M. Guzman, I. Grevemeyer, N. Zitellini, R. de Franco, Seismic structure of the Central Tyrrhenian basin: geophysical constraints on the nature of the main crustal domains, J. Geophys. Res. (**accepted**)

References:

Allaby, M. (2008), Oxford Dictionary of Earth Science, Oxford University Press Inc., New York, pp. 654.

Barberi, F., H. Bizouard, G. Capaldi, et al. (1978), Age and nature of basalts from the Tyrrhenian Abyssal Plain, in Hsu, K., L. Montadert et al. (Eds.), Init. Repts. of the DSDP, 42(Pt. 1), p.509-514, U.S. Govt. Printing Office, Washington, DC.

Bartole, R. (1995). The Norht Tyrrhenian-Northern Apennines post-collisional system: constraints for a geodynamic model, Terra Nova, 7, 7-30.

Bartolome, R., (2002) Evolución tecónica del margen continental oeste de México: Fosa Mesoamericana y golfo de California, PhD Thesis, Universidad de Barcelona, Spain, 301 pp.

Beccaluva, L., E. Bonatti, C. Dupuy, et al. (1990), Geochemistry and mineralogy of volcanic rocks from the ODP Sites 650, 651, 655 and 654 in the Tyrrhenian Sea, In Kastens, K.A., Mascle, J., et al. (Eds.), Proceedings of the Ocean Drilling Program, Scientific Results 107, pp. 49– 74.

Benes, V., N. Bocharova, E. Popov, S. D. Scott, and L. Zonenshain (1997), Geophysical and morpho-tectonic study of transition between seafloor spreading and continental rifting, western Woodlark Basin, Papua New Guinea, Marine Geology, 142, 85-98

Bertrand, H., P. Boivin, and C. Robin (1990), Petrology and geochemistry of basalts from the Vavilov basin (Tyrrhenian Sea), Ocean Drilling Program Leg 107, Holes 651A and 655, In Kastens, K.A., Mascle, J., et al. (Eds.), Proceedings of the Ocean Drilling Program, Scientific Results 107, pp. 75-92.

Beslier, M.-O., M. Ask, and G. Boillot, (1993). Ocean-continent boundary in the Iberia Abyssal Plain from multichannel seismic data, Tectonophysics, 218, 383-393

Biella, G., de Franco, R., Marsella, E., and G. Caielli (2007). Deep structures in Southem Italy. Evidences from the Gargano-Pantelleria seismic refraction experiment (1971), Boll. Soc. Geol. It. (It.J.Geo.sci.), 7, 163-175

Birch, F. (1961) The velocity of compressional waves in rocks to 10 kilobars, part 2, J. Geophys. Res., 66, 2199–2224

Boillot, G., S. Grimaud, A. Mauffret, D. Mougenot, J. Kornprobst, J. Mergoil-Daniel, and G. Torrent (1980) Ocean-continent boundary off the Iberian Margin: a serpentinite diapir west of the Galicia bank, Earth and Planet. Sci. Let., 48, 23-34

Boillot, G., Winterer, E.L., Meyer, A.W., et al., (1987a). Proc. ODP, Init. Repts., 103: College Station, TX (Ocean Drilling Program). doi:10.2973/odp.proc.ir.103.

Boillot, G., M. Recq, E.L. Winterer, A.W. Meyer, J. Applegate, M. Baltuck, J.A. Bergen, M.C. Comas, T.A. Davies, K. Dunham, C.A. Evans, J. Girardeau, G. Goldberg, J. Haggerty, L.F. Jansa, J.A. Johnson, J. Kasahara, J.P. Loreau, E. Luna-Sierra, M. Moullade, J. Ogg, M. Sarti, J. Thurow, and M. Williamson (1987b) Tectonic denudation of the upper mantle along passive margins: a model based on drilling results (ODP leg 103, western Galicia margin, Spain), Tectonophysics, 132, 335-342

Boillot, G., G. Féraud, M. Recq, J. Girardeau (1989).”Undercrusting” by serpentinite beneath rifted margins: the examples of the west Galicia margin (Spain), Nature, 341, 523–525

Bonatti, E., M. Seyler, J. Channell, J. Girardeau, and G. Mascle (1990), Peridotites drilled from the Tyrrhenian Sea, ODP Leg 107, In Kastens, K.A., Mascle, J., et al. (Eds.), Proceedings of the Ocean Drilling Program, Scientific Results 107, pp. 37– 48.

Booth-Rea, G., C. R. Ranero, J. M. Martínez-Martínez, and I. Grevemeyer (2007), Crustal types and Tertiary tectonic evolution of the Alborán sea, western Mediterranean, Geochem. Geophys. Geosyst., 8, Q10005, doi:10.1029/2007GC001639.

Bratt, S.R. and Purdy, G.M. (1984), Structure and variability of oceanic crust on the flanks of the East Pacific Rise between 11º and 13ºN. J. Geophys. Res., 89, 6111-25

Brun, J.P, and Beslier, M.O., (1996) Mantle exhumation at passive margins, Earth and Planet. Sci. Let., 142, 161-173.

Bruno, P. P., V. Di Fiore, and G. Ventura (2000), Seismic study of the ‘41st Parallel’ Fault System offshore the Campania-Latial continental margin, Italy, Tectonophysics, 324, 37-55.

Carlson, R.L., and C.N. Herrick (1990), Densities and Porosities in the Oceanic Crust and Their Variations With Depht and Age, J. Geophys. Res., 95 (B6), 9153-9170.

Carlson, R.L., and D.J. Miller (2003), Mantle wedge water contents estimated from seismic velocities in partially serpentinized peridotites, Geophys. Res. Let., 30 (No. 5), doi: 10.1029/2002GL016600.

Carrara, G., (2002), Evoluzione cinematica neogenica del margine occidentale del bacino Tirrencio. PhD Thesis, Parma University, Italy, 170 pp.

Cella, F., M. Fedi, G. Florio, V. Paoletti, and A. Rapolla (2008), A review of the gravity and magnetic studies in the Tyrrhenian Basin and its volcanic districts, Ann. Geophys., Vol. 51, N.1

Chamot-Rooke, N., Jestin, F., Gaulier, J., (1999). Constraints on Moho depth and crustal thickness in the Liguro–Provencal Basin from 3D gravity inversion: geodynamic implications. In: Durand, B., Jolivet, L., Horvath, F., Séranne, M. (Eds.), The Mediterranean Basins: Tertiary Extension within the Alpine Orogen. Special Pub. 156, The geological Society, London.

Cherchi, A., and Montadert, L. (1982), Oligo-Miocene rift of Sardinia and the early history of the western Mediterranean Basin, Nature, 298, 736–739.

Chian, D., C. Keen, I. Reid, and K.E. Louden (1995) Evolution of nonvolcanic rifted margins: New results from the conjugate margin of the Labrador Sea, Geology, v.23, p.589-592, doi: 10.1130/0091-7613

Chian, D., K. E. Louden, T. A. Minshull, and R.B. Whitmarsh (1999), Deep structure of the ocean-continent transition in the southern Iberia Abyssal Plain from seismic refraction profiles: Ocean Drilling Program (Legs 149 and 173) transect, J. Geophys. Res., 104, B4, 7443-7462.

Chiarabba, C., P. De Gori, and F. Speranza (2008), The southern Tyrrhenian subduction zone: Deep geometry, magmatism and Plio-Pleistocene evolution, Earth Planet. Sci. Let., 268, p. 408-423, doi: 10.1016/j.epsl.2008.01.036.

Christensen, N. I., (1978), Ophiolites, Seismic Velocities and Oceanic Crustal Structure, Tectonophysics, 47, pp. 131-157.

Christensen, N., and Mooney, W. (1995), Seismic velocity structure and composition of the continental crust: a global view, J. Geophys. Res, 100 (B7), doi:10.1029/95JB00259.

Colantoni P., A. Fabbri, P. Gallignani, R. Sartori, and J.P. Rehault, (1981) Carta Litologica e Stratigrafica dei Mari Italiani, scala 1/1.500.000, Litografia Artistica Cartografica, Firenze, Italy.

Contrucci, I., A. Nercessian, N. Béthoux, A. Mauffret, and G. Pascal (2001), A Ligurian (Western Mediterranean Sea) geophysical transect revisted, Geophys. J. Int., 146, 74-97.

Contrucci, I., A. Mauffret, C. Brunet, A. Nercessian, N. Béthoux, and J. Ferrandini (2005), Deep structure of the North Tyrrhenian Sea from multi-channel seismic profiles and on land wide angle reflection/refraction seismic recording (LISA cruise): Geodynamical implications, Tectonophysics, 406, 3–4, 141-163, doi:10.1016/j.tecto.2005.05.015.

Dean, S.M., T.A. Minshull, R.B. Whitmarsh, and K.E. Louden (2000), Deep structure of the ocean-continent transition in the southern Iberia abyssal plain from seismic refraction profiles: the IAM-9 transect at 40º20'N, J. Geophys. Res. B: Solid Earth, 105 (B3), 5859-5885.

Dewey, J.F., M.L. Helman, E.Turco, D.H.W. Hutton, and S.D. Knott (1989), Kinematics of the western Mediterranean, in Cowardm, P., D. Dietrich, and G. Park (Eds), Alpine Tectonics, Geological Society Special Publication No. 45, pp. 265-283.

Di Stefano, R., I. Bianchi, M. G. Ciaccio, G. Carrara, and E. Kissling (2011), Three-dimensional Moho topography in Italy: New constraints from receiver functions and controlled source seismology, Geochem. Geophys. Geosyst., 12, Q09006, doi:10.1029/2011GC003649.

Dietrich, V., R. Emmermann, J. Keller, and H. Puchelt (1977), Tholeitic basalts from the Tyrrhenian sea floor, Earth Planet. Sci. Let., 36, 285-296.

Doglioni, C., E. Gueguen, F. Sàbat, and M. Fernandez (1997), The Western Mediterranean extenional basins and the Alpine orogen, Terra Nova, 9, 109-112

Dunn, R.A., and Martinez, F. (2011), Contrasting crustal production and rapid mantle transitions beneath back-arc ridges, Nature, 469, 198-202, doi: 10.1038/nature09690.

Duschenes, J., M.C. Sinha, and K.E. Louden (1986), A seismic refraction experiment in the Tyrrhenian Sea, Geophys. J. R. Astron. Soc. 85, 139–160.

Ebinger, C. J., (1989). Tectonic development of the western branch of the East African Rift. Geological Society of America Bulletin, 101, 885–903.

Escartín, J., G. Hirth, and B. Evans (1997) Strenght of slightly serpentinized peridotites: Implications for the tectonics of oceanic lithosphere, Geology, v. 29, p. 1023-1026, doi: 10.1130/0091-7613

Fabbri, A., and Curzi, P. (1981), Distribution of the Messininan Deposits in the Tyrrhenian Sea (Based on the seismic evidence), scale 1:1.500.000, Giornale di Geologia, Vol. XLIII, Pl. XXIX.

Faccena, C., T.W. Becker, F. P. Lucente, L. Jolivet, and F. Rossetti (2001), History of subduction and back-arc extension in the Central Mediterranean, Geophys. J. Int., 145, 809-820.

Faccena, C., C. Piromallo, A. Crespo-Blanc, L. Jolivet, and F. Rossetti (2004), Lateral slab deformation and the origin of the western Mediterranean arcs, Tectonics, Vol. 23, TC1012, doi:10.1029/2002TC001488

Fahlquist, D. A., and J.B. Hersey (1969), Seismic refraction measurements in the Western Mediterranean Sea, Bull. Insr. Oceanogr. Monaco, 67, l-52.

Finetti, I.R., M. Boccaletti, M. Bonini, A. Del Ben, R. Geletti, M. Pipan, and F. Sani (2001), Crustal section based on CROP seismic data across the North Tyrrhenian-Northern Apennines-Adriatic Sea, Tectonophysics, 343, 135-163.

Finlayson, D.M., C.D.N Collins, I. Lukaszyk, and E.C. Chudyk (1998), A transect across Australia's southern margin in the Otway Basin region: crustal architecture and the nature of rifting from wide-angle seismic profiling, Tectonophysics, 288, 177-189

Fowler, C. M. R. (2005), The Solid Earth: An Introduction to Global Geophysics, Cambridge University Press, Cambridge, United Kingdom, 685 pp.

Funizello, R., M. Parotto, and A. Praturlonet (1981), Carta Tettonica d'Italia, scala 1:1.500.000, Grafica Editiriale Cartografica SpA, Roma, Italy

Funk, T., H. R. Jackson, K. E. Louden, S. A. Dehler, and Y. Wu (2004), Crustal structure of the northern Nova Scotia rifted continental margin (eastern Canada), J. Geophys. Res., 109, B09102, doi:10.1029/2004JB003008.

Gailler, A., F. Klingelhoefer, J.-L. Olivet, and D. Aslanian (2009), Crustal structure of a young margin pair: New results across the Liguro-Provencçal Basin from wide-angle seismic tomography, Earth Planet. Sci. Let., 289, 333-345. doi: 10.1016/j.epsl.2009.07.001.

Gallart, J., N. Vidal, A. Estévez, J. Pous, F. Sàbat, C. Santisteban, E. Suriñach and the ESCI-València Trough Group (1995), The ESCI-Valencia Trough vertical reflection experiment: a seismic image of the crust from the NE Iberian Peninsula to the Western Mediterranean, Rev. Soc. Geol. España, 8(4), 401-415.

Gattacceca, J., A. Deino, R. Rizzo, D.S. Jones, B. Henry, B. Beaudoin, and F. Vadeboin (2007), Miocene rotation of Sardinia: New paleomagnetic and geochronological constraints and geodynamic implications, Earth Planet. Sci. Let., 258, 359-377, doi: 10.1016/j.epsl.2007.02.003.

Geoffroy, L. (2005) Volcanic passive margins, C.R. Geoscience, 337, 1395-1408, doi:10.1016/j.crte.2005.10.006

Gernigon, L., F. Lucazeau, F. Brigaud, J.-C. Ringenbach, S. Planke, and B. Le Gall (2006), A moderate melting model for the Voring margin (Norway) based on structural observations and thermo-kinematical modeling: Implication for the meaning of the lower crustal bodies, Tectonophys., 412, 255-278, doi:10.1016/j.tecto.2005.10.038

Gladczenko, T.P, M.F. Coffin, O. Eldholm (1997), Crustal structure of the Ontong Java Plateau: Modeling of new gravity and existing seismic data, J. Geophys. Res., 102, pp. 22.711-22.729

Gvirtzman, Z., and Nur, A. (2001), Residual topography, lithospheric structure and sunken slabs in the central Mediterranean, Earth Planet. Sci. Let., 187, pp. 117-130.

Hamilton, E.L. (1978), Sound velocity-density relations in sea-floor sediments and rocks, J. Acoust. Soc. Am., 63, 366-377.

Heuret, A., and Lallemand, S. (2005) Plate motions, slab dynamics and back-arc deformation, Physics of the Earth and Planetary Interiors, 149, 31-51, doi:10.1016/j.pepi.2004.08.022

Hieke, W., Glaçon, G., Hasegawa, S., Müller, C., and Peypouquet, J.P., 1990. Sedimentation in the Marsili Basin during Quaternary (ODP Site 650, Tyrrhenian Sea). In Kastens, K.A., Mascle, J., et al., Proc. ODP, Sci. Results, 107: College Station, TX (Ocean Drilling Program), 255–289. doi:10.2973/odp.proc.sr.107.120.1990

Isack, B. L., and M. Barazangi (1977), Geometry of Benioff Zones: Lateral segmentation and downwards bending of the subducted lithosphere , in *Island Arcs, Deep Sea Trenches and Back-Arc Basins*, *Maurice Ewing Ser.*, vol. 1, pp. 99–114, AGU, Washington, D. C., doi:10.1029/ME001p0099.

Karig, D.E., (1970) Ridges and Basins of the Tonga-Kermedec Island Arc system, J. Geophys. Res., v. 75, n.2, 239-254

Kastens, K. A., J. Mascle, C. Auroux, et al. (1987). Proc. ODP, Int. Repts., 107: College Station, TX (Ocean Drilling Program), doi: 10.2973/odp.proc.ir.107.1987

Kastens, K., and Mascle, J. (1990), The geological evolution of the Tyrrhenian Sea: an introduction to the scientific results of ODP LEG 107, In Kastens, K.A., Mascle, J., et al. (Eds.), Proceedings of the Ocean Drilling Program, Scientific Results 107, pp. 3-26. doi:10.2973/odp.proc.sr.107.187.1990

Keneth et al. (1978), Site 373: Tyrrhenian Basin, In Hsü, K., Montadert, L., et al. (1978), Initial reports of the Deep Sea Drilling Project, Volume 42, Part 1: Washington (U.S. Government Printing Office).

Kennett, J.P. (1982), Marine Geology, Prentice-Hall, Englewood Cliffs, New Jersey, 813 pp.

Kern, H, and Tubia, J.M., (1993), Pressure and temperature dependence of P- and S-wave velocities, seismic anisotropy and density of sheared rocks from the Sierra Alpujata massif (Ronda peridotites, Southern Spain), Earth Planet. Sci. Let., 119, 191-205

King, S.D., and Anderson, D.L., (1995). An alternative mechanism of flood basalt formation. Earth Planet. Sci. Lett., 136:269‐ 279.

Klein, E., C.H. Langmuir, (1987) Global correlations of ocean ridge basalt chemistry with axial depth and crustal thickness, J. Geophys. Res., 92, 8089–8115.

Klingelhoefer, F., C.-S. Lee, J.-Y. Lin, and J.-C Sibuet (2009), Structure of the southernmost Okinawa Trough from reflection and wide-angle seismic data, Tectonophysics, 466, 281-288, doi:10.1016/j.tecto.2007.11.031

Korenaga, J., W. S. Holbrook, G. M. Kent, P. B. Kelemen, R. S. Detrick, H.-C. Larsen, J. R. Hopper, and T. Dahl-Jensen (2000), Crustal structure of the southeast Greenland margin from joint refraction and reflection seismic tomography, J. Geophys. Res., 105(B9), 21, 591–21, 614, doi:10.1029/2000JB900188.

Korenaga, J., and Kelemen, P.B. (2000), Major element heterogeneity in the mantle source of the North Atlantic igneous province, Earth and Planet. Sci. Lat., 184, 251-268

Korenaga, J., W.S. Holbrook, R.S. Detrick, and P.B. Kelemen (2001), Gravity anomalies and crustal structure at the southeast Greenland margin, J. Gophys. Res., 106 (B5), 8853-8870.

Korenaga, J., (2004). Mantle mixing and continental breakup magmatism. Earth Planet. Sci. Lett., 218:463‑473, doi:10.1016/ S0012-821X(03)00674-5.

Lavier, L.L., and Manatschal, G., (2006) A mechanism to thin the continental lithosphere at magma-poor margins. Nature, 440:324–328, doi:10.1038/nature04608.

Lêpretre, A., F. Klingelhoefer, D. Graindorge, P. Schnurle, M. O. Beslier, K. Yelles, J. Déverchère, and R. Bracene (2013), Multiphased tectonic evolution of the Central Algerian margin from combined wide-angle and reflection seismic data off Tipaza, Algeria, J. Geophys. Res.: Solid Earth, Vol. 118, pp. 1-18, doi:10.1002/jgrb.50318

Lonergan, L., and White, N., (1997) Origin of the Betic-Rif mountain belt, Tectonics, 16, n. 3, pp. 504-522

Louden, K.E., and Chian, D., (1999) The deep structure of non-volcanic rifted continental margins, Phil. Trans. R. Soc. Lond. 357, 767-805

Lowrie, W. (2007), Fundamental of Geophysics, Cambridge University Press, New York, pp. 374

Lustrino, M., S. Duggen, and C.L. Rosenberg (2011), The Central-Western Mediterranean: Anomalous igneous activity in an anomalous collisional tectonic setting, Earth-Science Reviews, 104, 1-40, doi:10.1016/j.earscirev.2010.08.002.

Maclennan, J., D. McKenzie, K. Gronvold, (2001), Plume-driven upwelling under central Iceland, Earth Planet. Sci. Lett., 194, 67-82

Malinverno, A. and Ryan, W.B.F. (1986), Extension in the Tyrrhenian Sea and shortening in the Apennines as result of arc migration driven by sinking of the lithosphere, Tectonics, 5, 2, 227-245, doi:10.1029/TC005i002p00227.

Marani, M.P., and Gamberi, F. (2004), Structural framework of the Tyrrhenian Sea unveiled by seafloor morphology, in Marani, P., F. Gamberi, and E. Bonatti (Eds.), Memorie Descrittive della carta Geologica d'Itlaia, From seafloor to deep mantle: Architecture of the Tyrrhenian backarc basin, Vol. LXIV, pp 97-108.

Martinez, F., P. Fryer, N. A. Baker, and T. Yamazaki (1995), Evolution of backarc rifting: Mariana Trough, 20º-24ºN, J. Geophys. Res., Vol. 100, No. B3, pp. 3807-3827

Martinez, F., and Taylor, B. (2002), Mantle wedge control on back-arc crustal accretion, Nature, Vol. 416, 417-420

Martinez, F., K. Okino, Y. Ohara, A.-L. Reysenbach, and S.K. Goffredi (2007), Back-arc basins, Oceanography, 20 (No.1), 116-127.

Mascle, J and Rehault, J.-P. (1990), A revised seismic stratigraphy of the Tyrrhenian Sea: Implications for the basin evolution, In Kastens, K.A., Mascle, J., et al. (Eds.), Proceedings of the Ocean Drilling Program, Scientific Results 107, pp. 617-636.

Mauffret, A., and I. Contruccci (1999), Crustal structure of the North Tyrrhenian Sea: first results of the multichannel seismic LISA cruise. in Durand, B., Jolivet, L., Horvath, F. & Seranne, M. (Eds) The Mediterranean Basins: Tertiary Extension within the Alpine Orogen. Geological Society London, Special Publications, 156, 169-193.

Mauffret, A., Contrucci, I., Brunet, C. (1999), Structural evolution of the northern Tyrrhenian Sea from new seismic data, Marine and Petroleum Geology, 16 (5), 381-407.

McKenzie, D. P. (1978) Some remarks on the development of sedimentary basins. Earth Planet.Sci. Lett. 40, 25-32.

Michael, P. J., C. H. Langmuir, H. J. B. Dick, J. E. Snow, S. L. Goldstein, D. W. Graham, K. Lehnert, G. Kurras, W. Jokat, R. Mühe, and H. N. Edmonds (2003), Magmatic and amagmatic seafloor generation at the ultraslow-spreading Gakkel ridge, Arctic Ocean, Nature, Vol 423, 956-961.

Moeller, S., I. Grevemeyer, C. R. Ranero, C. Berndt, D. Klaeschen, V. Sallarès, N. Zitellini, and R. de Franco (2013), Rifted structure in the northern Tyrrhenian Sea Basin: results from a combined wide-angle and multichannel seismic study, Geochem. Geophy. Geosy., doi: 10.1002/ggge.20180

Molnar, P., and Atwater, T. (1978), Interarc spreading and Cordillera tectonics as alternates related to the age of subducted oceanic lithosphere, Earth Planet. Sci. Let., 41, pp. 330-340

Moritz, H. (2000), Geodetic Reference System 1980, J. Geod., 74(1), pp. 128-162, doi:10.1007/S001900050278

Moser, T.J. (1991), Shortest path calculation of seismic rays, Geophysics, 56, 59-67.

Moser, T.J., G. Nolet, and R. Snieder (1992), Ray bending revisted, Bull. Seismol. Soc. Am., 82, 259-288.

Mutter, J. C., Talwani, M., and Stoffa, P. L. (1982). Origin of seaward-dipping reflectors in oceanic crust off the Norwegian margin by subaerial sea-floor spreading. Geology 10, 353–357

Newman, P. (1973), Divergence effects in a layered Earth, Geophysics, Vol. 38, N. 3

Nicolich, R. (1981), Il profilo Latina-Pescara et le registrazione mediante OBS nel mar Tirreno, in 1 ° Convegno del Gruppo Nazionale Geofisica terra solida, CNR, Rome.

Nur, A., J. Dvorkin, G. Mavko, and Z. Ben-Avraham (1993), Speculations on the origins and fate of backarc basins, Ann. Geofis., 36, 155 – 163.

Paige, C.C., and Saunders, M.A. (1982), LSQR: An algorithm for sparse linear equation and sparse least squares, Trans. Math. Software, 8, 43-71.

Parker, R.L. (1972), The rapid calculation of potential anomalies, Geophys. J. R. Astron. Soc., 31, 447-455.

Parson, L.M., and Wright, I.C., (1996) The Lau-Havre-Taupo back-arc basin: A southward-propagating, multi-stage evolution from rifting to spreading, Tectonophysics, 263, 1-22

Pascal, G., M. Torné, P. Buhl, A.B. Watts, and A. Mauffret (1992), Crustal and velocity structure of the Valencia trough (western Mediterranean), Part II. Detailed interpretation of five Expanded Spread Profiles, Tectonophysics, 203, 21-35.

Pascal, G.P., Mauffret, A., Patriat, P., (1993) The ocean–continent boundary in the Gulf of Lion from analysis of expanding spread profiles and gravity modelling, Geophys. J. Int. 113, 701–726.

Peacock, K.L. and Treitel, S. (1969), Predictive Deconvolution: Theory and Practice, Geophysics, Vol. 34, No.2, pp. 155-169.

Peacock, S. M. (1996). Thermal and petrologic structure of subduction zones, Geophysical Monograph Series, 96, 119-133.

Pérez-Gusinyé, M., and T. J. Reston (2001), Rheological evolution during extension at nonvolcanic rifted margins: Onset of serpentinization and development of detachments leading to continental breackup, J. Geophys. Res., Vol. 106, No. B3, pp. 3961-3975

Pérez-Gusinyé, M., C. R. Ranero, T. J. Reston, and D. Sawyer (2003), Mechanisms of extension at nonvolcanic margins: Evidence from the Galicia interior basin, west of Iberia, J. Geophys. Res., Vol. 108, No. B5, doi: 10.1029/2001JB000901

Pérez-Gussinyé, M., J.P. Morgan, T.J. Resto, C.R. Ranero, (2006) The rift to drift transition at non-volcanic margins: Insights from numerical modelling, Earth and Planet. Sci. Let., 244, 458-473, doi:10.1016/j.epsl.2006.01.059

Pichon, X.L., and Sibuet, J.-C. (1981), Passive marigns: A model of Formation, J. Geophys. Res., vol 86, B5, pp3708-3720

Pinheiro, L.M., R. B. Whitmarsh, and P. R. Miles (1992), The ocean-continent boundary off the western continental margin of Iberia-II. Crustal structure in the Tagus Abyssal Plain, Geophys. J. Int., 109, 106-124

Pluijm, B. A. V. der, and Marshak, S., (2004) Earth Structure: An Introduction to Structural Geology and Tectonics, 2nd Edition, W.W. Norton & Company, New York, US.

Ranero, C.R., J.P. Morgan, K. McIntosh, C. Reichert (2003), Bending, faulting and mantle serpentinization at the Middle America Trench, Nature, 425, 367–373.

Ranero, C. R., and M. Pérez-Gusinyé (2010), Sequential faulting explains the asymmetry and extension discrepancy of conjugate margins, Nature, Vol. 468, pp. 294-300, doi: 10.1038/nature09520

Reid, I., H.R. Jackson, (1987) Oceanic spreading rate and crustal thickness, Mar. Geophys. Res. Lett. 14 1238–1241.

Reid, I. (1994), Crustal structure of a nonvolcanic rifted margin east of Newfoundland, J. Geophys. Res., Vol. 99, No. B8, pp. 15.161-15.180

Reid, I., and Jackson, H. R., (1997) Crustal structure of the northern Baffin Bay: Seismic refraction and tectonic implications, J. Geophys. Res., Vol 102; No B1, 523-542.

Recq, M., J.P Rehault, L. Steinmetz, A. Fabbri (1984), Amincissement de la croute et accretion au centre du basin Tyrrhénien d'après la sismique refraction, Mar. Geol., 85, 411 – 428.

Rehault, J. P., E. Moussat, and A. Fabbri (1987), Structural evolution of the Tyrrhenian Back-arc basin, Marine Geology, 74, pp. 123-150.

Reston, T. J., C. M. Krawczyk, and D. Klaeschen, (1996) The S reflector west of Galicia (Spain): Evidence from prestack depth migration for detachment faulting during continental breakup, J. Geophys. Res., 101, 8075– 8091

Reston, T., (2007) Extension discrepancy at North Atlantic nonvolcanic rifted margins: Depth-dependent stretching or unrecognized faulting?, Geology, v. 35, n.4, p. 367–370; doi: 10.1130/G23213A.1

Robin, C., P. Colantoni, M. Gennesseaux, and J.P. Rehault (1987), Vavilov seamount: a mildly alkaline Quaternary volcano in the Tyrrhenian basin, Mar. Geol., 78, 125-136.

Rollet, N., J. Déverchère, M.-O. Beslier, P. Guennoc, J.-P. Rehault, M. Sosson and C. Truffert (2002), Back-arc extension, tectonic inheritance, and volcanism in the Ligurian Sea, Western Mediterranean, Tectonics, 21 (No.3), doi: 10.1029/2001TC900027.

Rosenbaum, G., and G. S. Lister (2004), Neogene and Quaternary rollback evolution of the Tyrrhenian Sea, The Apennines, and the Sicilian Maghrebides, Tectonics, vol. 23, TC1013, doi:10.1029/2003TC001518, 2004.

Royden, L.H. (1993), The tectonic expression slab pull at continental convergent boundaries, Tectonics, 12 (No.2), 303-325.

Sallarès, V., J.J. Dañobeitia, and E.R. Flueh (2001), Lithospheric structure of the Costa Rican Isthmus: Effects of subduction zone magmatism on an oceanic plateau, J. Geophys. Res., 106 (B1), 621-643.

Sallarès, V., and Charvis, P., (2003) Crustal thickness constraints on the geodynamics evolution of the Galapagos Volcanic Province, Earth and Planet. Sci. Let., 214, 545-559, doi:10.1016/S0012-821X(03)00373-X

Sallarès, V., and C. R. Ranero (2005), Structure and tectonics of the erosional convergent margin off Antofagasta, north Chile (23_300S), J. Geophys. Res., 110, B06101, doi:10.1029/2004JB003418.

Sallarès, V., A. Gailler, M.-A. Gutscher, D. Graindorge, R. Bartolomé, E. Gràcia, J. Díaz, J.J. Dañobeitia, and N. Zitellini (2011), Seismic evidence for the presence of Jurassic oceanic crust in the central Gulf of Cadiz (SW Iberian margin), Earth Planet. Sci. Lett., doi:10.1016/j.epsl.2011.09.003

Sallarès, V., S. Martinez-Loriente, M. Prada, E. Gràcia, C. Ranero, M.-A. Gutscher, R. Bartolomé, A. Gailler, J.J. Dañobeitia, and N. Zitellini (2013a), Seismic evidence of exhumed mantle rock basement at the Gorringe Bank and the adjacent Horseshoe and Tagus abyssal plains (SW Iberia), Earth Planet. Sci. Let., 365, 120-131, doi: 10.1016/j.epsl.2013.01.021.

Sallarès, V., A. Meléndez, M. Prada, C. R. Ranero, K. McIntosh, and I. Grevemeyer (2013b), Overriding plate of the Nicaragua convergent margin: Relationship to the seismogenic zone of the 1992 tsunami earthquake, Geochem. Geophys. Geosyst., doi: 10.1002/ggge.20214

Sartori, R. (1990), The main results of ODP Leg 107 in the frame of Neogene to Recent geology of perityrrhenian areas, in Kastens, K.A., Mascle, J., et al. (Eds.), Proceedings of the Ocean Drilling Program. Scientific Results 107, pp. 715– 730.

Sartori, R., C. Carrara, L. Torelli, N. Zitellini (2001), Neogene evolution of the southwestern Tyrrhenian Sea (Sardinia Basin and western Bathyal Plain), Mar. Geol., 175, 47–66.

Sartori, R. (2003), The Tyrrhenian back-arc basin and subduction of the Ionian lithosphere, Episodes, 26 (3), 217-221.

Sartori, R., L.Torelli, N. Zitellini, G. Carrara, M. Matteo, P. Mussoni (2004), Crustal features along a W–E Tyrrhenian transect from Sardinia to Campania margins (Central Mediterranean), Tectonophysics, 383, 3–4, 171-192, doi: 10.1016/j.tecto.2004.02.008.

Savelli, C. (1988), Late Oligocene to Recent episodes of magmatism in and around the Tyrrhenian sea: implications for the processes of opening in a young inter-arc basin of intra-orogenic (Mediterranean) type, Tectonophysics 146, 163–181.

Savelli, C. (2002), Time-space distribution of magmatic activity in the western Mediterranean and peripheral orogens during the past 30 Ma (a stimulus to geodynamic considerations), J. Geodyn., 34, 99-126.

Schettino, A., and Turco, E. (2011), Tectonic history of the western Tethys since the Late Triassic, Geological Society of America Bulletin, 123 (No.1/2), 89-105, doi: 10.1130/B30064.1.

Serri, G., F. Innocenti, and P. Maetti (1993), Geochemical and petrological evidence of the subduction of delaminated Adriatic continental lithosphere in the genesis of the Neogene-Quaternary magmatism of central Italy, Tectonophysics, 223, pp. 117-147

Shipboard Scientific Party, (1987), Site 654: Upper Sardinia Margin. In Kastens, K. A., Mascle, J., Auroux, C , et al., Proc, Init. Repts. (Pt. A) ODP, 107, 10, p 747-857, doi:10.2973/odp.proc.ir.107.110.1987

Sibuet, J.-C. (1992) Formation of non-volcanic passive margins: a composite model applies to the conjugate Galicia and southeastern Flemish Cap margins, Geophys. Res. Let., Vol. 19, No. 8, pp. 769-772

Sibuet, J.-C., S. Sirvastava, and G. Manatschal (2007) Exhumed amntle-forming transitional crust in the Newfoundland-Iberia rift and associated magnetic anomalies, J. Geophys. Res., Vol. 112, 06105, doi:10.1029/2005JB003856

Spakman, W. and Wortel, R. (2004), A tomographic view on the Western Mediterranean Geodynamics, in: The TRANSMED Atlas, The Mediterranean Region from Crust to Mantle, Edited by: Cavazza, W., Roure, F., Spakman, W., Stamgli, G.M., Ziegler, P., pp.31-52

Steinmetz, L., F. Ferrucci, A. Hirn, C. Morelli, and R. Nicolich (1983), A 550 km long Moho traverse in the Tyrrhenian Sea from O.B.S. Recorded Pn waves, Geophys. Res. Let., 10 (No.6), 428-431.

Syracuse, E.M., P.E. van Keken, and G.A. Abers (2010) The global range of subduction zone thermal model, Physics and Earth and Planetary Interiors, 183, 73-90, doi:10.1016/j.pepi.2010.02.004

Taylor, B. (1995), Backarc Basins: Tectonics and Magmatism, Plenum Press, New York, 524 pp.

Taylor, B., A. Goodliffe, F. Martinez, and R. Hey, (1995), Continental and initial sea-floor spreading in the Woodlark basin, Nature, Vol. 374, p. 534-537

Taylor, S.R., (1967) The origin and growth of continents, Tectonophysics, 4(1), 17-34

Tarantola, A., and Valette, B., (1982) Inverse Problems=Quest for Information, J. Geophys., 50, 159-170

Tarantola, A. (1987), Inverse Problem Theory: Methods for Data Fitting and Model Parameter Estimation, Elsevier Science, New York. 613 pp.

Todd, B. J. and Reid, I., (1989) The continent–ocean boundary south of Flemish Cap: constraints from seismic refraction and gravity, Canadian Journal of Earth Sciences, Vol. 26, No. 7 : pp. 1392-1407 (doi: 10.1139/e89-119)

Toomey, D.R., and G.R. Foulger (1989), Tomographic inversion of local earthquake data from Hengill-Grensdalur central volcano complex, Iceland, J. Geophys. Res., 94, 17497-17510.

Toomey, D.R., S.C. Solomon, and G.M. Purdy (1994), Tomographic imaging of the shallow crustal structure of the East Pacific Rise at 9º30’N, J. Geophys. Res., 99, 24.135-24.157

Trincardi, F., and N. Zitellini (1987), The rifting of the Tyrrhenian Basin, Geo-Marine Letters, 7, 1-6, doi: 10.1007/BF02310459.

Tucholke, B.E., Sawyer, D.S., and Sibuet, J.-C., (2007), Breakup of the Newfoundland-Iberia rift. In Karner, G.D., Manatschal, G., and Pinheiro, L.M. (Eds.), Imaging, Mapping and Modeling Continental Lithosphere Extension and Breakup, Geol. Soc., Spec. Publ., 282:9‑46.

Turcotte, D. L., and Schubert, G. (2002), Geodynamics, Second Edition, Cambridge University Press, Cambridge, United Kingdom, 456 pp.

Turner, I.M., C. Peirce, and M.C. Sinha (1999), Seismic imaging of the axial region of the Valu Fa Ridge, Lau Basin—the accretionary processes of an intermediate back-arc spreading ridge, Geophys. J. Int., 138, 495-519.

Van Avendonk, H.J.A., W.S. Holbrook, G.T. Nunes, D.J. Shillington, B.E. Tucholke, K.E. Louden, H.C. Larsen, and J.R. Hoope (2006), Seismic velocity structure of the rifte margin of the eastern Grand Banks of Newfoundland, Canada, J. Geophys. Res., Vol. 111, B11404, doi:10.1029/2005JB004156

Vignaroli, G., C. Faccena, F. Rossetti, and L. Jolivet (2009), Insights from the Apennines metamorphic complexes and their bearing on the kinematics evolution of the orogen, in VAN HINSBERGEN, D. J. J., M. A. EDWARDS, and R. GOVERS (Eds), Collision and Collapse at the Africa-Arabia-Eurasia Subduction Zone. The Geological Society, London, Special Publications, 311, 235–256.

White, R., and McKenzie, D. (1989) Magma at Rift Zones: The Generation of Volcanic Continental Margins and Flood Basalts, J. Geophys. Res., Vol. 94, No. B6, pp 7685-7729

White, R.S., D. McKenzie, and R.K. O'Nions (1992), Oceanic crustal thickness from seismic measurements and rare earth element inversions. J. Geophys. Res. 97, 19683–19715.

White, R.S., L.K. Smith, A.W. Roberts, P.A.F. Christie, N.J.Kusznir, and the rest of the iSIMM Team (2008) Lower-crustal intrusion on the North Atlantic continental margin, Nature, Vol. 452, doi:10.1038/nature06687460

Whitmarsh, R.B., and Wallace, P.J., 2001. The rift-to-drift development of the west Iberia nonvolcanic continental margin: a summary and review of the contribution of Ocean Drilling Program Leg 173. In Beslier, M.-O., Whitmarsh, R.B., Wallace, P.J., and Girardeau, J. (Eds.), Proc. ODP, Sci. Results, 173: College Station, TX (Ocean Drilling Program), 1–36. doi:10.2973/odp.proc.sr.173.017.2001

Yilmaz, O., (2001). Seismic data processing. Society of exploration geophysicists, ed.:Doherty, S., Tulsa, US, 522 pp.

Zelt, C.A., and Smith, R.B., (1992) Seismic traveltime inversion for 2-D crustal velocity structure, Geophys. J. Int., 108, 16-34

Zhang, J., and Toksöz, M.N, (1998) Nonlinear refraction traveltime tomography, Geophysics, 63, 1726-1737

Zitellini N., F. Trincardi, M. Marani, and A Fabbri (1986), Neogene tectonics of the northern Tyrrhenian Sea, Giorn. Geol, 48, 1, 2.

Websites:

http://www.earth.northwestern.edu/people/seth/202/new_2004/wilson_cycle.html
http://earthquake.usgs.gov/earthquakes/world/seismicity_maps/index.php
http://earthquake.usgs.gov/learn/topics/plate_tectonics/plates.php
http://www.glossary.oilfield.slb.com/en/Terms/s/stack.aspx
http://pubs.usgs.gov/gip/dynamic/inside.html
http://pubs.usgs.gov/publications/text/fire.html
http://www.xsgeo.com/course/basic.htm#radon

Annex

A.1 Wide-angle seismic records

A.1.1 Line GH

From top to bottom, record section, data fit and ray-tracing of all the receivers used to obtain the 2D P-wave velocity model of Line GH (Figure 6.2a). In the data fit panels, the black and white circles correspond to the picked and calculated data, respectively. While the thick black line in the ray-tracing panels represents the inverted Moho geometry, and the white circle the receiver location.

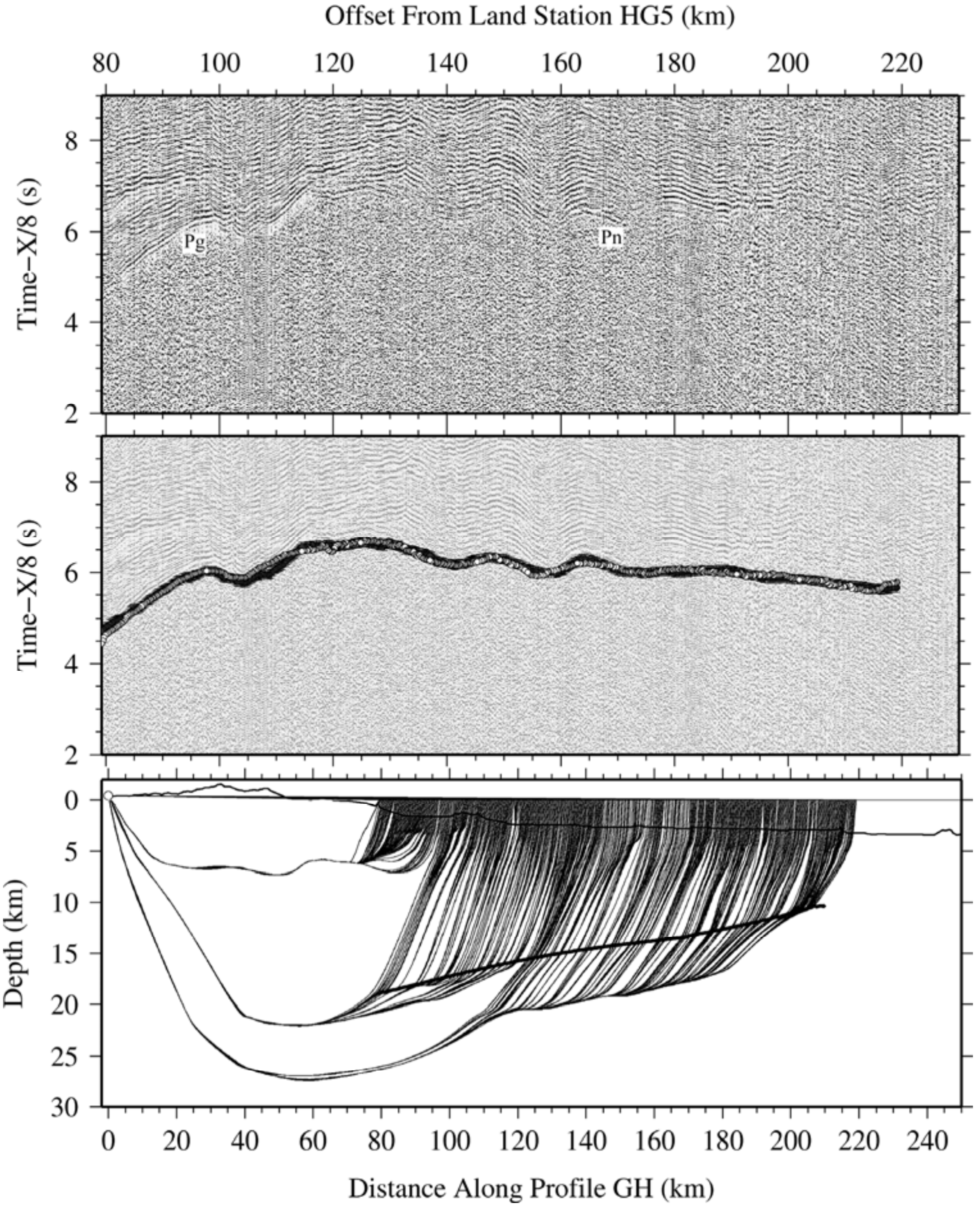

Figure A.1.1.1.-*Land station HG 5*

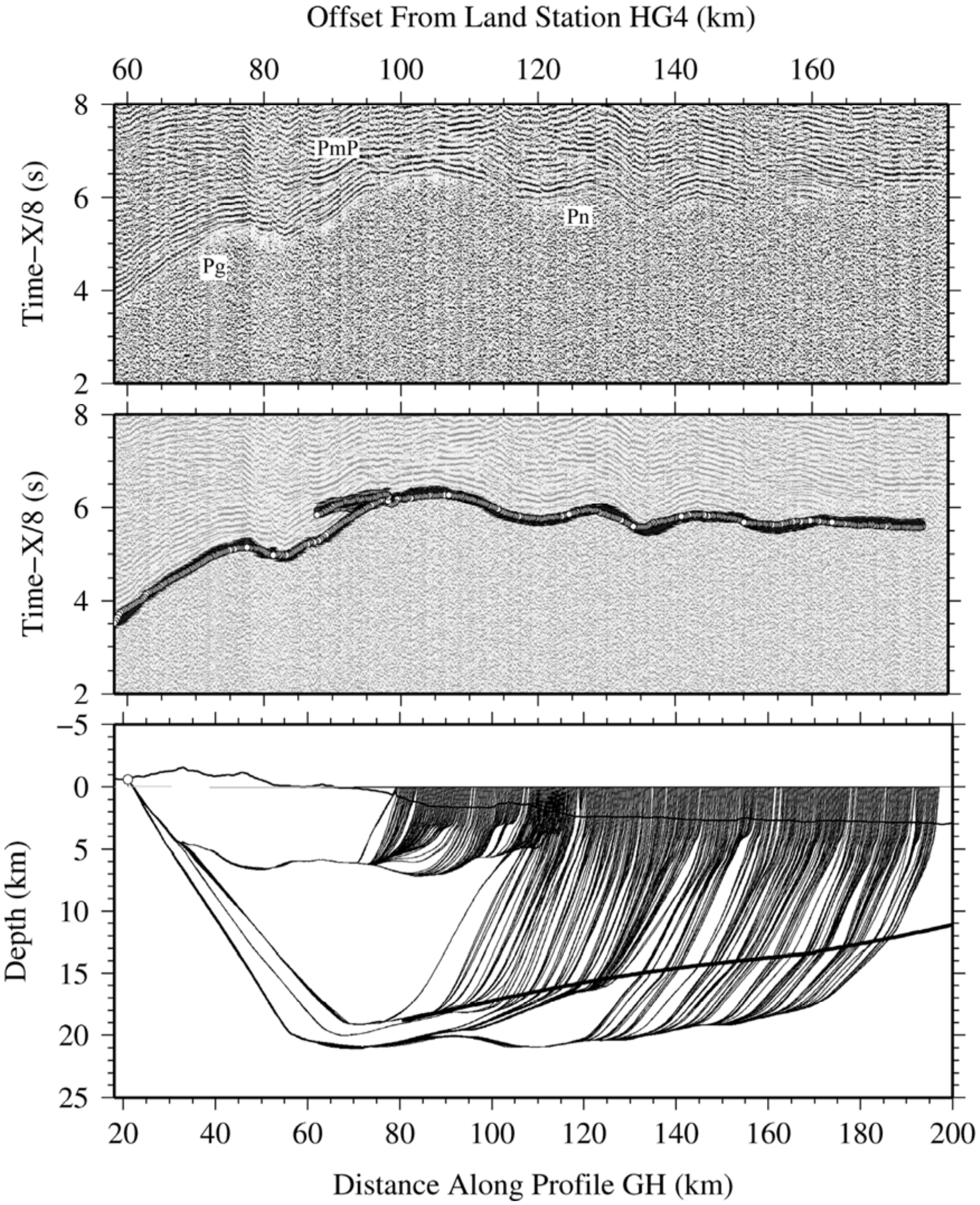

Figure A.1.1.2.-*Land station HG 4*

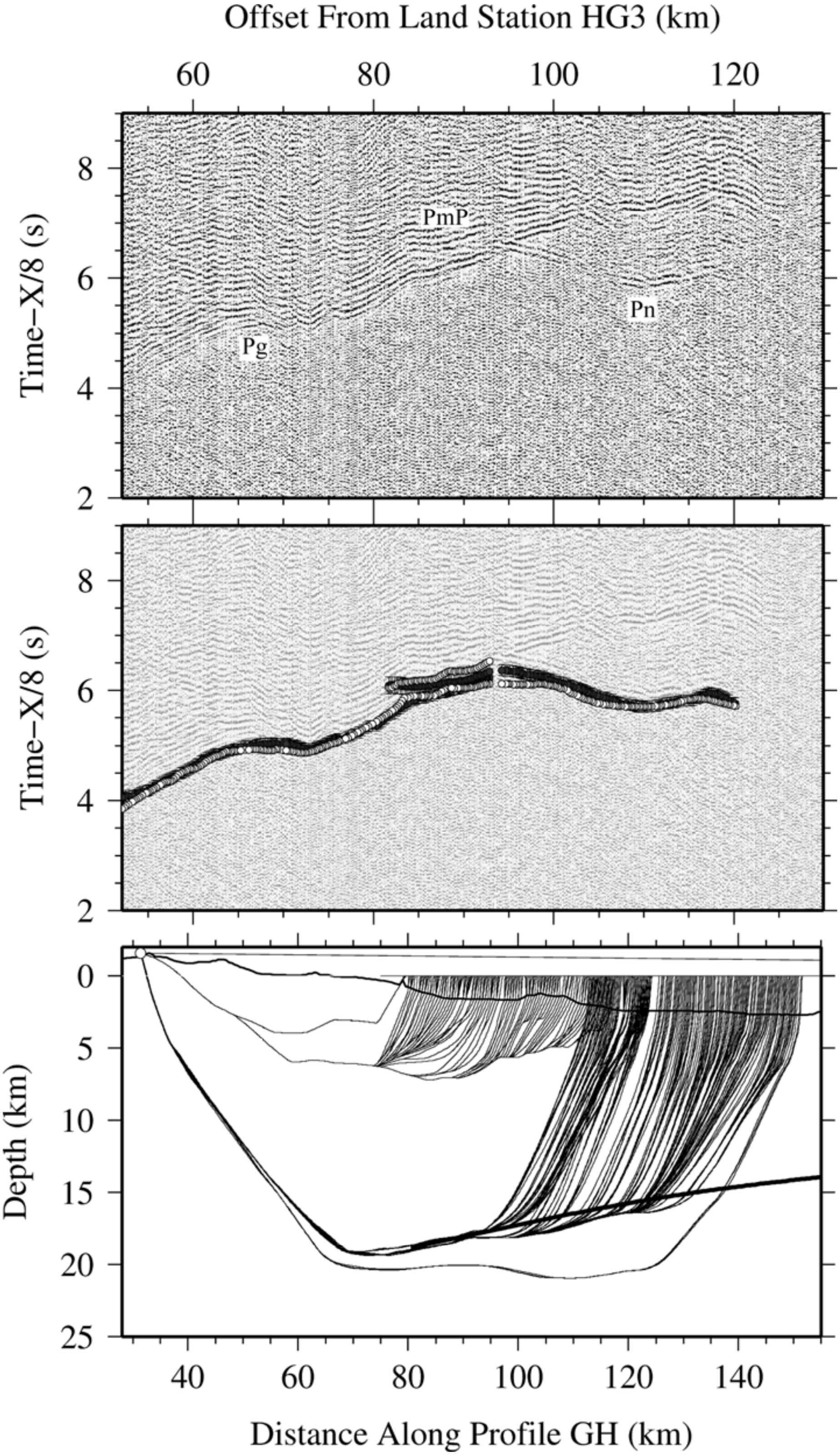

Figure A.1.1.3.-*Land station HG 3*

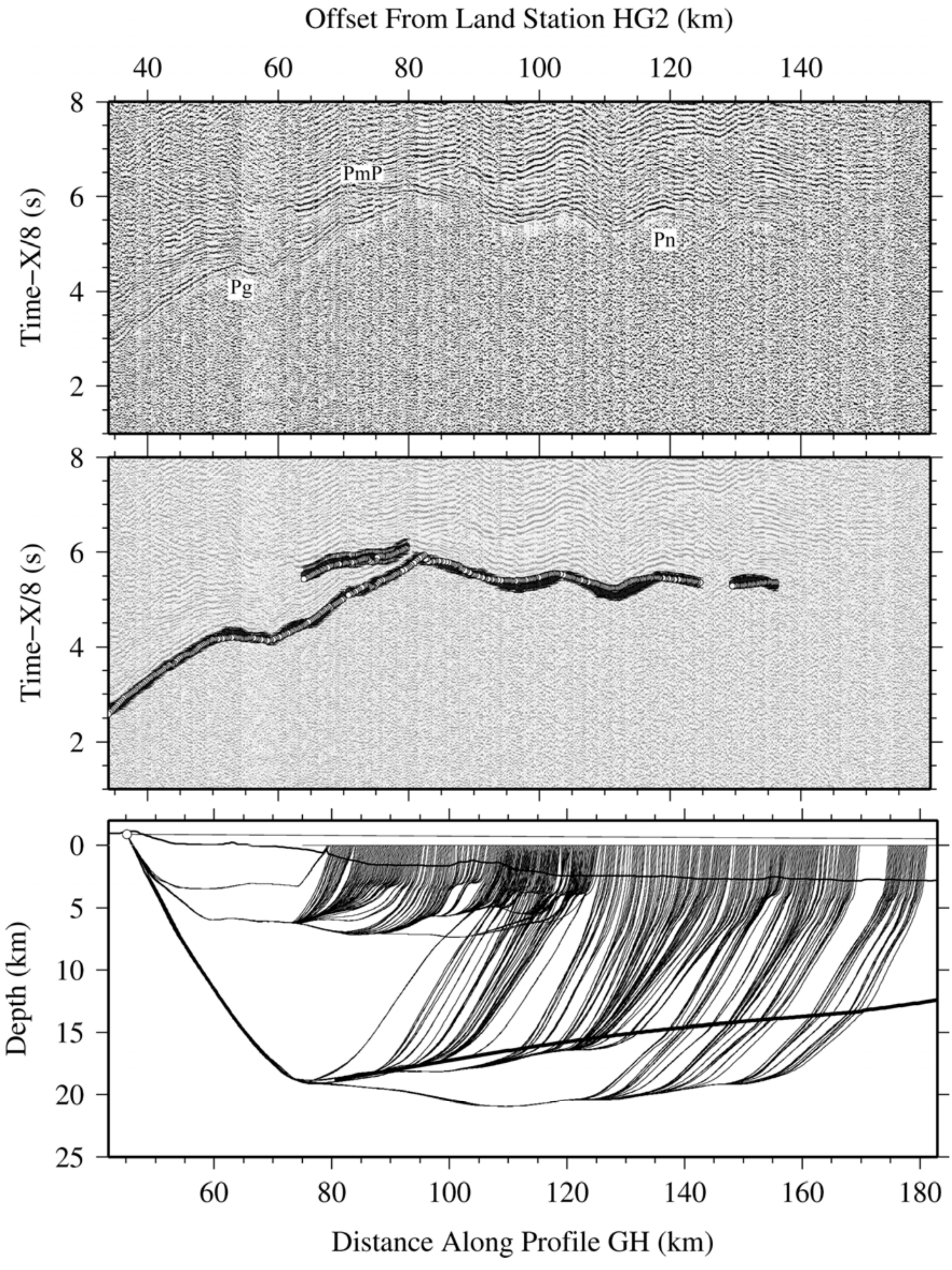

Figure A.1.1.4.-*Land station HG 2*

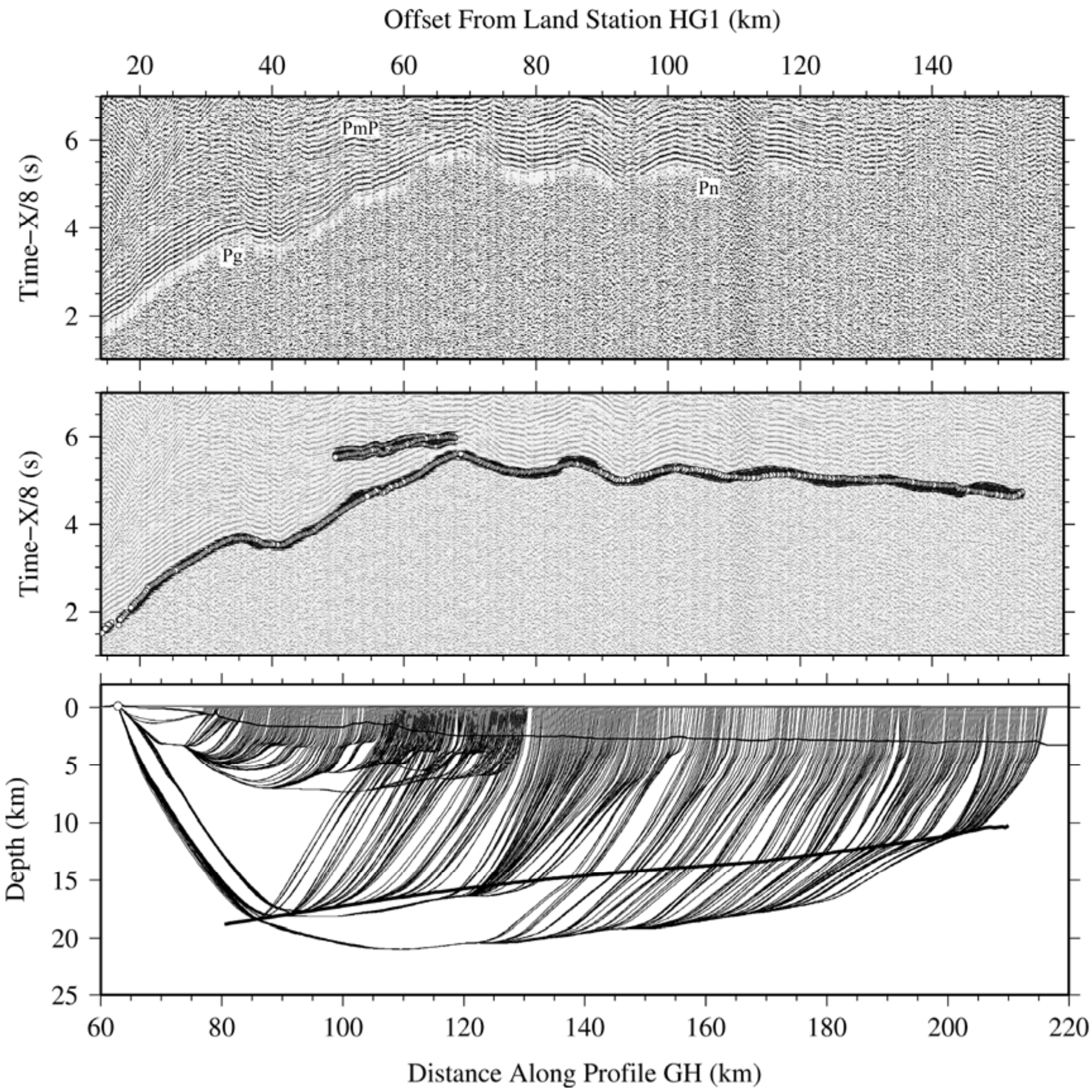

Figure A.1.1.5.-*Land station HG 1*

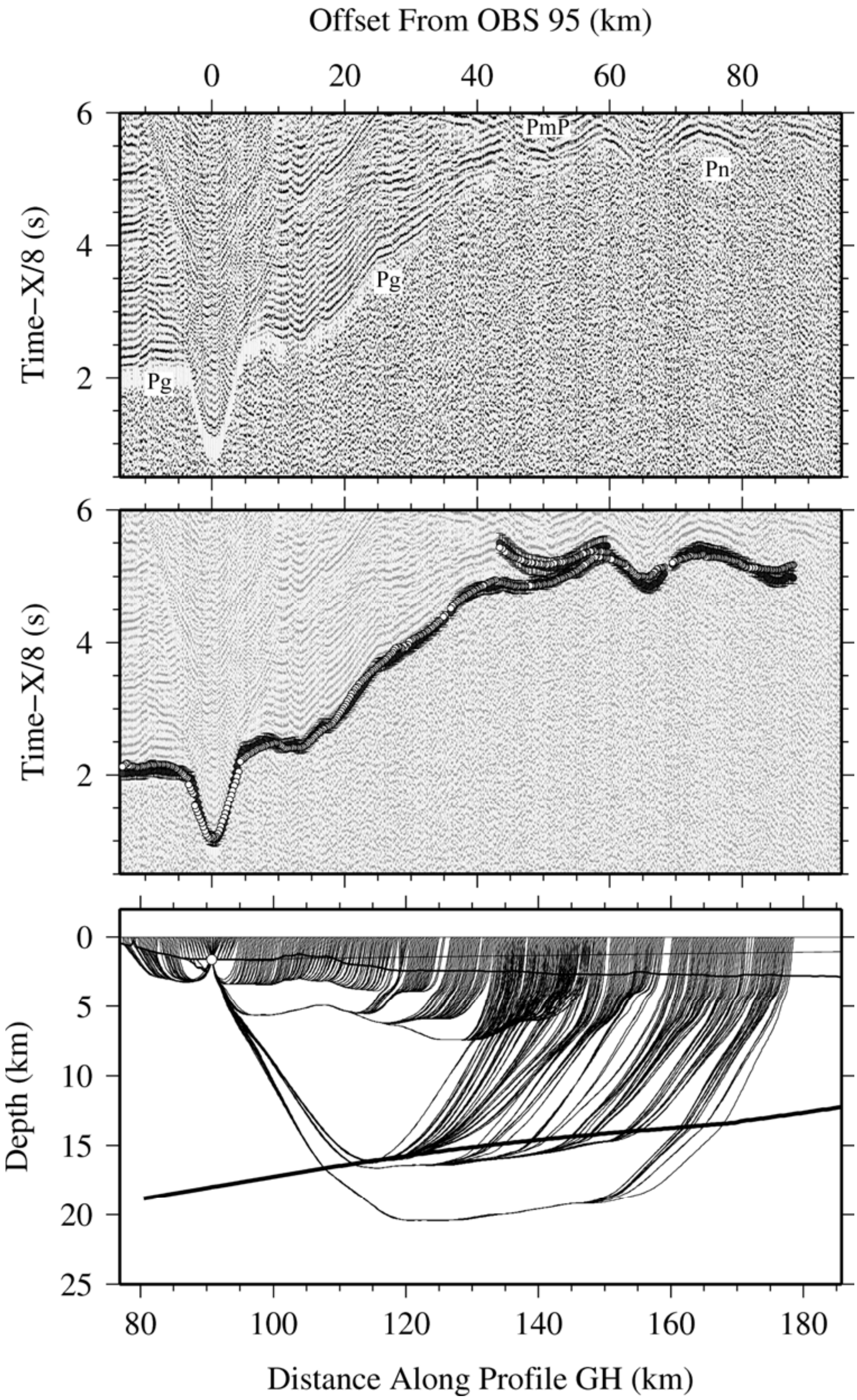

Figure A.1.1.6.-*OBS 95*

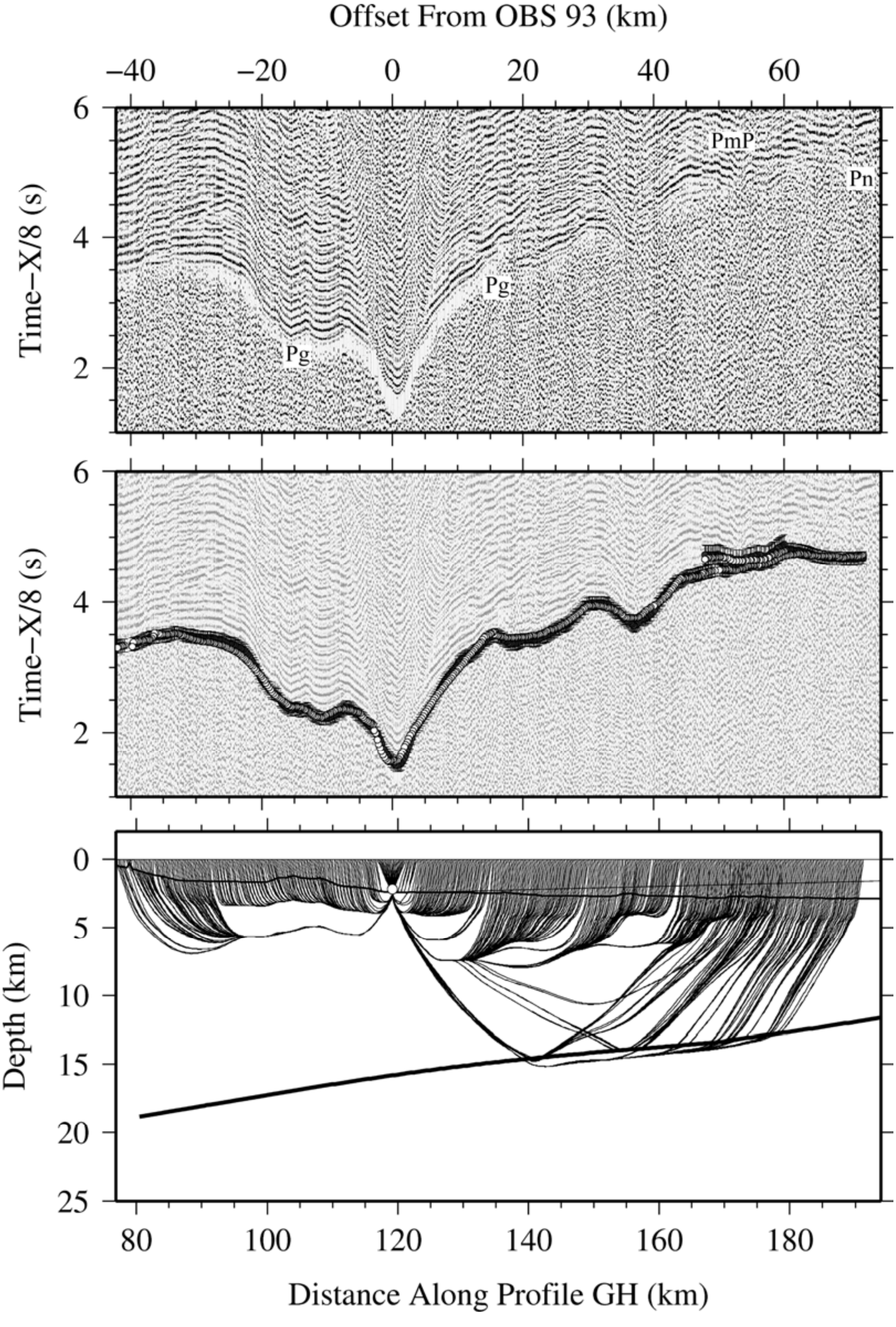

Figure A.1.1.7.-*OBS 93*

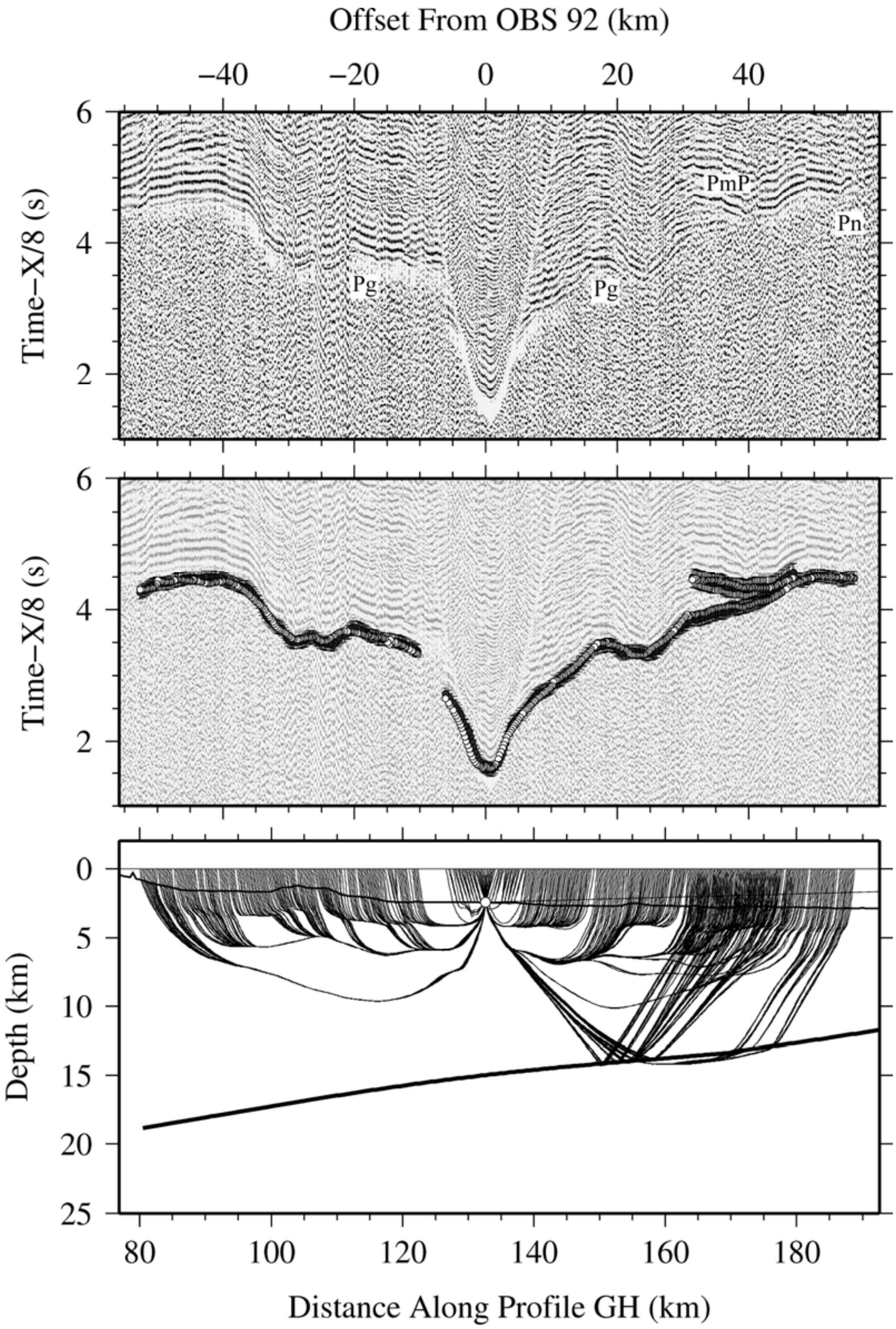

Figure A.1.1.8.-*OBS 92*

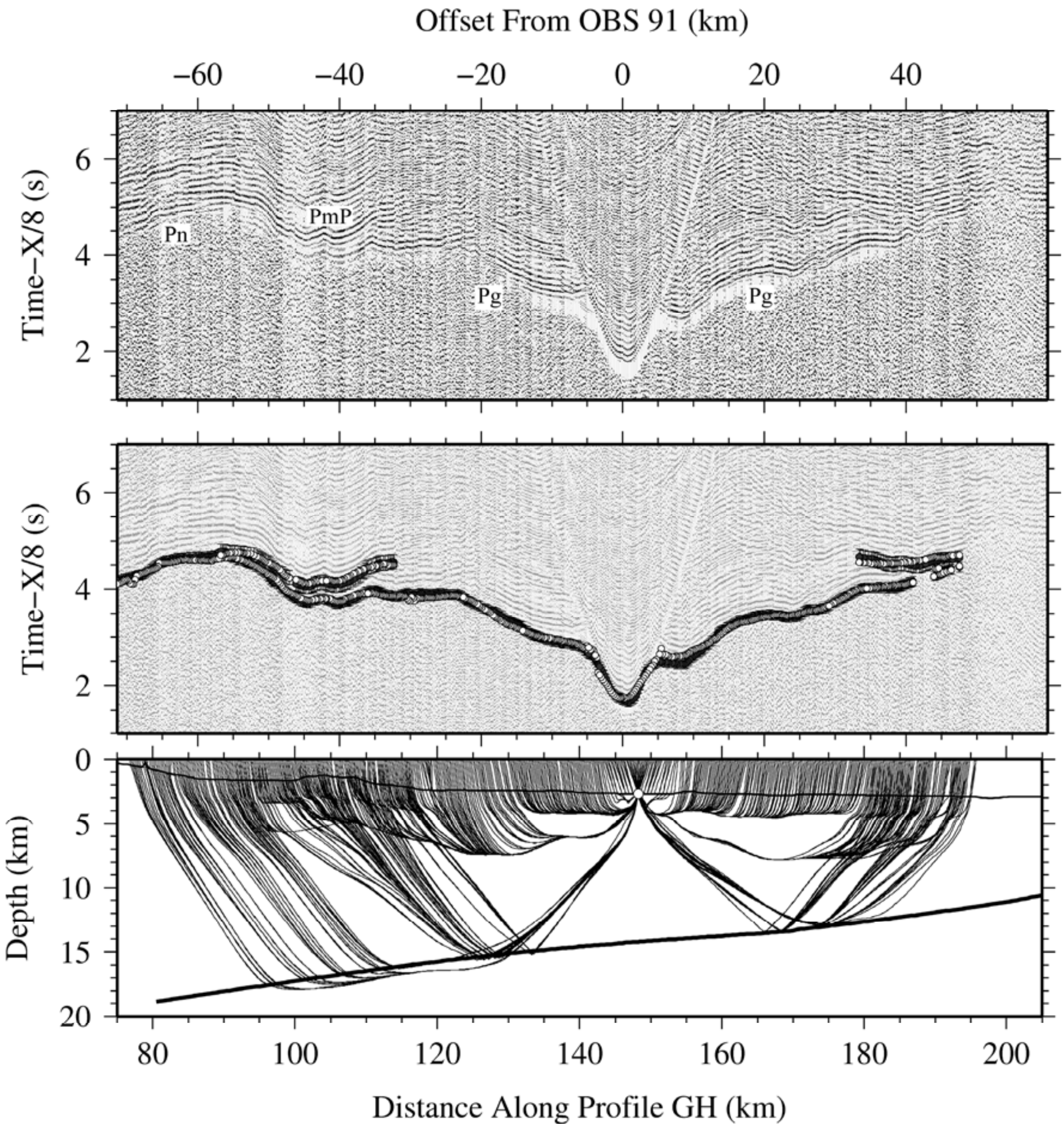

Figure A.1.1.9.-*OBS 91*

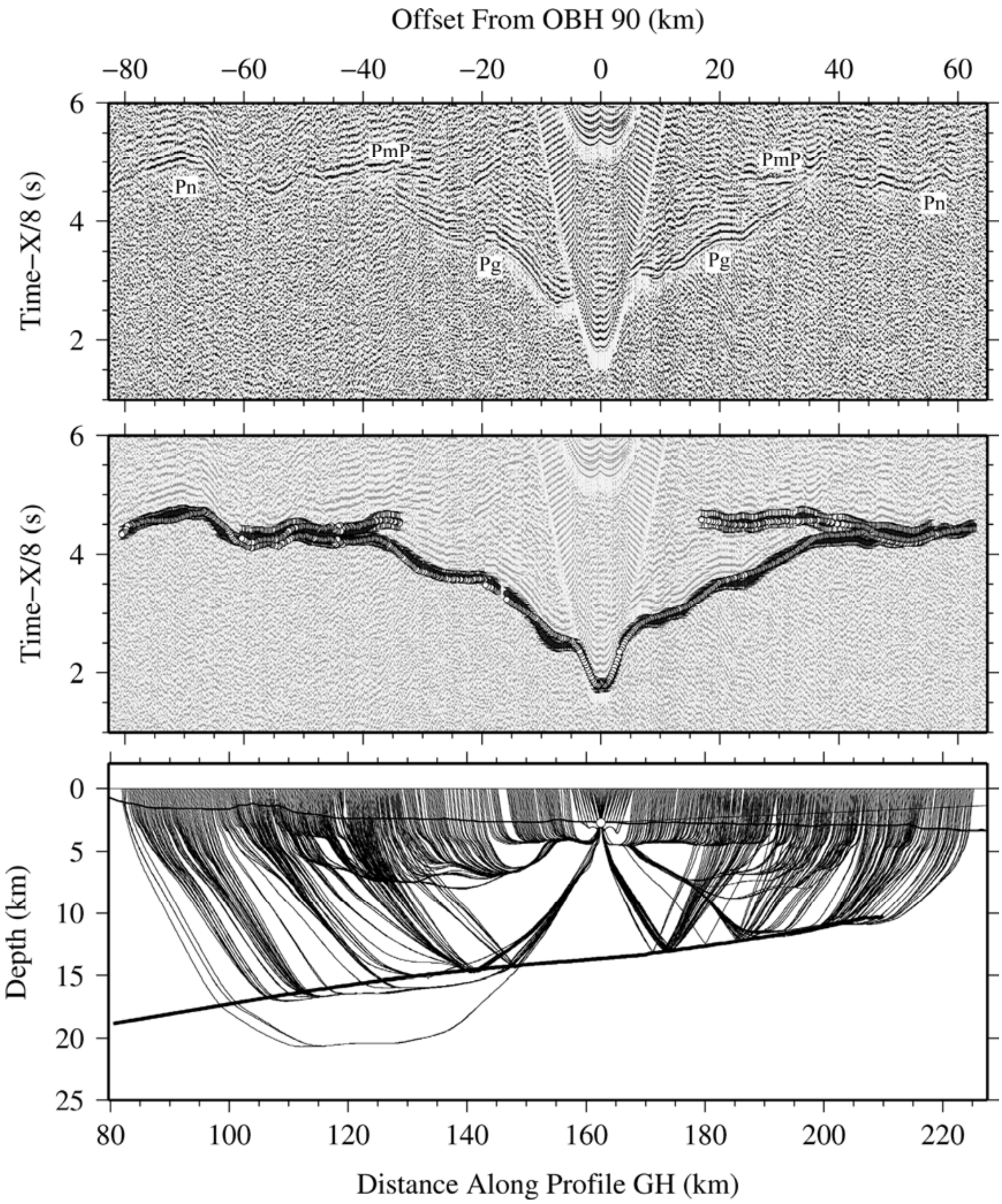

Figure A.1.1.10.-*OBH 90*

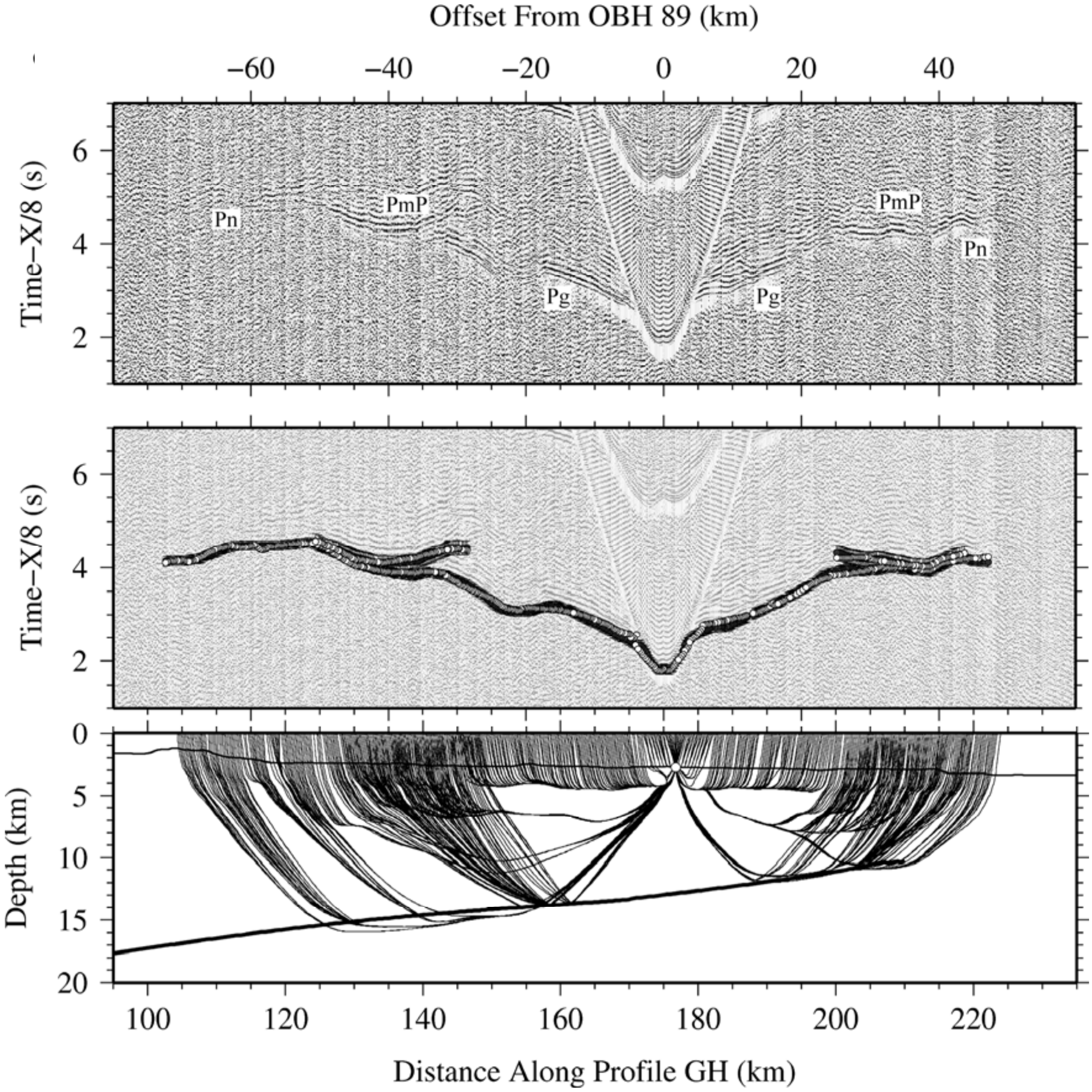

Figure A.1.1.11.-*OBH 89*

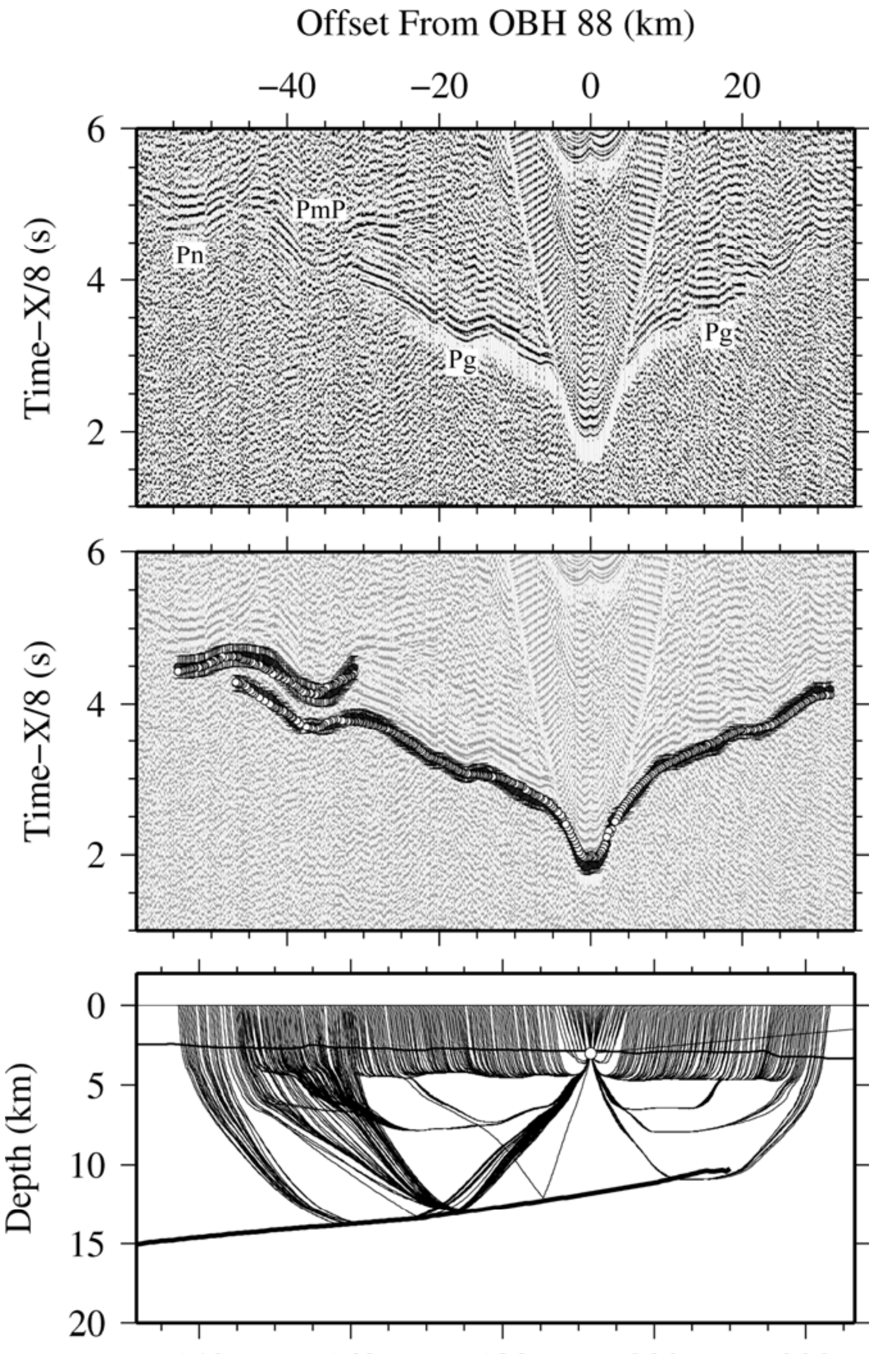

Figure A.1.1.12.-*OBH 88*

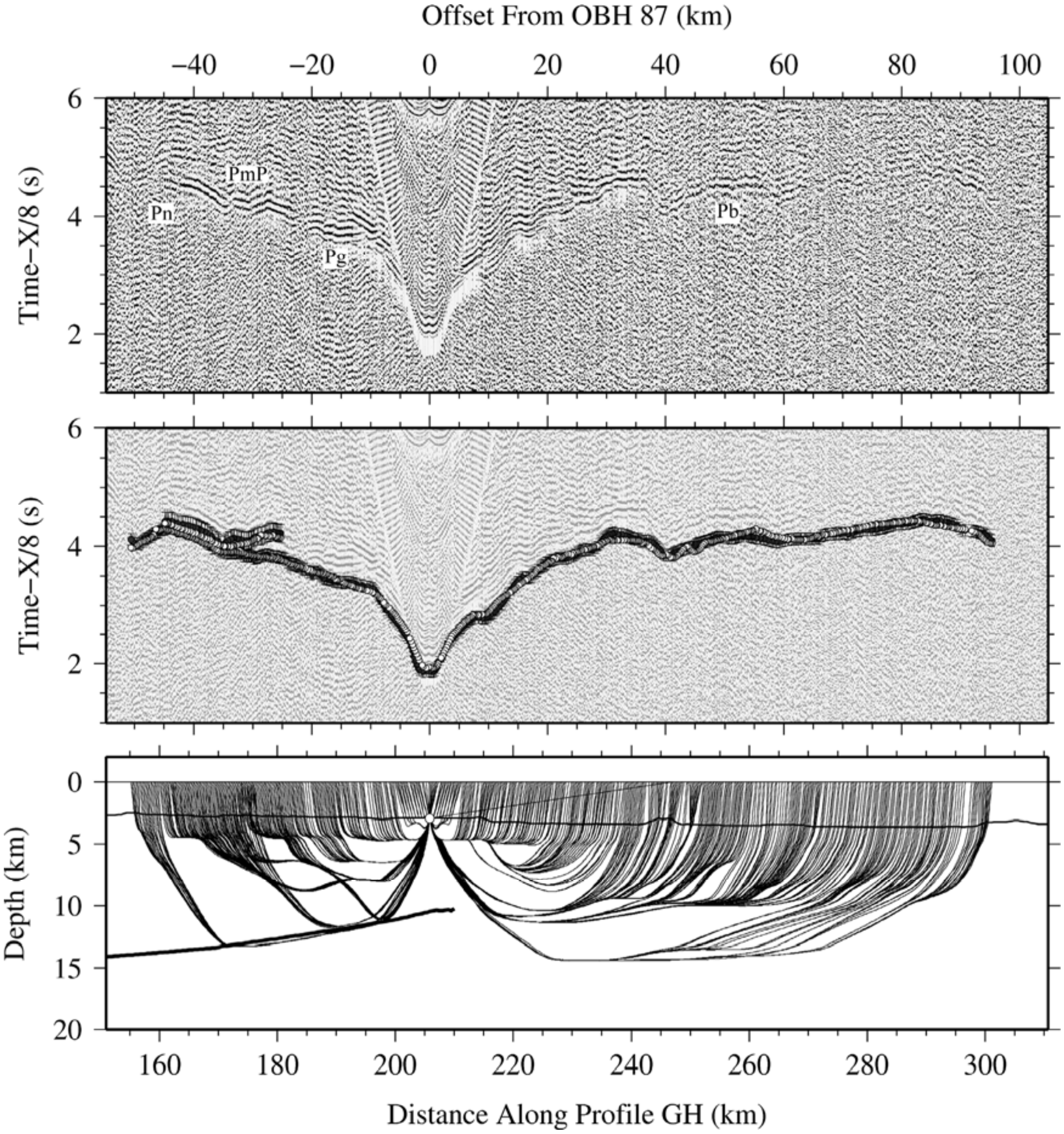

Figure A.1.1.13.-*OBH 87*

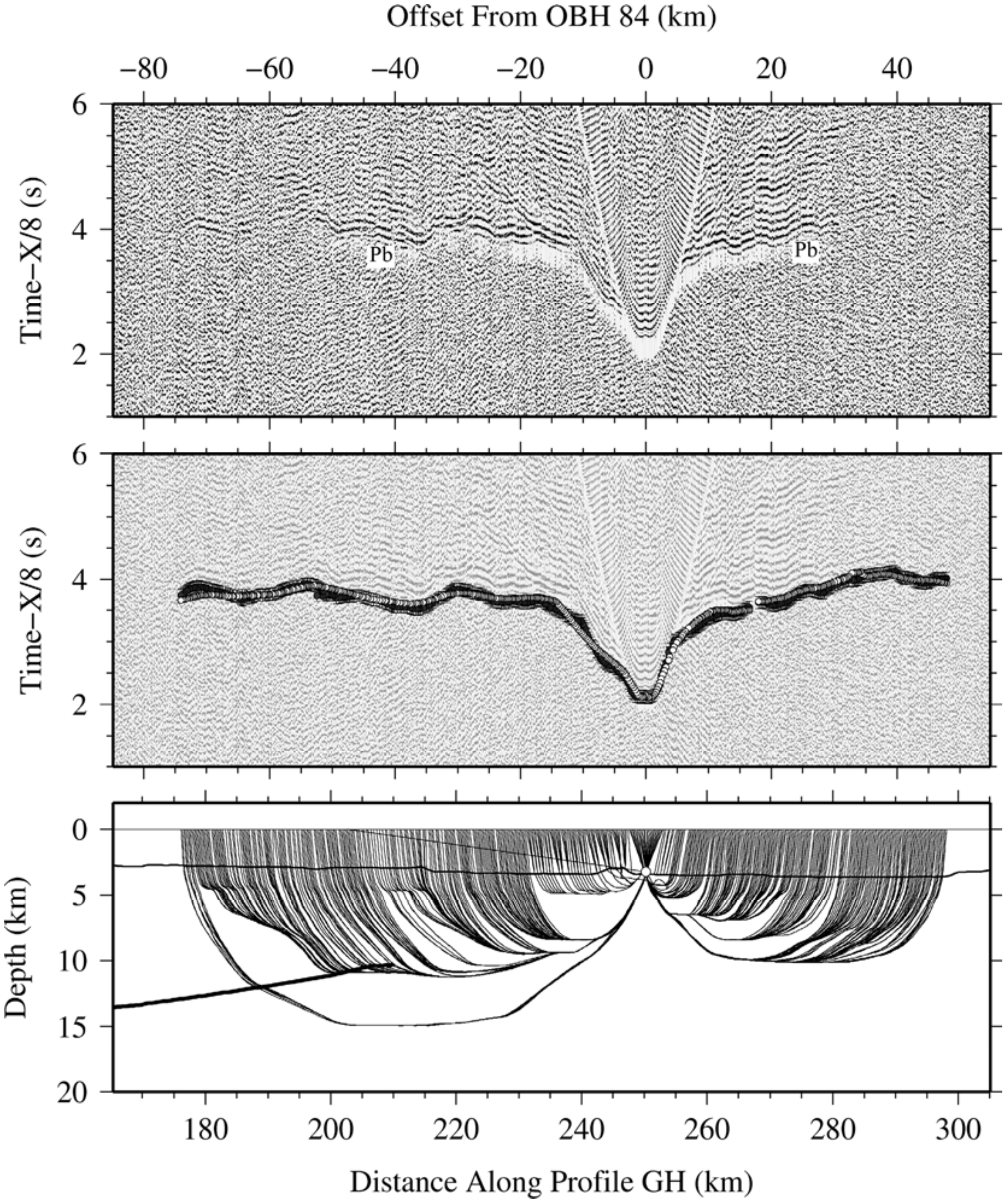

Figure A.1.1.14.-*OBH 84*

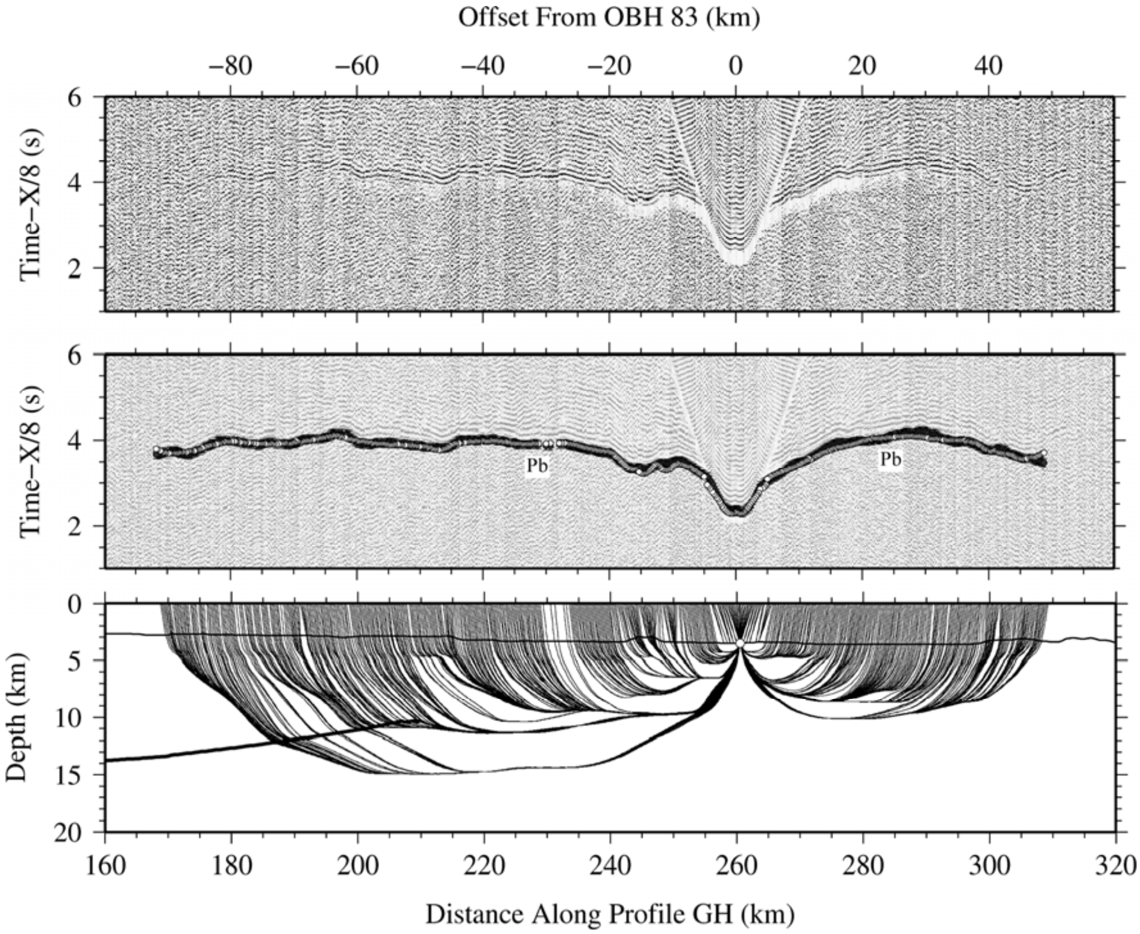

Figure A.1.1.15.-*OBH 83*

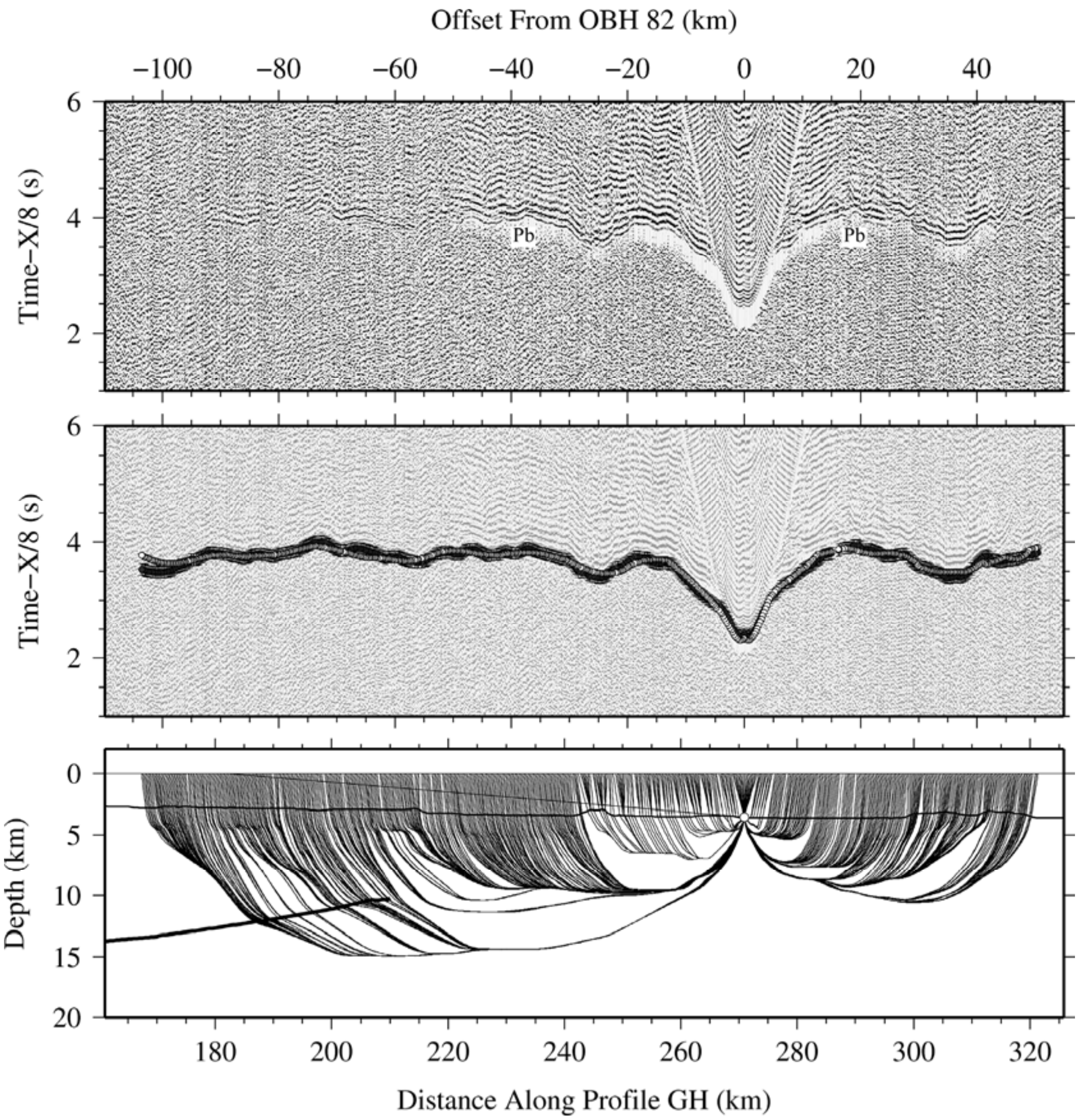

Figure A.1.1.16.-*OBH 82*

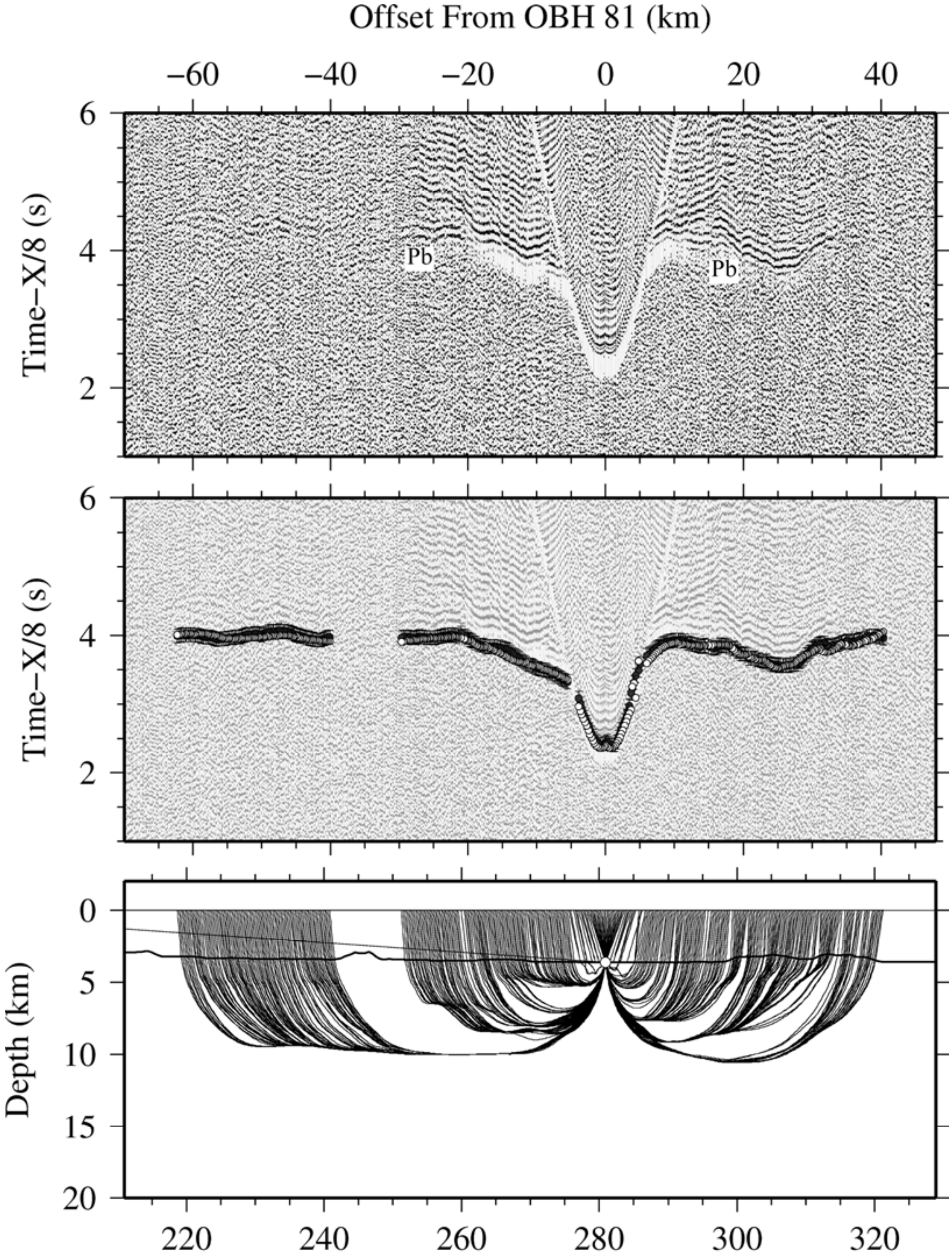

Figure A.1.1.17.-*OBH 81*

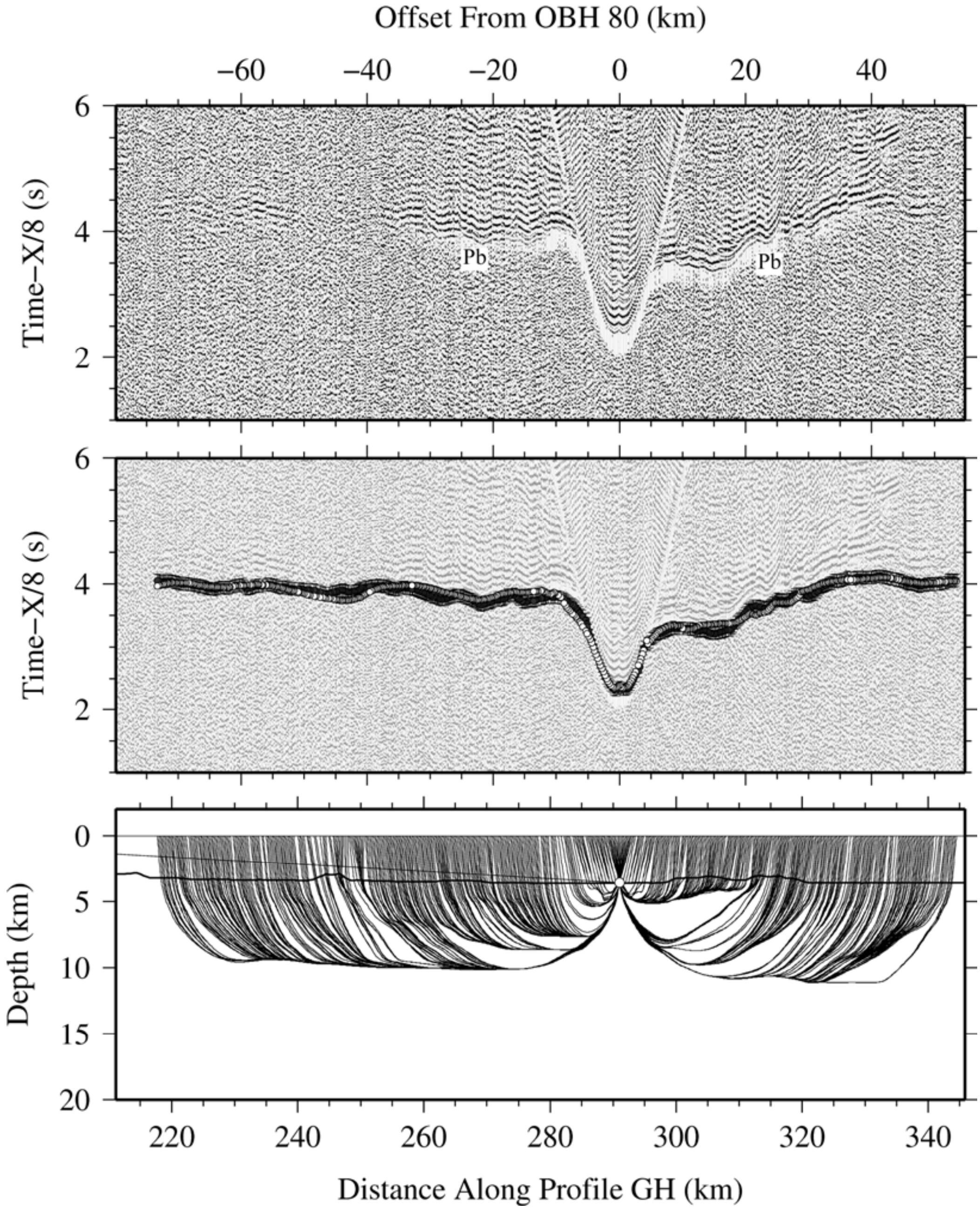

Figure A.1.1.18.-*OBH 80*

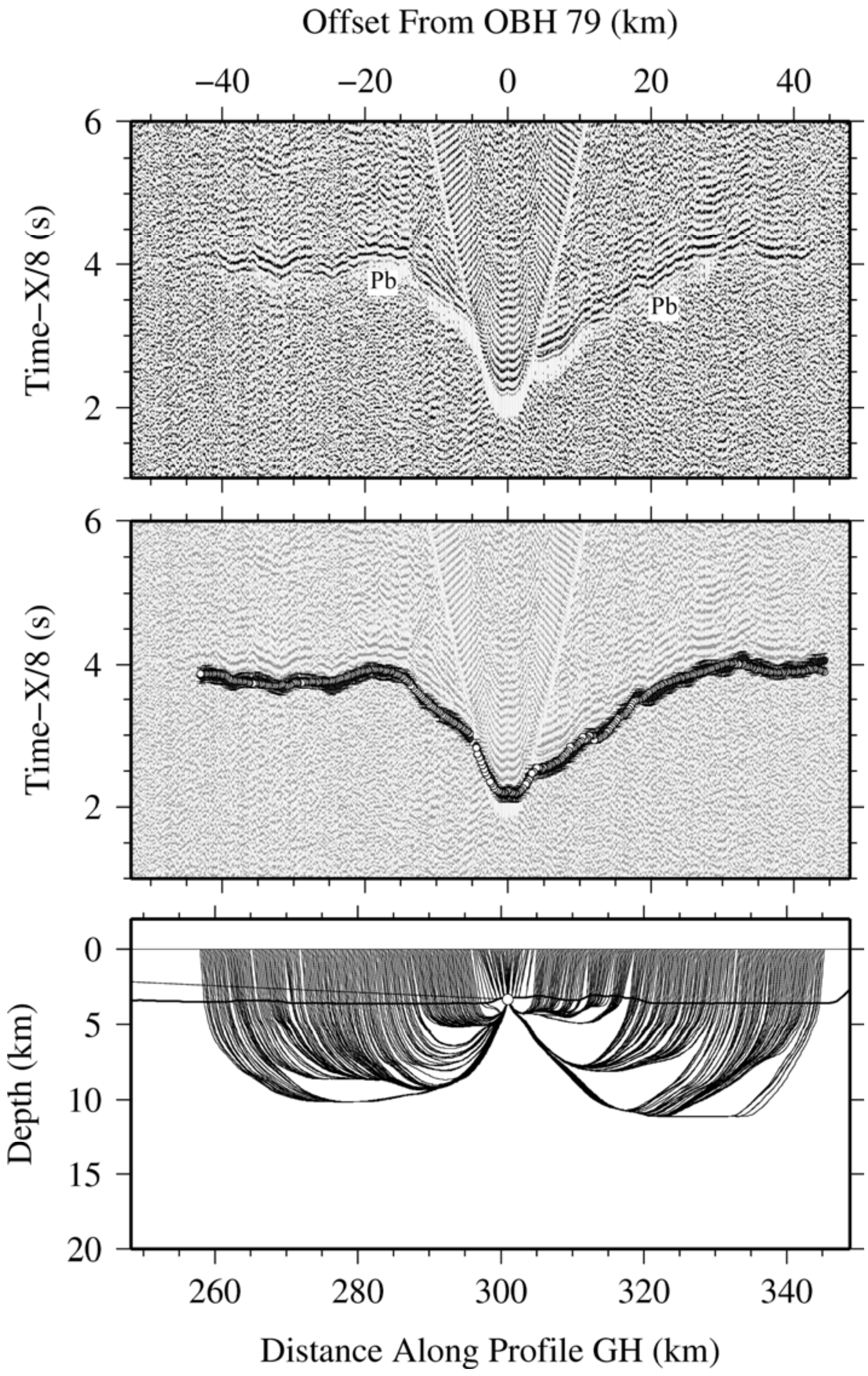

Figure A.1.1.19.-*OBH 79*

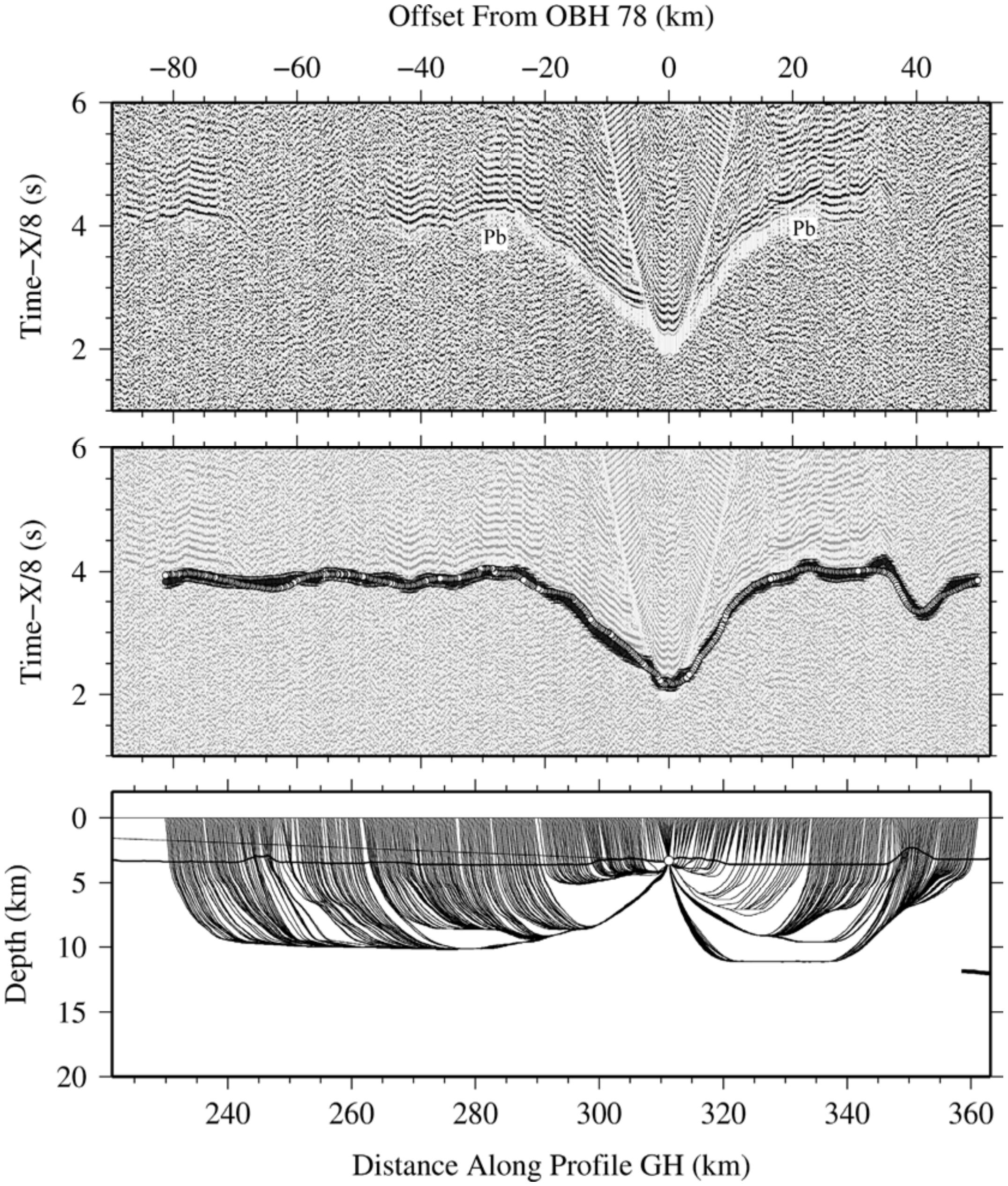

Figure A.1.1.20.-*OBH 78*

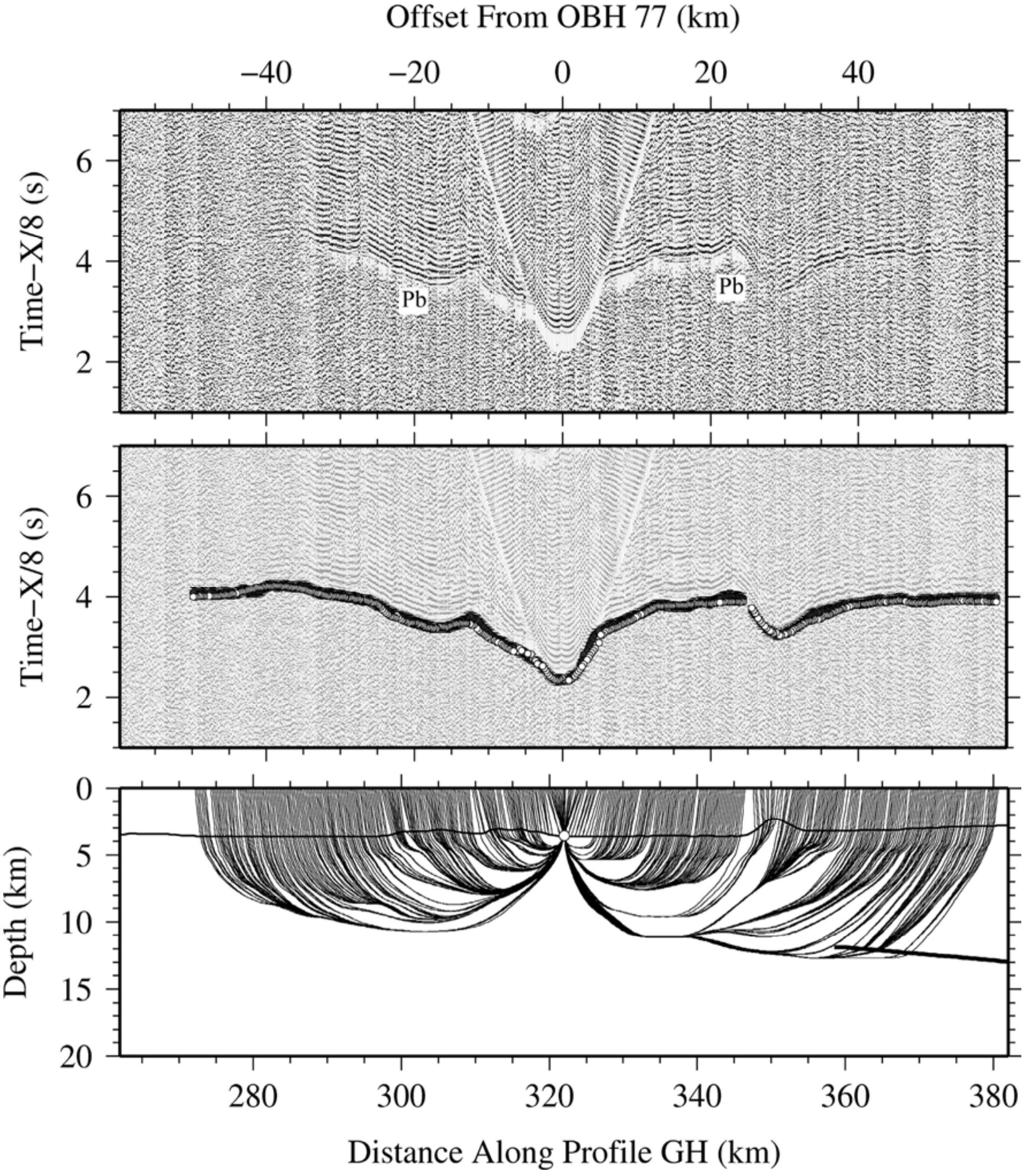

Figure A.1.1.21.-*OBH 77*

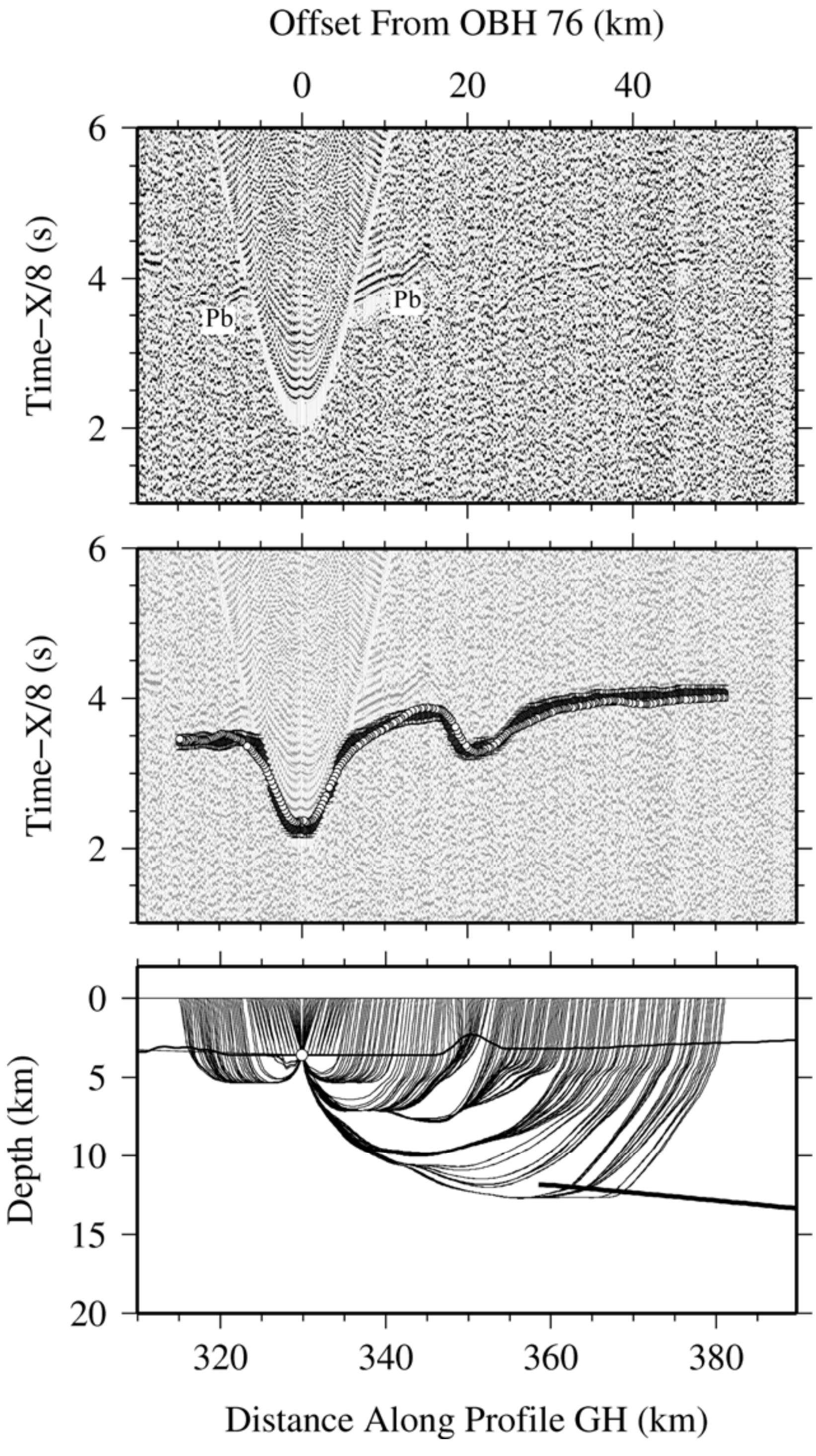

Figure A.1.1.22.-*OBH 76*

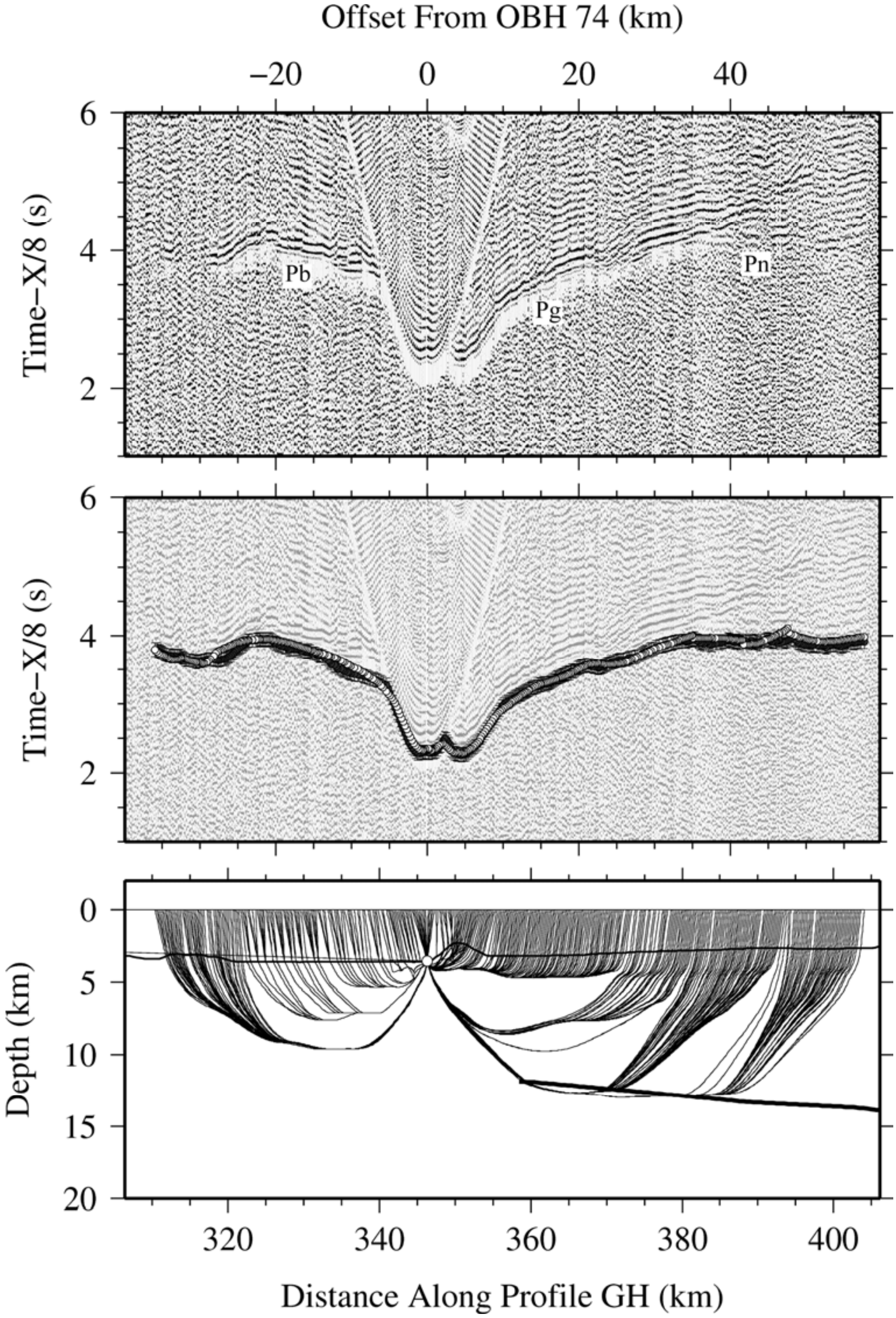

Figure A.1.1.23.-*OBH 74*

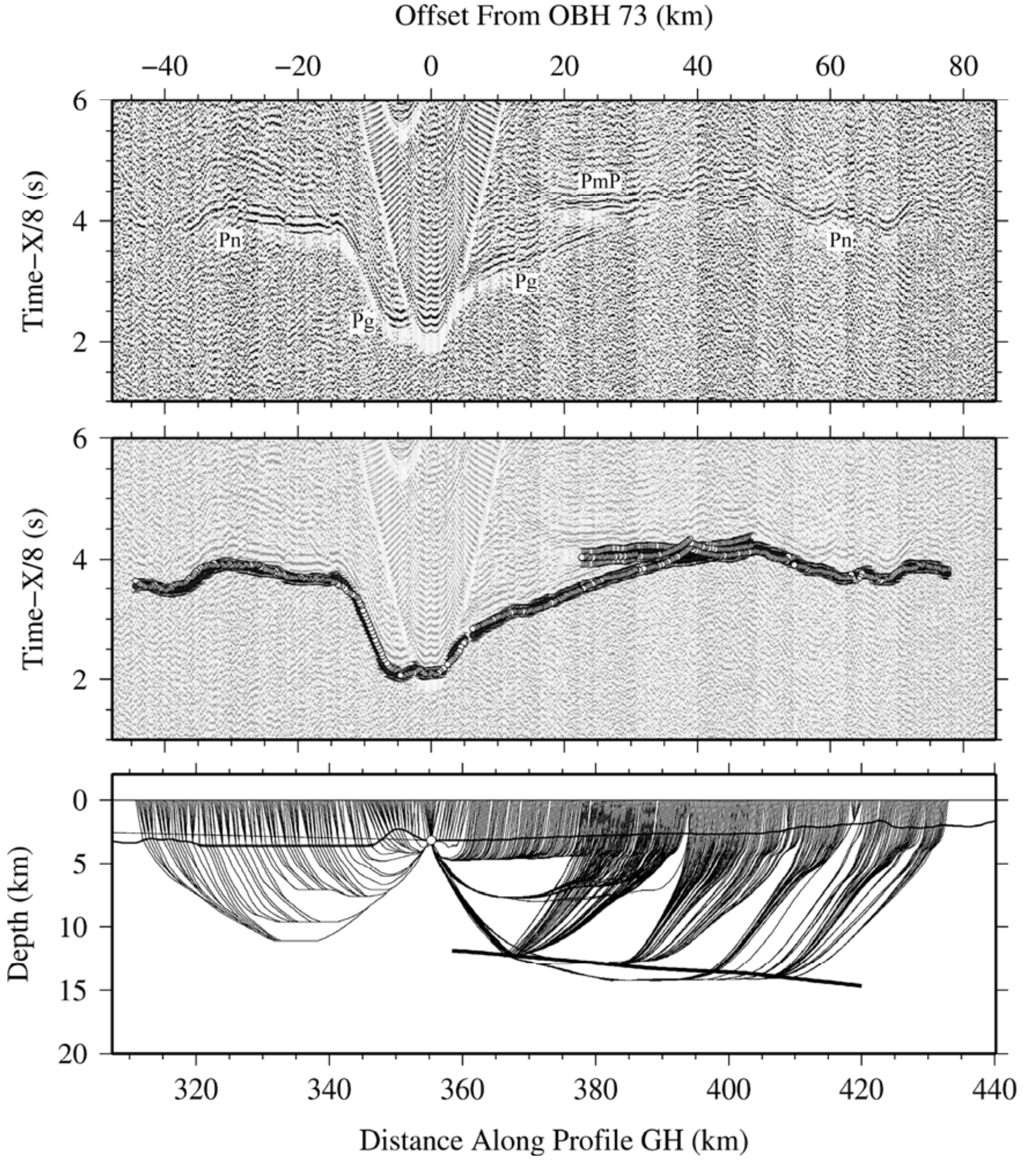

Figure A.1.1.24.-*OBH 73*

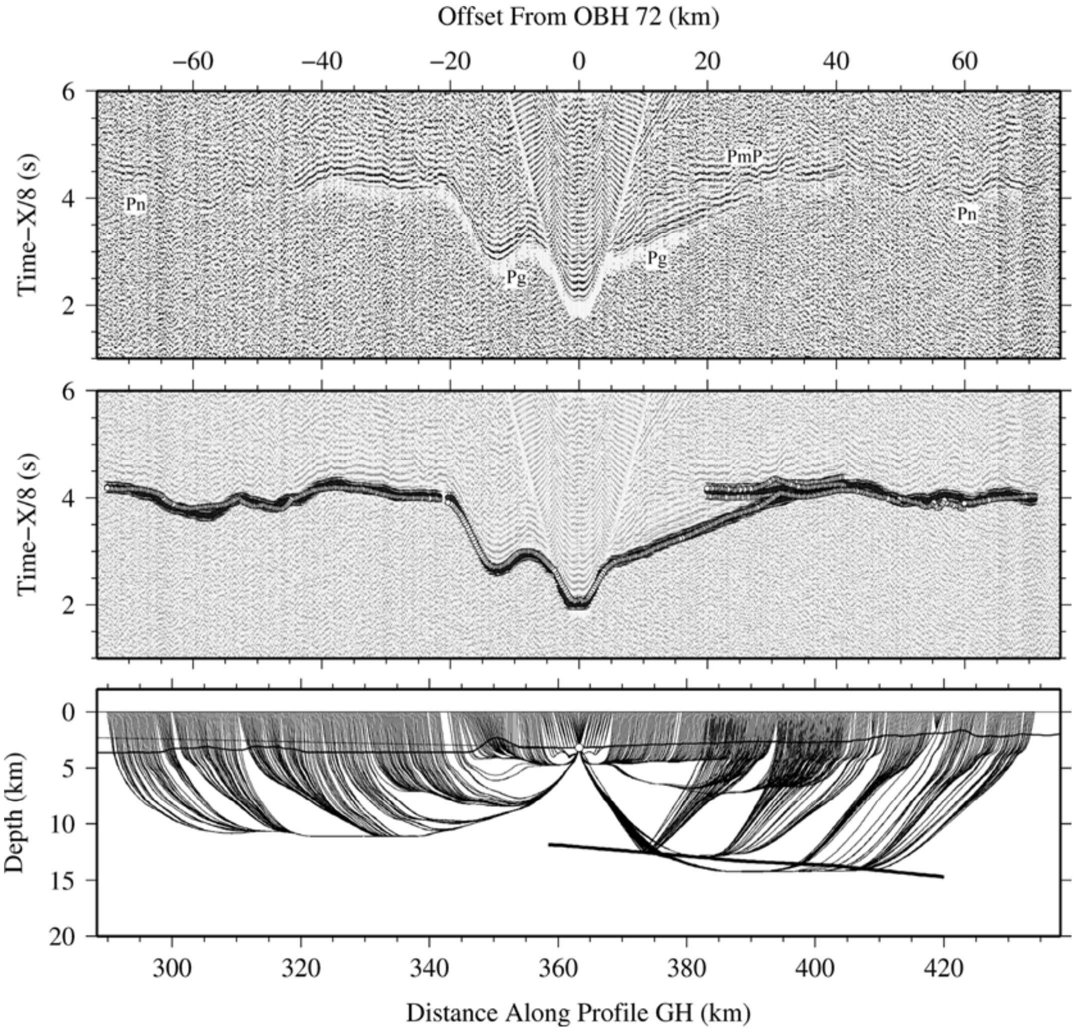

Figure A.1.1.25.-*OBH 72*

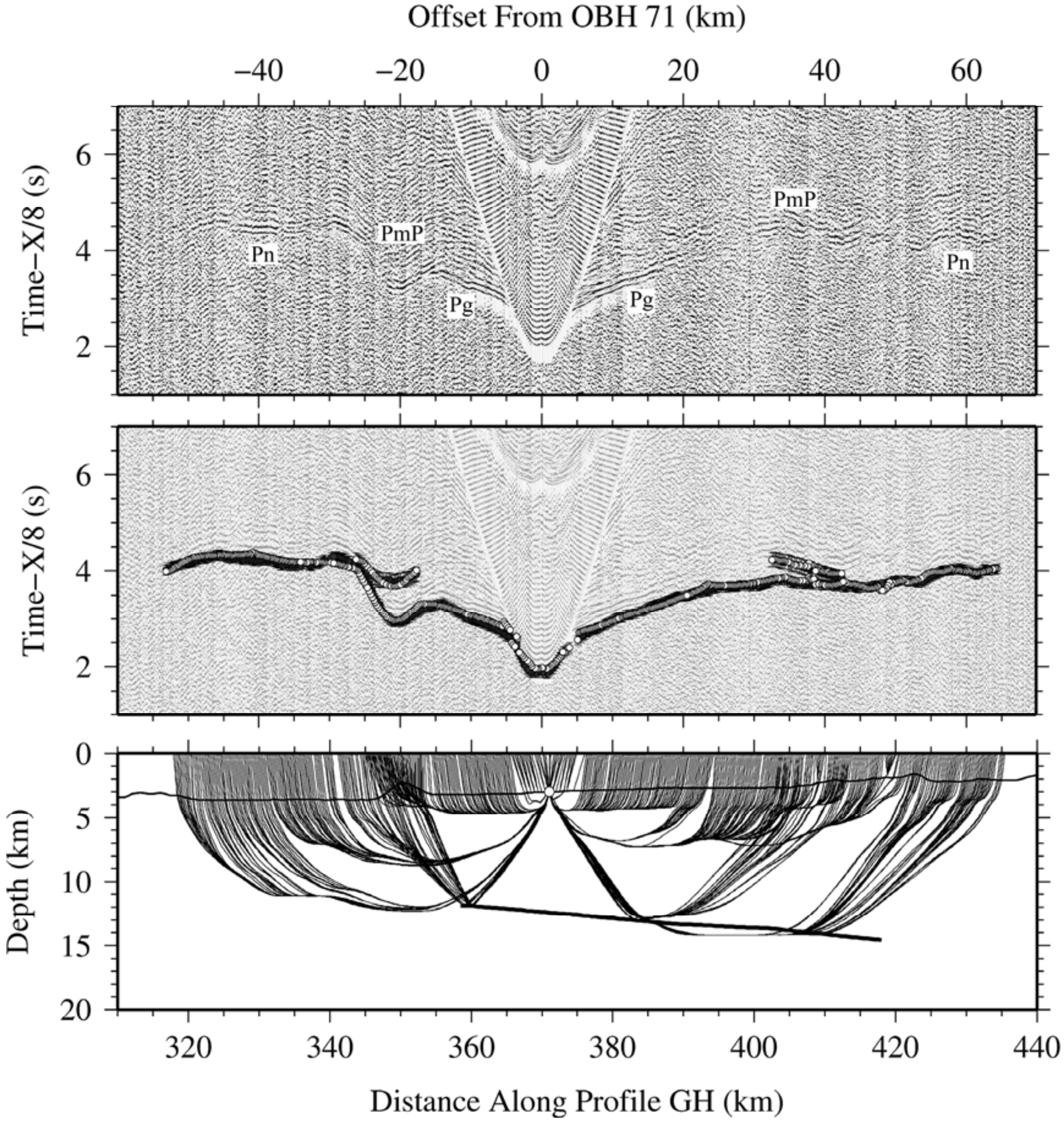

Figure A.1.1.26.-*OBH 71*

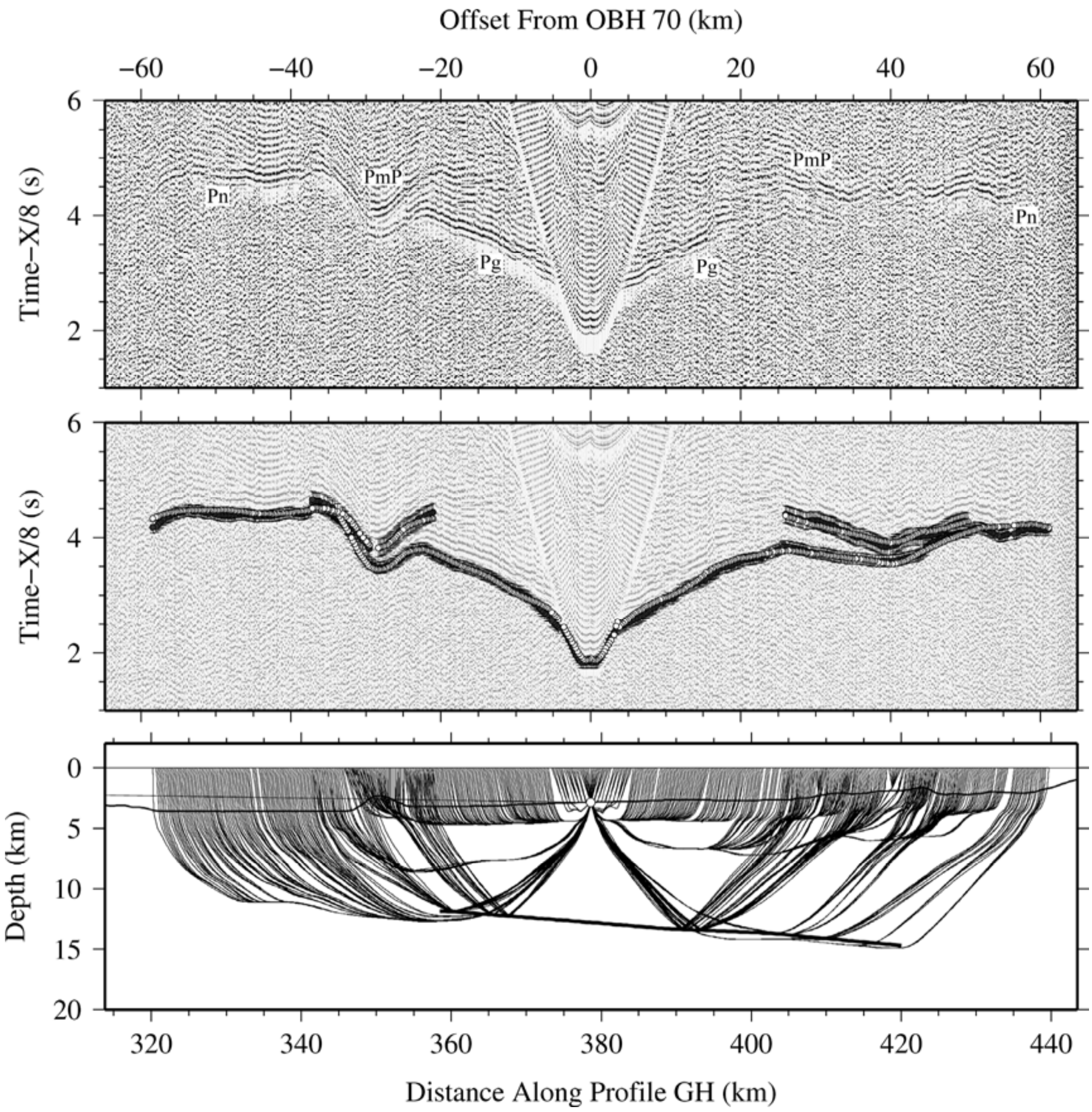

Figure A.1.1.27.-*OBH 70*

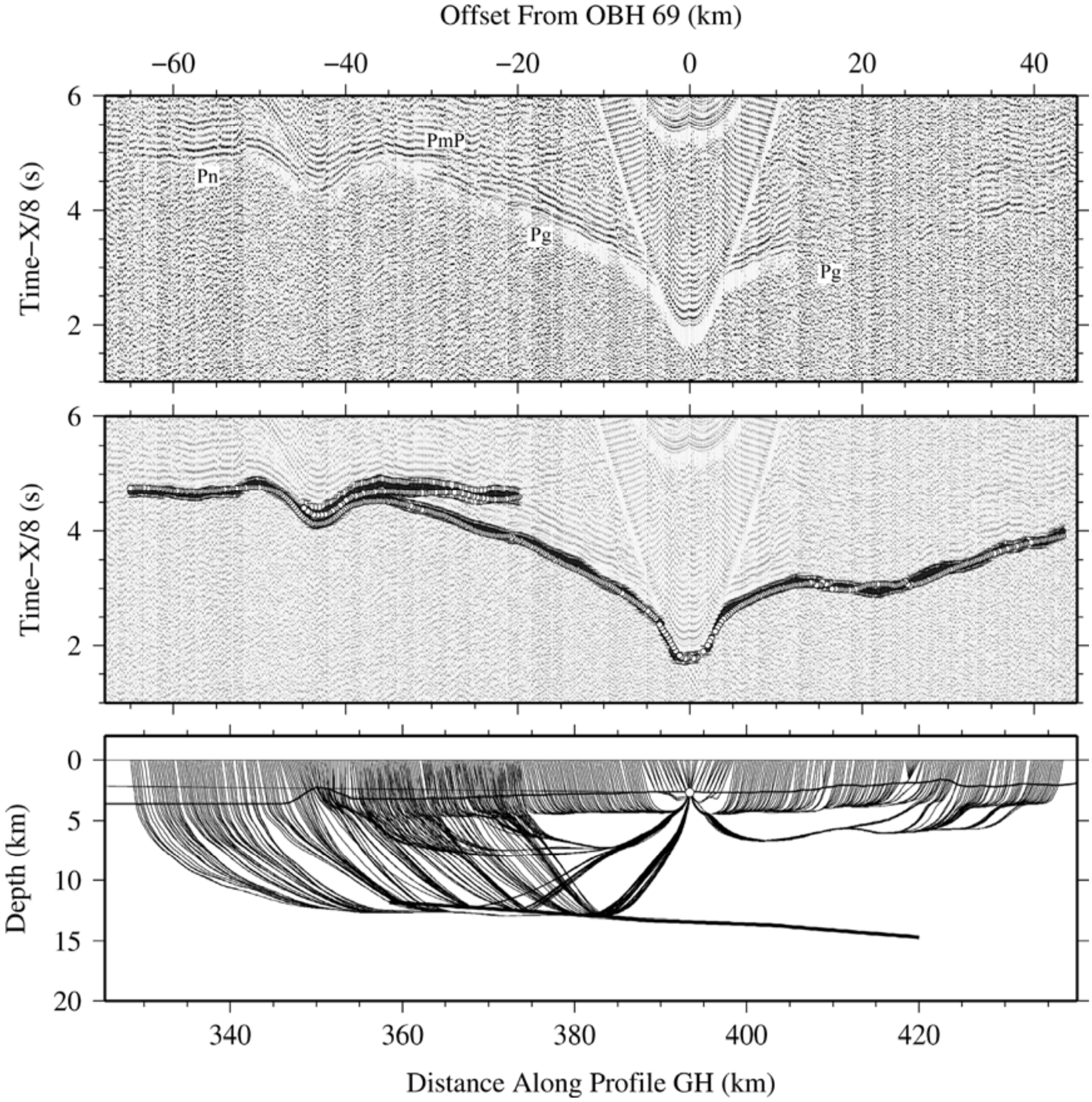

Figure A.1.1.28.-*OBH 69*

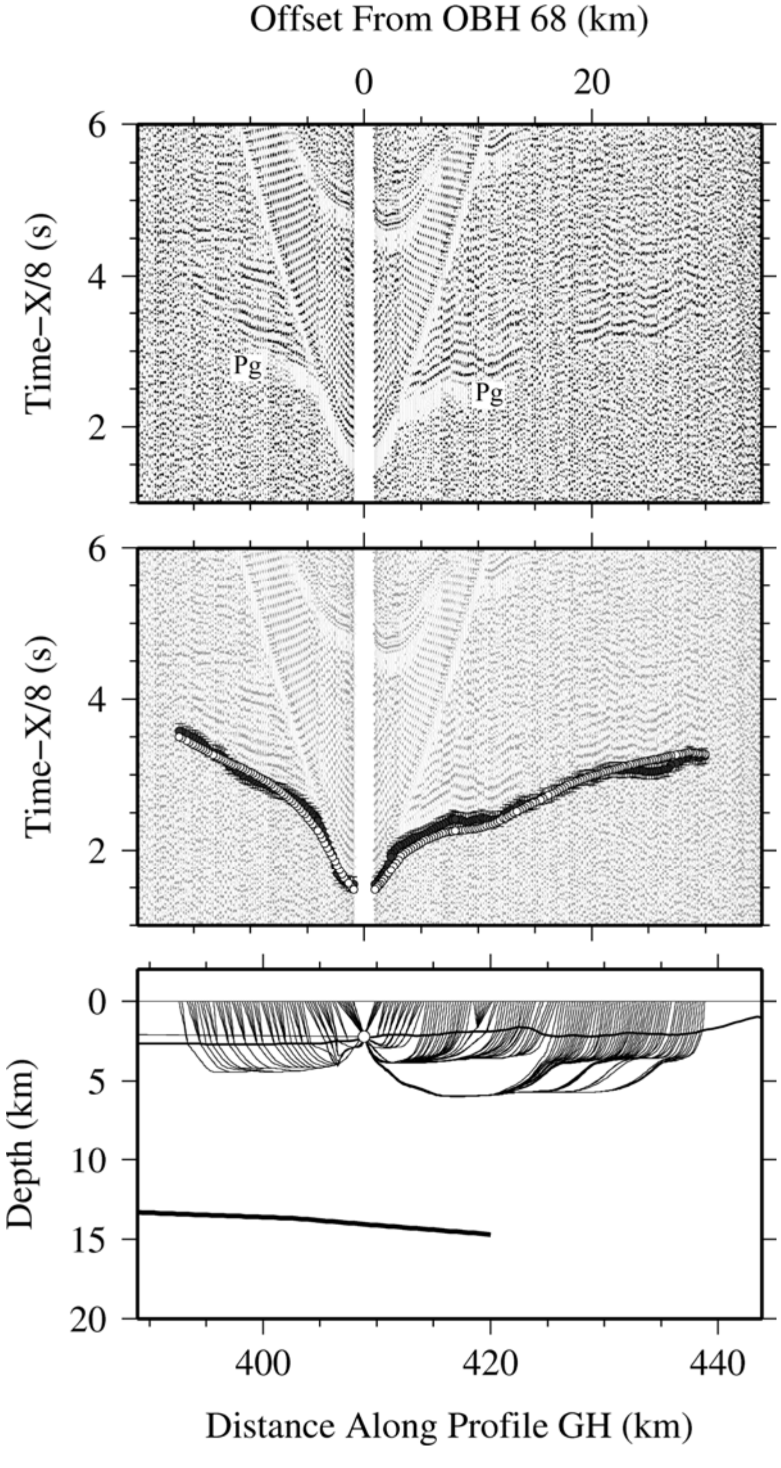

Figure A.1.1.29.-*OBH 68*

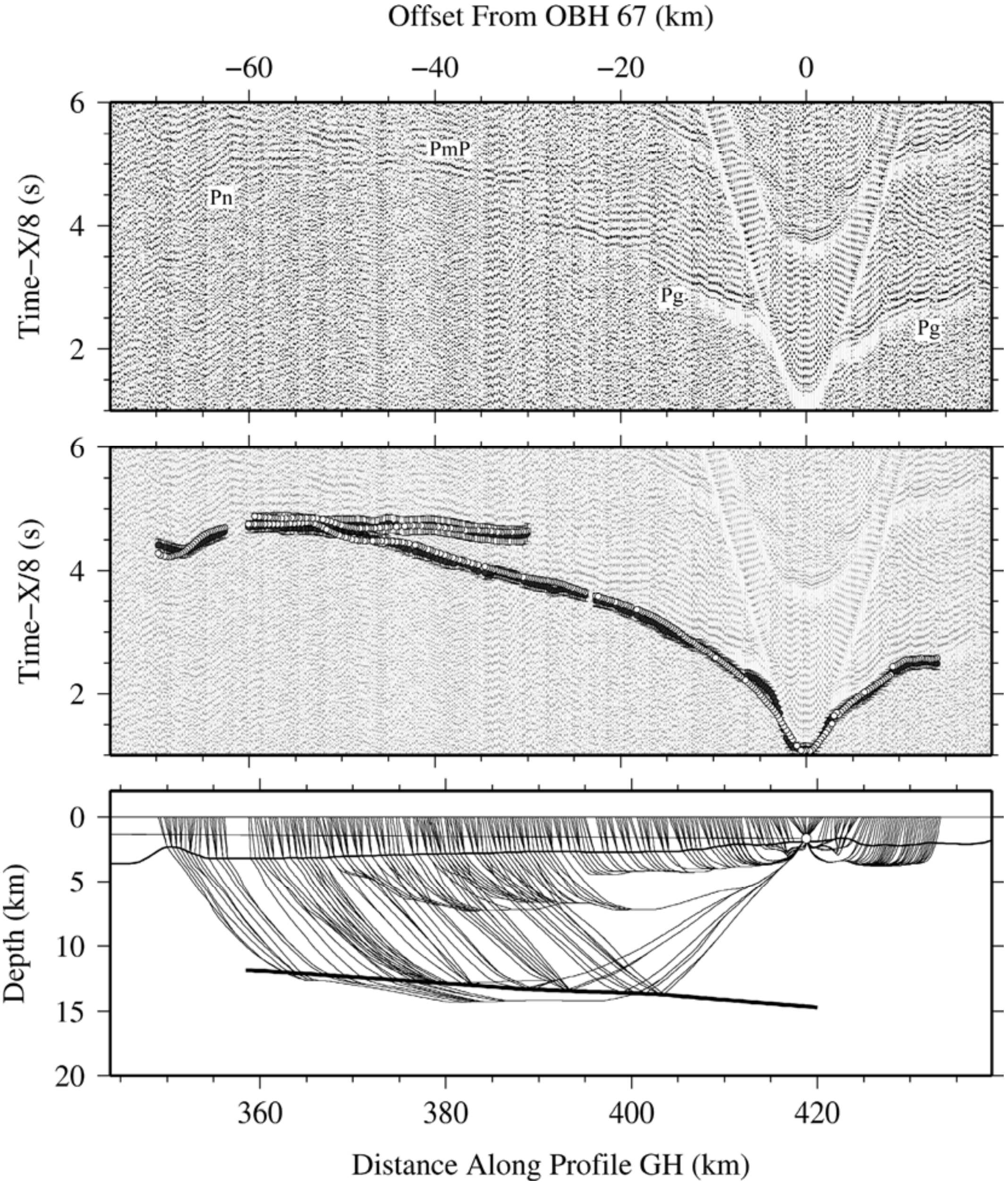

Figure A.1.1.30.-*OBH 67*

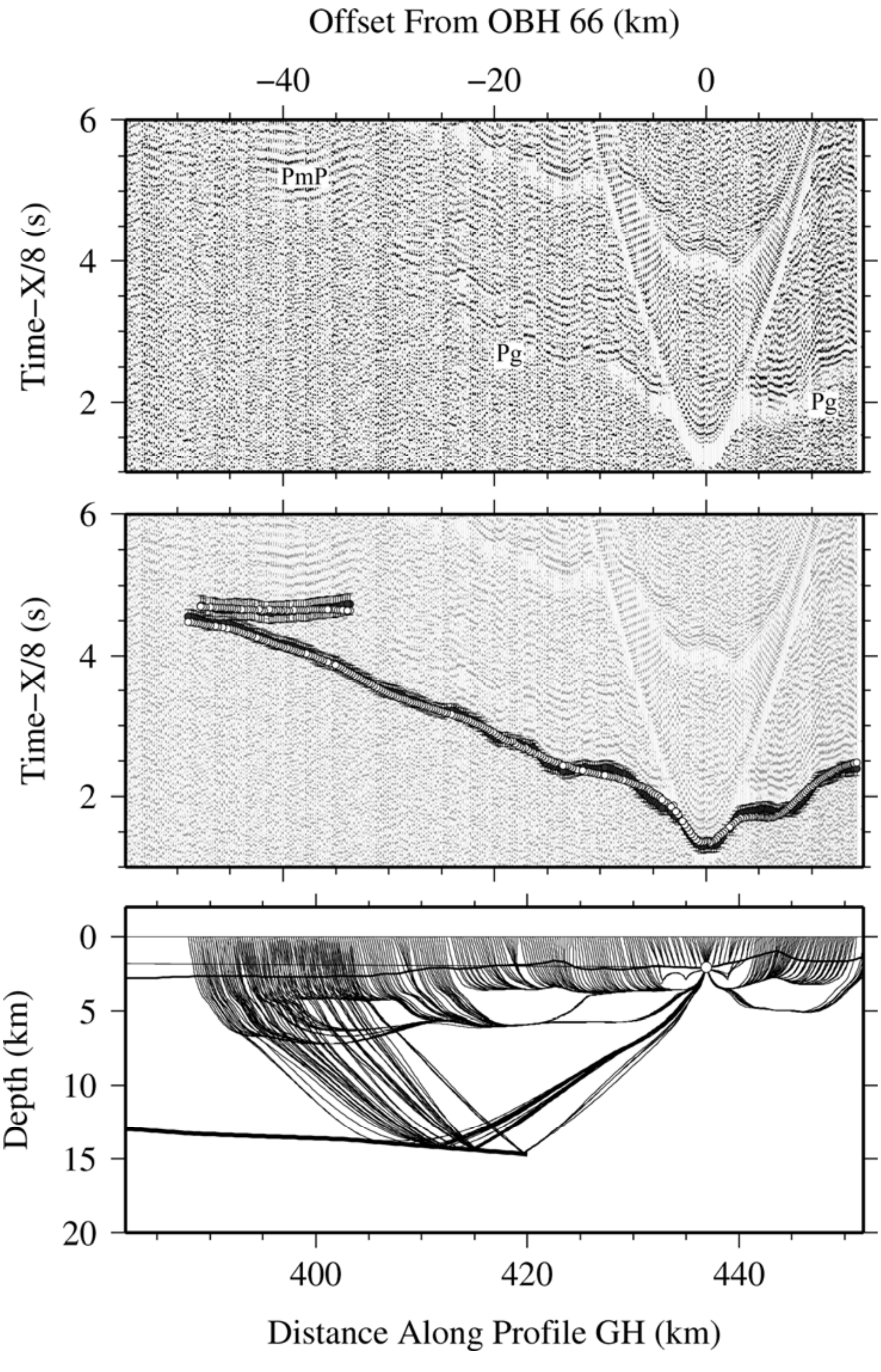

Figure A.1.1.31.-*OBH 66*

A.1.2 Line EF

From top to bottom, record section, data fit and ray-tracing of all the receivers used to obtain the 2D P-wave velocity model of Line EF (Figure 7.2a). In the data fit panels, the black and white circles correspond to the picked and calculated data, respectively. While the thick black line in the ray-tracing panels represents the inverted Moho geometry, and the white circle the receiver location.

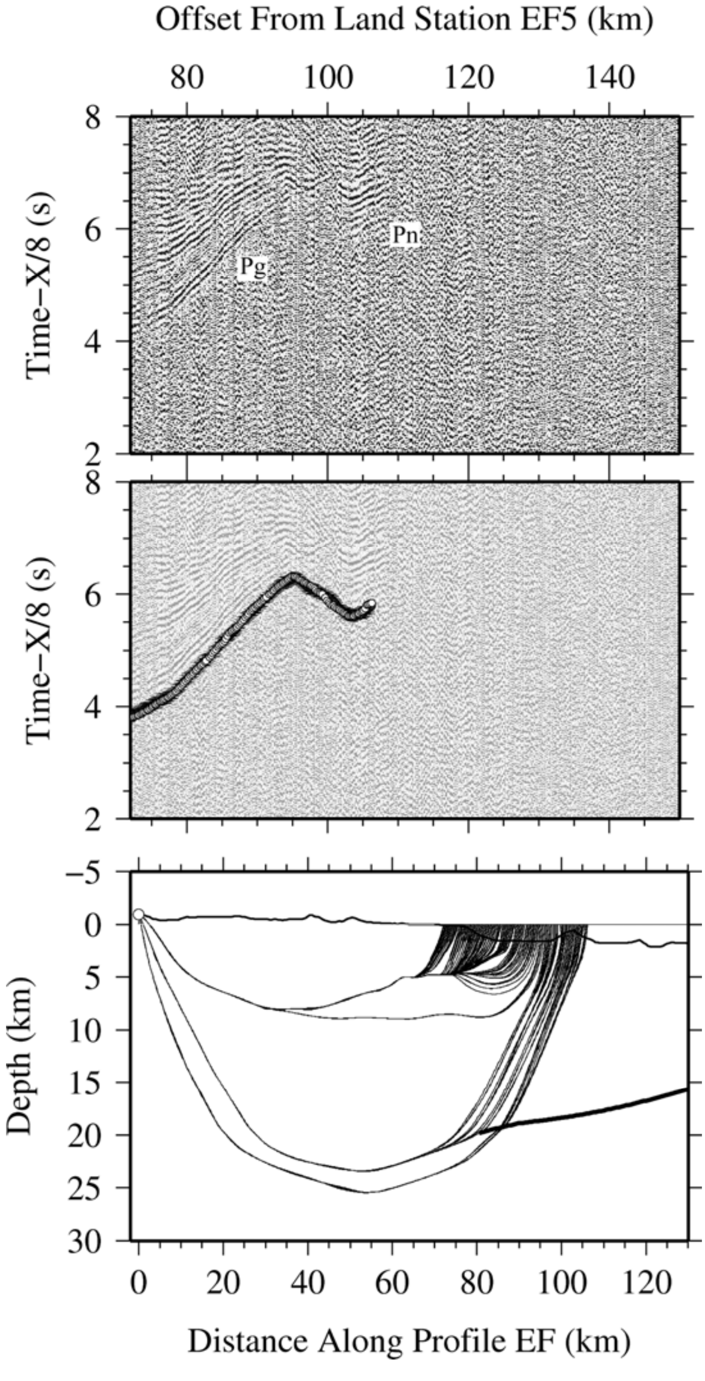

Figure A.1.2.1.- *Land Station EF5*

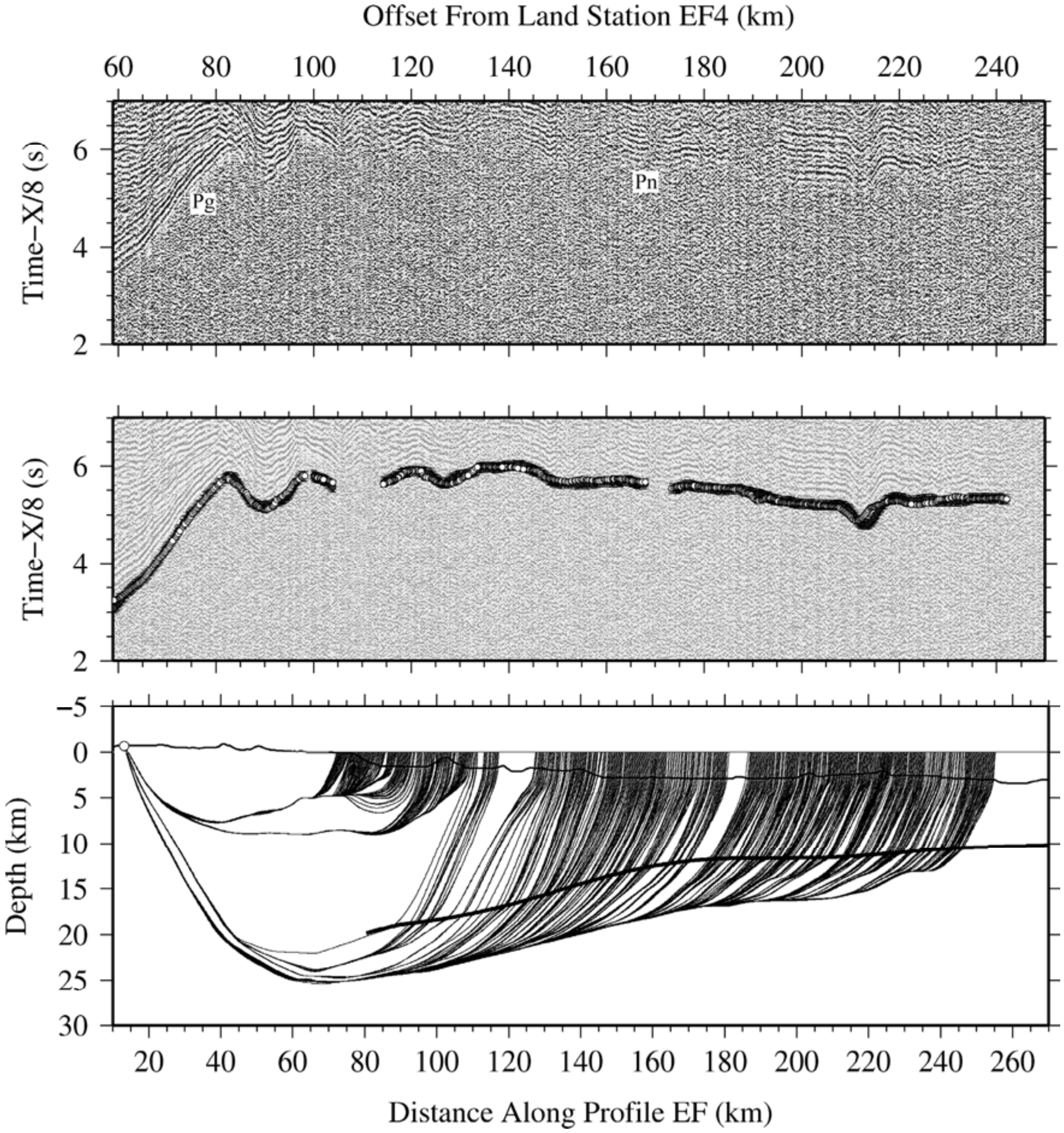

Figure A.1.2.2.- *Land Station EF4*

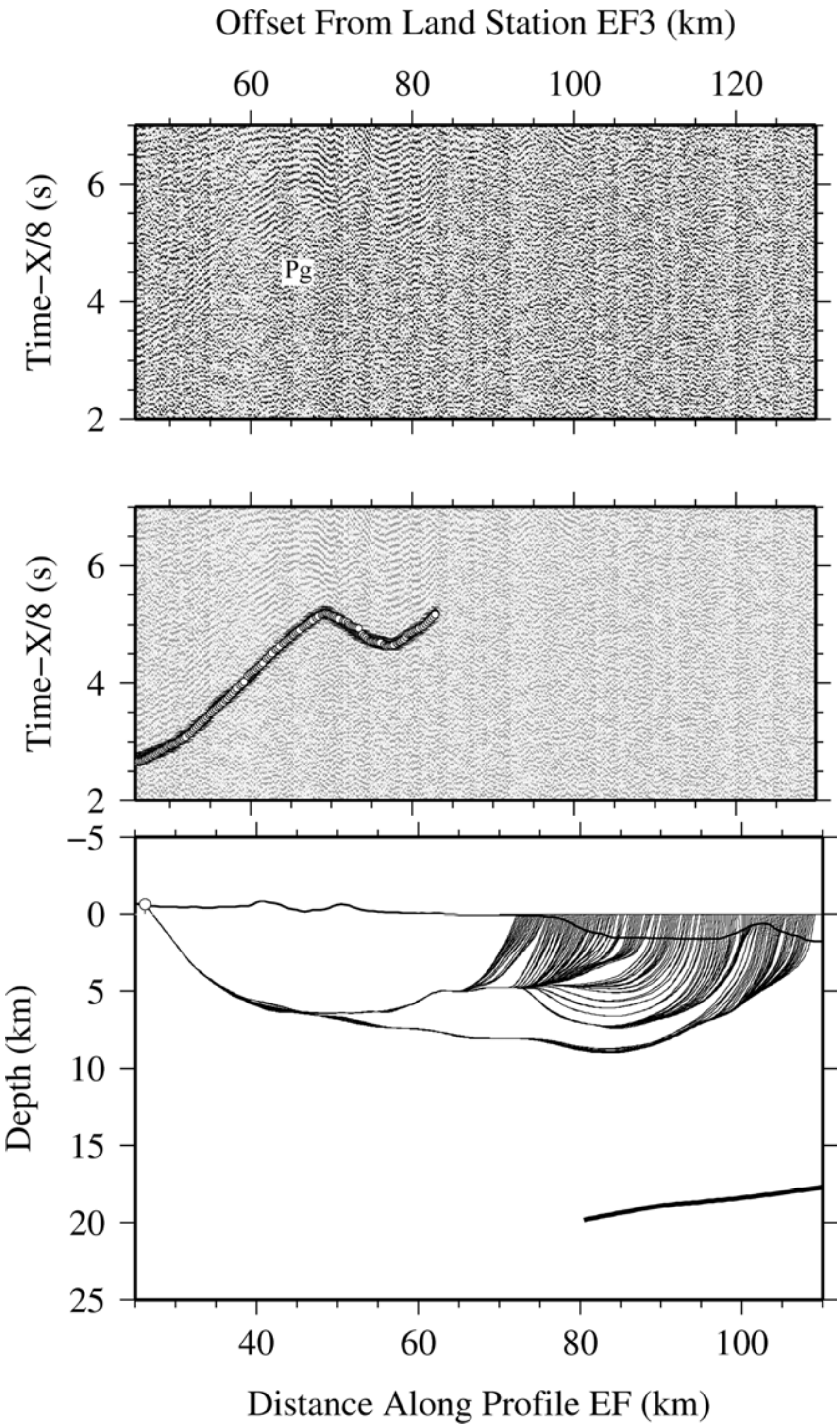

Figure A.1.2.3.- *Land Station EF3*

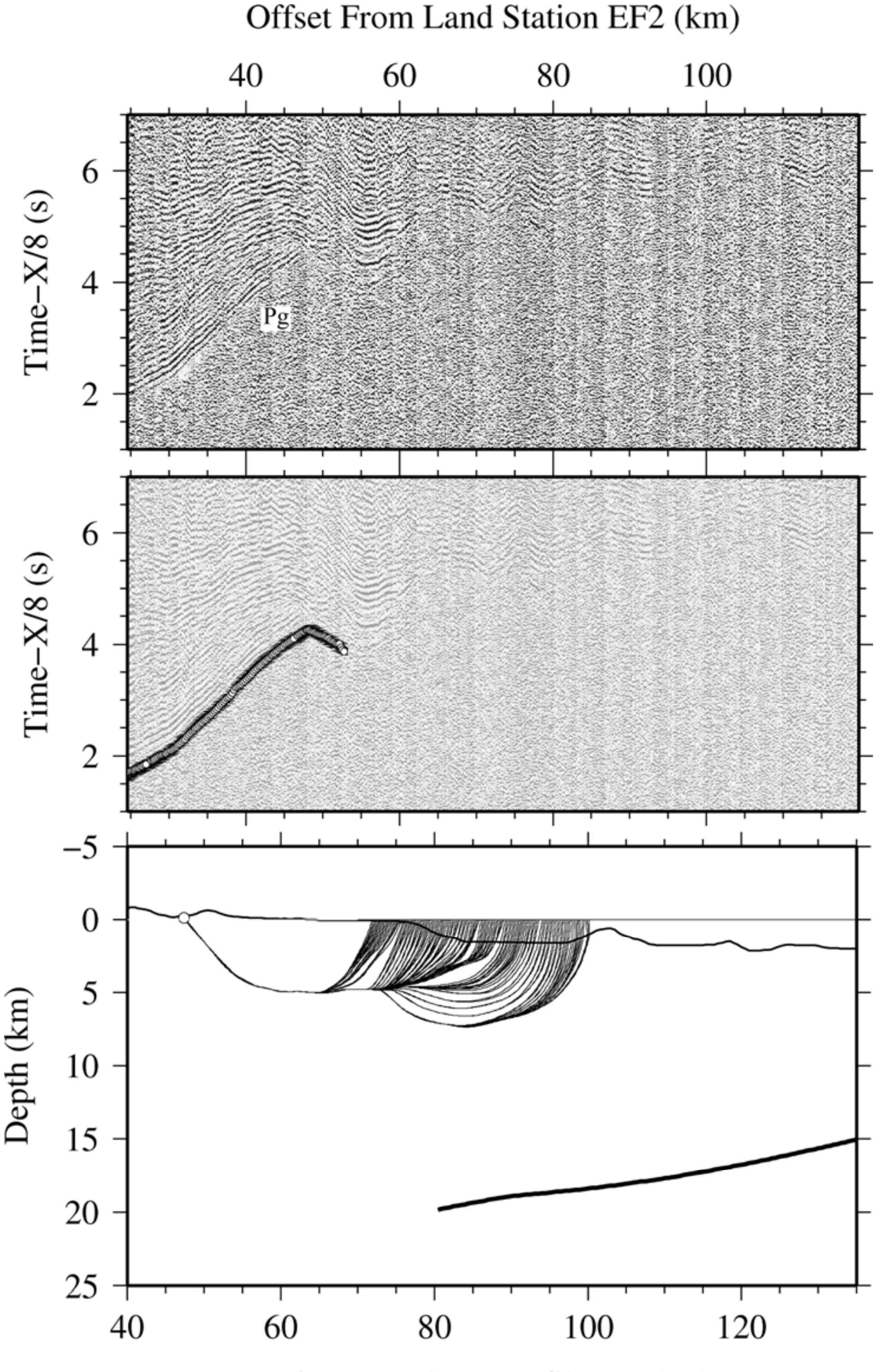

Figure A.1.2.4.- *Land Station EF2*

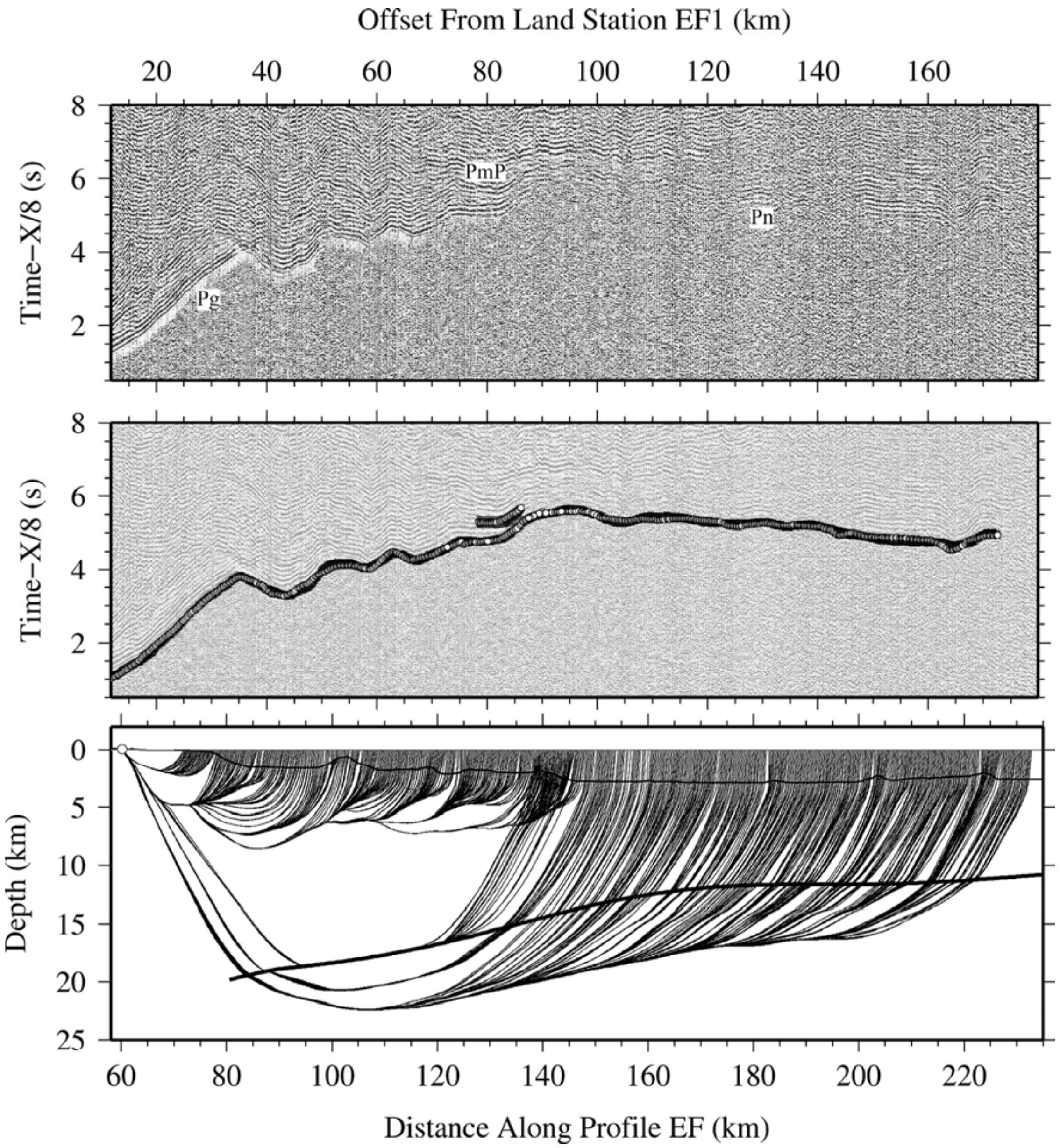

Figure A.1.2.5.- *Land Station EF1*

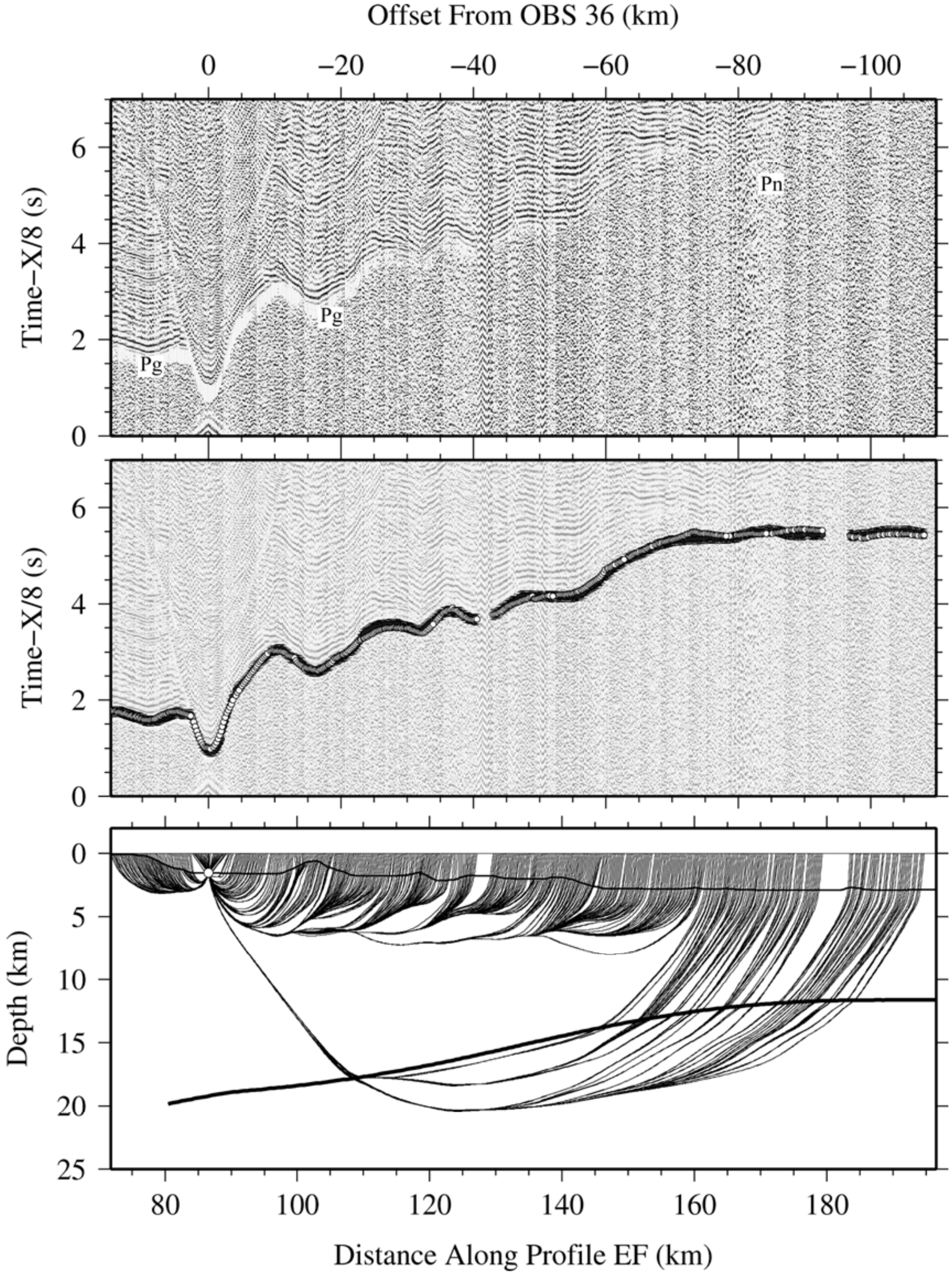

Figure A.1.2.6.- *OBS 36*

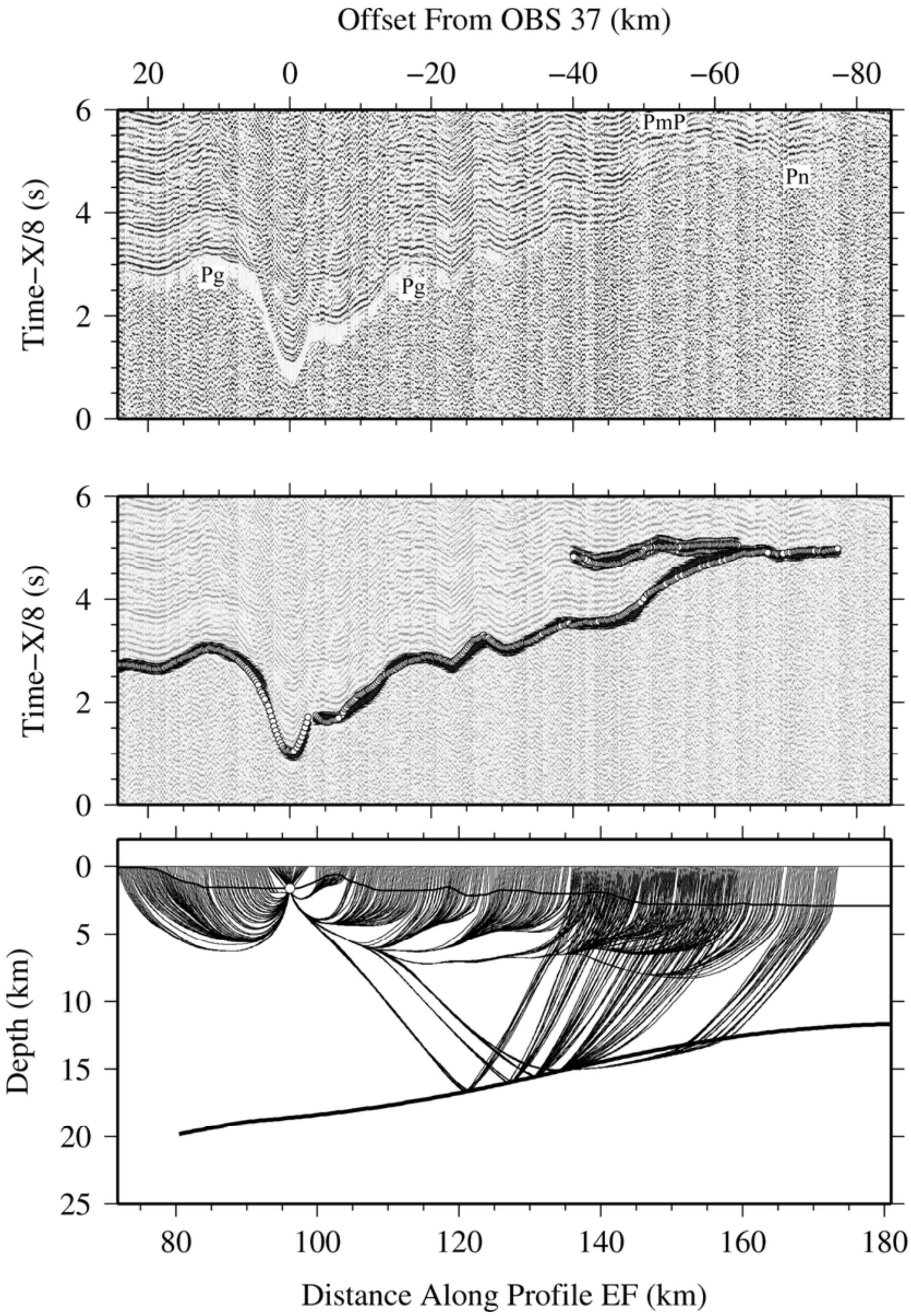

Figure A.1.2.7.- *OBS 37*

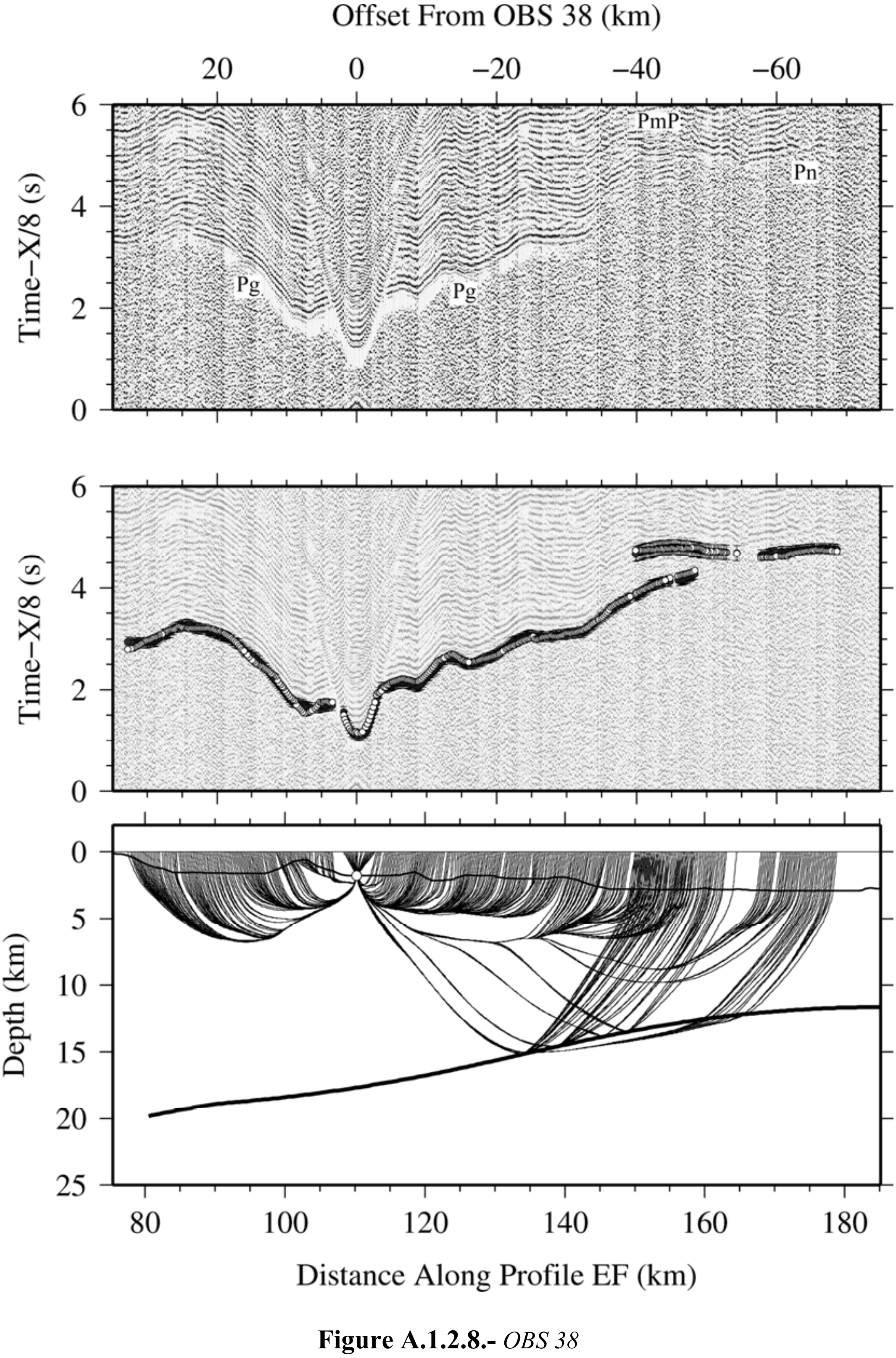

Figure A.1.2.8.- *OBS 38*

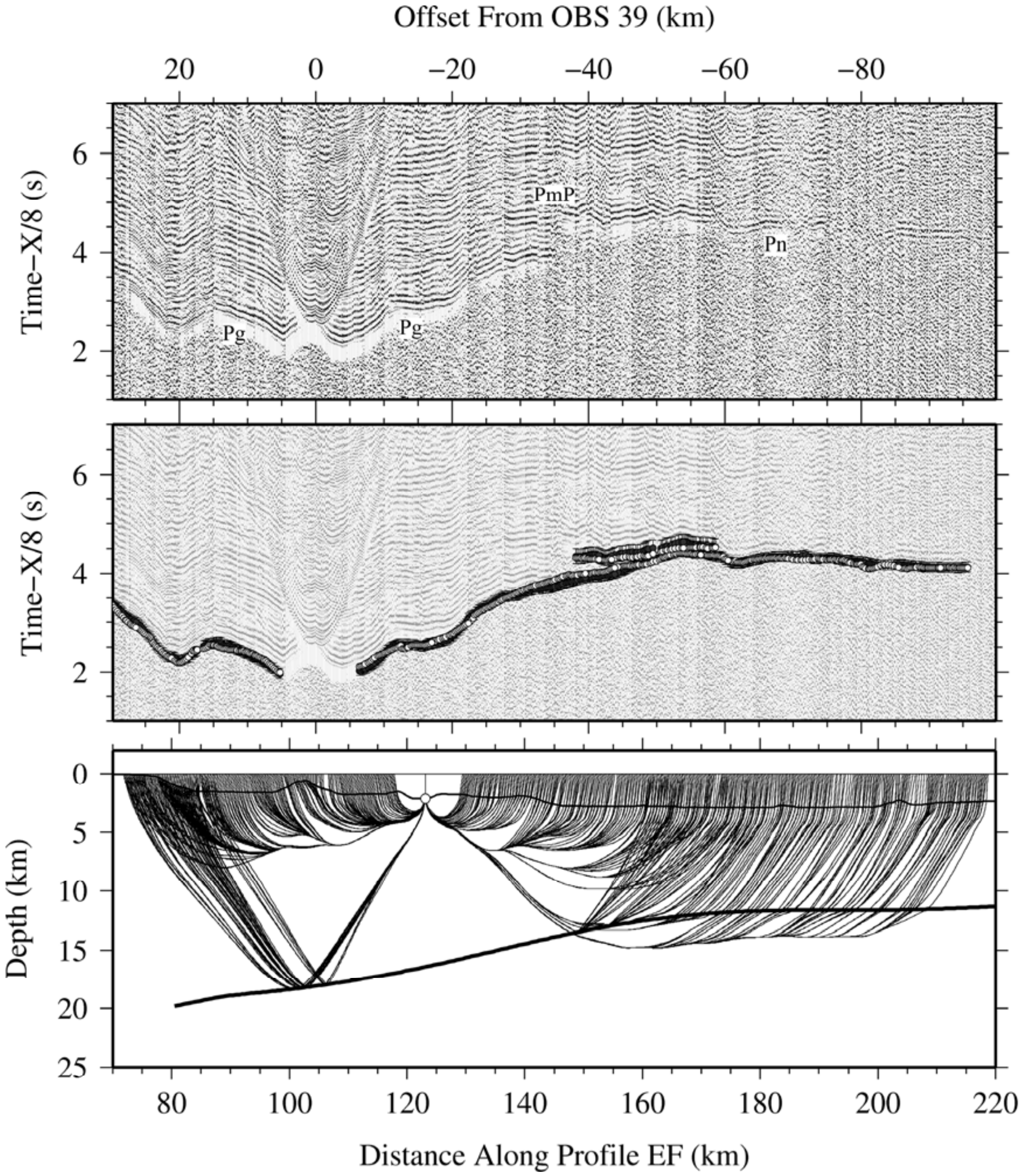

Figure A.1.2.9.- *OBS 39*

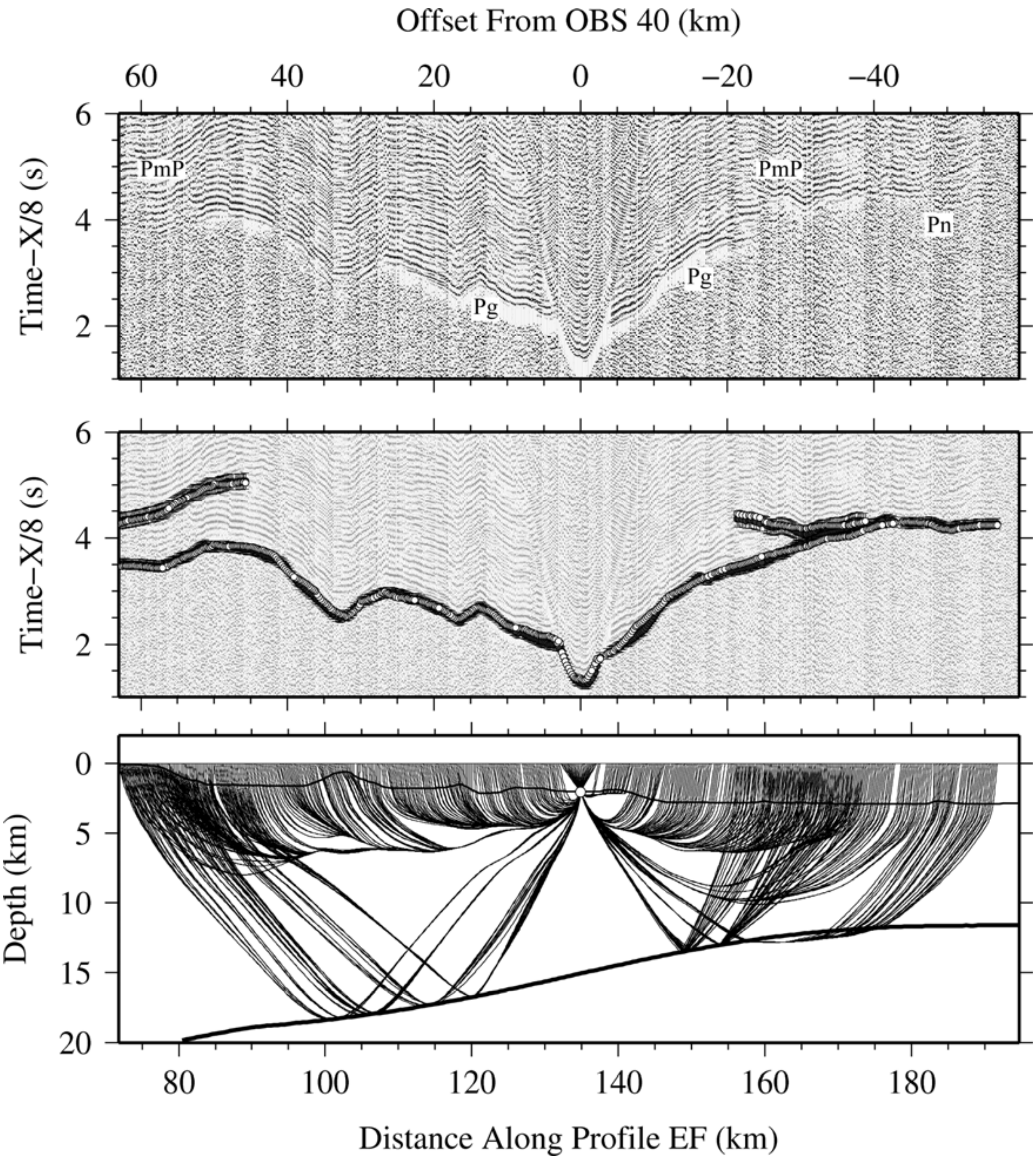

Figure A.1.2.10.- *OBS 40*

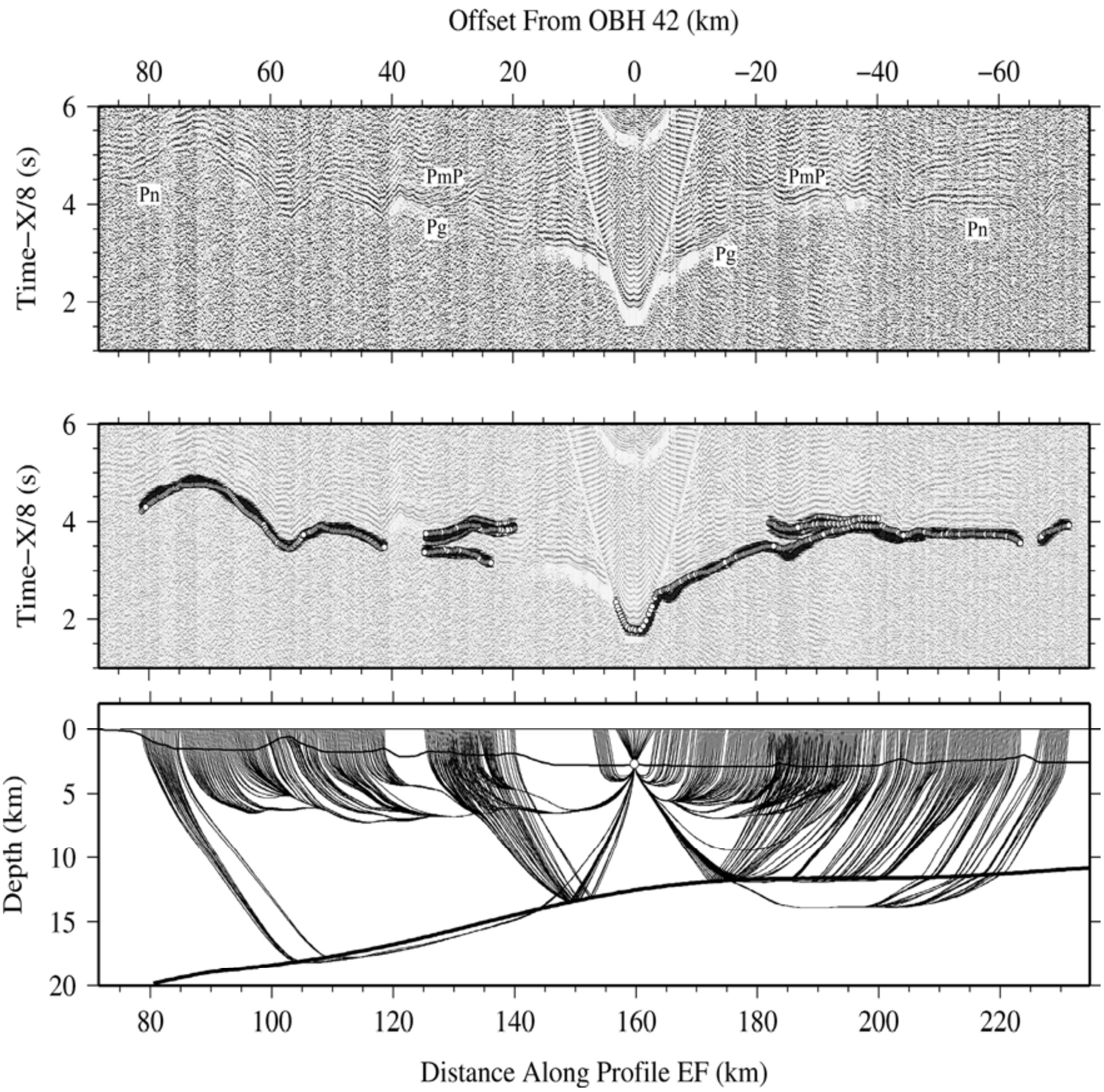

Figure A.1.2.11.- *OBH 42*

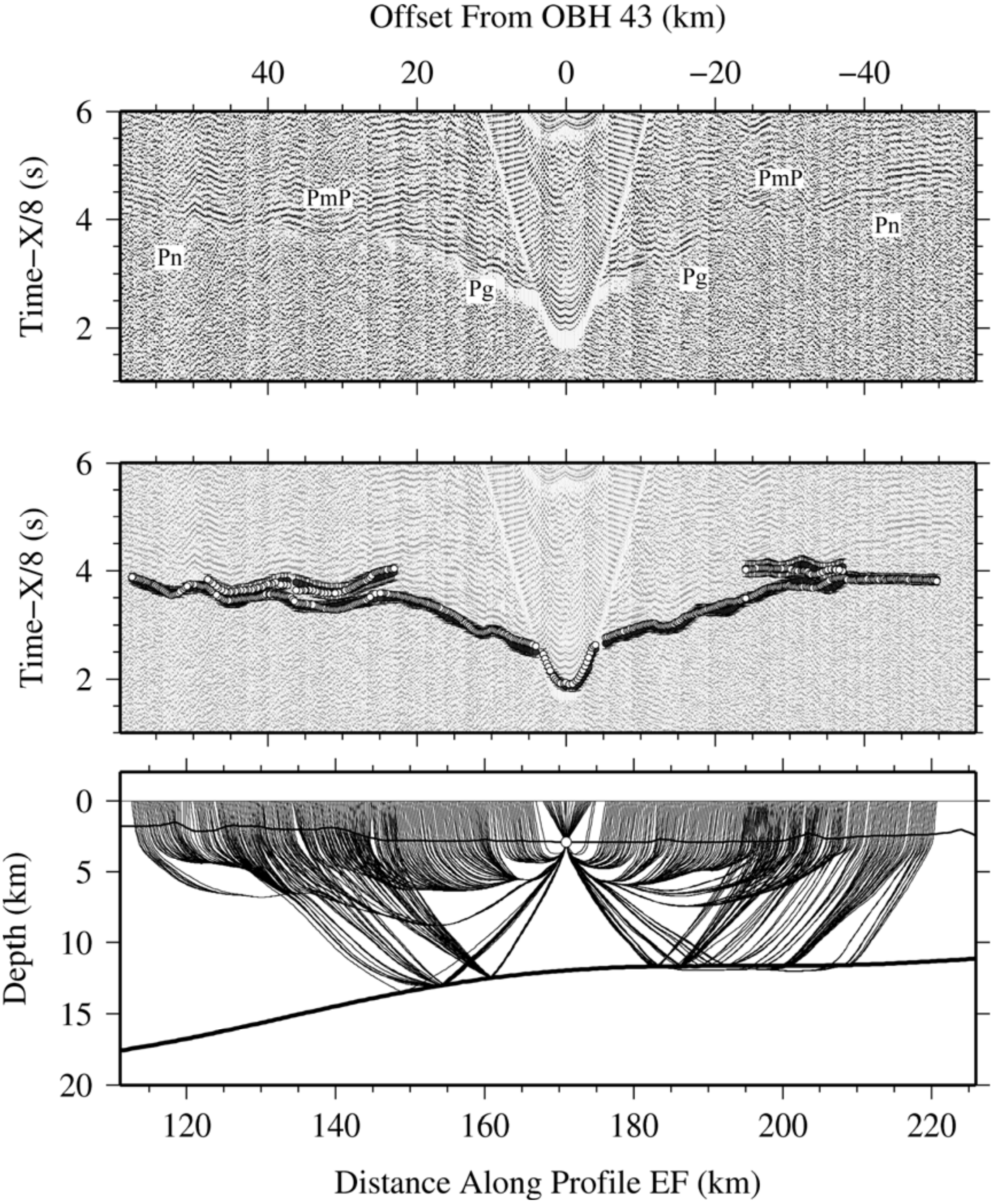

Figure A.1.2.12.- *OBH 43*

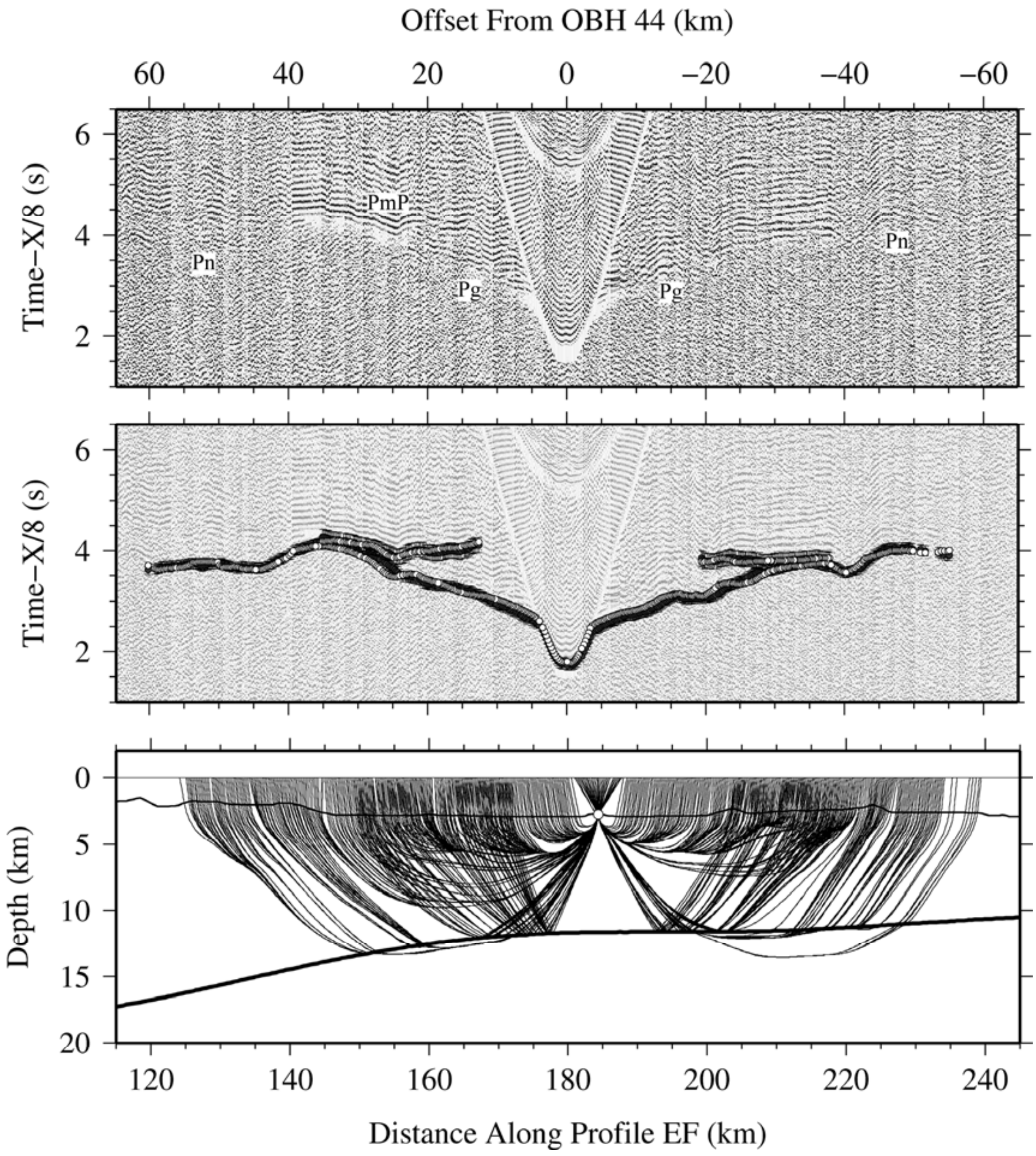

Figure A.1.2.13.- *OBH 44*

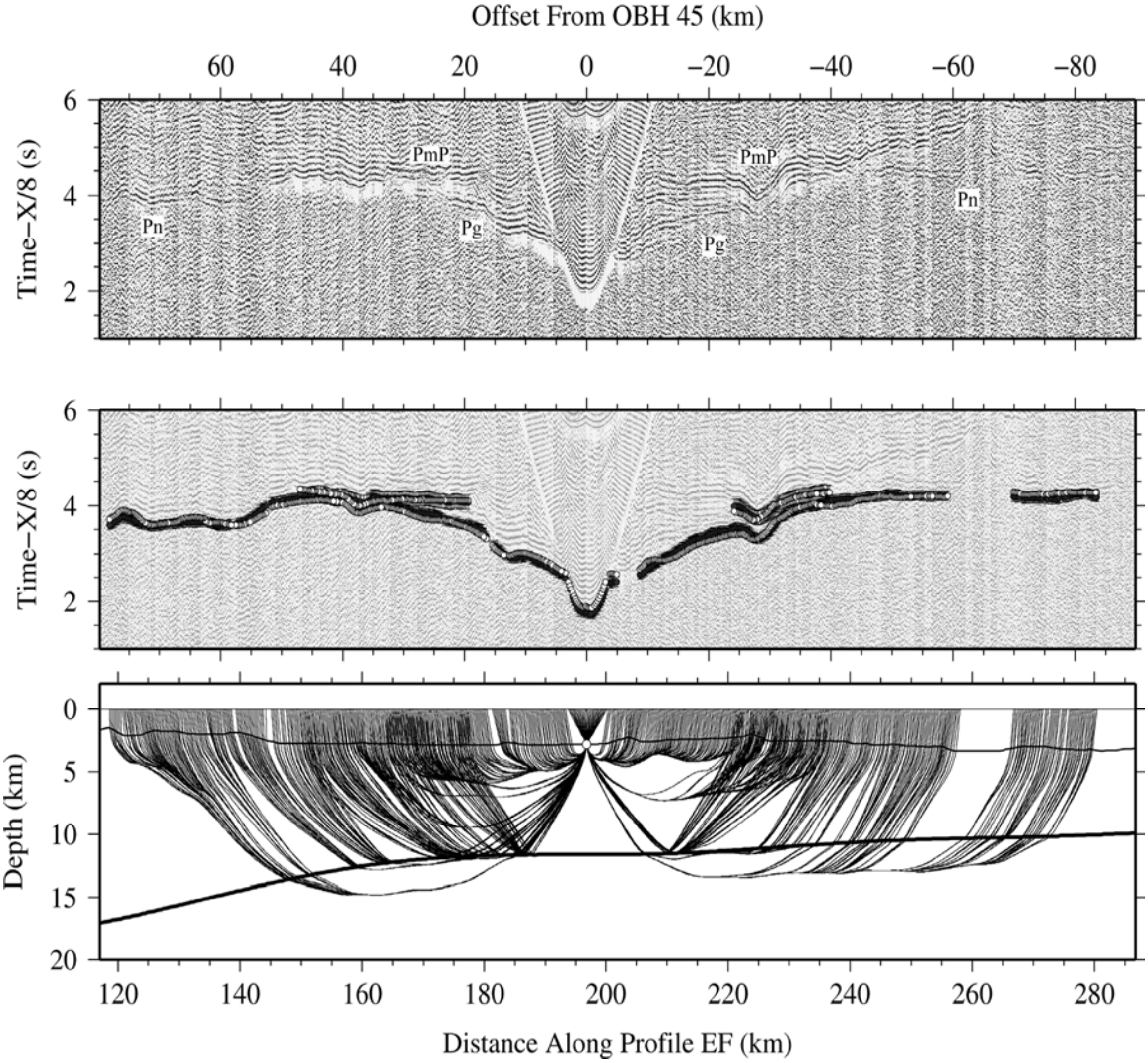

Figure A.1.2.14.- *OBH 45*

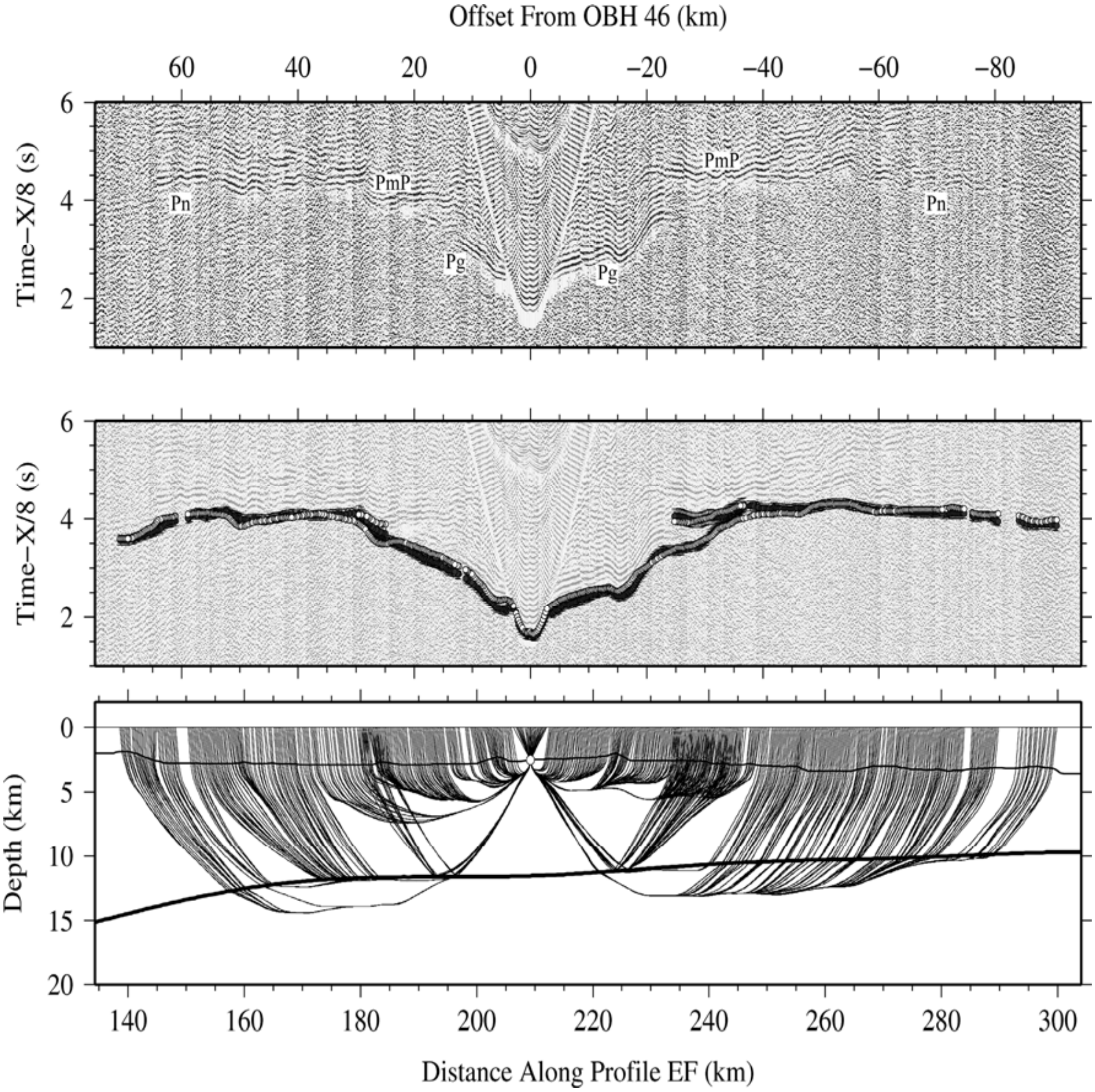

Figure A.1.2.15.- *OBH 46*

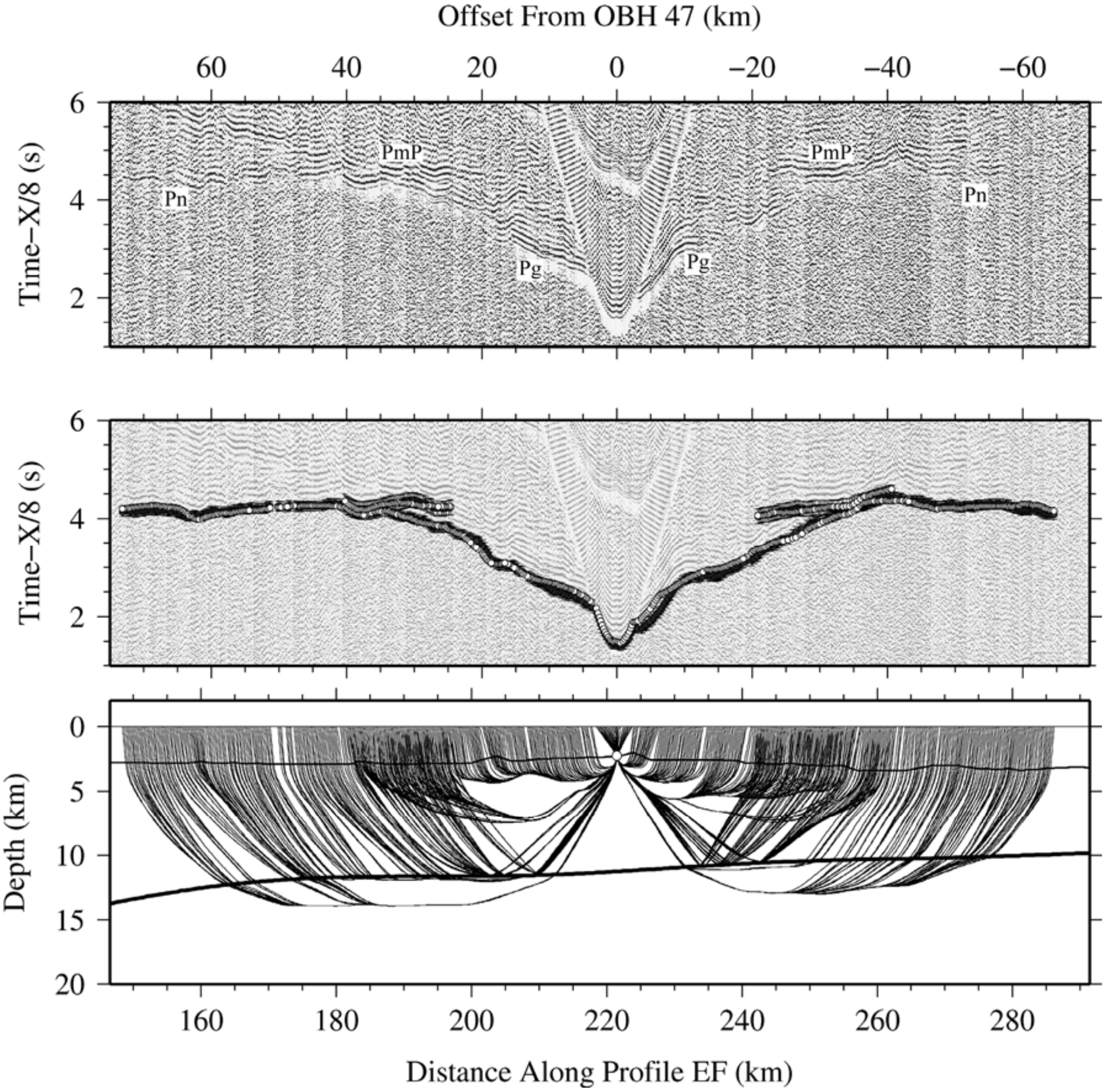

Figure A.1.2.16.- *OBH 47*

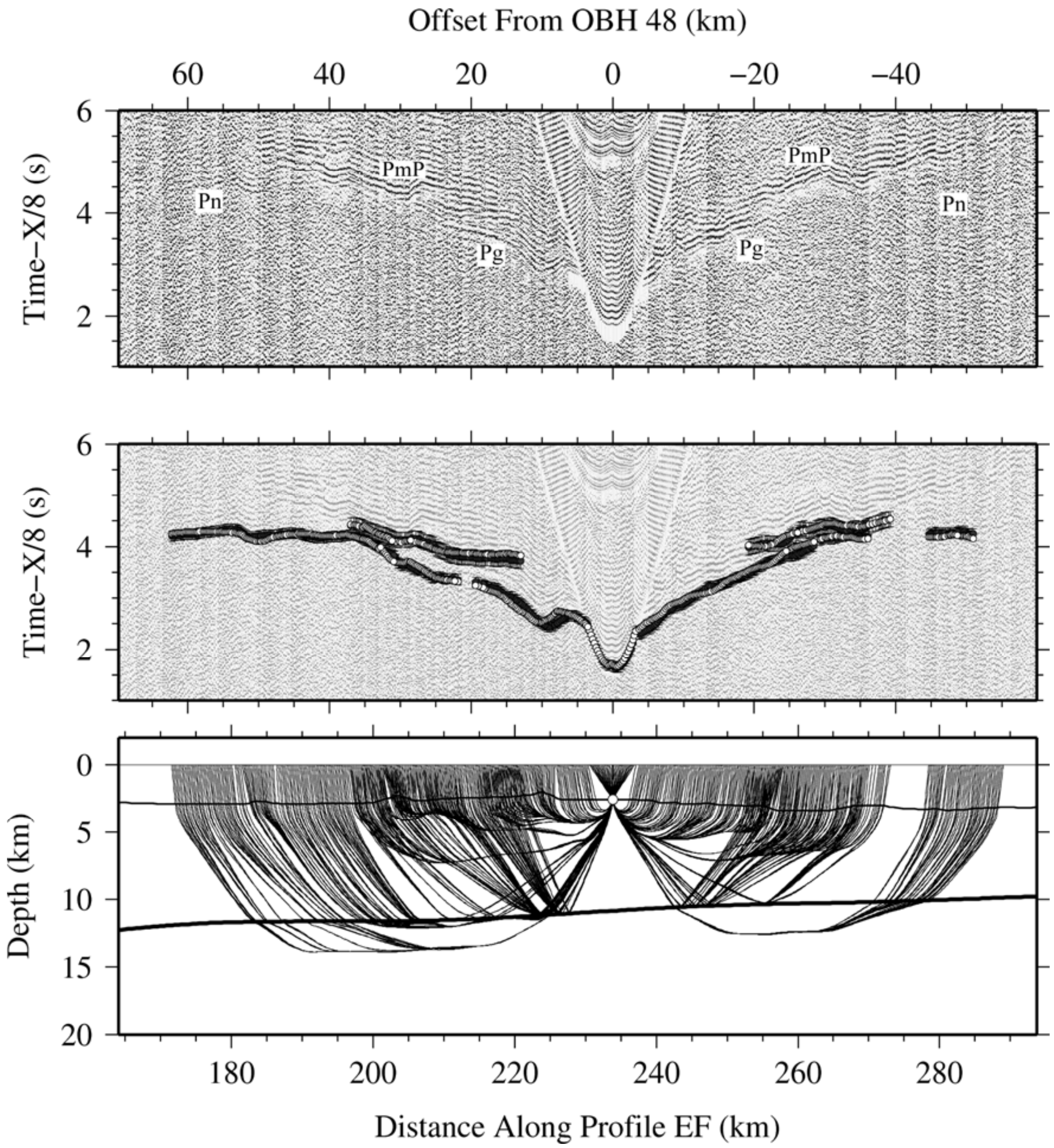

Figure A.1.2.17.- *OBH 48*

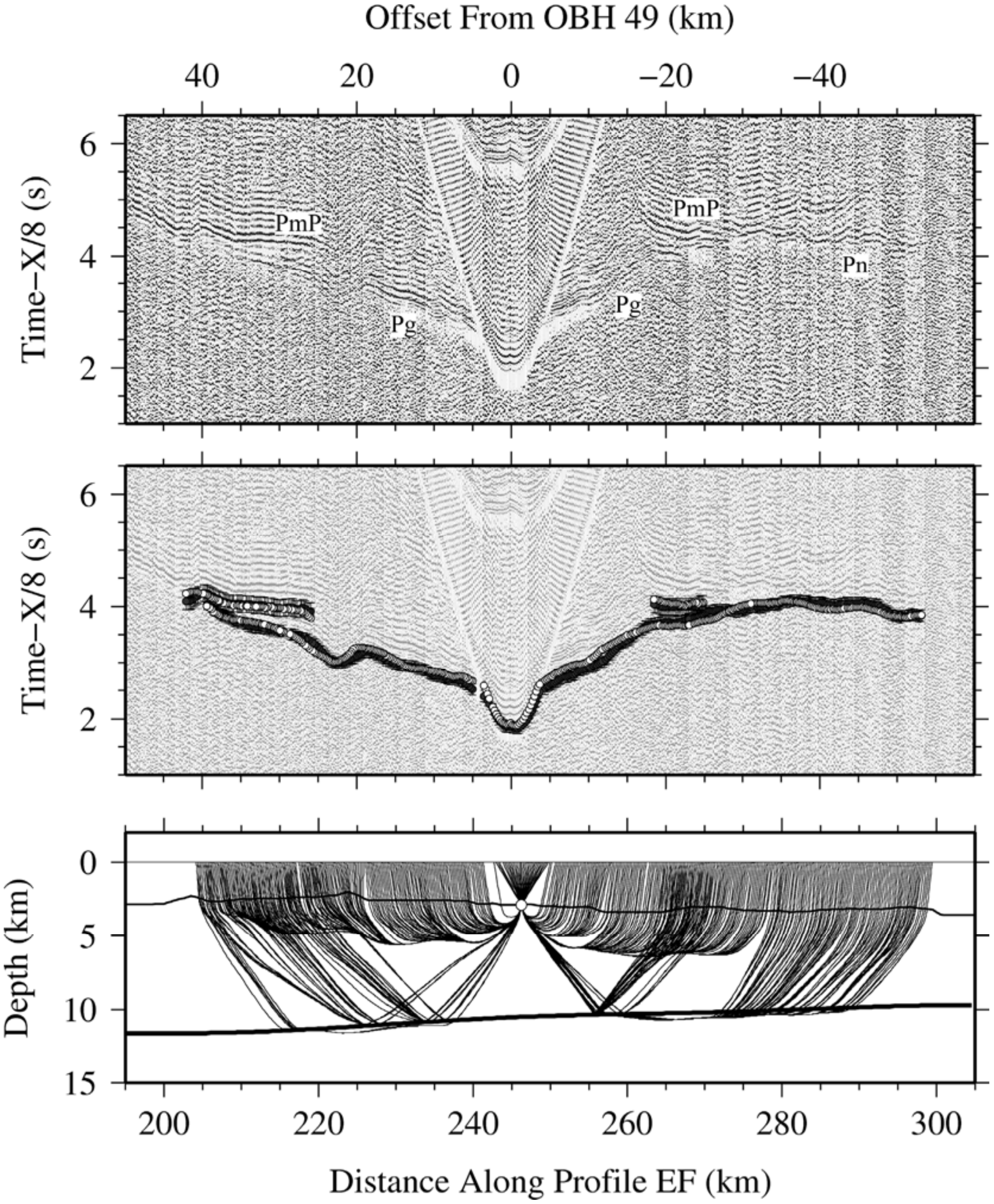

Figure A.1.2.18.- *OBH 49*

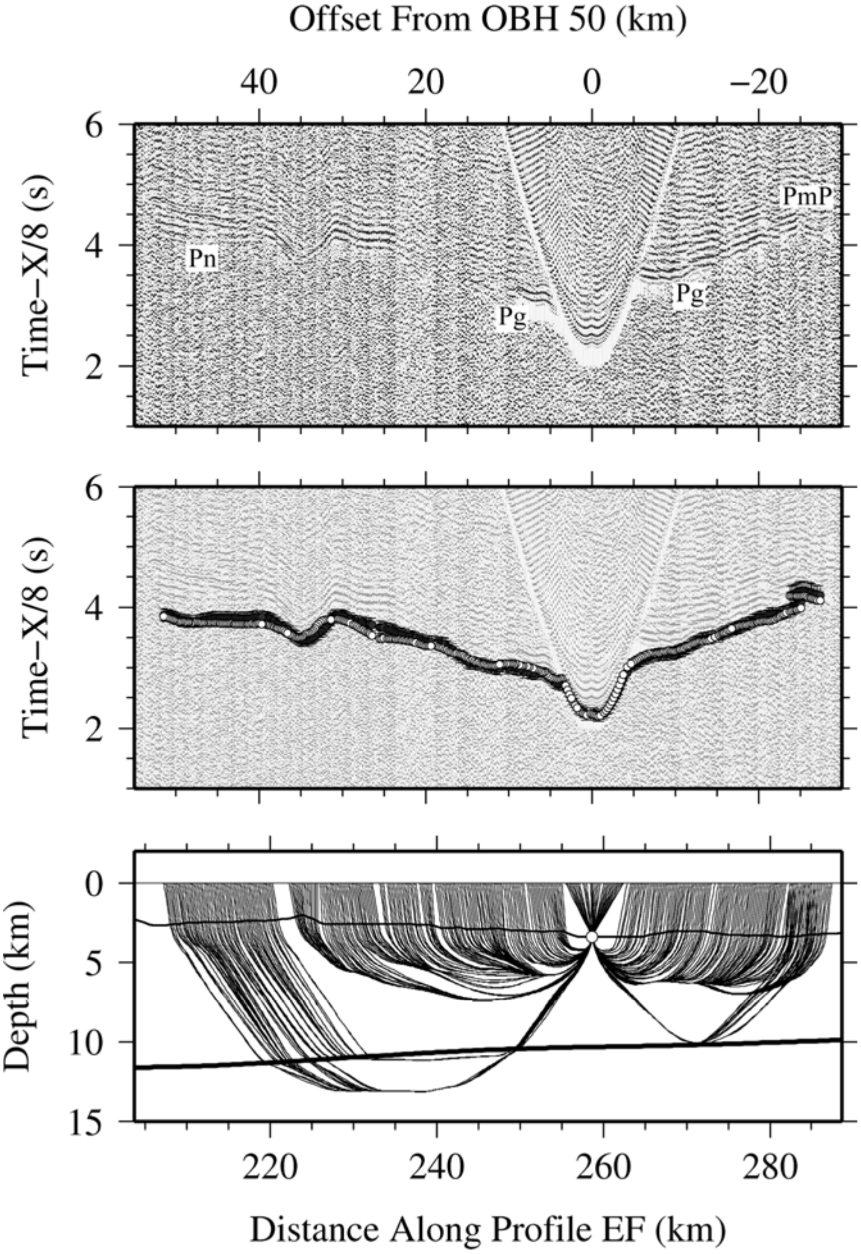

Figure A.1.2.19.- *OBH 50*

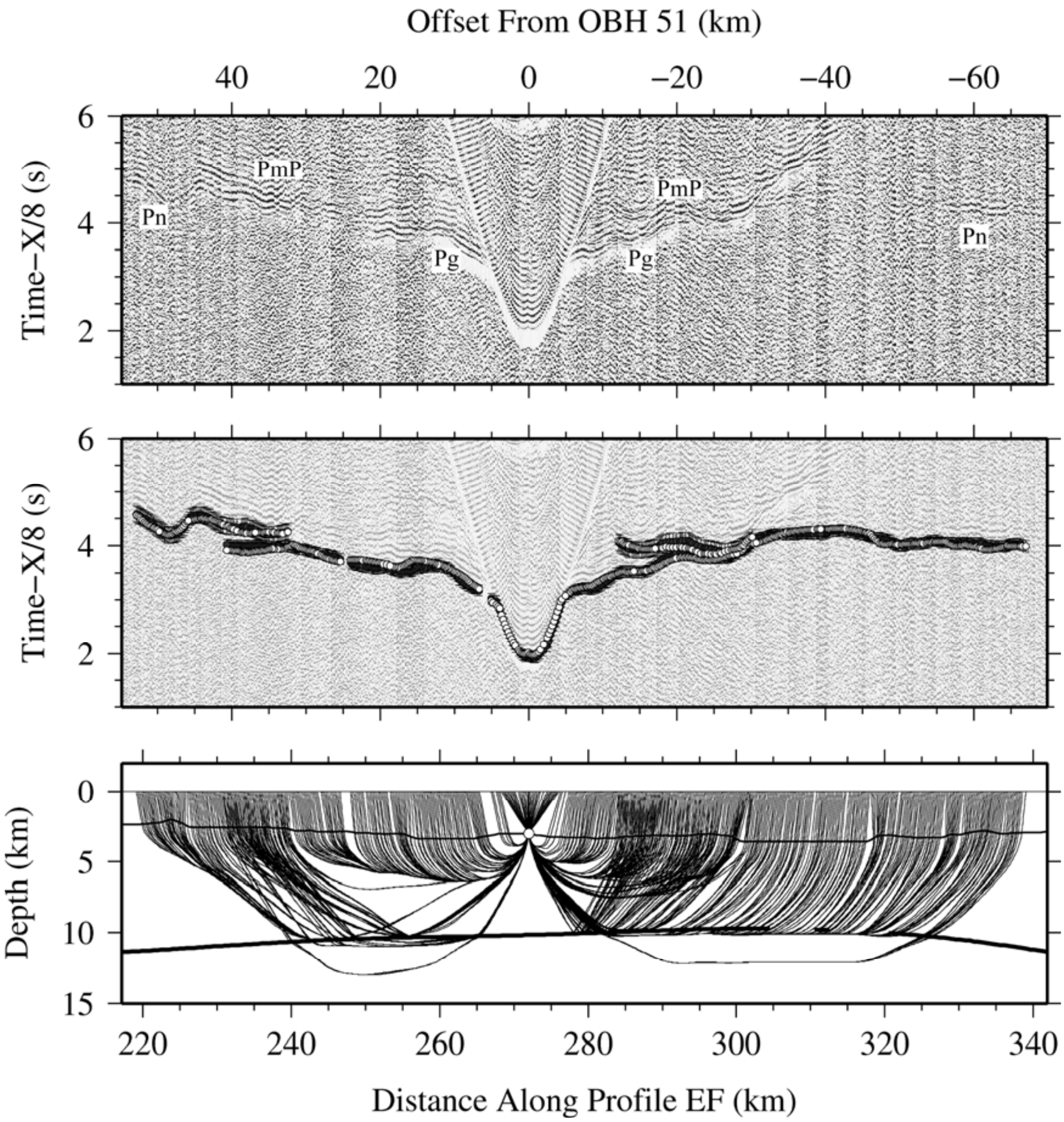

Figure A.1.2.20.- *OBH 51*

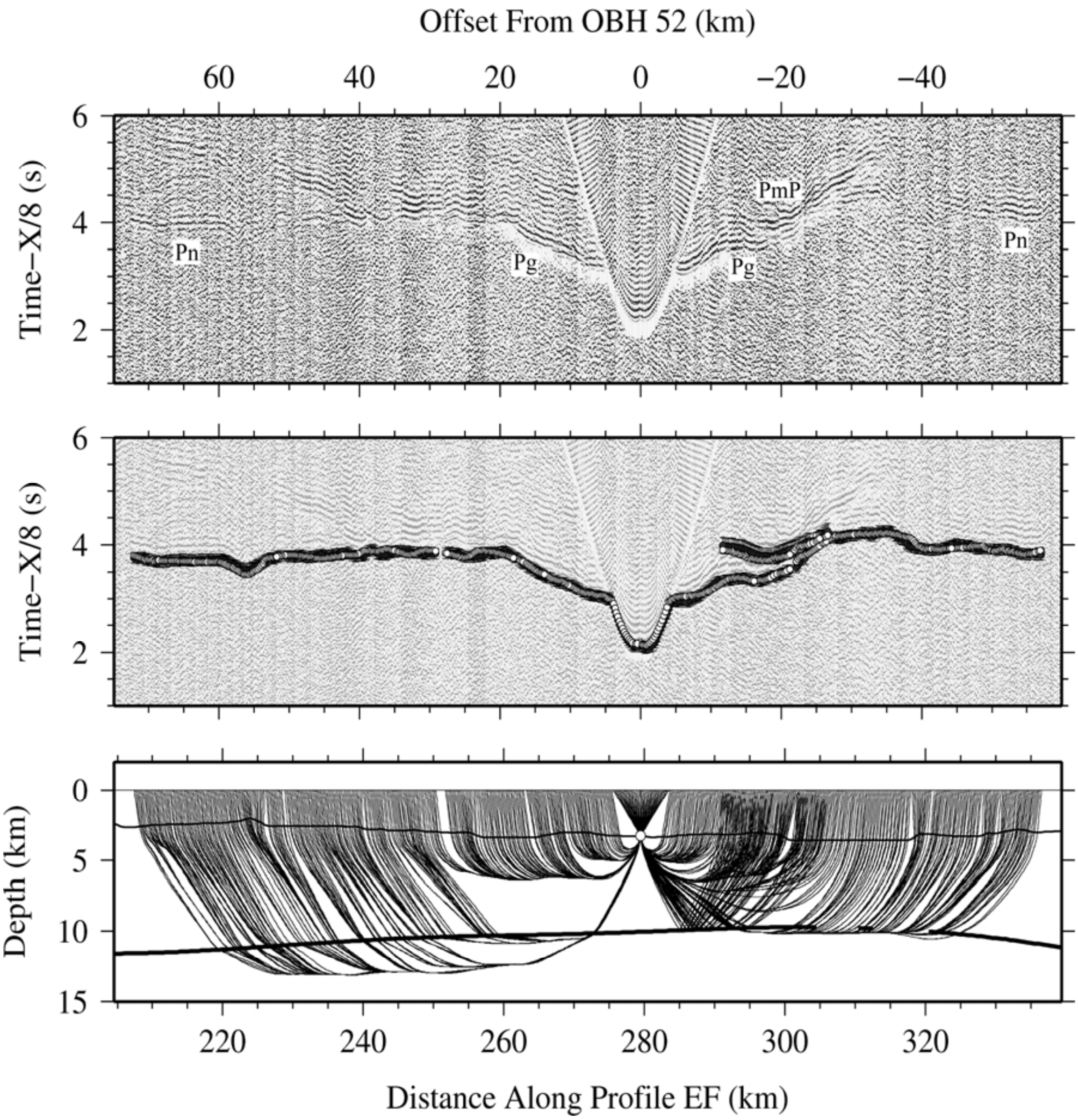

Figure A.1.2.21.- *OBH 52*

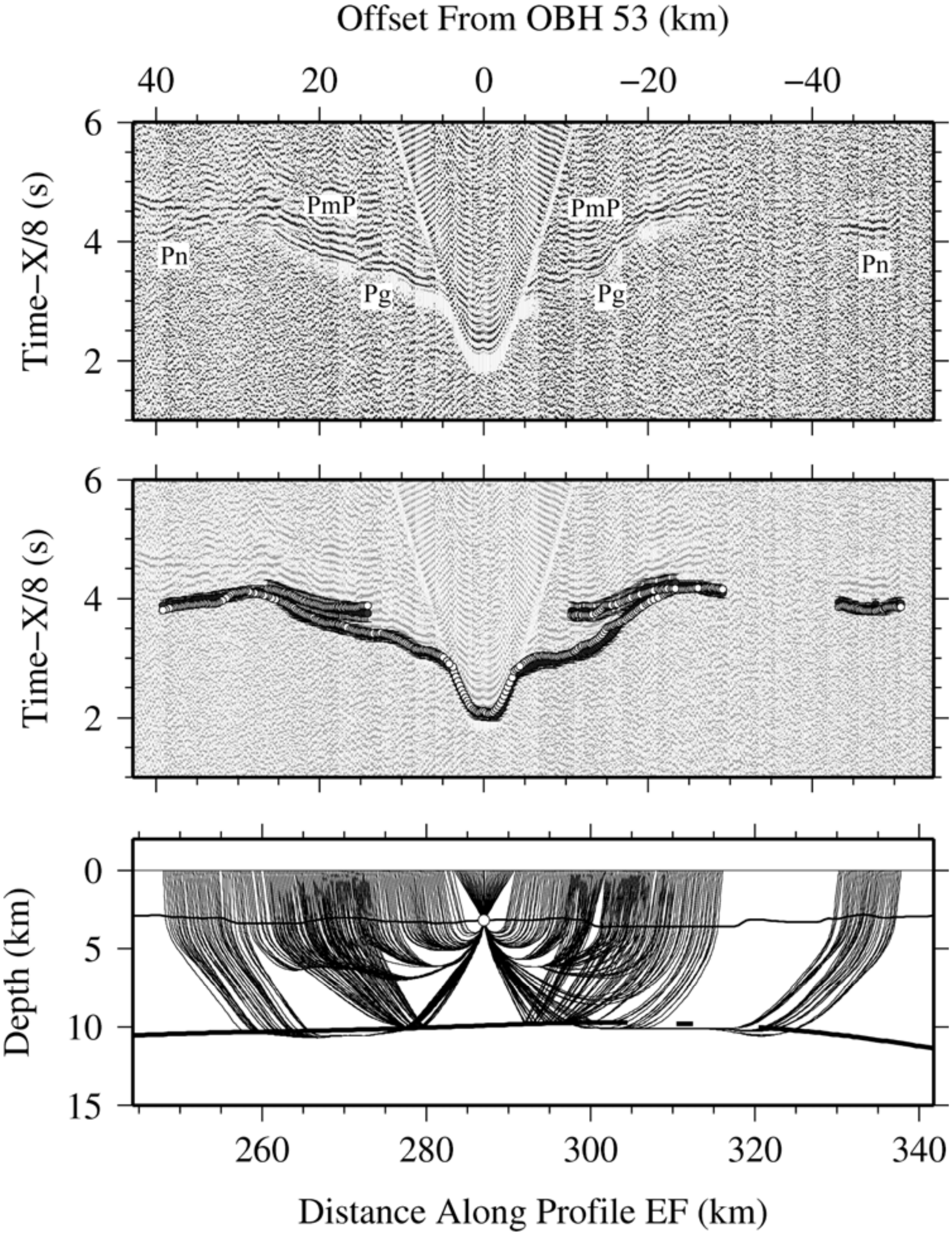

Figure A.1.2.22.- *OBH 53*

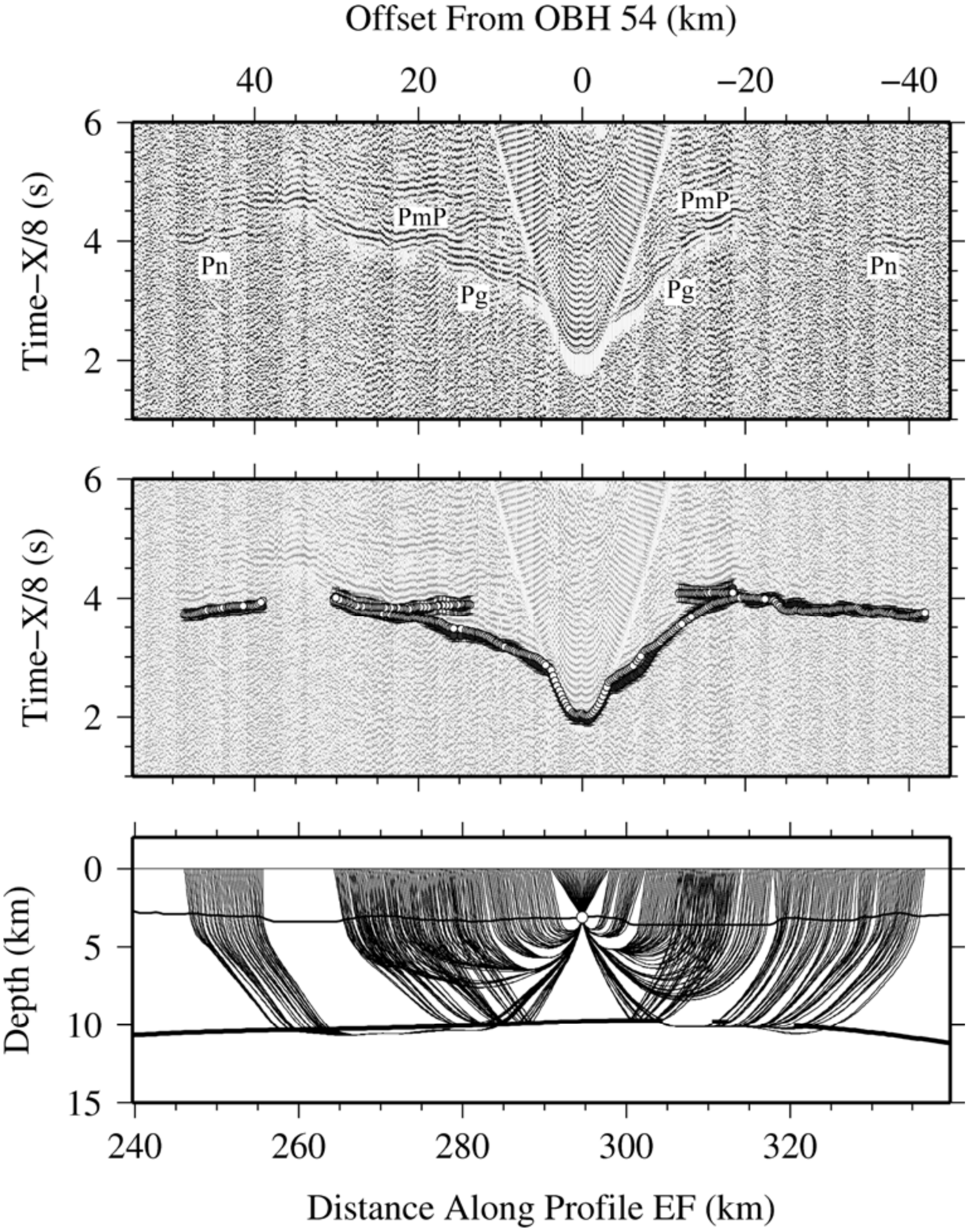

Figure A.1.2.23.- *OBH 54*

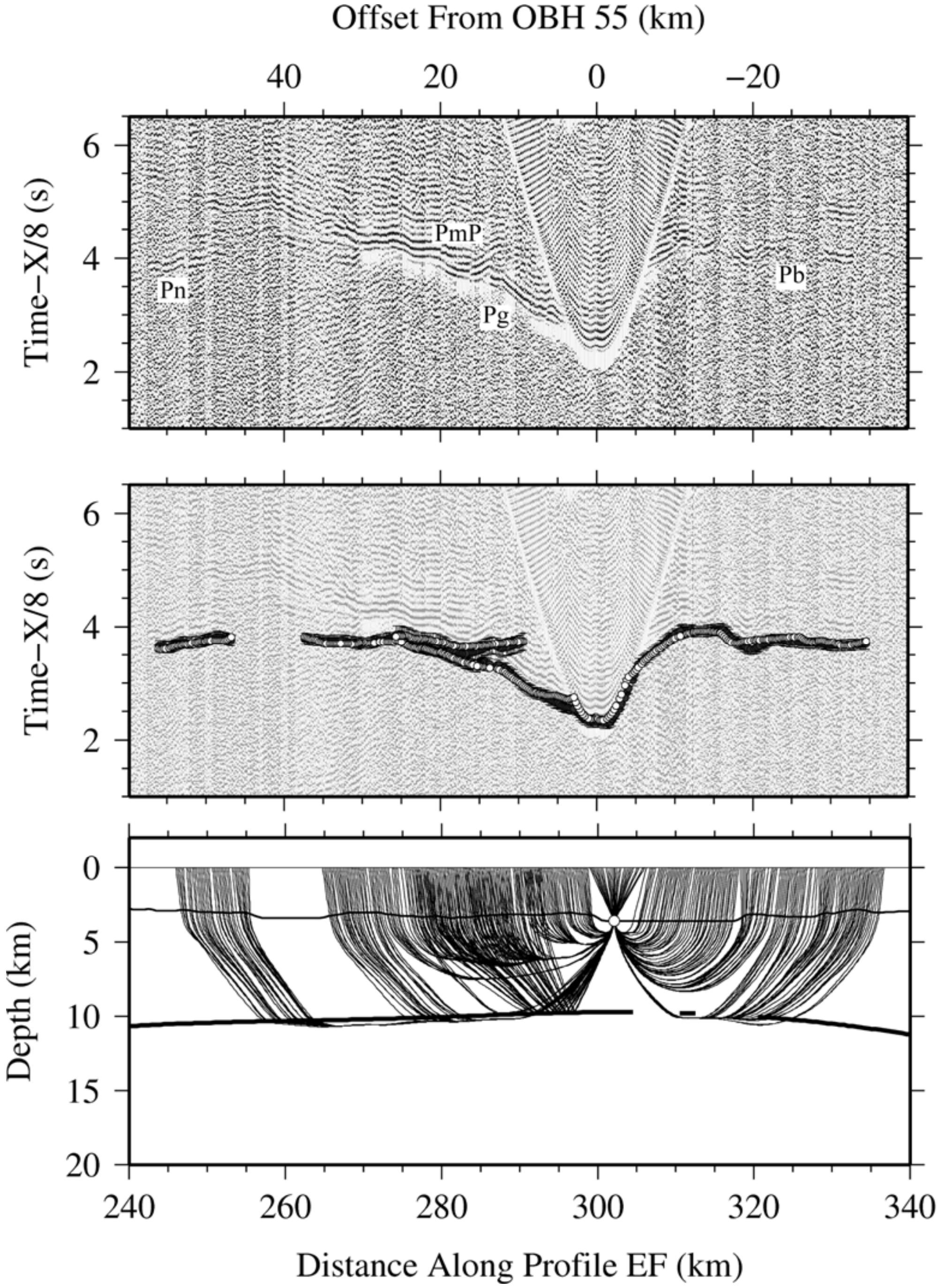

Figure A.1.2.24.- *OBH 55*

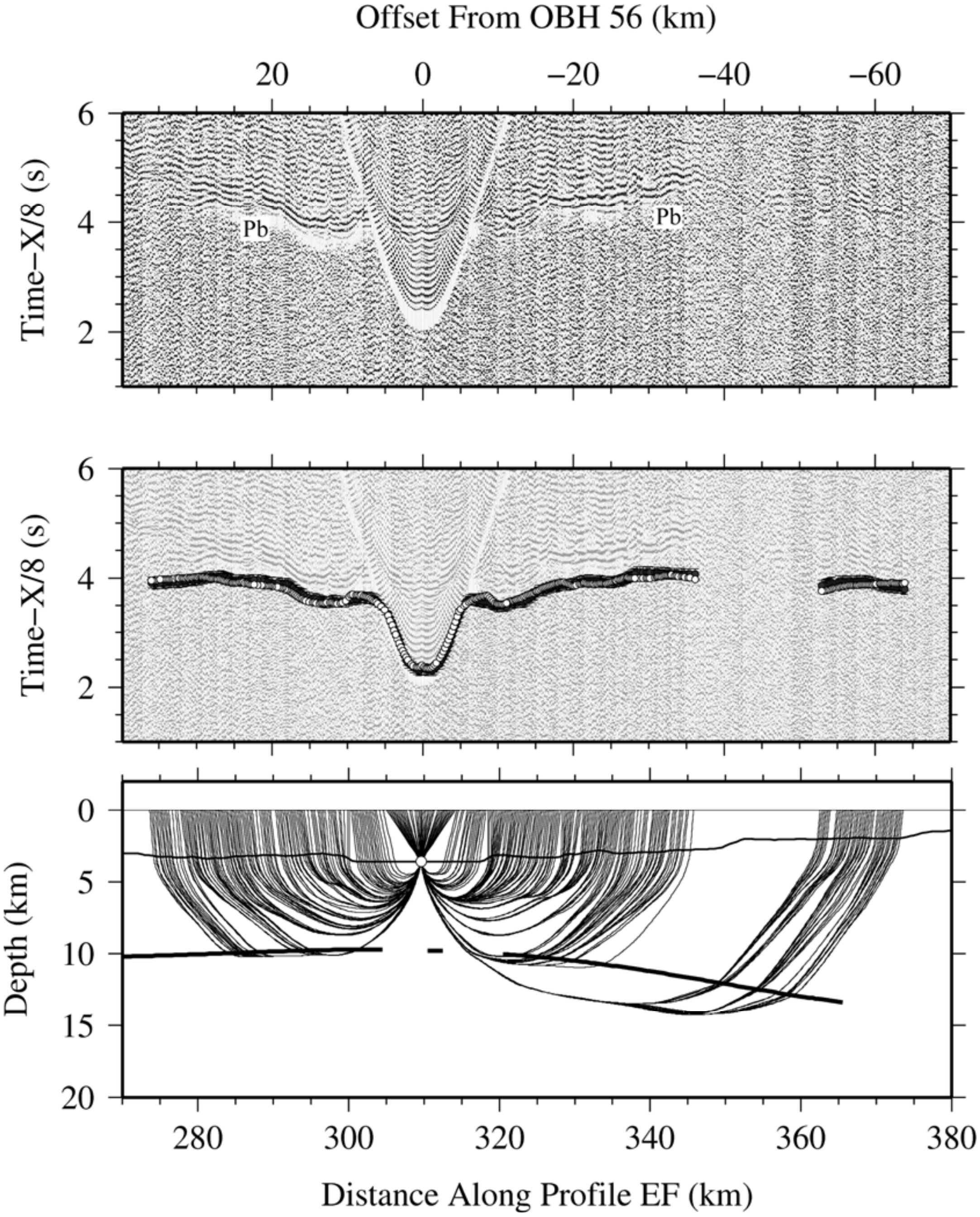

Figure A.1.2.25.- *OBH 56*

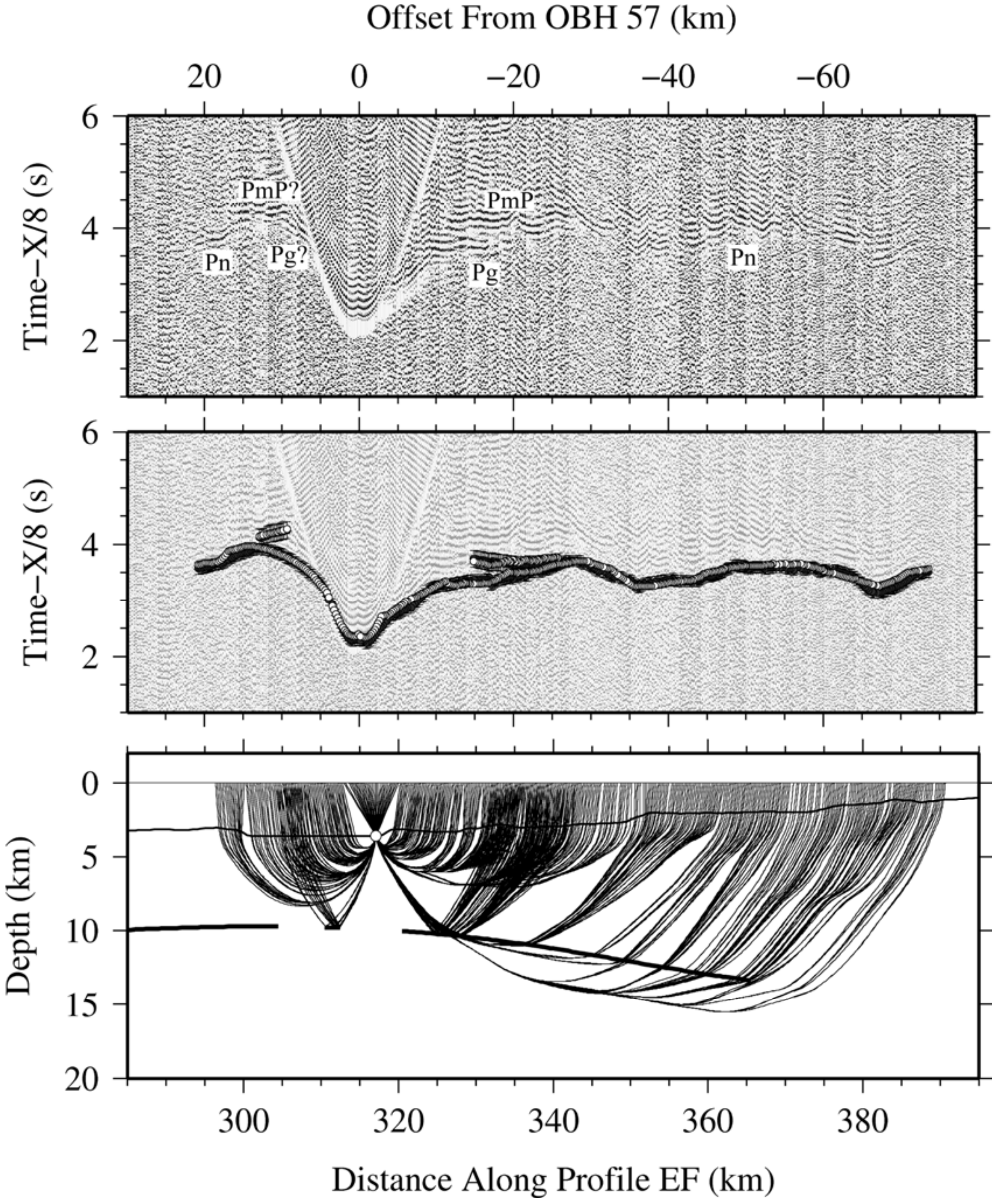

Figure A.1.2.26.- *OBH 57*

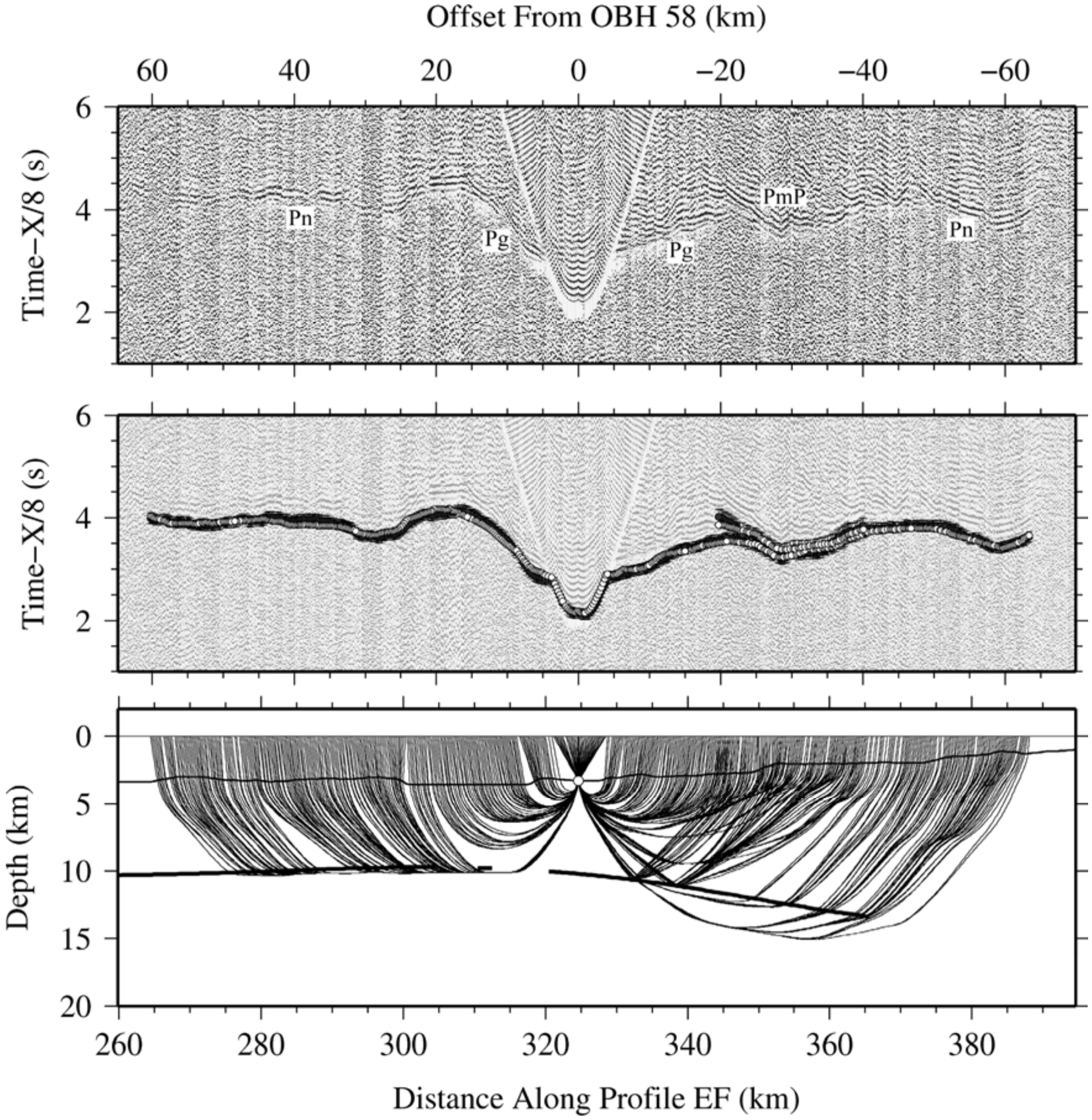

Figure A.1.2.27.- *OBH 58*

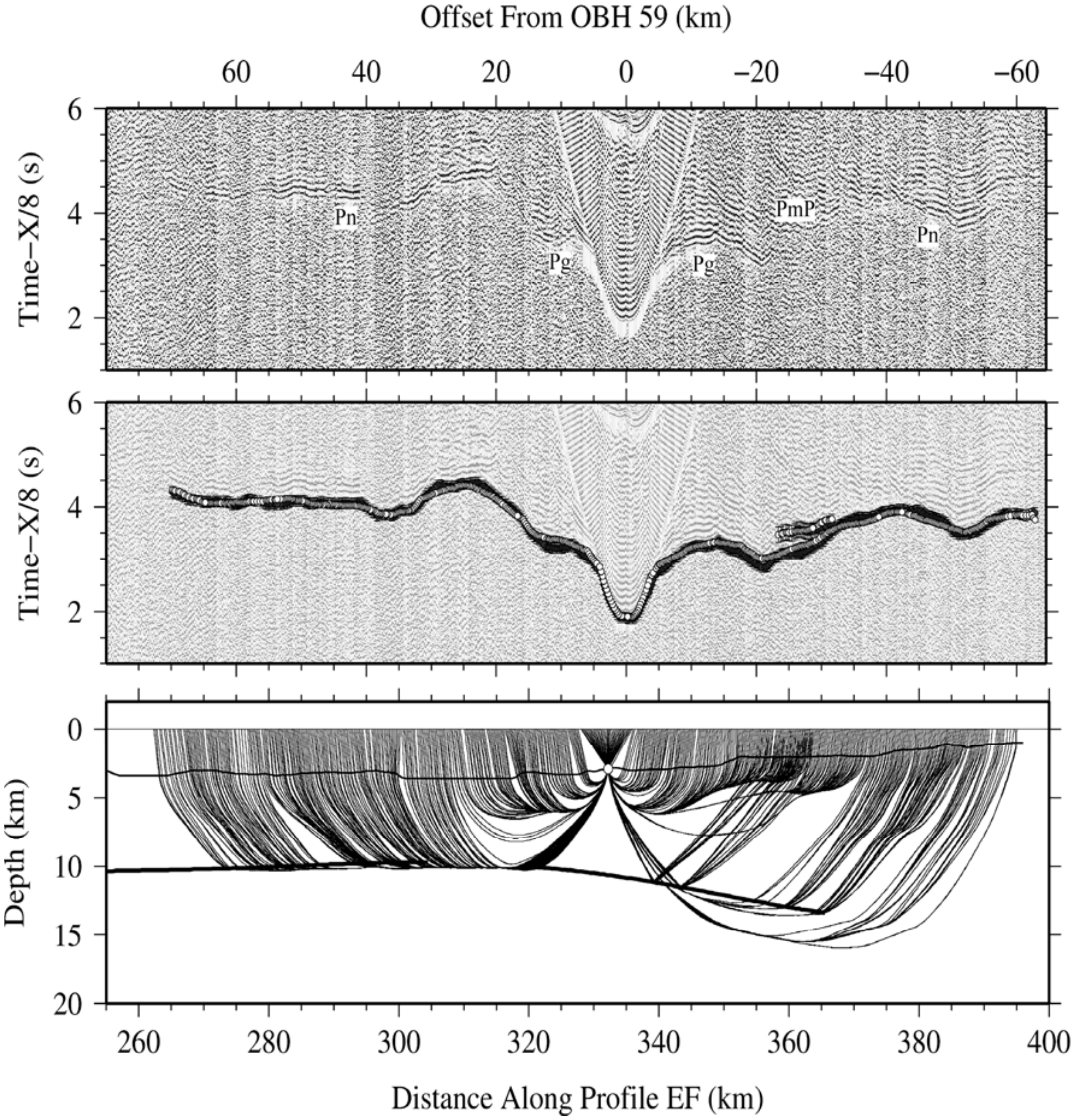

Figure A.1.2.28.- *OBH 59*

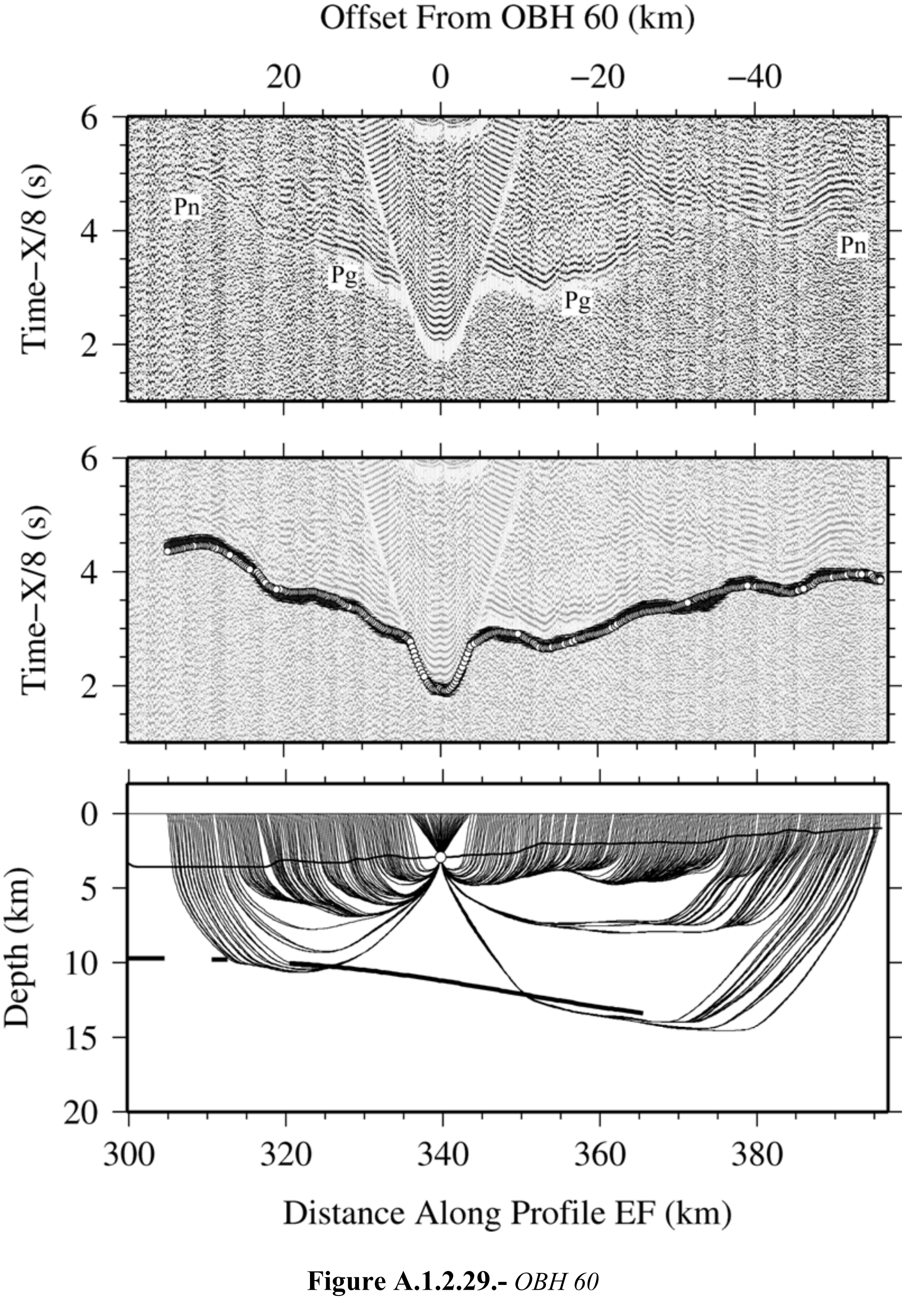

Figure A.1.2.29.- *OBH 60*

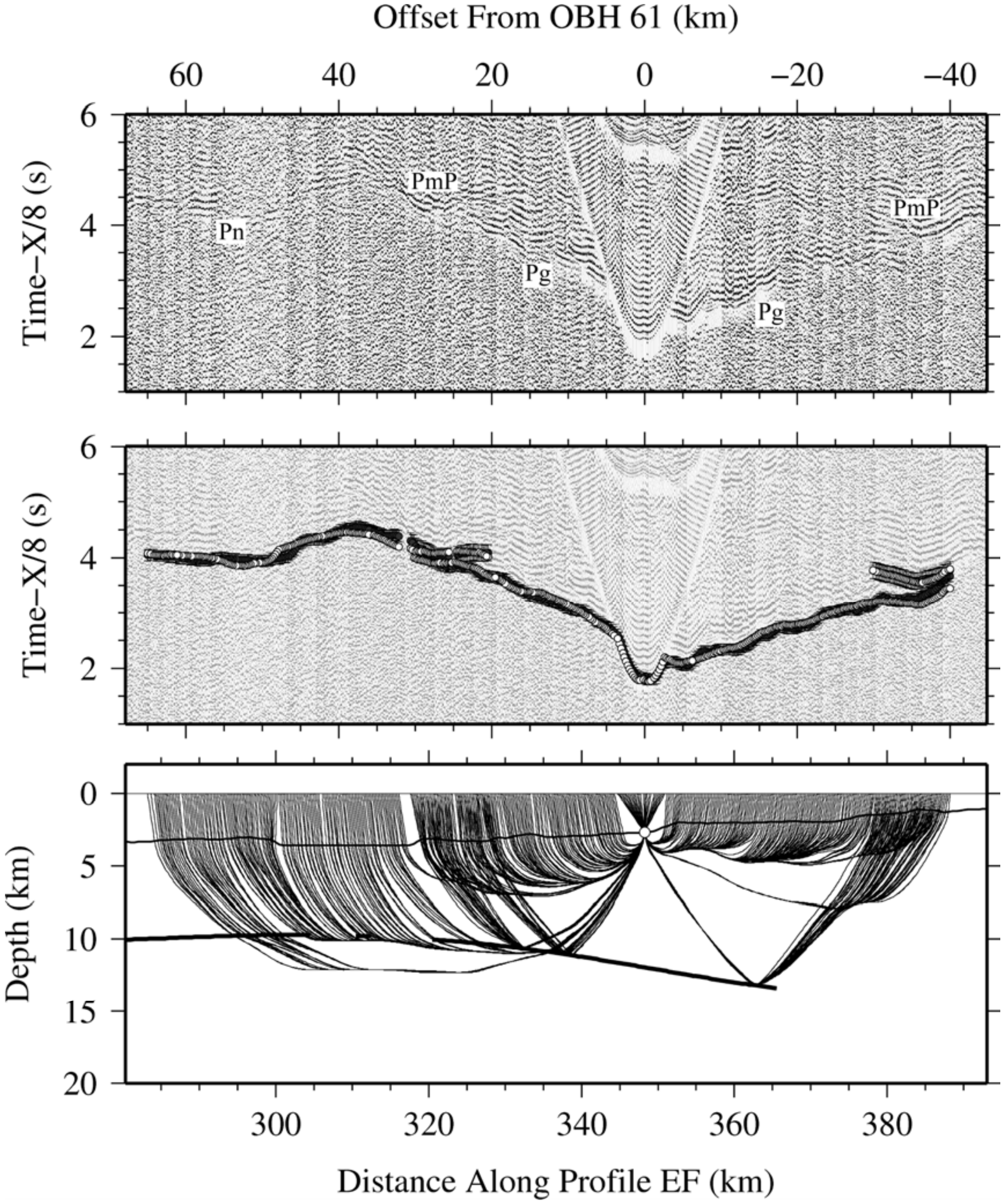

Figure A.1.2.30.- *OBH 61*

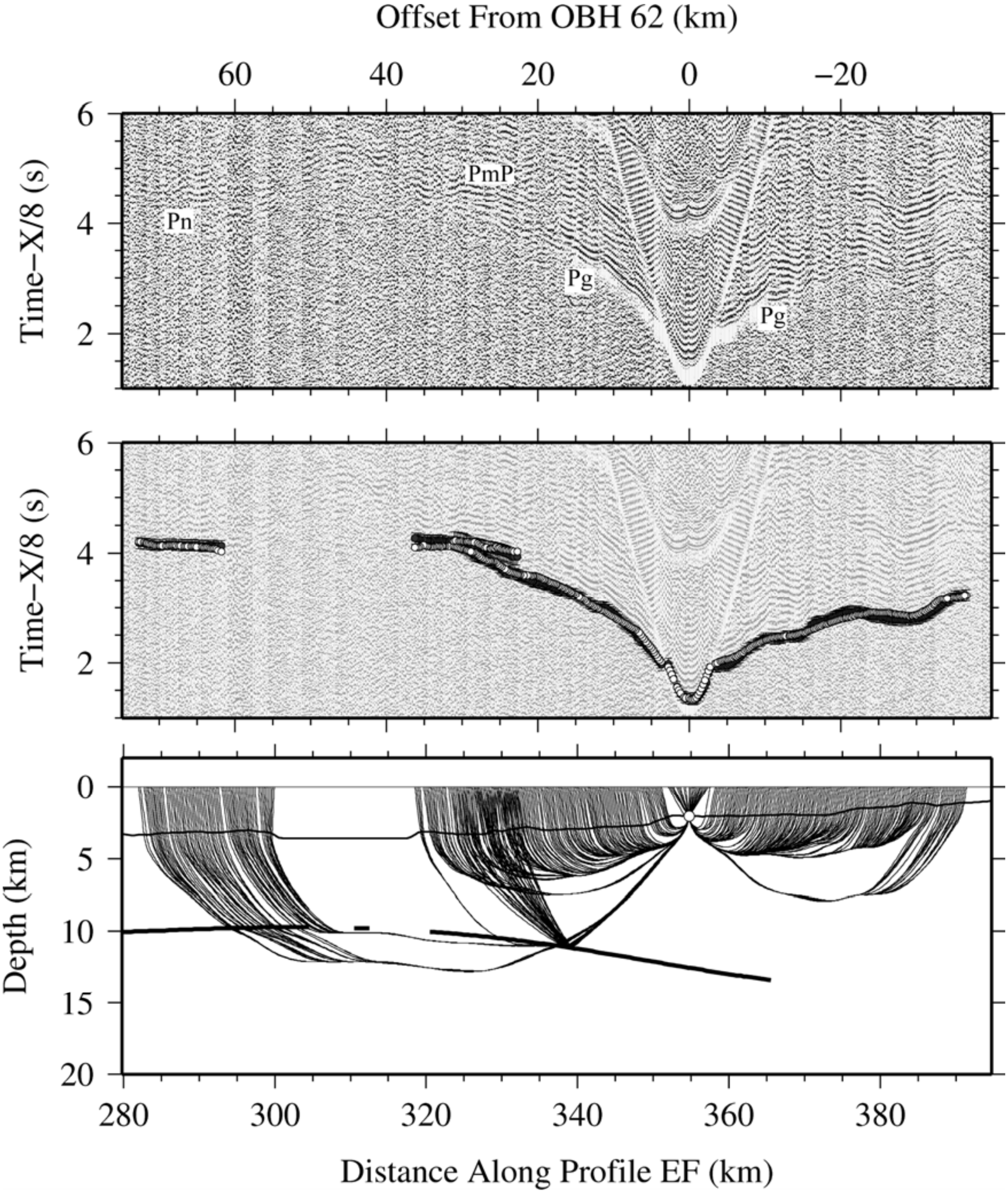

Figure A.1.2.31.- *OBH 62*

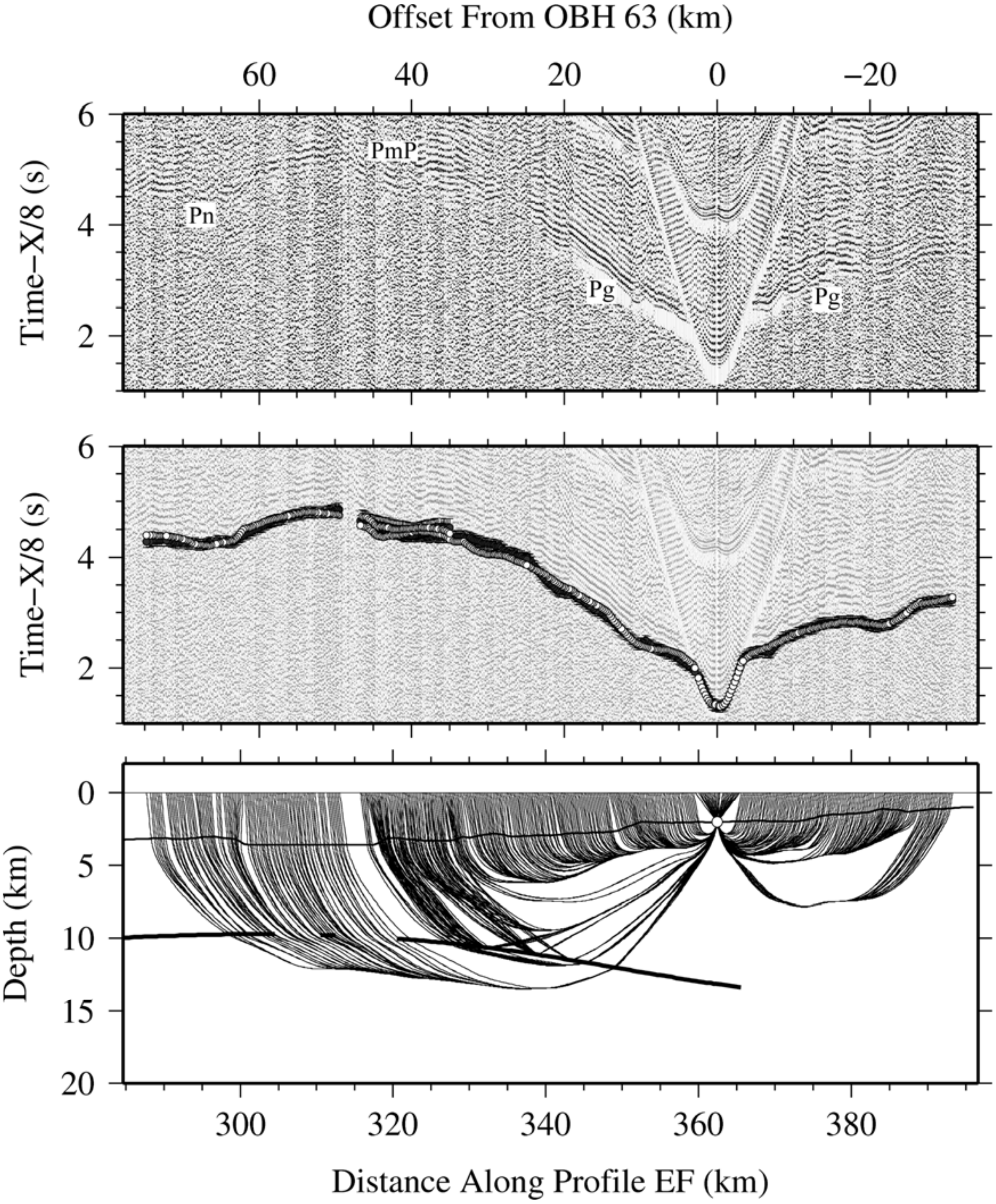

Figure A.1.2.32.- *OBH 63*

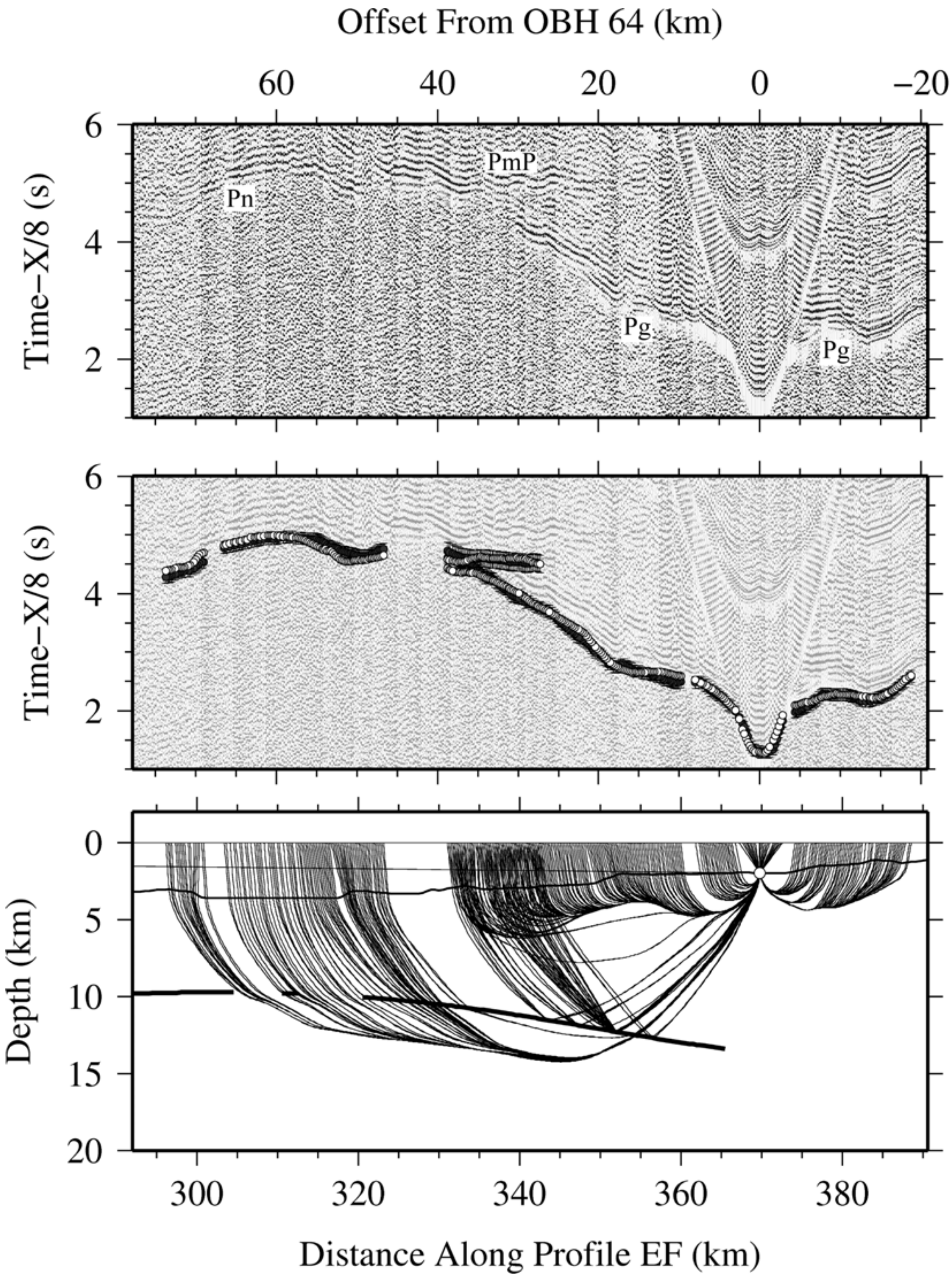

Figure A.1.2.33.- *OBH 64*

A.2 Multichannel seismic profiles

A.2.1 MEDOC 6

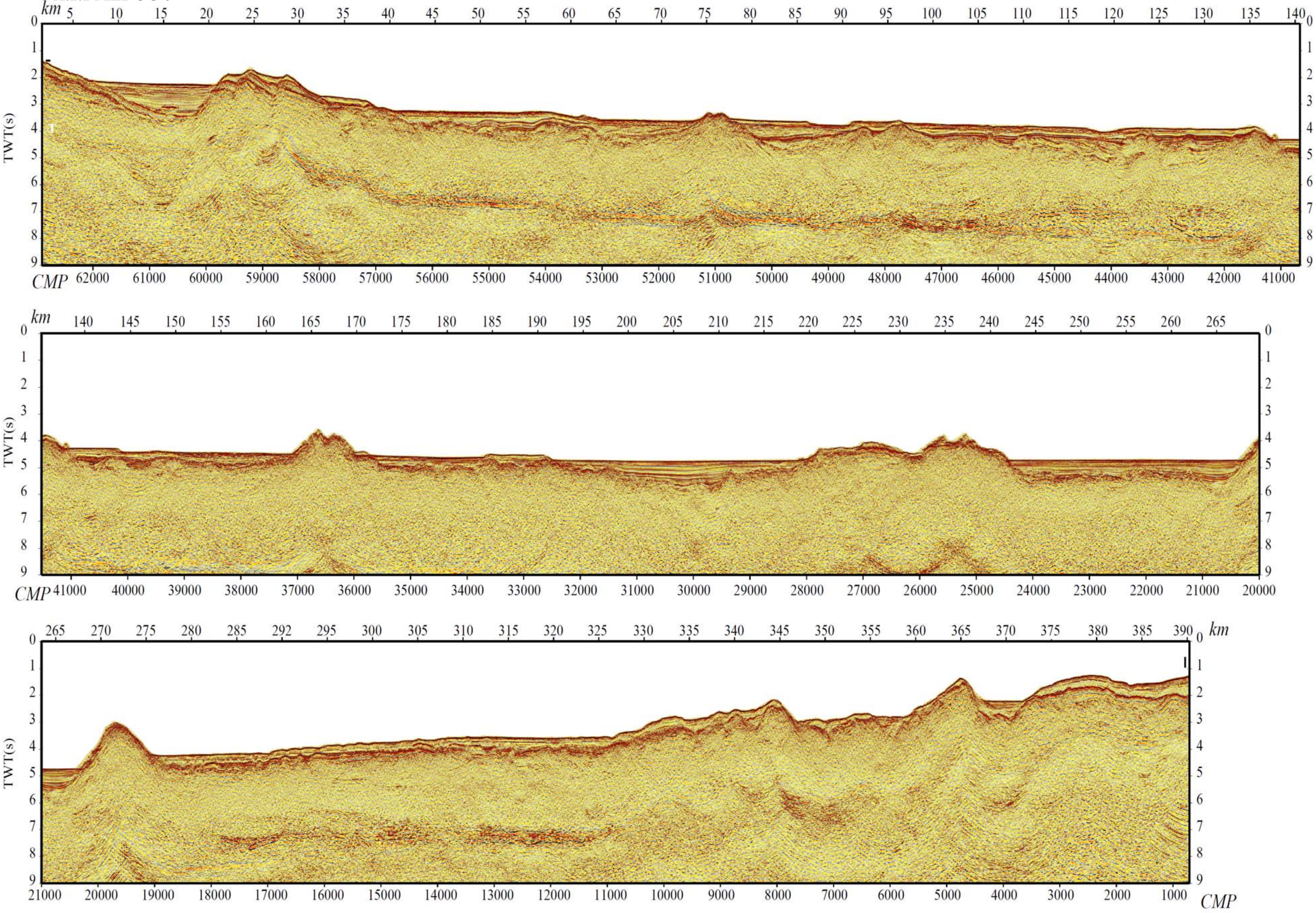

A.2.2 MEDOC 4

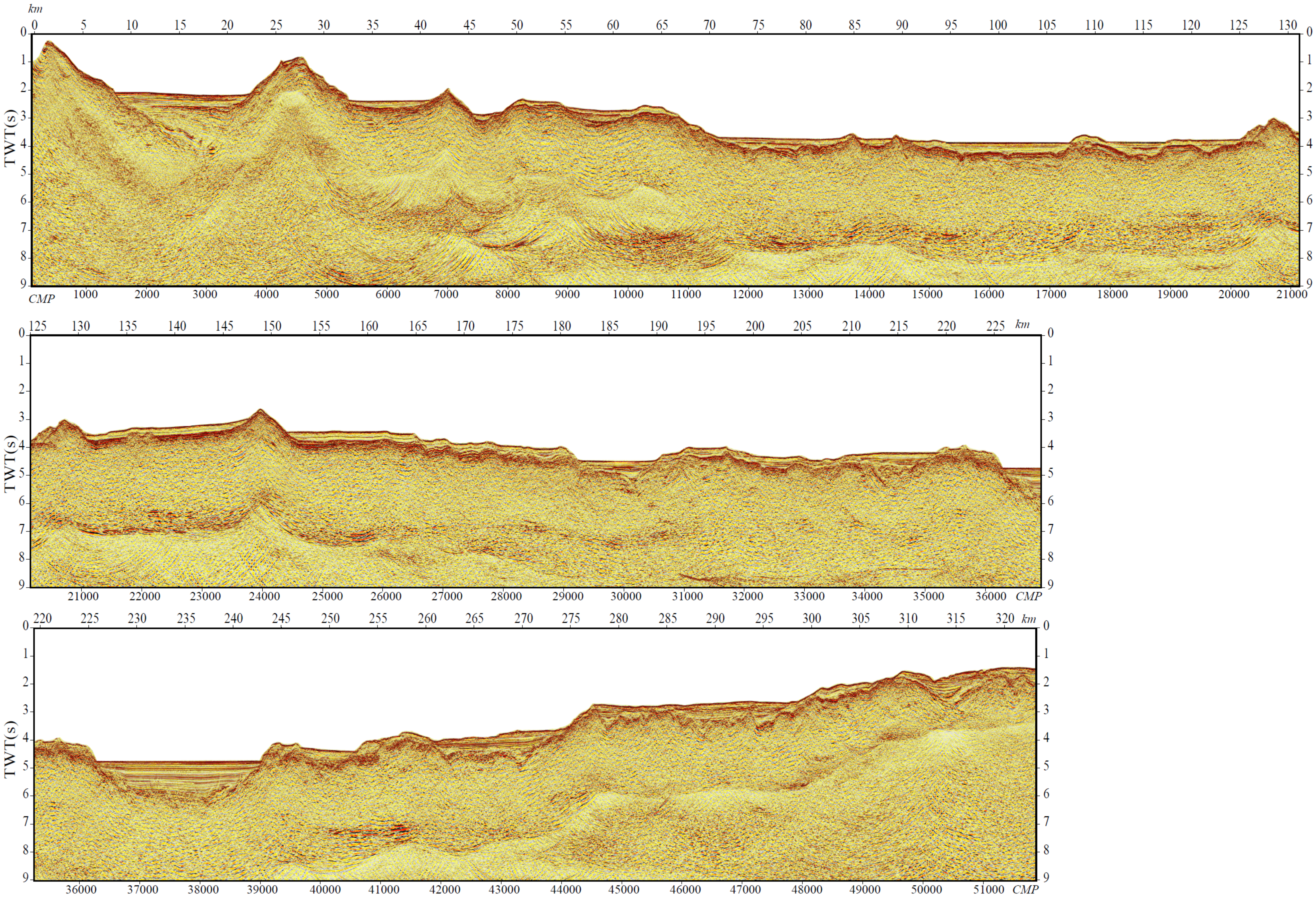
km
0 5 10 15 20 25 30 35 40 45 50 55 60 65 70 75 80 85 90 95 100 105 110 115 120 125 130
TWT(s)
0 1 2 3 4 5 6 7 8 9
CMP
1000 2000 3000 4000 5000 6000 7000 8000 9000 10000 11000 12000 13000 14000 15000 16000 17000 18000 19000 20000 21000
125 130 135 140 145 150 155 160 165 170 175 180 185 190 195 200 205 210 215 220 225 km
21000 22000 23000 24000 25000 26000 27000 28000 29000 30000 31000 32000 33000 34000 35000 36000 CMP
220 225 230 235 240 245 250 255 260 265 270 275 280 285 290 295 300 305 310 315 320 km
36000 37000 38000 39000 40000 41000 42000 43000 44000 45000 46000 47000 48000 49000 50000 51000 CMP

A.2.2.1 MEDOC 4 Processing evolution

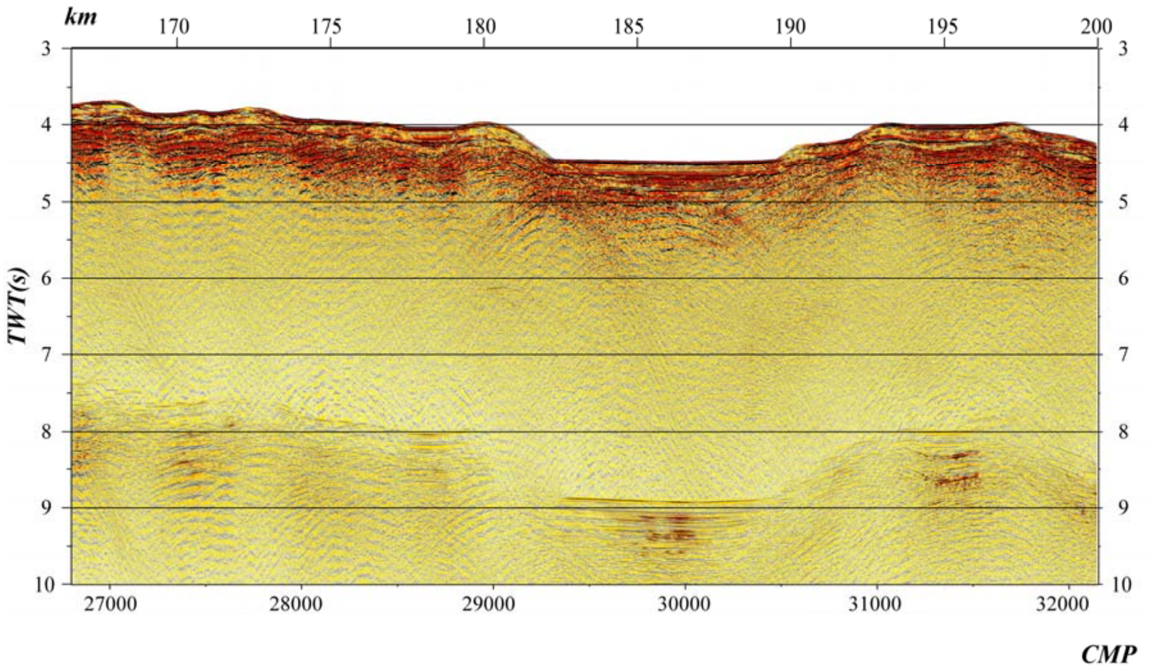

Figure A.2.2.1 .-. *Close-up of the brute stack section corresponding to profile MEDOC 4 obtained using a water velocity model.*

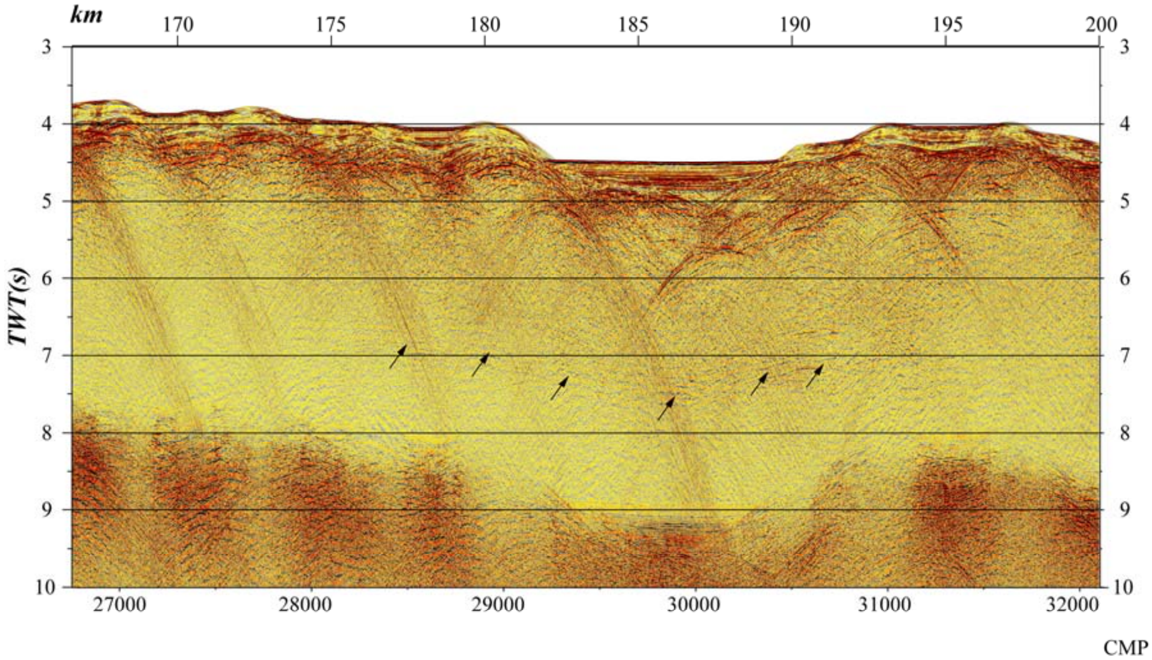

Figure A.2.2.2 .-. *Same close-up of Figure A.2.2.1showing the stack section after spherical divergence correction and predictive deconvolution. This stack has been obtained using velocities from the first velocity analysis. Note that the interpreted crust-mantle reflections are recovered (arrows).*

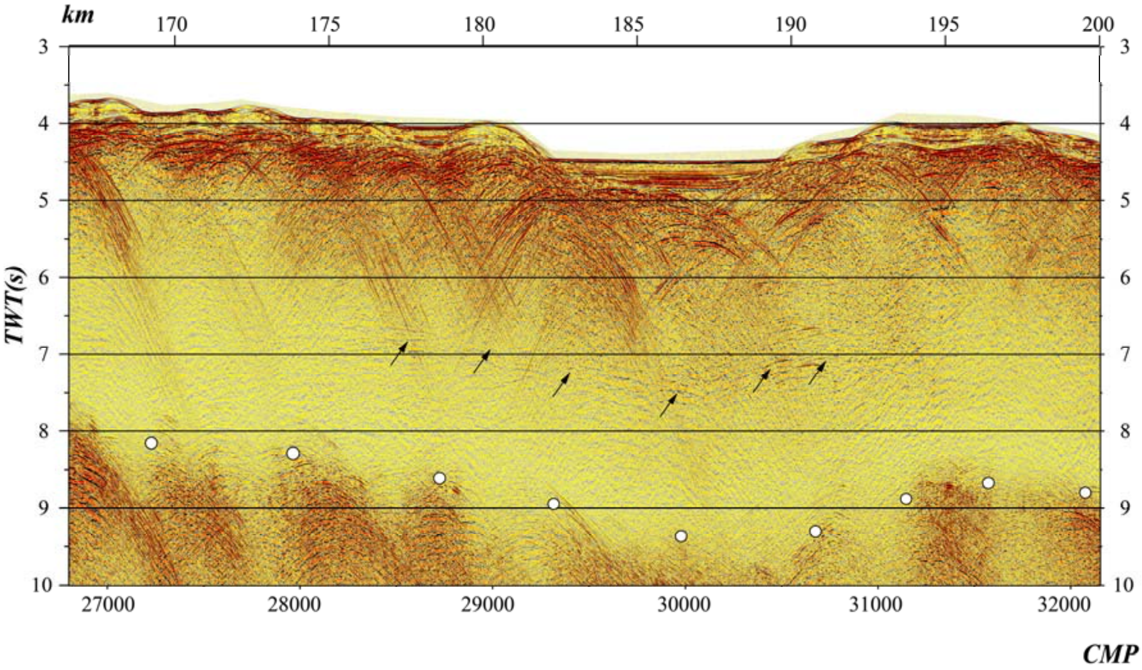

Figure A.2.2.3 .-. *Same close-up of Figure A.2.2.1 showing the stack section after spherical divergence correction, predictive deconvolution, parabolic radon demultipling and pre-stack FK filtering. The stack has been obtained using velocities from the second velocity analysis. Note the interpreted crust-mantle reflections (black arrows), and that multiple is attenuated (white circles).*

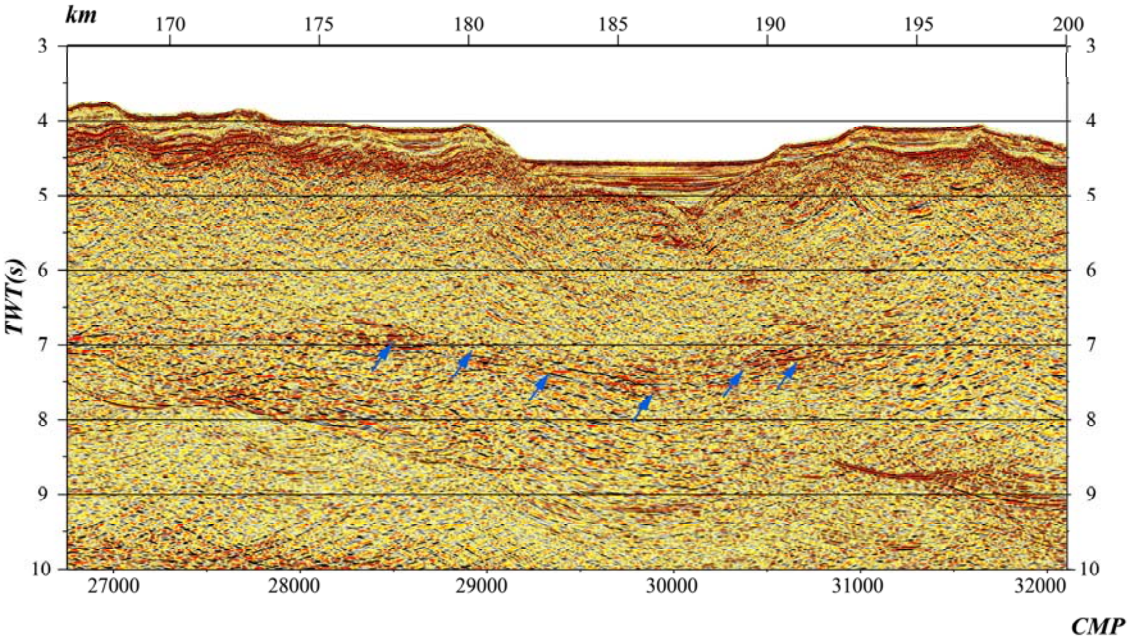

Figure A.2.2.4 .-. *Final stack section of Figure A.2.2.1 after time migration. Blue arrows depict the interpreted crust-mantle boundary.*